National Library
of Canada

Bibliothèque nationale
du Canada

Canadian Theses Service

Service des thèses canadiennes

Ottawa, Canada
K1A 0N4

NOTICE

The quality of this microform is heavily dependent upon the quality of the original thesis submitted for microfilming. Every effort has been made to ensure the highest quality of reproduction possible.

If pages are missing, contact the university which granted the degree.

Some pages may have indistinct print especially if the original pages were typed with a poor typewriter ribbon or if the university sent us an inferior photocopy.

Reproduction in full or in part of this microform is governed by the Canadian Copyright Act, R.S.C. 1970, c. C-30, and subsequent amendments.

AVIS

La qualité de cette microforme dépend grandement de la qualité de la thèse soumise au microfilmage. Nous avons tout fait pour assurer une qualité supérieure de reproduction.

S'il manque des pages, veuillez communiquer avec l'université qui a conféré le grade.

La qualité d'impression de certaines pages peut laisser à désirer, surtout si les pages originales ont été dactylographiées à l'aide d'un ruban usé ou si l'université nous a fait parvenir une photocopie de qualité inférieure.

La reproduction, même partielle, de cette microforme est soumise à la Loi canadienne sur le droit d'auteur, SRC 1970, c. C-30, et ses amendements subséquents.

NL-339 (r. 88/04) c

Canada

UNIVERSITY OF ALBERTA

Analysis of Electrical and Physical Properties of Ion-Selective Liquid Membranes

BY

Andy Dart Chi Chan ©

A Thesis Submitted
To The Faculty of Graduate Studies and Research
In Partial Fulfillment Of The Requirements For The Degree Of
Doctor of Philosophy

Department of Chemistry

Edmonton, Alberta

Spring, 1992

National Library
of Canada

Bibliothèque nationale
du Canada

Canadian Theses Service

Service des thèses canadiennes

Ottawa, Canada
K1A 0N4

The author has granted an irrevocable non-exclusive licence allowing the National Library of Canada to reproduce, loan, distribute or sell copies of his/her thesis by any means and in any form or format, making this thesis available to interested persons.

L'auteur a accordé une licence irrévocable et non exclusive permettant à la Bibliothèque nationale du Canada de reproduire, prêter, distribuer ou vendre des copies de sa thèse de quelque manière et sous quelque forme que ce soit pour mettre des exemplaires de cette thèse à la disposition des personnes intéressées.

The author retains ownership of the copyright in his/her thesis. Neither the thesis nor substantial extracts from it may be printed or otherwise reproduced without his/her permission.

L'auteur conserve la propriété du droit d'auteur qui protège sa thèse. Ni la thèse ni des extraits substantiels de celle-ci ne doivent être imprimés ou autrement reproduits sans son autorisation.

ISBN 0-315-73136-2

Canada

UNIVERSITY OF ALBERTA

RELEASE FORM

NAME OF AUTHOR: **Andy D. C. Chan**

TITLE OF THESIS: **Analysis of Electrical and Physical Properties of Ion-Selective Liquid Membranes**

DEGREE: **Doctor of Philosophy**

YEAR THIS DEGREE GRANTED: **1992**

Permission is hereby granted to the University of Alberta Library to reproduce single copies of this thesis and to lend or sell such copies for private, scholarly or scientific research purposes only.

The author reserves all other publication and other rights in association with the copyright in the thesis, and except as hereinbefore provided neither the thesis nor any substantial portion thereof may be printed or otherwise reproduced in any material form whatever without the author's prior written permission.

AUTHOR'S SIGNATURE: andy C

PERMANENT ADDRESS: **299 Whitmore Drive**
Waterloo, Ontario
N2K 2M5

DATE: **January 31, 1992**

UNIVERSITY OF ALBERTA

FACULTY OF GRADUATE STUDIES AND RESEARCH

The undersigned certify that they have read, and recommend to the Faculty of Graduate Studies and Research for acceptance, a thesis entitled **Analysis of Electrical and Physical Properties of Ion-Selective Liquid Membranes** submitted by **Andy D. C. Chan** in partial fulfillment of the requirements for the degree of **Doctor of Philosophy**.

SUPERVISOR: Jed Harrison
Dr. D. J. Harrison

F. F. Cantwell
Dr. F. F. Cantwell

Dr. N. J. Dovichi

George Kotovych
Dr. G. Kotovych

I. Filanovsky
Dr. I. Filanovsky

EXTERNAL READER:
Dr. L. G. Bachas
University of Kentucky

DATE: **January 28, 1992**

Abstract

A better understanding of ion-selective response mechanisms is desired for liquid membrane ion-selective electrodes (ISEs) based on plasticized poly(vinyl chloride) (PVC) matrices. The research presented in this work contributes to this effort by examining both electrical and physical properties of these membranes.

The implementation of a fast Fourier transform based electrochemical impedance spectroscopy system is described. This technique is used to investigate neutral species behavior in the membrane phase. It is demonstrated that subtle physical changes in the membrane matrix induced by additives can be very significant compared to direct ionic changes in determining membrane electrical behavior. A transport theory involving adsorbed carrier-complexed species is also presented to account for unique "inductive" impedance behavior observed in a Ca^{+2}-sensitive ion exchanger ISE membrane system.

Physical properties of the membrane matrix are also investigated using Fourier transform infrared, ^{1}H and ^{2}D variable temperature nuclear magnetic resonance (NMR) spectroscopies, ^{13}C spin-lattice NMR relaxation, gravimetry, and tensilometry. A detailed study of the nature of water within the membrane phase is presented. Results indicate that water exists in the membrane as small (*ca.* 0.016 μm diameter) clusters at low concentrations, and as larger droplets at higher concentrations. The uptake of water is shown to affect the properties of the membrane matrix, particularly the mobility of the plasticizer component. Evidence is also given for the existence of a surface rich water region in the membrane.

Acknowledgements

During the course of my studies at the University of Alberta, I have had the pleasure of working with several talented people. They have all contributed to my education and made my time here more enjoyable.

First, and foremost, my most sincere thanks go to Professor D. Jed Harrison, my research advisor, without whom none of the work presented in this thesis would have materialized. I thank you for your patient guidance and for always managing to find the time when I needed advice. You may not have been aware, but you have been (and always will be) a continued source of inspiration.

I thank also all the other members in Professor Harrison's research group for sharing their experience and wisdom over the years. In particular, Sabeth Verpoorte for her sage advice in the initial stages of the impedance studies, Xizhong Li for his helpful discussions of water in ISE membranes, and Alebachew Demoz for his insights, scientific and otherwise. And, I am grateful to Dan Raymond, Paul Glavina, Zhonghui Fan, Kwok-Keung Shiu, Alem Teclemariam, Rob Turner, and Zhong Li for their friendship and support. They have all helped make the bad times good, and the good times better.

My appreciation is also extended to the various shops and services within the Department of Chemistry. In particular, the members of the magnetic resonance laboratory for their help during the NMR studies: Tom Brisbane, Glen Bigam, Gerdy Aarts, Dr. Tom Nakashima and Lai C. Kong. Special thanks go to Ernie Young of the machine shop for the design and construction of the impedance cells and water jacket. I'd like to also acknowledge the assistance of Daryl Goertzen (Department of Mechanical Engineering) in the tensilometry experiments presented in Chapter 8.

To my parents, brothers and sisters, I thank you for the love and support you have given me throughout my student years. Thanks for always believing in me during the rough times!

Finally, to my varied sources of inspiration and motivation: Coppi, Bartali, Longo and LeMond . . . . .

Table of Contents

Chapter 1 Introduction 1

1.1 The Ion-Sensitive Electrode 2
  1.1.1 Historical Perspective 3
  1.1.2 Principles and Design 4
  1.1.3 Ion Transport Theory 7
1.2 *AC* Impedance Analysis 8
  1.2.1 Introduction to *AC* Impedance 8
  1.2.2 Electrochemical Impedance Spectroscopy 12
1.3 NMR Spin-Lattice Relaxation 18
  1.3.1 NMR Basics 18
  1.3.2 NMR Relaxation 19
  1.3.3 Determination of T_1 Relaxation Times 20
  1.3.4 Applications of NMR Relaxation Measurements 22
1.4 Scope of Present Work 22
1.5 References 25

Chapter 2 The Implementation of a System for Fast Fourier Transform Electrochemical Impedance Spectroscopy 28

2.1 Introduction 28
2.2 Electrochemical Impedance Spectroscopy 29
  2.2.1 Concepts 29
  2.2.2 Frequency Domain Measurement 30
  2.2.3 Time Domain Measurement 31
2.3 Fast Fourier Transform Electrochemical Impedance Spectroscopy Measurement System 36
  2.3.1 Instrumentation 36
  2.3.2 Waveform Generation 40
  2.3.3 EIS Measurement 43
  2.3.4 EIS Calculations 47
  2.3.5 EIS System Calibration 48
  2.3.6 EIS Data Presentation 51

2.3.7 Automated EIS Experiments 51
2.4 Characterization of Electrochemical Impedance Spectroscopy Measurement Systems 58
2.4.1 Dummy Cell Circuits 58
2.4.2 Computer Modelling of Dummy Cell Circuits 58
2.4.3 Lock-In EIS System Characterization 61
2.4.4 FFT-EIS System Characterization 67
2.5 Conclusions 71
2.6 References 73

Chapter 3 *AC* Impedance Analysis of Neutral Species Behavior in Ion-Selective Electrode Membranes 74

3.1 Introduction 74
3.2 Experimental 76
3.3 Results and Discussion 81
3.3.1 Reproducibility of *AC* Impedance Membrane Data 81
3.3.1.1 Measurement Specific Variables 82
3.3.1.2 Sample Specific Variables 88
3.3.1.3 Overall Reproducibility of *AC* Impedance Membrane Data 97
3.3.2 Impurities in Membrane Matrices 99
3.3.2.1 DOA Plasticizer Component 99
3.3.2.2 PVC Polymer Component 101
3.3.2.3 Analysis of Plasticizer Impurities 103
3.3.3 Neutral Species Behavior 112
3.3.3.1 Origins of Membrane Bulk and Charge Transfer Resistivities 113
3.3.3.2 Benzoic Acid-Containing Membranes 115
3.3.3.3 Methyl Benzoate-Containing Membranes 121
3.3.3.4 Comparison Between Benzoic Acid and Methyl Benzoate Behavior 126
3.4 Conclusions 127
3.5 References 129

Chapter 4 *AC* Impedance Study of a Plasticized Poly(vinyl chloride) Ca^{+2} Ion-Exchanger Electrode 132

4.1 Introduction 132
4.2 Theoretical Treatment 133
  4.2.1 Background 133
  4.2.2 Proposed Transport Model 134
  4.2.3 Derivation of the Impedance 136
  4.2.4 Proposed Overall Membrane Equivalent Circuit 142
  4.2.5 Impedance Behavior of Proposed Overall Membrane Equivalent Circuit 143
4.3 Experimental 149
4.4 Results and Discussion 151
  4.4.1 General Impedance Characteristics 151
    4.4.1.1 Blank *versus* Normal Membranes 151
    4.4.1.2 Bulk Impedance Behavior 151
    4.4.1.3 Warburg Impedance Behavior 155
    4.4.1.4 Inductive Impedance Behavior 156
  4.4.2 Equivalent Circuit Analysis 159
    4.4.2.1 Extraction of Equivalent Circuit Elements 159
    4.4.2.2 Significance of Equivalent Circuit Elements 160
  4.4.3 Specific Impedance Characteristics 164
    4.4.3.1 Effect of Amplitude of Potential Perturbation 165
    4.4.3.2 Effect of Bathing Solution Concentration 168
    4.4.3.3 Surface Active Reagents 169
    4.4.3.4 Voltage Effects 170
      4.4.3.4.1 Current-Voltage Curves 170
      4.4.3.4.2 Effect of Electrolysis 175
4.5 Tendency Towards Inductive Impedance Behavior 176
4.6 Conclusions 180
4.7 References 181

Chapter 5 Carbon-13 Spin-Lattice Relaxation Studies of Ion-Selective Membranes 184

5.1 Introduction 184
5.2 Experimental Section 187
5.3 Results 188
5.4 Discussion 197
  5.4.1 Neat DOA Plasticizer 198
  5.4.2 DOA and PVC Mixtures 199
  5.4.3 Effect of Water Exposure 203
5.5 Conclusions 207
5.6 References 209

Chapter 6 An Investigation Of Water Absorbed Inside An Ion-Selective Membrane 212

6.1 Introduction 212
6.2 Experimental 216
6.3 Results and Discussion 218
  6.3.1 Water in Neat DOA Plasticizer 218
  6.3.2 Water in 66 % DOA/PVC Membranes 221
    6.3.2.1 Low $KBPh_4$ Membranes 232
    6.3.2.2 High $KBPh_4$ Membranes 238
  6.3.3 Effect of Temperature on EMF Measurements 243
6.4 Conclusions 246
6.5 References 247

Chapter 7 Water Desorption From An Ion-Selective Electrode Membrane 249

7.1 Introduction 249
7.2 Experimental 251
7.3 Results and Discussion 253
  7.3.1 General Effects of Water Exposure 253
  7.3.2 Determination of Membrane Density 257

7.3.3 Determination of Equilibrium Water Concentration 257
7.3.4 Kinetics of Water Desorption 258
7.3.4.1 Initial Interpretation of Desorption Behavior 258
7.3.4.1.1 Overall Desorption from a Solid Cylinder 258
7.3.4.1.2 Correlation with Related Optical Studies 264
7.3.4.2 Modified Interpretation of Desorption Behavior 268
7.3.4.2.1 Initial Desorption from a Surface Rich Region 268
7.3.4.2.2 Subsequent Desorption from a Solid Cylinder 273
7.3.5 Proposed Interpretation of Desorption Behavior 274
7.4 Conclusions 278
7.5 References 280

Chapter 8 Quantitative Measurements of Membrane Adhesion onto Solid Substrates 282

8.1 Introduction 282
8.2 Experimental 284
8.3 Results 285
8.4 Discussion 290
8.5 Conclusions 292
8.6 References 294

Chapter 9 Conclusions 295

9.1 Summary of Contributions 295
9.2 Directions for Future Research 298
9.3 References 301

Appendix A: Chapter 2 Computer Programs 302

Program A.1: ASYST file NEWWDATA.ASY 302
Program A.2: ASYST file RS232.PAR 305

Program A.3: ASYST file COMM.PAR 308
Program A.4: ASYST file IMPCALC.ASY 312
Program A.5: ASYST file CORRIMP.ASY 315
Program A.6: ASYST file HPPLOT.ASY 316
Program A.7: ASYST file HPLASER.ASY 318
Program A.8: ASYST file START.PAR 319
Program A.9: ASYST file AUTOEXPT.ASY 320
Program A.10: ASYST file CALSAVE.ASY 323
Program A.11: ASYST file SAVE.ASY 325
Program A.12: ASYST file READ.ASY 326
Program A.13: ASYST file PLOT.ASY 327
Program A.14: ASYST file FASTCMDS.ASY 329
Program A.15: ASYST file RCMODEL.ASY 332

Appendix B: Chapter 7 Computer Programs 334

Program B.1: ASYST file BALANCE.ASY 334
Program B.2: BASIC file BALANCE.BAS 336
Program B.3: ASYST file READBAS.ASY 337
Program B.4: ASYST file DIFFUS.ASY 338

Appendix C: Blank Membrane Data 340

List of Tables

Table

1.1 *AC* impedances and admittances for circuit elements 15
2.1 Typical frequencies measured by lock-in impedance measurement system 32
2.2 Frequency component composition of FFT waveform shown in Figure 2.4 42
2.3 Memory partitioning of PAR-273 on-board microprocessor for impedance experiments 44
2.4 Recommended IGAIN setting as a function of current level 46
2.5 Suitable calibration resistors for various current ranges 50
2.6 Memory configuration for IMPTEMP image of base ASYST system 52
2.7 ASYST programs saved in IMPTEMP image 54
2.8 Parameter settings for EIS spectra from 20 mHz to 2.3 kHz using waveform defined in Table 2.2 55
2.9 Array variables used for automated EIS experiments 56
2.10 Summary of user-level colon definitions in IMPTEMP image 57
2.11 *AC* impedances and admittances for circuit elements 62
2.12 Summary of lock-in EIS impedance measurement system characterization 68
2.13 Summary of FFT-EIS impedance measurement system characterization 72
3.1 Effective membrane surface area exposed to bathing solution for various impedance cells 80
3.2 Effect of soaking time for a typical impedance measurement 89
3.3 Impedance data for blank master membrane #1 cast together on the same day as blank master membrane #2 92
3.4 Impedance data for blank master membrane #2 cast together on the same day as blank master membrane #1 93
3.5 Impedance data from pool of measured data for blank DOA/PVC membranes 98
3.6 Impedance data for blank master membranes cast with different purities of DOA plasticizer component 100
3.7 Impedance data for blank master membranes cast with various commercial types of PVC polymer 102

3.8 Gas chromatographic analysis of purity for Fluka DOA plasticizers 105

3.9 Gas chromatography-mass spectrometry analytical data for Fluka Pract DOA lot #267253986 107

3.10 Gas chromatographic analysis of purity for DOS plasticizers 109

3.11 Gas chromatography-mass spectrometry analytical data for Aldrich reagent grade DOS 110

3.12 Gas chromatography-mass spectrometry analytical data for Fluka Pract grade DOS 111

4.1 Equivalent circuit values for a Ca^{+2} ion-exchanger membrane bathed in symmetric 0.1 M $CaCl_2$ bathing solution 161

4.2 Effect of amplitude of waveform perturbation on impedance behavior 166

4.3 Dependance of inductive loop diameter on $[Ca^{+2}{}_{(aq)}]$ for Ca^{+2} buffered bathing solutions 171

4.4 *DC* and *AC* specific resistances as a function of bathing solution concentrations 174

5.1 ^{13}C NMR chemical shift data for a 66 % DOA/PVC membrane 191

5.2 ^{13}C NMR spin-lattice relaxation times for neat DOA plasticizer and for a 66% DOA/PVC membrane 192

5.3 Changes in ^{13}C NMR spin-lattice relaxation times for 66 % DOA/PVC membranes containing $KBPh_4$ equilibrated with water 196

6.1 ^1H NMR integrations of H_2O-saturated DOA samples 220

7.1 Weight data format from Mettler AE200 balance with Option 011 Data Output Interface 254

7.2 Summary of water desorption data from 66% DOA/PVC membranes 256

7.3 Summary of calculated results for water desorption from overall membrane 265

7.4 Summary of calculated results for water desorption from surface region of membrane 272

7.5 Summary of calculated results for water desorption from bulk region of membrane 276

7.6 Summary of measured properties of water in a 66% DOA/PVC membrane 279

8.1 Results of adhesive testing for various samples 289

List of Figures

Figure

1.1 Representative ion-sensing compounds: (a) di-[4-(2,2-dimethylhexyl)phenyl]phosphate ion-exchanger, (b) valinomycin antibiotic, and (c) ETH 1001 synthetic ionophore 5

1.2 Schematic diagram of an electrochemical cell for ion measurement with an ISE 6

1.3 Graphical representations of the impedance vector 11

1.4 Nyquist plot for a resistor R and a capacitor C in parallel 13

1.5 Model of a plasticized PVC ISE membrane. (a) equivalent circuit representation and (b) corresponding Nyquist plot 17

1.6 T_1 measurement by inversion-recovery method: (a) pulse sequence, and (b) magnetization vector description 21

2.1 Conversion between the time-domain and frequency-domain via the Fourier transformation for one and three frequency components 33

2.2 Block diagram of FFT-EIS system 37

2.3 Schematic of devices controlled by host computer 39

2.4 Typical WDATA excitation waveform consisting of 50 frequency components with equal amplitude and random phase angle 41

2.5 Equivalent circuit representation of an ISE membrane system 59

2.6 Dummy cell electronic circuits for (a) blank and (b) ionophore-containing ISE membranes 60

2.7 Computer-modelled EIS spectrum for double parallel RC circuit ... 63

2.8 Computer-modelled EIS spectrum for single parallel RC circuit.... 64

2.9 Measured lock-in EIS spectrum of a double parallel RC dummy cell circuit 65

2.10 Measured lock-in EIS spectrum of a single parallel RC dummy cell circuit 66

2.11 Measured FFT-EIS spectrum of a double parallel RC dummy cell circuit 69

2.12 Measured FFT-EIS spectrum of a single parallel RC dummy cell circuit 70

3.1 Side and end views of the Teflon cell and brass water jacket used for membrane impedance measurements 79

3.2 Membrane torque study on older cell design 84

3.3 Membrane torque study on newer cell design................................85

3.4 Effect of temperature for a typical impedance measurement..........87

3.5 Effect of soaking time for a typical impedance measurement.........90

3.6 Mass spectra of DOA plasticizer: (a) electron impact source and (b) chemical ionization source.. 106

3.7 Calibration curves for the change in membrane bulk and charge transfer resistivities as a function of weight percent of benzoic acid additive incorporated into the membrane during its preparation 116

3.8 Calibration curves for the change in membrane bulk and charge transfer resistivities as a function of weight percent of methyl benzoate additive incorporated into the membrane during its preparation.. 122

4.1 Proposed model for the transport of Ca^{+2} ions through the membrane.. 135

4.2 Equivalent circuits for the interfacial adsorption: (a) $B < 0$ condition, and (b) $B > 0$ condition.. 141

4.3 Proposed equivalent circuit for the overall ISE membrane system... 144

4.4 Model impedance plot for the inductive branch of the overall membrane equivalent circuit....................................... 147

4.5 Model impedance plot for the overall membrane equivalent circuit.. 148

4.6 Impedance plane plot of a blank Ca^{+2} membrane (DOPP/PVC) in 1 mM $CaCl_2$ 152

4.7 Impedance plane plot of a normal Ca^{+2} membrane in 1 mM $CaCl_2$: (a)Frequency range 40 kHz to 0.98 mHz, and (b) frequency range 2280 Hz to 0.98 mHz...................................... 153

4.8 Steady-state current-voltage curves in 1 mM $CaCl_2$ bathing solution.. 172

5.1 Molecular structure of bis(2-ethylhexyl) adipate (DOA) showing peripheral and central chain segments........................ 189

5.2 Fully relaxed ^{13}C NMR spectrum of a 66 % DOA/PVC membrane.. 190

5.3 Plasticization level dependence of the DOA methylene (C-3/4 and C-10) ^{13}C relaxation times 193

5.4 Plasticization level dependence of the DOA methyl (C-8), methine (C-5) and carbonyl (C-9) ^{13}C relaxation times................. 194

5.5 Plasticization level dependence of the PVC polymer ^{13}C relaxation times 195
6.1 ^{1}H NMR spectrum of pure neat DOA plasticizer 219
6.2 FTIR spectra of neat DOA plasticizer: (a) pure and (b) saturated with H_2O 222
6.3 Diffuse reflectance FTIR spectrum of a H_2O-soaked 66% DOA/PVC membrane sample 225
6.4 Normal transmission FTIR spectra of a 66% DOA/PVC membrane sample: (a) dry and (b) H_2O-soaked 226
6.5 ^{13}C NMR spectrum of a dry 66% DOA/PVC membrane sample 230
6.6 ^{1}H NMR spectrum of a dry 66% DOA/PVC membrane sample 231
6.7 ^{1}H NMR spectrum of a H_2O-soaked 66% DOA/PVC membrane containing 0.01% $KBPh_4$ salt 233
6.8 Variable temperature ^{2}D NMR spectra of a D_2O-soaked 66% DOA/PVC membrane containing 0.01% $KBPh_4$ salt 235
6.9 ^{1}H NMR spectrum of a H_2O-soaked 66% DOA/PVC membrane containing 0.1% $KBPh_4$ salt 239
6.10 Variable temperature ^{2}D NMR spectra of a D_2O-soaked 66% DOA/PVC membrane containing 0.1% $KBPh_4$ salt 242
6.11 Potentiometric data for K^+-sensitive ISE membrane as a function of temperature: (a) calibration slopes and (b) standard potentials 244
7.1 Experimental configuration for water desorption employing a gravimetric method of measurement 252
7.2 Typical water desorption curve for a 66% DOA/PVC membrane 255
7.3 Plot of M_t/M_∞ *versus* square root of time for overall water desorption from membrane sample #2 261
7.4 Expanded plot of M_t/M_∞ *versus* square root of time for overall water desorption from membrane sample #2 262
7.5 Theoretical and experimental data for overall water desorption from membrane sample #2 263
7.6 Light scattering profile in a 66% DOA/PVC membrane containing valinomycin after 40 hrs equilibration with water on both sides 267
7.7 Plot of M_t/M_∞ *versus* square root of time for water desorption from surface region of membrane sample #2 271
7.8 Plot of M_t/M_∞ *versus* square root of time for water desorption from bulk region of membrane sample #2 275

7.9 Theoretical and experimental data for water desorption from bulk regions of membrane sample #2 ... 277
8.1 Schematic diagram of membrane sample for adhesive testing ... 286
8.2 Schematic diagram of configuration for adhesive testing ... 287
8.3 Typical peel-force curves for different samples on SiO_2 substrates ... 288

Chapter 1

Introduction

Ion-selective electrode (ISE) technology has developed rapidly over the past twenty years. Analytical methods based on these electrochemical sensors now find widespread use in a number of divergent applications [1-3]. For example, blood and urine electrolytes are routinely determined by ISEs in clinical chemical analyses. Despite their practical usefulness, however, the operation of these devices is not yet fully understood.

In recent years, considerable effort has been directed towards elucidating the mechanism of ion selectivity and probing the physical chemistry of these ISE systems. One of the primary objectives is to obtain a better understanding of the ion-selective response mechanisms. Practically, this would enable a more systematic approach towards dealing with common problems encountered with the use of ISEs in difficult media, such as biological or lipophilic solutions. Equally, if not more important, this understanding would provide the important theoretical basis required to transfer existing conventional ISE technology to new devices such as the ion-sensitive field effect transistor (ISFET) and optically-based ion sensors.

The studies discussed in this thesis examine some electrical and physical properties of ISE membranes. The first part investigates the transport of ions with particular emphasis on processes occurring at the membrane/solution interface. This is important for understanding ion-selectivity and electrode response mechanisms. The effects of additives on transport processes are also considered. The technique most extensively utilized in these studies is *ac* impedance analysis.

The second part of this work examines physical characteristics of the membrane, particularly the nature of water within the membrane. Water functions in a complicated matter by affecting various chemical equilibria in the membrane, and the properties and function of water must be clarified in order to better understand its complex role. The main analytical tools employed in these studies are nuclear magnetic resonance (NMR) spin-lattice relaxation, NMR spectroscopy, infrared (IR) spectroscopy and gravimetric desorption.

Finally, there has been considerable interest in developing potentiometric solid-state ion sensors utilizing conventional plasticized polymeric ISE membranes as transducers. Several advantages have been cited, including miniaturization, easier mass fabrication and integration of signal processing circuitry. In addition to several fundamental obstacles to this new technology, there are also several practical problems. A consideration of the problem of physical adhesion of the membrane to these devices is briefly addressed.

1.1 The Ion-Sensitive Electrode

ISE electrodes can be classified as crystalline and non-crystalline electrodes. Crystalline electrodes can be further subdivided into homogeneous (*e.g.* LaF_3 single crystal for F^-) and heterogeneous (*e.g.* AgCl imbedded in polyethylene for Ag^+). The noncrystalline electrodes can be divided into glasses (*e.g.* silicate glasses for Na^+ and H^+) and liquid membranes. Earlier liquid membrane electrodes were retained in a rigid porous support such as a Millipore filter or glass frit. Following the pioneering work of Bloch, Shatkay and Saroff in 1967 [4], however, liquid membrane ISEs are now usually immobilized in a much more sturdy polymer matrix. The work in this thesis is concerned with these types of liquid membranes electrodes.

1.1.1 Historical Perspective

Liquid organic phases containing ion-exchange sites can impart ion-selective properties. As early as 1906, Cremer reported a very slight response to monovalent cations for electrodes containing phenol and nitrobenzene using picric acid as the liquid ion-exchange phase [5]. A practical Ca^{+2}-sensitive liquid ion-exchanger electrode was first reported in 1967 by Ross [6]. This consisted of the calcium salt of didecylphosphoric acid dissolved in di-*n*-octylphenyl phosphonate. If the ion-exchanger sites are positively charged, then anion-selective electrodes result. Thus, systems containing dimethyldistearyl ammonium cation respond to Cl^- ions [7].

In 1964, Moore and Pressman reported K^+-solvating behavior for the naturally occurring valinomycin antibiotic in biological membrane systems [8]. Only three years later, the first liquid membrane electrode based on a nonactin antibiotic ion-selective phase was described by Stefanac and Simon [9]. This eventually led to the construction of a K^+-selective electrode in which valinomycin was dissolved in either a nujol/2-octanol mixture or in diphenyl ether [10-11].

The antibiotics provide for the formation of complexes whereby the ions are stabilized in molecular cavities by ion-dipole forces [12]. This leads to excellent ion-selectivity, and presumably also accounts for the extraordinary specificity of biological cells for certain ions. In 1967, ion-selective properties were reported by Pedersen for synthetic crown ether complexes of similar structure [13]. The development of synthetic molecules with custom-made ion-selectivity has been the latest progression in the search for better ion-selective reagents [14]. Molecular modelling techniques have proven to be very useful in this regard. These serve to guide the design of synthetic complexing agents which incorporate many of the desired design features for use in ISEs [15-16]. Much of this effort has originated from Simon and his group at the Swiss Federal Institute of Technology (ETH) in Zürich. Out of several hundred molecules prepared, many practical ion carriers have been obtained, *e.g.* (-)-(R,R)-N,N'-bis-[11-

(ethoxycarbonyl)undecyl]-N,N'-4,5-tetramethyl-3,6-dioxaoctane-diamide or "ETH 1001" which is selective for Ca^{+2}.

Earlier work in the field concentrated on an intensive search for novel electrode materials and new construction designs. While this still continues, since the late 1970s this has given way to more fundamental studies on ion selectivity and electrode response mechanisms [17-23].

1.1.2 Principles and Design

The most successful type of ISE electrode is based on plasticized polymeric membranes [24]. These usually consist of ≈ 1 wt% ion-sensing component, ≈ 66 wt% plasticizer and ≈ 33 wt% polymer. Very often, low concentrations (≈ 0.01 wt%) of lipophilic salts are also added to enhance Donnan exclusion. The ion-sensing component determines the desired ion-selectivity of the ISE. It can be either an electrically charged liquid ion-exchanger (*e.g.* dialkyl or diaryl phosphate) or a non-dissociable ion-specific ligand known as an ionophore. Common ionophores are naturally occurring antibiotics (*e.g.* valinomycin, nonactin, nigericin, *etc.*) or synthetic molecules (*e.g.* ETH 227, ETH 1001, ETH 2220). Figure 1.1 gives the structures of some representative ion-sensing compounds. The plasticizer provides a low dielectric solvent for the ion-sensing component, and is typically a long chain ester such as bis(2-ethylhexyl) adipate (DOA). The polymer provides structural integrity to the liquid membrane, and is almost exclusively poly(vinyl chloride) (PVC).

The ISE electrode consists of an ion-selective membrane, an internal standard solution of analyte ions, and an internal reference electrode. This is immersed, along with an external reference electrode, into a test solution containing analyte ions with an activity a_i as shown in Figure 1.2. For a given cell assembly, a Nernstian response is expected, and the cell potential is given by:

$$E = E^0 + 2.303 \frac{RT}{z_i F} \log (a_i) \qquad (1.1)$$

(a) Di-[4-(2,2-dimethylhexyl)phenyl]phosphate (Ca^{+2}-selective)

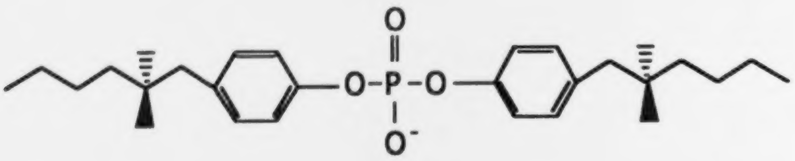

(b) Valinomycin (K^{+}-selective)

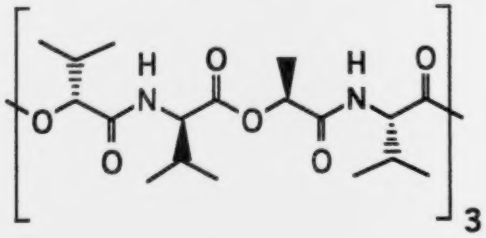
H
O
H
O
O
N
O
N
O
O
3

(c) ETH 1001 (Ca^{2}-selective)

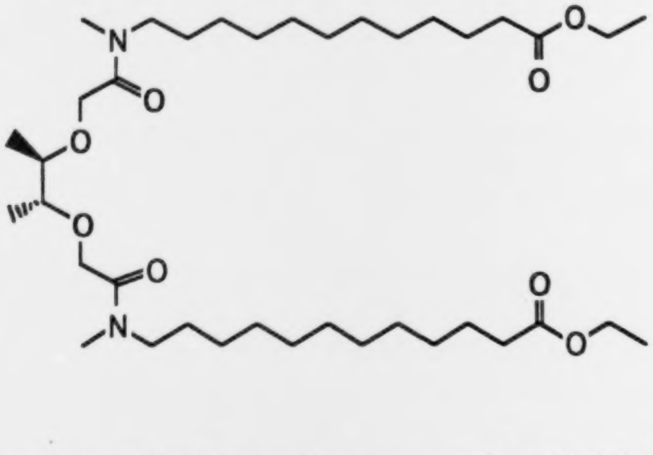
N
O
O
O
O
O
O
N
O
O
O

Figure 1.1 Representative ion-sensing compounds: (a) di-[4-(2,2-dimethylhexyl)phenyl]phosphate ion-exchanger, (b) valinomycin antibiotic, and (c) ETH 1001 synthetic ionophore.

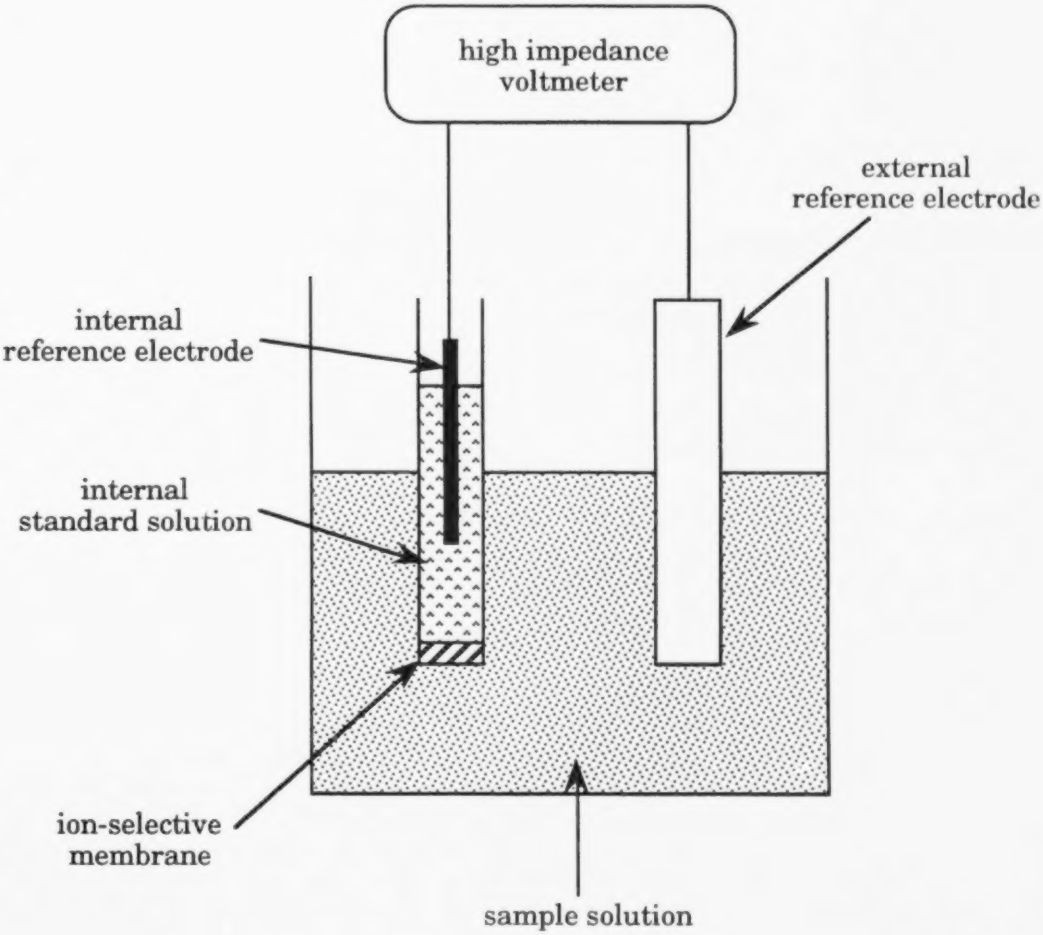
high impedance voltmeter
external reference electrode
internal reference electrode
internal standard solution
ion-selective membrane
sample solution

Figure 1.2 Schematic diagram of an electrochemical cell for ion measurement with an ISE.

where R = the gas constant
T = the absolute temperature
F = the Faraday constant
z_i = the charge of the analyte ion

In this equation, E^0 represents a standard cell potential which includes the liquid-junction potential of the external reference electrode. In practice, in the presence of interfering species in the sample solution, ideal specific response is not attained and the actual cell potential is instead described by the Nicolsky equation:

$$E = E^0 + 2.303 \frac{RT}{z_i F} \log \left[a_i + \sum_{j \neq i} K_{ij} (a_j)^{z_i/z_j} \right] \tag{1.2}$$

where a_j = the activity of the jth interfering species
z_j = the charge of the jth interfering species
K_{ij} = selectivity coefficients

The fundamentals of ISE electrochemical response have been reviewed in several texts [1,18].

1.1.3 Ion Transport Theory

Many theories have been proposed to explain the selective permeation by either cations or anions (permselectivity) and the transport behavior of ionophore-based membranes [18]. Currently, the most widely accepted theory involves membrane-trapped fixed or mobile anionic sites. The original theory was developed by Morf *et al* in 1976 [25] and has been since corroborated by ample experimental evidence. This model is generally known as the "closed-circuit shuttle carrier" mechanism and the principle concepts are found in the work of Simon [17,19], Buck [22,26-27] and

Armstrong [20,28-29]. The K^+-sensitive membrane incorporating valinomycin (val) provides the standard system for describing this model.

The membrane is assumed to contain a val carrier concentration that is at least equal to the site concentration. A very large complex formation constant of $\approx 10^8$ L/mol [20] results in predominantly carrier-complexed $Kval^+$ ions as the membrane counterions. The mechanism of ion transport through the membrane, therefore, involves a closed-circuit flux of the val carrier. Under an applied potential perturbation, K^+ enters at one interface where it is complexed by free val carrier. A translocation of carrier complexes subsequently occurs whereby $Kval^+$ moves from site-to-site without dissociation. Free carrier is released at the exiting interface where K^+ leaves the membrane, but remains trapped in the membrane and is subject to back-diffusion in the opposite direction according to Fick's laws. In the steady-state, the total flux of carrier molecules approximates zero since free val back-diffuses with a flux that balances the current carried by $Kval^+$.

1.2 *AC* Impedance Analysis

1.2.1 Introduction to *AC* Impedance

When a potential is applied across an electrochemical cell, a movement of ions through the electrolyte occurs as determined by the reaction mechanisms. This movement of ions constitutes a flow of electric current. Typically, the applied potential is a sinusoid and this may be expressed as:

$$E = \Delta E \sin \omega t \qquad (1.3)$$

where ΔE = voltage amplitude

ω = angular frequency in radians/second (2π times the conventional frequency)

t = time in seconds

The resulting current flow generally will not be in phase with the input voltage and will be separated by a phase angle. It may be expressed as:

$$I = \Delta I \sin(\omega t + \phi) \tag{1.4}$$

where ΔI = current amplitude
ϕ = phase shift in radians

The relationship between the input voltage and the output current in a circuit is given by the impedance (Z):

$$\vec{Z} = \frac{\vec{E}}{\vec{I}} \tag{1.5}$$

where vector representation has been employed. This expression is analogous to the relationship given by Ohm's law for *dc* circuits:

$$R = \frac{E}{I} \tag{1.6}$$

Thus, it can be seen that impedance is simply the *ac* analogue of *dc* resistance since both imply an obstruction to current flow. For *dc*, only resistors oppose current flow. For *ac*, the current is opposed by the capacitance and inductance of the circuit in addition to the resistance. These elements can affect not only the magnitude of the output current but also its phase characteristics. Often, it is advantageous to analyze *ac* circuits by the reciprocal of impedance which is known as the admittance:

$$\vec{Y} = \frac{1}{\vec{Z}} = \frac{\vec{I}}{\vec{E}} \tag{1.7}$$

The admittance is analogous to the conductance in *dc* circuits:

$$G = \frac{1}{R} = \frac{I}{E} \tag{1.8}$$

These definitions are especially useful for the analysis of parallel circuits because the overall admittance is simply the sum of the individual admittances.

Since the impedance is a vector quantity, it can be conveniently characterized in a number of ways. The first is through the polar coordinate system whereby the impedance vector is defined by a magnitude $|Z|$ and an argument ϕ as shown in Figure 1.3a. The second is to represent the vector as a coordinate (x,y) pair in the Cartesian system as shown in Figure 1.3b. A more convenient approach for numeric analysis, however, is to represent the vector in the complex plane as shown in Figure 1.3c. In this plane the abscissa is defined as the real, Z', axis and the ordinate is defined as the imaginary, Z", axis. The mathematical convention for this coordinate system is to multiply the Z" coordinate value by $(-1)^{1/2}$, symbolized by j. The impedance vector can therefore be written as a complex number in the form:

$$\vec{Z} = Z' - jZ'' \tag{1.9}$$

By convention, negative of the imaginary component, -Z", is actually plotted along the positive imaginary axis. From analytical geometry, the magnitude of the impedance vector is given by:

$$\left|\vec{Z}\right| = \sqrt{(Z')^2 + (Z'')^2} \tag{1.10}$$

and the phase angle is:

$$\phi = \arctan\left(\frac{-Z''}{Z'}\right) \tag{1.11}$$

Note that the phase angle is measured from the real axis in the counterclockwise direction. The quadrants in the complex plane are normally referenced as follows: first quadrant ($Z' > 0$, $-Z'' > 0$, $0 < \phi < 90$), second quadrant ($Z' < 0$, $-Z'' > 0$, $90 < \phi < 180$), third quadrant ($Z' < 0$, $-Z'' < 0$, $180 < \phi < 270$), and fourth quadrant ($Z' > 0$, $-Z'' < 0$, $270 < \phi < 360$).

(a) Polar coordinate system

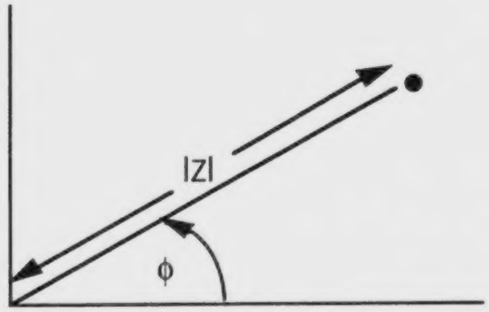

(b) Cartesian coordinate system

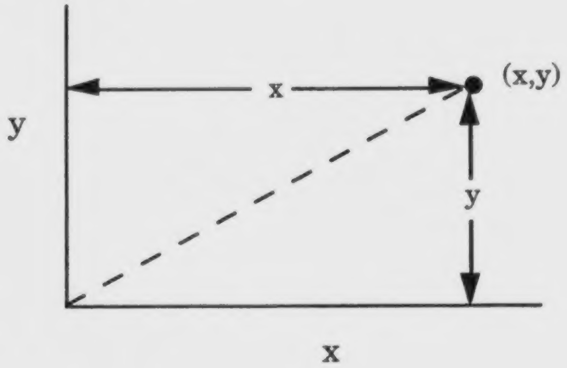

(c) Complex plane

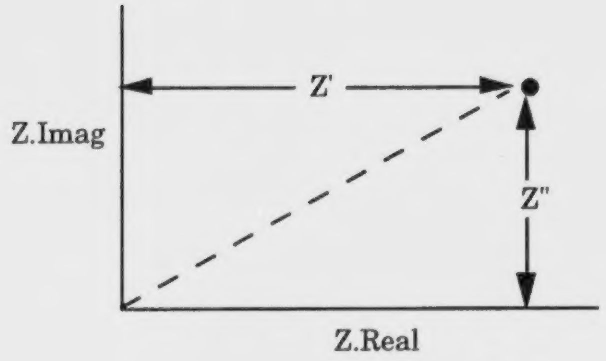
Z'
Z.Imag
Z''
Z.Real

Figure 1.3 Graphical representations of the impedance vector.

1.2.2 Electrochemical Impedance Spectroscopy

The basic expression for calculating impedance is given by equation (1.7). In electrochemical impedance spectroscopy (EIS), the impedance behavior of a test system is characterized by measuring its impedance as a function of the input voltage frequency. This yields a frequency domain profile of the admittance (*i.e.* reciprocal of impedance) which can be represented as A(ω). Thus, equation (1.7) may be generalized for multiple frequencies as:

$$\vec{A}(\omega) = \frac{\vec{I}(\omega)}{\vec{E}(\omega)} \tag{1.12}$$

where $\vec{A}(\omega)$ = admittance at frequency ω
$\vec{E}(\omega)$ = input voltage at frequency ω
$\vec{I}(\omega)$ = current flow at frequency ω

A variety of formats can be used to present the measured data.

The Nyquist plot is one of the most convenient methods of data presentation. The imaginary Z'' component of impedance is plotted *versus* the real Z' component of impedance for each excitation frequency in the complex plane. An example is given in Figure 1.4. This format is used almost exclusively throughout this work. Other types of display optimize data interpretation for certain conditions. These include the Bode plot (log $|Z|$ and θ *versus* log ω), the Randles plot (Z' *versus* $\omega^{-1/2}$), and the Admittance plot (Y''/ω *versus* Y'/ω).

Any electrochemical cell may be represented by an equivalent electronic circuit which models its observed impedance behavior. The constituent circuit elements (resistors, capacitors and inductors) can then be interpreted as various discrete steps in the overall electrochemical behavior (*e.g.* charge-transfer resistance, double-layer capacitance, diffusional impedance, *etc.*). The equivalent circuits related to electrochemical cells generally consist of serial and parallel RC circuits [30]. Therefore, in order to interpret EIS data from real electrochemical

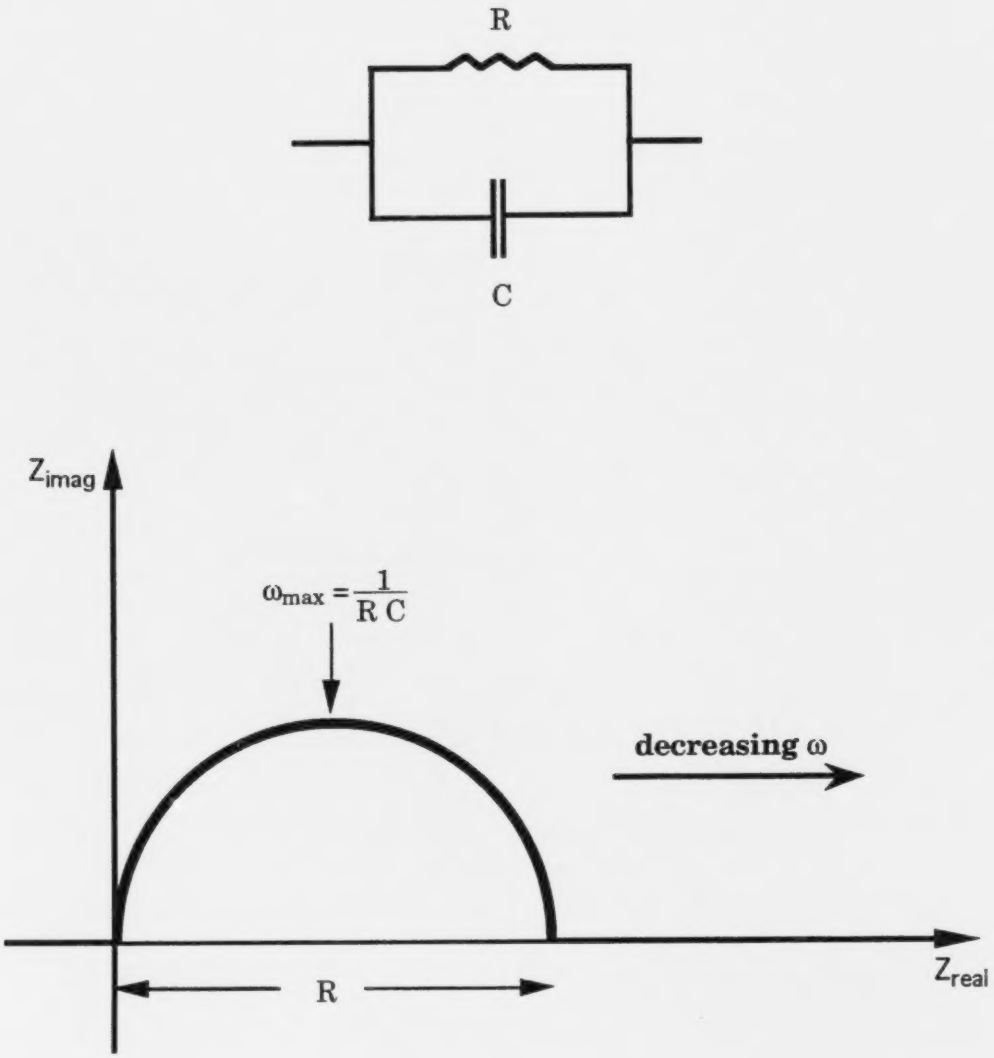
R
C
Z_{imag}
$\omega_{max} = \frac{1}{R\,C}$
decreasing ω
Z_{real}
R

Figure 1.4 Nyquist plot for a resistor R and a capacitor C in parallel.

systems, it is expedient to consider the appearance of Nyquist plots for some simple circuits. The impedance and admittance relationships for various circuit elements given in Table 1.1 will be utilized.

The Nyquist plots for pure circuit elements are trivial cases: for a resistor R, a single point on the Z' axis corresponds to Z' = R; for a capacitor C, frequency dependent points on the Z" axis correspond to Z" = 1/ωC; and for an inductor L, frequency dependent points on the Z" axis correspond to Z" = -ωL.

The Nyquist plot of a parallel RC network is characterized by a semicircle in the first quadrant as shown in Figure 1.4. This behavior can be mathematically analyzed as follows. Admittances in parallel add directly, hence, for a parallel RC circuit:

$$\vec{Y} = \frac{1}{R} + j\omega C \tag{1.13}$$

From equations (1.7) and (1.9),

$$\vec{Z} \equiv Z' - j\,Z'' = \frac{1}{\vec{Y}} = \frac{R - j\omega R^2 C}{1 + (\omega RC)^2} \tag{1.14}$$

Thus,

$$Z' = \frac{R}{1+(\omega RC)^2} \tag{1.15}$$

$$Z'' = \frac{\omega R^2 C}{1+(\omega RC)^2} \tag{1.16}$$

The square of the magnitude can be calculated from equation (1.10):

$$\begin{aligned} \left|\vec{Z}\right|^2 &= (Z')^2 + (Z'')^2 \\ &= \frac{R^2 + \omega^2 R^4 C^2}{[1 + (\omega RC)^2]^2} \\ &= \frac{R^2}{1 + (\omega RC)^2} \\ &= R\,Z' \end{aligned} \tag{1.17}$$

Table 1.1 *AC* impedances and admittances for circuit elements.

Impedance: $\vec{Z} = Z' - j Z''$

Admittance: $\vec{Y} = Y' + j Y''$

circuit element	**Z'**	**Z"**	**Y'**	**Y"**
resistor	R	0	1/R	0
capacitor	0	1/ωC	0	ωC
inductor	0	-ωL	0	-1/ωL

Thus,

$$\left(Z' - \frac{R}{2}\right)^2 + (Z'')^2 = \left(\frac{R}{2}\right)^2 \qquad (1.18)$$

Consequently, the Nyquist plot of Z" *versus* Z' gives a semicircle that is centered at Z' = R/2 with a radius of R/2. The angular frequency ω_{max} for which Z" attains its maximum value occurs at:

$$Z'(\omega_{max}) = \frac{R}{2} \qquad (1.19)$$

Substituting equation (1.15) into equation (1.19),

$$\frac{R}{1 + (\omega_{max}RC)^2} = \frac{R}{2} \qquad (1.20)$$

From this relation, ω_{max} may be calculated:

$$\omega_{max} = \frac{1}{RC} \qquad (1.21)$$

The time constant for this RC network is simply the reciprocal of ω_{max}, *i.e.* $\tau = RC$. Thus, values for R and C may be determined from the Nyquist plot as shown in Figure 1.4.

In an analogous fashion, equivalent circuit parameters for more complex circuits can be determined from the corresponding impedance spectrum. For example, an equivalent circuit representation for a plasticized PVC ISE membrane has been given by Armstrong [31]. This is shown in Figure 1.5a. The series resistor (R_s) corresponds to the solution resistance. The R_bC_g parallel network corresponds to the bulk membrane and consists of a bulk resistance (R_b) and a geometric capacitance (C_g). The $R_{ct}C_{dl}$ parallel network corresponds to the membrane/solution interface and consists of a charge transfer resistance R_{ct} and a double-layer capacitance (C_{dl}). The Nyquist plot for this circuit is given in Figure 1.5b.

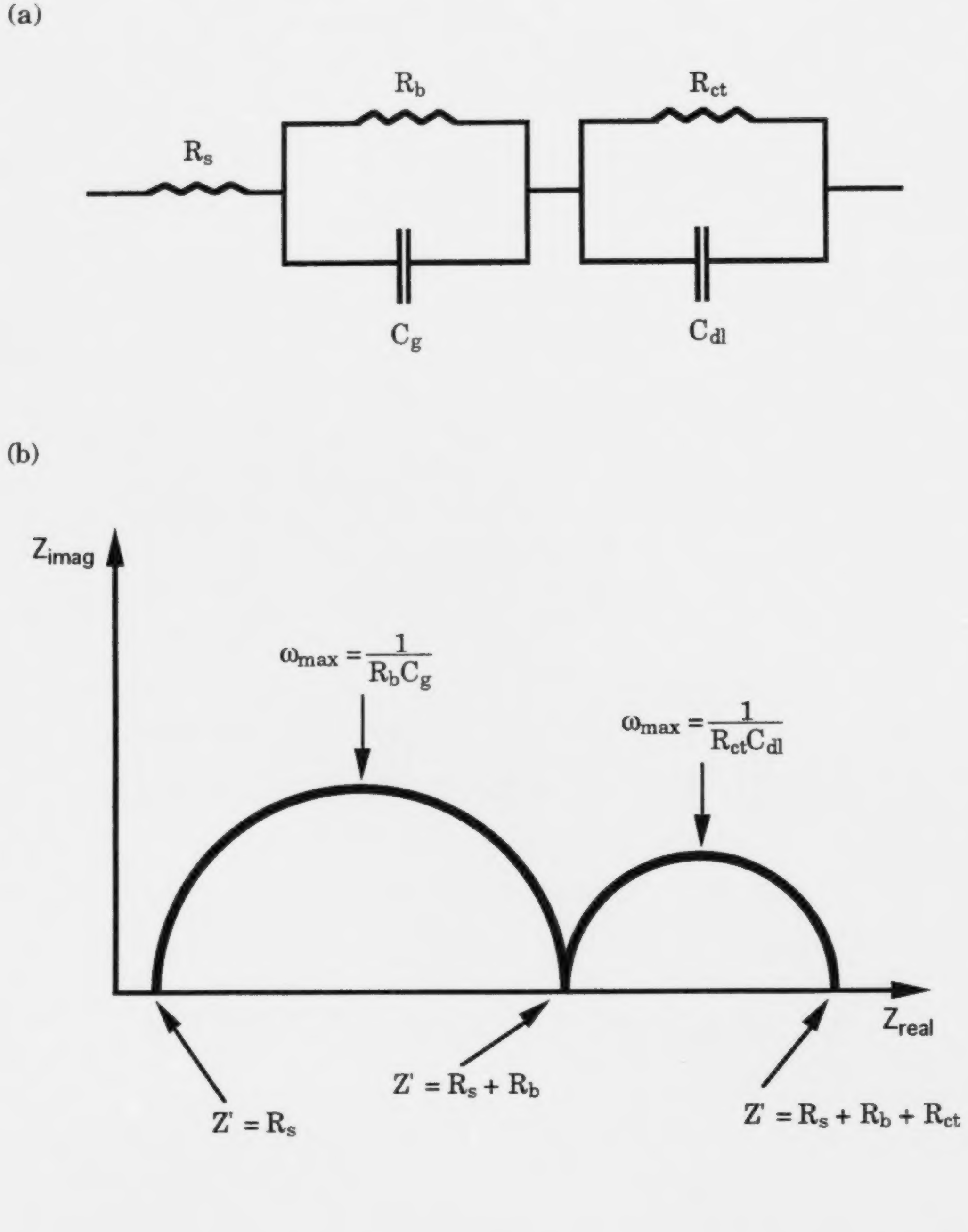
(a)
R_b
R_ct
R_s
C_g
C_dl
(b)
Z_imag
ω_max = 1/(R_bC_g)
ω_max = 1/(R_ctC_dl)
Z_real
Z' = R_s
Z' = R_s + R_b
Z' = R_s + R_b + R_ct

Figure 1.5 Model of a plasticized PVC ISE membrane. (a) equivalent circuit representation and (b) corresponding Nyquist plot.

Note that real systems do not always give pure semicircles in the Nyquist plot [32]. Vertical lines can appear for systems with capacitive coupling at *dc*. Diffusional Warburg impedance can give rise to 45° straight lines. Semicircles can overlap if parallel RC networks in series have similar time constants differing by less than a factor of about ten. Also, if the equivalent circuit consists of many parallel RC elements in series, and their respective time constants are randomly distributed about a mean value, then a "sunken" semicircle appears, *i.e.* its center lies below the real axis.

1.3 NMR Spin-Lattice Relaxation

Conventional nuclear magnetic resonance (NMR) spectroscopy is a familiar technique to all chemists [33-34]. Techniques employing NMR relaxation, however, are not as widespread. In this section, the fundamental principles of NMR relaxation will be described.

1.3.1 NMR Basics

In an NMR experiment, there is a static applied external magnetic field (B_0) parallel to the z-axis. (The coordinate system typically used to describe NMR processes is the rotating frame whereby the x and y axes rotate about the z-axis at the spectrometer frequency.). For a system of spin 1/2 nuclei, this results in two possible energy levels. At equilibrium, a small excess population of nuclei will reside in the lower energy state, as dictated by the Boltzmann distribution. The result is a net magnetization (M_0) aligned with B_0. If one represents the M_0 vector by two components M_z (parallel with the z-axis) and M_{xy} (lying in the xy plane), then at equilibrium it is evident that $M_z = M_0$ and $M_{xy} = 0$. In Fourier transform (FT) NMR, the sample is irradiated with a short, powerful pulse of rf energy. This is converted by the probe into a corresponding pulsed field, B_1, that is applied perpendicularly to the static field B_0. This causes the M_0 vector to tip some angle θ from equilibrium such that $M_z = M_0\cos\theta$ and $M_{xy} = M_0\sin\theta$. The rf pulse can, therefore, be designated by the value of θ that it produces. Hence, a $\pi/2$ pulse rotates the M_0 vector by 90^0 completely into the xy plane, *i.e.* $M_z = 0$, $M_{xy} = M_0$. The typical duration of a $\pi/2$ pulse is $\approx$ 10 μsec. Immediately following the excitation pulse, the magnetization returns to equilibrium (*i.e.* relaxes) in a manner that can be depicted as the independent return of M_z to M_0 and M_{xy} to zero. The decay of the M_{xy} is normally detected by an rf receiver coil situated in the xy plane. This results in a free induction decay (FID) which is the Fourier partner of the familiar NMR frequency spectrum.

1.3.2 NMR Relaxation

Sophisticated NMR applications go beyond simple first-order chemical shift and spin-spin splitting analysis. The relaxation of the excited NMR state depends on specific interaction between the nucleus and the environment. Six types of interaction have been identified: dipole-dipole (nuclear-nuclear and electron-nuclear), spin-rotation, chemical shift anisotropy, nuclear electric quadrupole, scalar coupling and paramagnetic species effects [35]. Thus, NMR relaxation can be used as an additional probe of molecular structure and molecular dynamics.

The relaxation of M_z to M_0 and M_{xy} to zero, following an excitation pulse, generally obeys simple first-order kinetics with associated time constants. The spin-lattice (or longitudinal) relaxation time constant (T_1) describes the recovery of the M_z component and quantifies the rate of transfer of energy from the nuclear spin system to its surroundings (*i.e.* the lattice). The spin-spin (or transverse) relaxation time constant (T_2) describes the decay of the M_{xy} component and involves the loss of phase coherence of the individual nuclear moments in the xy plane. T_2 relaxation includes T_1 relaxation and depends on magnetic inhomogeneity in addition to low and zero frequency effects such as chemical and spin exchange. In the solid (or near solid) state, low frequency local magnetic fluctuations significantly shorten T_2 while lack of motion-induced relaxation may give rise to very long T_1's. Both T_1 and T_2 values contain useful information about molecular dynamics and structure, but the T_1 relaxation times are generally more significant for chemists since they are more easily interpretable than T_2 [36].

1.3.3 Determination of T_1 Relaxation Times

There are several methods that can be used to determine T_1 values. The more sophisticated techniques are designed to remove systematic errors introduced by instrumental factors or make the acquisition of data more efficient. The most accurate (and probably the most common) of these methods is based on an inversion-recovery multi-pulse sequence [37-38].

In the inversion-recovery experiment, a π pulse is first applied to completely invert the magnetization so that $M_z = -M_o$ and $M_{xy} = 0$. The system then relaxes back towards the +z-axis whereby M_z goes from $-M_o$ through to zero to its equilibrium value M_o. At a certain time (τ) after the initial pulse, a $\pi/2$ pulse can be applied to tip the z-magnetization into the xy plane so that now $M_{xy} = M_z(\tau)$. A FID results and Fourier transformation produces an NMR spectrum whose peak intensities (I) are directly proportional to $M_z(\tau)$. By repeating the experiment for different values of τ, a graph of I *versus* τ is obtained for each individual resonance. This plot is a direct analogue to a plot of M_z *versus* τ. The value for T_1 can best be calculated according to the three-parameter equation suggested by Kowalewski *et al* [39]:

$$I(\tau) = A + B \exp(-\tau/T_1) \qquad (1.22)$$

where A, B and T_1 are adjustable parameters. A schematic outline of the inversion-recovery experiment is shown in Figure 1.6.

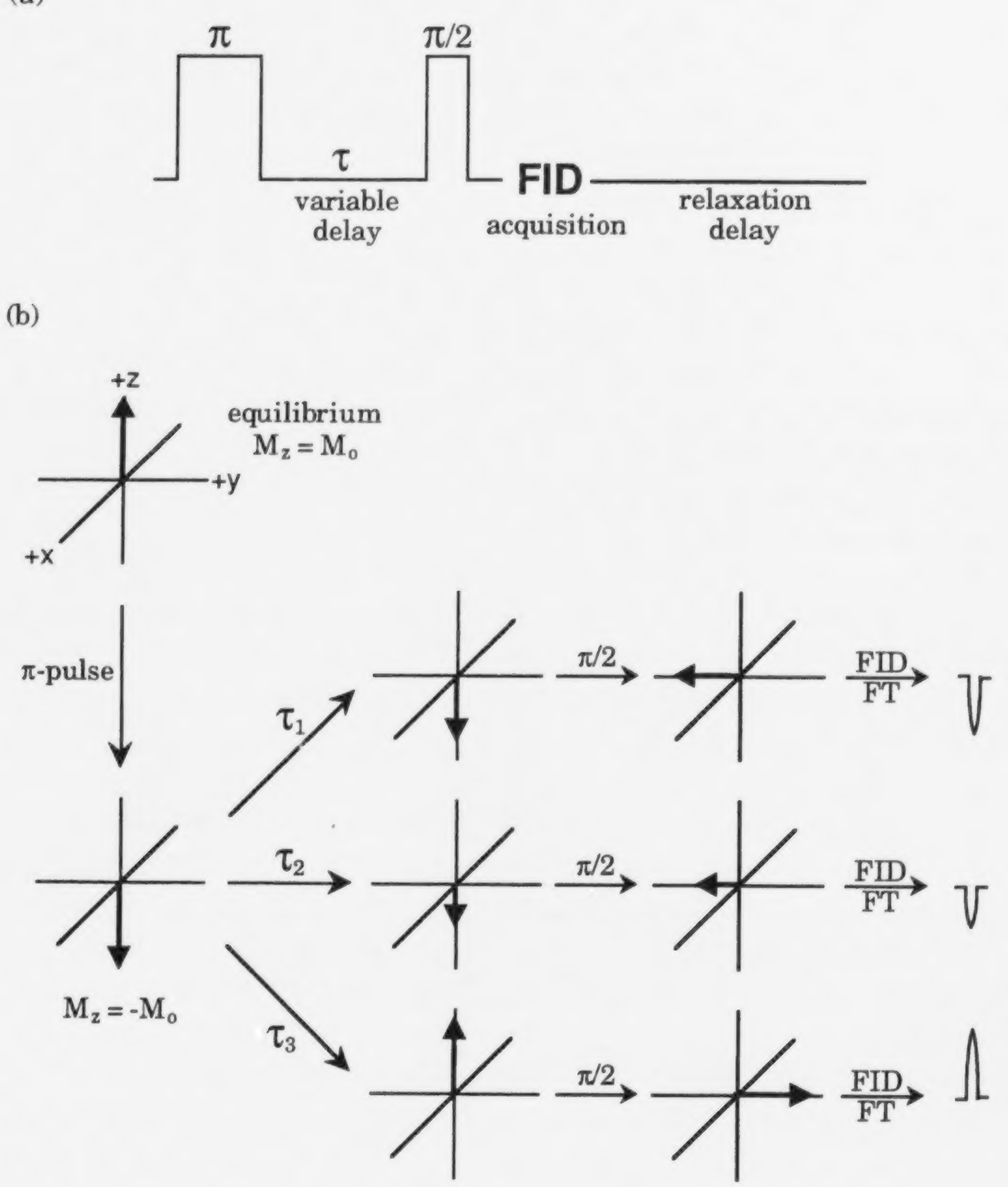
(a)
π
π/2
τ
variable delay
FID
acquisition
relaxation delay
(b)
+z
+y
+x
equilibrium
$M_z = M_o$
π-pulse
$M_z = -M_o$
τ_1
τ_2
τ_3
π/2
π/2
π/2
FID
FT
FID
FT
FID
FT

Figure 1.6 T_1 measurement by inversion-recovery method: (a) pulse sequence, and (b) magnetization vector description (shown in the rotating frame).

For ^{13}C NMR, a single π-τ-$\pi/2$ pulse sequence will not give sufficient signal strength. For signal averaging, the pulse sequence that must be used is expressed as:

$$[\pi - \tau - \pi/2 - \text{FID} - \text{wait}]_n \qquad (1.23)$$

where n is the number of repetitions. The waiting period is required to ensure complete relaxation between individual π-τ-$\pi/2$ sequences. In practice, this is usually five times the longest T_1 to be determined since at $5T_1$, $M_z = 0.993\ M_o$. This long waiting period makes T_1 measurements by inversion-recovery long experiments, hence it is the main disadvantage of the method. The advantages of this method, however, include the large range of peak intensity change (theoretically -1 to +1) and the relative insensitivity to errors in the π and $\pi/2$ pulse lengths [37]. Typically, ^{13}C T_1 values are accurate and reproducible to 5 - 15 % [40].

1.3.4 Applications of NMR Relaxation Measurements

T_1 and T_2 relaxation time measurements have been extensively used to study polymers and the effects of additives [41]. While the majority of these studies have exploited the superior resolution of solid state NMR, solution state experiments have also been reported for certain polymer systems. A more extensive discussion of these studies is reserved until Chapter 5 where ^{13}C T_1 relaxation measurements are used to study physical properties of the ISE membrane matrix and the effect of water.

1.4 Scope of Present Work

There are two general focuses to the present work. In Chapters 2 to 4, the transport of ions in these membranes is investigated with particular emphasis on processes occurring at the membrane/solution interface. These chapters primarily deal with understanding electrical processes which occur in the ISE membrane system. In Chapters 5 to 8, physical properties of the ISE membrane are examined with particular attention to the nature of water in the membrane phase. It is important to clarify the behavior of water in order to better understand its complex role in determining electrical properties. A brief description of each chapter in this thesis is given below.

In Chapter 2, the implementation of a system for fast Fourier transform electrochemical impedance spectroscopy is described. This powerful technique is based on *ac* impedance analysis, and is the most efficient method for acquiring data in the low frequency regime. Typically frequencies from between 2.5 kHz to 20 mHz are analyzed with this method.

In Chapter 3, *ac* impedance analysis is used to study neutral species behavior in ISE membranes. Amongst other things, this allows insight into the effects by which permeating interfering species can influence electrode response. Poor reproducibility has been the bane of studies of membrane behavior by the *ac* impedance method and, consequently, this issue is also carefully addressed in this chapter.

In Chapter 4, the observation of inductive behavior in the *ac* impedance analysis of ISE membranes is discussed. Since previously only resistive and capacitive behavior has ever been reported, much of this chapter is theoretical and devoted towards understanding this inductive characteristic.

In Chapter 5, ^{13}C spin-lattice relaxation studies are used to probe plasticizer motions in the ISE membrane. The effects of water, as mediated by the presence of lipophilic salts, on these motions is presented.

In Chapter 6, a more detailed study of water within the ISE membrane is presented. Fourier transform infrared (FTIR) and variable-temperature ^{1}H and ^{2}D NMR spectroscopies are all used to probe the microscopic nature of water.

In Chapter 7, macroscopic water desorption from the ISE membrane is studied gravimetrically. When coupled with previous optical studies of water behavior, significant information can be gained from this study of water transport.

Finally, in Chapter 8, a consideration of the physical adhesion of the ISE membrane to solid surfaces is discussed. This consideration is important with regards to the development of solid state ion sensors. A modified peel-test employing a tensilometer is used to quantify adhesion of membranes prepared with new materials.

1.5 References

1. Cammann, K. *Working with Ion-Selective Electrodes*, Springer-Verlag: New York, 1979.

2. Orion Research, *Handbook of Electrode Technology*, Orion Research Inc.: Cambridge, 1982.

3. Ammann, D.; Morf, W.E.; Anker, P.; Meier, P.C.; Pretsch, E.; Simon, W. *Ion-Selective Electrode Rev.* **1983**, *5*, 3.

4. Bloch, R.; Shatkay, A.; Saroff, H.A. *Biophys. J.* **1967**, *7*, 865.

5. Cremer, M.; *Z. Biol.* **1906**, *47*, 562.

6. Ross, J.W. *Science* **1967**, *156*, 1378.

7. Ross, J.W. *NBS Spec. Publ.* **1969**, *314*, 57.

8. Moore, C.; Pressman, B.C. *Biochem. Biophys. Res. Commun.* **1964**, *15*, 562.

9. Stefanac, Z.; Simon, W. *Microchem. J.* **1967**, *12*, 125.

10. Simon, W.; Pioda, L.A.R. *Chimia* **1969**, *23*, 72.

11. Simon. W. *Angew. Chem.* **1970**, *82*, 433.

12. Steinrauf, L.K.; Hamilton, J.A.; Sabesan, M.N. *J. Am. Chem. Soc.* **1982**, *104*, 4085.

13. Pedersen, C.J. *J. Am. Chem. Soc.* **1967**, *89*, 7017.

14. Ammann, D.; Pretsch, E.; Simon, W. *Tetrahedron Letters* **1972**, *24*, 2473.

15. Pretsch, E.; Badertscher, M.; Welti, M.; Maruizumi, T.; Morf, W.E; Simon, W. *Pure & Appl. Chem.* **1988**, *60*, 567.

16. Rouilly, M.V.; Badertscher, M.; Pretsch, E.; Suter, G.; Simon, W. *Anal. Chem.* **1988**, *60*, 2013.

17. Thoma, A.P.; Viviani-Nauer, A.; Arvanltis, S.; Morf, W.E.; Simon, W. *Anal. Chem.* **1977**, *49*, 1567.

18. Morf, W.E. *The Principles of Ion-Selective Electrodes and of Membrane Transport*, Elsevier: New York, 1981.

19. Morf, W.E.; Simon, W. *Helv. Chim. Acta* **1986**, *69*, 1120.

20. Armstrong, R.D. *Electrochim. Acta* **1987**, *32*, 1549.

21. Pungor, E.; Tóth, K. *Analytical Sciences* **1987**, *3*, 387.

22. Iglehart, M.L.; Buck, R.P. *Talanta* **1989**, *36*, 89.

23. Armstrong, R.D.; Horvai, G. *Electrochim. Acta* **1990**, *35*, 1.

24. Moody, G.J.; Oke, R.B.; Thomas, J.D.R. *Analyst* **1970**, *95*, 910.

25. Morf, W.E.; Wuhrmann, P.; Simon, W. *Anal. Chem.* **1976**, *48*, 1031.

26. Iglehart, M.L.; Buck, R.P.; Pungor, E. *Anal. Chem.* **1988**, *60*, 290.

27. Lindner, E.; Gráf, E.; Niegreisz, Z.; Tóth, K.; Pungor, E.; Buck, R.P. *Anal. Chem.* **1988**, *60*, 295.

28. Armstrong, R.D.; Nikitas, P. *Electrochim. Acta* **1985**, *30*, 1627.

29. Armstrong, R.D.; Lockhart, J.C.; Todd, M. *Electrochim. Acta* **1986**, *31*, 591.

30. Linder, E.; Tóth, K.; Pungor, E. *Dynamic Characteristics of Ion-Selective Electrodes*; CRC Press: Boca Raton, 1988.

31. Armstrong, R.D.; Covington, A.K.; Evans, G.P. *J. Electroanal. Chem.* **1983**, *159*, 33.

32. Buck, R.P. *Ion-Selective Electrode Rev.* **1982**, *4*, 3.

33. Becker, E.D. *High Resolution NMR: Theory and Chemical Applications*; 2nd ed.; Academic Press: New York, 1980.

34. Harris, R.K. *Nuclear Magnetic Resonance Spectroscopy*, Harlow: London, 1986.

35. Shaw, D. *Fourier Transform N.M.R. Spectroscopy*, 2nd ed.; Elsevier: New York, 1984.

36. Lyerla, J.R.; Levy, G.C. *Top. Carbon-13 NMR Spectrosc.* **1974**, *1*, 79.

37. Frye, J.S. *Concepts Magn. Reson.* **1989**, *1*, 27.

38. Levy, G.C.; Peat, I.R. *J. Magn. Reson.* **1975**, *18*, 500.

39. Kowalewski, J.; Levy, G.C.; Johnson, L.F.; Palmer, L. *J. Magn. Reson.* **1977**, *26*, 533.

40. Levy, G.C. *Acc. Chem. Res.* **1973**, *6*, 161.

41. Voelkel, R. *Angew. Chem. Int. Ed. Engl.* **1988**, *27*, 1468.

Chapter 2

The Implementation of a System for Fast Fourier Transform Electrochemical Impedance Spectroscopy

2.1 Introduction

Electrode reactions may be studied by imposing large perturbations on the system and monitoring the resultant current or potential response. For example, potential sweeps, potential steps and current steps are employed, respectively, in the classical techniques of cyclic voltammetry, chronoamperometry and chronopotentiometry [1]. The major disadvantage of these methods is that the system is perturbed to a condition far from equilibrium. Thus, the measured current or potential response as the system returns to equilibrium is generally a transient signal. For this reason, the use of alternating voltage and current perturbations for the study of electrode processes has been developed over the past few decades. In these methods, small amplitude sinusoidal perturbations are applied to the cell, and the system response is monitored at steady state [2].

There are many distinct advantages of the *ac* techniques over the *dc* techniques. First, there is only minimal perturbation of the test system from equilibrium since very small amplitude signals are involved. Detailed knowledge of the current-potential characteristics over large ranges of overpotential are therefore not required. One can usually treat the response theoretically in the linear working range. This leads to dramatic simplifications in interpreting the data. Second, the time-invariant nature of the system response allows long term averaging for high-precision measurements. Third, measurements may be made in low conductivity media where *dc* techniques are prone to serious potential-control errors.

2.2 Electrochemical Impedance Spectroscopy

2.2.1 Concepts

The relationship between input voltage (E) and output current (I) in any system can be characterized by either the impedance (Z) or the admittance (Y):

$$\vec{Z} = \frac{1}{\vec{Y}} = \frac{\vec{E}}{\vec{I}} \qquad (2.1)$$

where vector representation has been employed. Impedance and admittance can be considered as *ac* equivalents to resistance and conductance in *dc* circuits.

In electrochemical impedance spectroscopy (EIS), the impedance behavior of a test system is characterized by measuring its impedance as a function of the input voltage frequency. This yields a frequency domain profile of the admittance which can be represented as A(ω). Thus, equation (2.1) may be generalized for multiple frequencies as:

$$A(\omega) = \frac{I(\omega)}{E(\omega)} \qquad (2.2)$$

where $A(\omega)$ = admittance at frequency ω
$E(\omega)$ = input voltage at frequency ω
$I(\omega)$ = current flow at frequency ω

Techniques for acquiring EIS data can operate either in the frequency domain or in the time domain. These are discussed in the following sections.

2.2.2 Frequency Domain Measurement

The most conceptually simple method for acquiring impedance spectra is via a point-by-point assessment of the impedance response at various frequencies using pure sinusoidal applied potential signals. This is the basis for the phase-sensitive detection method which is a widely used technique. Instrumentation consists of a phase-sensitive detector (such as a lock-in amplifier), a waveform generator and a potentiostat which provides potentiostatic control and current measurement. The waveform generator provides a variable-frequency, small amplitude (< 10 mV peak-to-peak) sinusoidal function which is applied to the test cell. The resulting current flow is then fed into the lock-in amplifier which provides directly an output signal that is proportional to the in-phase and out-of-phase components of the current response with respect to the phase of the applied potential. From this data, the real and imaginary components of the impedance may readily be calculated at each applied frequency. Note that the instrument system itself often introduces slight frequency-dependent phase shifts to the output signal. These may be compensated by replacing the electrochemical system with a capacitor and adjusting the in-phase component of current to zero at each frequency. In this way, a calibration curve of the changes in phase shifts as a function of frequency may be constructed. Specific details for this procedure can be found in reference [3].

The phase-sensitive detection method is instrumentally simple and capable of providing high precision impedance data. Its main disadvantage, however, is that it operates in the so-called frequency domain, that is, the data is obtained and analyzed frequency by frequency. At least one full *ac* excitation cycle must be applied at each frequency and normally several data points are required per decade of frequency studied. While this does not present any problem at the higher frequencies, however, it does lead to excessively long data acquisition times at the lower frequencies. For example, the period for a 1 mHz sine wave is 1000 seconds. Therefore, it would take 1000 seconds or 16.7 minutes for just one excitation cycle at this one frequency. It can readily be seen that measurement times become objectionably long when multiple excitation cycles are applied for a set of low frequency experiments. Thus, low frequency operation requires much time and patience, but it also proves to be unsuitable for studying unstable systems such as actively corroding electrodes. The typical frequencies measured by the lock-in impedance system currently in use in our research group are listed in Table 2.1 along with their corresponding phase shift corrections.

2.2.3 Time Domain Measurement

A significantly different way to obtain EIS spectra is through a Fast Fourier Transform (FFT) technique. The use of the Fourier transformation is extensive in the field of spectroscopy as exemplified by the techniques of Fourier transform infrared spectroscopy (FT-IR) and Fourier transform nuclear magnetic resonance spectroscopy (FT-NMR). The main advantage of the Fourier transform methods over the conventional methods is the capability for simultaneous measurements using several different excitation signals. This is known as the multiplex advantage (Fellget's advantage) of Fourier transform methods and is equally significant in both electrochemical and spectroscopic techniques.

Any waveform may be represented as either amplitude plotted against time or amplitude of each frequency plotted against frequency. These two representations are referred to as time-domain and frequency-domain representations, respectively [4]. The Fourier transform can be regarded as a process that converts information between these two domains. This is shown in Figure 2.1 for waveforms having one and three frequency components. Mathematically, the Fourier transformation of a digitized waveform can be accomplished with the discrete Fourier transform [5]:

$$F_m = \frac{1}{N} \sum_{k=0}^{N-1} T_k \exp\left(\frac{-2\pi jmk}{N}\right) \tag{2.3}$$

Table 2.1 Typical frequencies measured by lock-in impedance measurement system (50 mV peak-to-peak excitation, 10 μA current scale).

frequency (Hz)	phase shift correction	frequency (Hz)	phase shift correction
40000	321.75	1000	360.6
20000	342.3	850	360.6
12500	350.0	750	360.65
9000	353.4	650	360.75
7000	355.3	600	360.75
5500	356.75	400	360.9
4500	357.5	300	360.95
3500	358.5	200	361.05
3000	358.95	100	361.15
2500	359.4	75	361.2
2300	359.5	50	361.2
2000	359.75	35	360.0
1800	360.0	25	360.2
1500	360.2	15	360.2
1400	360.5	10	360.0
1200	360.55		

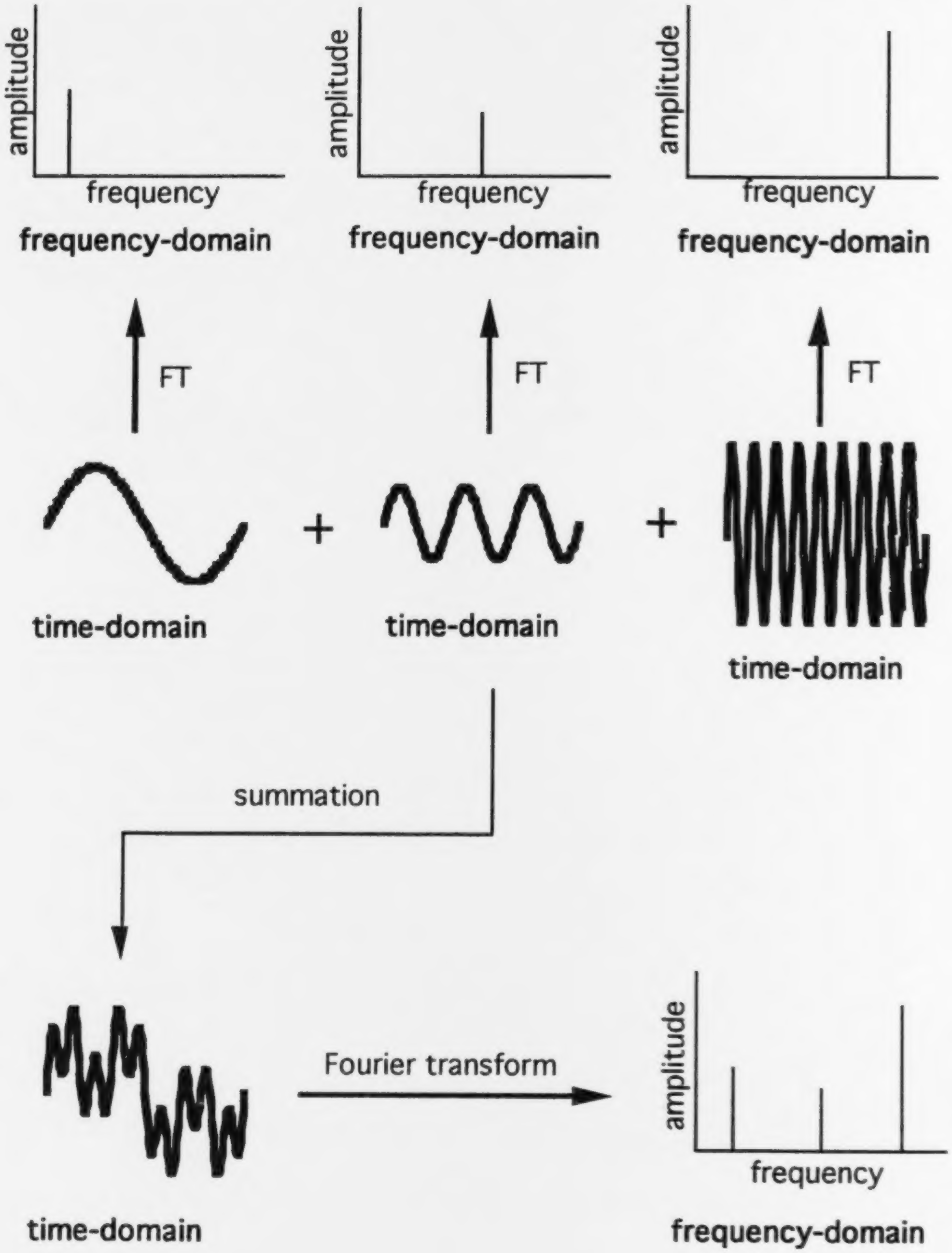
amplitude
frequency
frequency-domain
amplitude
frequency
frequency-domain
amplitude
frequency
frequency-domain
FT
FT
FT
+
+
time-domain
time-domain
time-domain
summation
Fourier transform
time-domain
amplitude
frequency
frequency-domain

Figure 2.1 Conversion between the time-domain and frequency-domain via the Fourier transformation for one and three frequency components.

where N = the number of data points considered
T_k = kth point in the time domain
F_m = mth point in the frequency domain
$j = \sqrt{-1}$

It would appear that this equation requires N multiplications for each point or N^2 multiplications for the entire spectrum. Fourier transformations take a very long time to compute, however, an algorithm known as the Fast Fourier Transformation (FFT) has been developed which speeds up the calculations by a factor of N/log2N. This algorithm involves taking advantage of the harmonics of a given frequency and calculating all such harmonics at one time. The method was originally reported by Cooley and Tukey in 1965 and has been described by many others since [6]. The most commonly used algorithms are power-of-two algorithms which restrict the number of points to be transformed to those that are integer powers of two.

The implementation of EIS with the FFT technique involves applying a mixture of excitation frequencies simultaneously to the test system. Equivalent frequency domain representation of the time domain waveforms can then be generated via the Fourier transformation. This contrasts with the pure sinusoid signals employed with the phase-sensitive detection method. The frequency domain admittance profile can then be calculated from equation (2.2). Since the potential and current profiles will contain amplitude and phase characteristics, a more convenient form for equation (2.2) is given as:

$$A(\omega) = \frac{I(\omega)\,E^*(\omega)}{E(\omega)\,E^*(\omega)} \tag{2.4}$$

where $E(\omega)$ = frequency domain spectrum of the applied potential
$E^*(\omega)$ = complex conjugate of $E(\omega)$
$I(\omega)$ = frequency domain spectrum of the current response

The vector products $I(\omega)E^*(\omega)$ and $E(\omega)E^*(\omega)$ are usually referred to as crosspower and autopower spectra, respectively [7].

The time domain waveform employed in FFT-EIS is a complex periodic signal that can be described by a conventional Fourier series of sine waves. That is, it may be regarded as an algebraic sum of a set of discrete sinusoidal components that are harmonics of a single fundamental frequency. As outlined by Smith *et al* [8], the choice of waveform directly affects measuring efficiency. The preferred signal consists of an odd-harmonic, phase-varying, pseudo-random white noise waveform. This is constructed from odd harmonics of a fundamental Fourier component, *i.e.* frequency = (2N-1) F, where F is the frequency of the fundamental Fourier component and N is any integer. By including only odd harmonics, the second harmonics, as well as the modulation components, will all fall at even frequencies which can subsequently be ignored in the data analysis. The amplitudes of the individual components are set equal ("white noise") so that each will carry the same weight. The use of randomized phase relations minimizes the maximum deviations of the test signal from zero. For example, if the phase relationship were identical for all components, extremely large excursions would occur at those points where all the component harmonics constructively interfere. This would be most noticeable at the beginning and the end of each waveform cycle. Additionally, it is important to ensure that all frequency components in the applied waveform contain an integral number of cycles. Artifacts such as "leakage" will occur when there are frequency components that are inharmonic. This is manifested as severe apodization of the single frequency component in the Fourier transformation. Leakage may be avoided by simply matching the data acquisition period with the period of the waveform's fundamental harmonic. This consideration is not a problem with digital waveform generation, but it must be seriously addressed when utilizing analog sources [8].

The upper frequency limit accessible by the FFT technique is established by the maximum instrumental sampling rate according to the sampling theorem. At least two points per cycle are required in order to correctly represent any sine wave at a given frequency. Therefore, the highest frequency component must be less than one half the sampling rate. For example, at a maximum sampling rate of 150 μsec, the highest frequency component measurable is only 3333 Hz. The main advantage of the FFT technique, however, is for the collection of impedance data in the low frequency regime. For example, a 2048-point waveform with a fundamental frequency of 1 mHz can be constructed with 50 frequency components. This would allow the simultaneous measurement of 50 different frequencies from between 1 mHz and 1 Hz in about 1000 seconds. In contrast, it would take 1000 seconds to acquire just the 1 mHz frequency point alone by a phase-sensitive detection method.

2.3 Fast Fourier Transform Electrochemical Impedance Spectroscopy Measurement System

The majority of the impedance studies contained in this work used the FFT technique. The development of a practical EIS system using this method will be thoroughly discussed in this section. First, the instrumental configuration will be presented followed by an explanation of how a computer-generated FFT waveform can be used to produce impedance spectra. Calibration procedures for obtaining meaningful impedance data will also be included. This will provide an overview of the essential features for implementing FFT-EIS. Next, a discussion of practical software routines will be given which allow for rapid and efficient collection of EIS spectra in actual experiments. Finally, a discussion of computer-modelling routines will also be presented.

2.3.1 Instrumentation

A block diagram of the EIS system is shown in Figure 2.2. At the heart of the system is an EG&G Princeton Applied Research Model 273 Potentiostat/Galvanostat (PAR-273), a state-of-the-art instrument possessing an on-board microprocessor and on-board memory. Two 14-bit digital-to-analog converters (DACs) provide flexible and precise control of

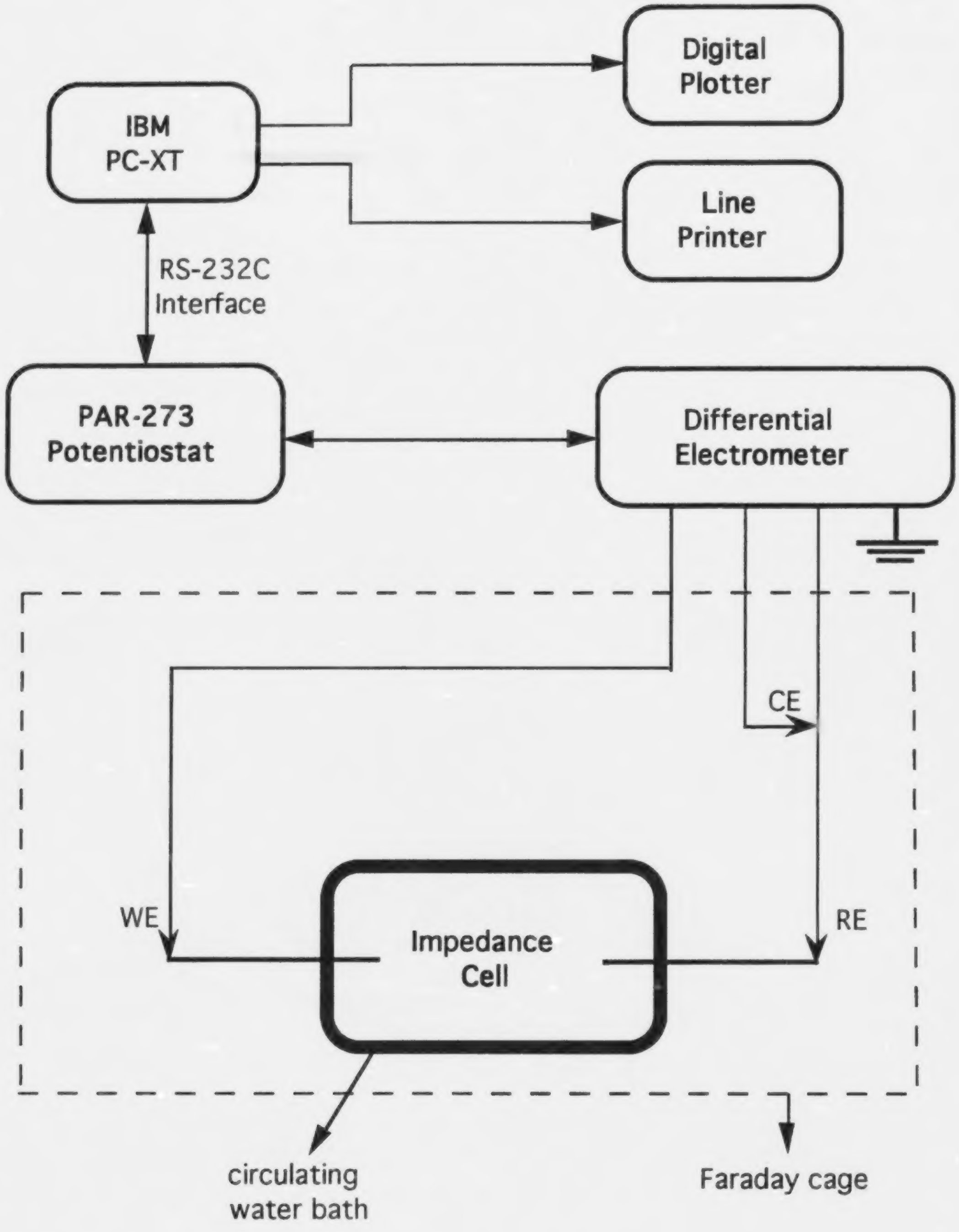
Digital
Plotter
IBM
PC-XT
Line
Printer
RS-232C
Interface
PAR-273
Potentiostat
Differential
Electrometer
CE
WE
Impedance
Cell
RE
circulating
water bath
Faraday cage

Figure 2.2 Block diagram of FFT-EIS system.

the potential and are used to apply virtually any digitally created waveform. A 12-bit analog-to-digital converter (ADC) allows rapid and convenient current and potential data acquisition. As shown, the PAR-273 also uses an external differential electrometer which allows the use of two electrodes to control the potential across an interface such as a membrane. Since impedance experiments utilize small test signals, electrical interferences from outside sources are minimized by enclosing the impedance cell within a Faraday cage. Temperature control is provided by a Colora Ultra-Thermostat circulating water bath. During impedance experiments, operation of the PAR-273 is totally controlled by the external IBM PC-XT host computer. The only exception is the CELL ENABLE switch which allows override of computer control of the cell at any time. Communication between the PAR-273 and the host computer is accomplished through a serial RS-232C interface. Computer control of the PAR-273 is facilitated by EG&G PARC's Electrochemical Command Set which is a group of over 100 mnemonic software statements specifically designed for electrochemical applications. Software routines for the host computer used for waveform generation, experiment control, data acquisition, data calculation, data presentation and modelling were all written in ASYST (Macmillan, version 1.5). This is a versatile high-level computer language which allows the development of new user-designed words known as "colon definitions". A listing of all ASYST programs can be found in Appendix A. All ASYST files reside on the 10M-byte fixed disk while experimental data are stored on 320K-byte floppy diskettes. Final impedance results are displayed on a Panasonic KX-P1091 line printer, Hewlett-Packard 7475A plotter or Hewlett-Packard LaserJet III printer. Note that control of an IEEE 488-interfaced device such as the plotter requires the addition of an Iotech Serial 488A Bus Converter. A schematic of all relevant devices attached to the host computer is given in Figure 2.3.

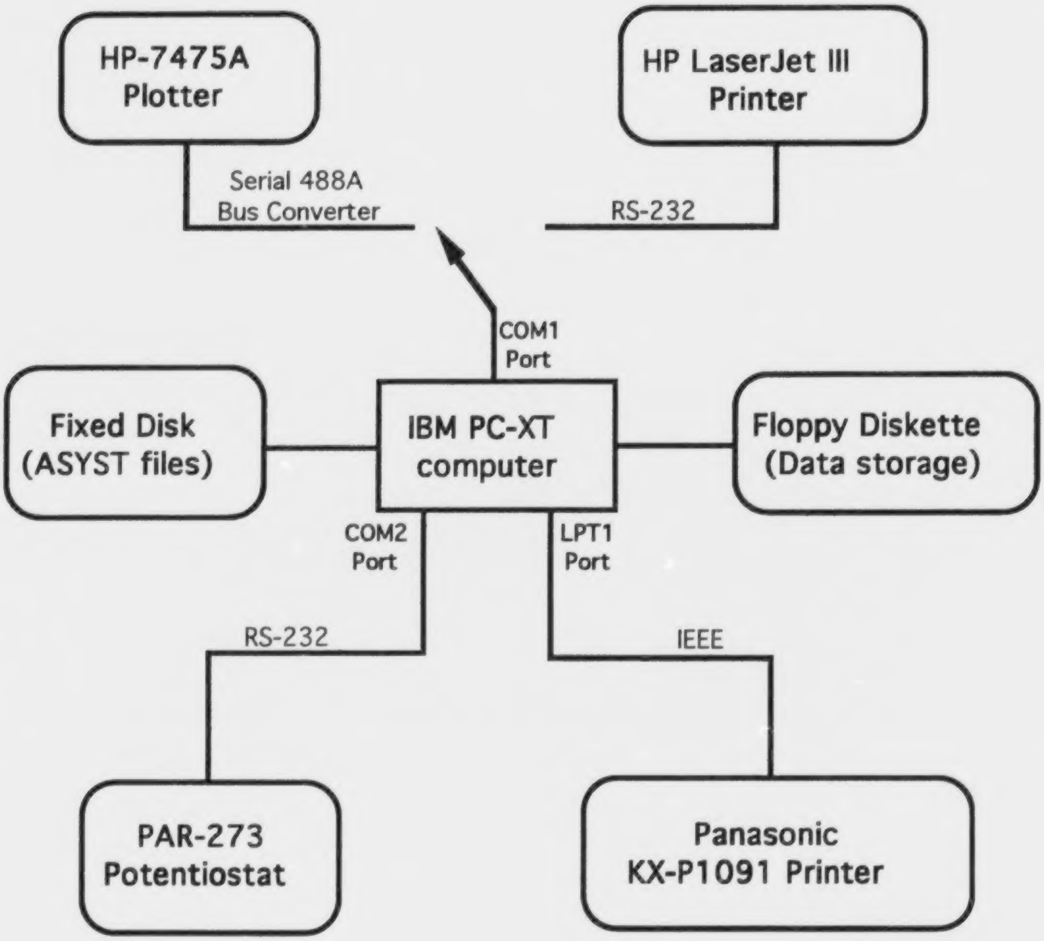
HP-7475A
Plotter
HP LaserJet III
Printer
Serial 488A
Bus Converter
RS-232
COM1
Port
Fixed Disk
(ASYST files)
IBM PC-XT
computer
Floppy Diskette
(Data storage)
COM2
Port
LPT1
Port
RS-232
IEEE
PAR-273
Potentiostat
Panasonic
KX-P1091 Printer

Figure 2.3 Schematic of devices controlled by host computer.

2.3.2 Waveform Generation

The computer-generated time domain waveform is created by a Fourier synthesis of sine waves. This waveform resides in computer memory as a 2048-point array called WDATA and it is constructed by routines in the ASYST file NEWWDATA.ASY (Program A.1). The frequencies of the individual Fourier components are determined by specifying the number of integral wave cycles for each component within the 2048-point array. Thus,

$$\mathrm{WDATA(t)} = \sum_{n=1}^{\mathrm{COMPONENTS}} \mathrm{AMP}_n \sin\left[\frac{2\pi\ \mathrm{WAVE.CYCLES}_n\ t}{2048} + \mathrm{PHI}_n\right] \qquad (2.5)$$

where COMPONENTS = number of Fourier components
n = reference to nth Fourier component
t = arbitrary time scale from 0 to 2047
AMP_n = amplitude of nth component
PHI_n = phase angle of nth component
$\mathrm{WAVE.CYCLES}_n$ = number of wave cycles of nth component

Following suggestions by Smith [8], the amplitudes for each component are set identical and the phase angles are all randomized. This randomization of phase angles is accomplished by filling in the phase angle array PHI with a uniform random distribution of numbers from 0 to 2π. Furthermore, the choice of frequency components should be made such that they are approximately equally separated in square root of frequency space. A typical FFT waveform that has been successfully employed is shown in Figure 2.4. It was constructed from 50 frequency components each of amplitude 800 counts as shown in Table 2.2. Note that full-scale modulation of the DAC on the PAR-273 is only 8000 counts and thus the minimum and maximum limits on any acceptable waveform must be scaled to within ± 8000 counts. Once a satisfactory waveform has been constructed, it is saved onto disk for later use in EIS experiments.

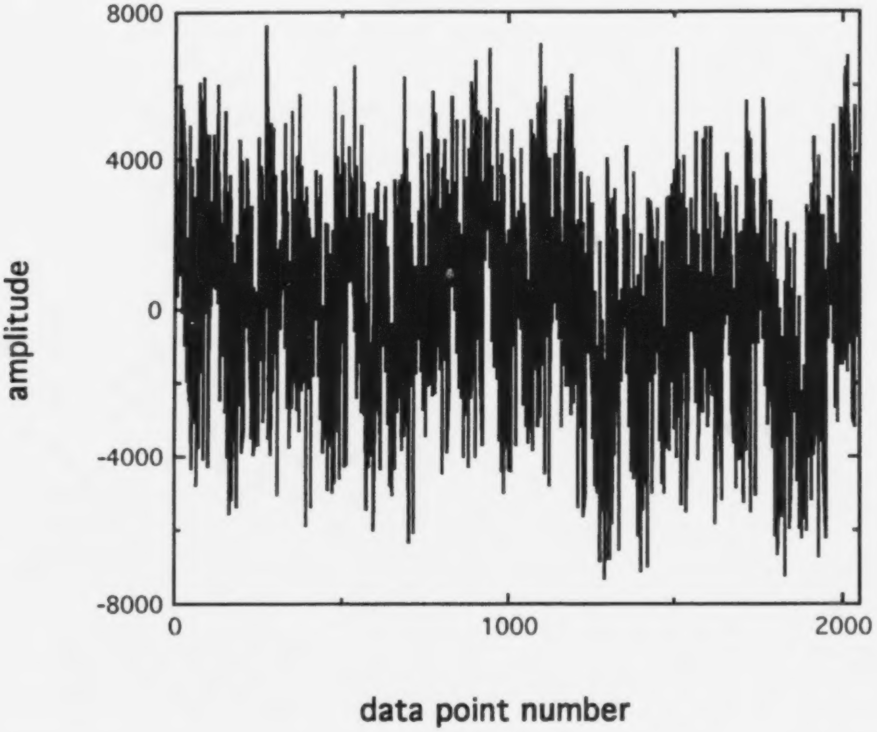

Figure 2.4 Typical WDATA excitation waveform consisting of 50 frequency components with equal amplitude and random phase angle.

Table 2.2 Frequency component composition of FFT waveform shown in Figure 2.4.

n	wave cycles	n	wave cycles	n	wave cycles
1	1	18	140	35	480
2	2	19	160	36	500
3	3	20	180	37	520
4	4	21	200	38	540
5	5	22	220	39	560
6	7	23	240	40	580
7	10	24	260	41	600
8	15	25	280	42	620
9	20	26	300	43	630
10	25	27	320	44	640
11	30	28	340	45	650
12	35	29	360	46	660
13	40	30	380	47	670
14	60	31	400	48	680
15	80	32	420	49	690
16	100	33	440	50	700
17	120	34	460		

2.3.3 EIS Measurement

Software routines used to establish RS-232C communications with the PAR-273 are contained in the ASYST file RS232.PAR (Program A.2). More specific commands which allow the PAR-273 to perform electrochemical experiments are contained in the ASYST file COMM.PAR (Program A.3). These routines also partition the on-board microprocessor memory of the PAR-273 into three 2048 data point blocks according to Table 2.3. Each of these 2048 data point memory blocks is addressed by a unique curve number (0, 2 or 4).

The 2048-point waveform contained in the WDATA array is first transmitted to the PAR-273 using the SEND.CURVE colon definition where it is stored as the modulation source waveform in curve number 0. During the impedance experiment, this modulation waveform is applied point-by-point to the cell at a rate determined by the TIMEBASE (TMB) and SAMPLE-PER-POINT (S/P) settings. The TMB setting sets the time interval between samples where in this context a sample is whenever the potential or current is measured and an analog-to-digital conversion done on the measured value. The S/P setting is used to set the number of samples to be taken for each actual data point (*i.e.* sample placed in memory). Thus, the time between data points is given by TMB multiplied by S/P. Generally TMB is left at a low value such as 500 μsec and S/P is varied in order to obtain the desired frequencies. The INTERPOLATION (INTRP=1) function is always enabled so that the modulation DAC is updated once per sample rather than once per data point. This allows the modulation to advance in small steps which results in a smoother modulation waveform. This is especially important in experiments for which S/P is set at a high value. The full-scale potential range of the modulation DAC is controlled by the MODULATION RANGE (MR) setting. Usually MR = 1, giving a peak-to-peak modulation of approximately ± 180 mV for the waveform shown in Figure 2.4 and a resolution of 0.025 mV. The resultant current waveform is measured and this is stored in curve number 2. Note that the full-scale current range (I/E) must be set to an appropriate value and, for best accuracy, the current gain (IGAIN)

Table 2.3 Memory partitioning of PAR-273 on-board microprocessor for impedance experiments.

curve number	memory address	contents
0	0 - 2047	modulation source waveform
2	2048 - 4095	measured current waveform
4	4096 - 6143	measured voltage waveform

should be as high as possible consistent with avoiding current overload. Recommended IGAIN settings are given in Table 2.4. The electrometer monitor potential is also measured and this is stored in curve number 4. For a ± 180 mV waveform, a potential gain (EGAIN) setting of 50 is recommended. Following an experiment, these current and potential waveforms are subsequently transferred to the host computer where they are scaled to actual units of amperes and volts and then stored in data arrays IDATA and EDATA, respectively. This is all accomplished with the GET.IE colon definition which contains the required sub-definitions for data retrieval and scaling. These waveform transfers are most rapidly executed with the BINARY DUMP (BD) and BINARY LOAD (BL) commands of the PAR-273. Data in binary is transferred with two bytes per point with the high order byte always followed by the low order byte. Note that high-speed binary transfers are very susceptible to communication errors so that adequate error trapping must be incorporated in the software routines.

The entire impedance experiment may be executed with the AUTO.RUN colon definition for automatic data acquisition and transfer. Alternatively, the RUN colon definition may be used to initiate the experiment. When the experiment is finished, the END.RUN colon definition is then used to retrieve the data from the PAR-273. The advantage of this latter procedure is that the host computer is not tied up waiting for experiments with excessively long modulation rates. Other tasks may be performed by the computer and data can be collected later at the operator's convenience. As mentioned, in a typical experiment TMB = 500, and the S/P value is varied in order to obtain the desired applied frequencies. For very high frequencies, TMB may be set as low as 100 µsec, however, at this timebase the PAR-273 uses a special high speed data acquisition mode in which only the current waveform can be measured. In this case, a previously acquired EDATA waveform must be used for the data calculation routines.

There are two methods by which the signal-to-noise is improved in the experiment. First, POINT AVERAGING MODE (PAM = 1) is engaged in order to average the number of samples taken at each point as

Table 2.4 Recommended IGAIN setting as a function of current level.

current **(% of full-scale setting)**	**recommended** **IGAIN**
< 4 %	50
4 - 20 %	10
20 - 40 %	5
> 40 %	1

determined by the S/P parameter. Second, linear averaging of the time domain response can be performed (SWEEP AVERAGING MODE, SAM = 1). A maximum of 16 sweeps through the waveform stored in curve number 0 can be averaged in this manner as determined by the number of sweeps setting (SWPS).

A *dc* bias (BIAS) may also be applied to the cell during the experiment. In this case the impedance experiment itself may be delayed by an arbitrary delay value (DELAY) in order to allow for stabilization following the bias application.

2.3.4 EIS Calculations

The impedance data is calculated from the measured IDATA and EDATA waveforms by routines in the ASYST file IMPCALC.ASY (Program A.4). The actual frequencies applied in the experiment are first determined by the CALC.TIME&FREQ colon definition:

$$\mathrm{FREQ}_n = \frac{\mathrm{WAVE.CYCLES}_n}{\mathrm{TMB}\,\frac{\mu\mathrm{sec}}{\mathrm{sample}} \times 10^{-6}\,\frac{\mathrm{sec}}{\mu\mathrm{sec}} \times \mathrm{S/P}\,\frac{\mathrm{samples}}{\mathrm{point}} \times 2048\ \mathrm{points}} \tag{2.6}$$

For example, at TMB = 500 and S/P = 10, the waveform period is 10.24 seconds. Thus, a component having 15 integral wave cycles would have a frequency of 1.46 Hz.

The admittance calculations are performed only at those fifty frequencies actually applied to the cell. These are deduced by the PICKOUT.DATA routine whereby an autopower spectrum of WDATA(ω) is first determined. Then by picking out maxima in this spectrum, the indices IND corresponding to the actual applied frequencies may thus be determined. In the DATA.CALC routine these indices can, in turn, be used to pick out the same frequencies from the overall I(ω) and E(ω) data arrays, EDATA.FFT1 and IDATA.FFT1, respectively. This creates two new abbreviated fifty-point data arrays, EDATA.FFT and IDATA.FFT, which may then finally be used to calculate the admittance from crosspower and autopower spectra according to equation (2.4). The advantage of this procedure is that spurious frequency components are conveniently ignored. From the admittance, real and imaginary components of impedance and the magnitude of the impedance vector may all be calculated:

$$Z' = \text{Z.REAL} = \frac{A_{real}}{A_{real}^2 + A_{imag}^2} \tag{2.7}$$

$$Z'' = \text{Z.IMAG} = \frac{A_{imag}}{A_{real}^2 + A_{imag}^2} \tag{2.8}$$

$$|\vec{Z}| = \text{Z.MAG} = \sqrt{(Z_{real})^2 + (Z_{imag})^2} \tag{2.9}$$

The calculated impedance data may be presented as either a Nyquist plot in the complex plane or as a Bode plot of log Z_{mag} *versus* log ω. These are drawn by the NYQUIST.PLOT and BODE.PLOT colon definitions, respectively.

2.3.5 EIS System Calibration

For every particular set of experimental conditions, such as frequencies, current and modulation ranges, *etc*., an instrument calibration is required to compensate for any transfer functions introduced by the measuring system. These can result, for example, from distortion in the analog amplifiers used to convert the digital waveform to an analog signal. Colon definitions for calibrating or correcting impedance data are contained in the ASYST file CORRIMP.ASY (Program A.5). The calibration procedure involves duplicating the measurement operation in which the sample cell is replaced by a dummy cell of precisely known admittance. This may be a calibrated resistor, R_{cal}, or capacitor, C_{cal}, for which the true or known admittance, $A(\omega)_{true}$, may be calculated:

$$A(\omega)_{\mathrm{true}} = \frac{1}{R_{\mathrm{cal}}} \tag{2.10}$$

$$A(\omega)_{\mathrm{true}} = j\omega C_{\mathrm{cal}} \tag{2.11}$$

From the experimentally observed admittance of the dummy cell, $A(\omega)_{\mathrm{obs}}$, a frequency-dependent correction function, $G(\omega)$, may then be readily calculated:

$$G(\omega) = \frac{A(\omega)_{\mathrm{true}}}{A(\omega)_{\mathrm{obs}}} \tag{2.12}$$

These calculations are performed by the colon definitions RESPONSE.R and RESPONSE.C which are executed after the experiment and impedance calculations are performed on the appropriate resistor or capacitor, respectively. Table 2.5 provides a convenient list of calibration resistors for the various combinations of current ranges (I/E) and current gains (IGAIN) typically employed. Subsequent impedance spectra can then be corrected by applying equation (2.12) using the CORR.IMP colon definition. It is important to note that this instrument calibration procedure must precede any actual impedance measurements since individual IDATA and EDATA waveforms are not saved.

It can be remarked that the calibration procedure is essentially the same as deconvolution of an instrument response function (IRF) from an observed signal to yield the true signal. Thus,

$$A(\omega)_{\mathrm{obs}} = A(\omega)_{\mathrm{true}} \times \frac{1}{G(\omega)} \tag{2.13}$$

and the observed admittance results from the convolution of the true signal with the IRF, $1/G(\omega)$. Deconvolution, which is a division operation in the Fourier domain, simply attempts to reverse this convolution operation.

Table 2.5 Suitable calibration resistors for various current ranges (MR = 1, EGAIN = 50).

I/E	IGAIN	resistor
100 nA	50	30 MΩ
100 nA	10	10.14 MΩ
100 nA	5	4.59 MΩ
100 nA	1	1.746 MΩ
1 μA	50	4.59 MΩ
1 μA	10	1.746 MΩ
1 μA	5	471.3 kΩ
1 μA	1	332.8 kΩ
10 μA	50	471.3 kΩ
10 μA	10	332.8 kΩ
10 μA	5	55.65 kΩ
10 μA	1	31.85 kΩ

2.3.6 EIS Data Presentation

Following an impedance experiment and the calibration sequence, the impedance results are found in the Z.REAL and Z.IMAG data arrays. The most common form of data presentation is a Nyquist plot in the complex plane. Colon definitions for generating plots on the HP-7475A plotter are contained in HPPLOT.ASY (Program A.6). The plotting routine is initiated with HPPLOT and actual plotting of the data is performed with HPPLOT.DATA once the x and y data arrays have been placed on the number stack. Plotting is terminated with HPPLOT.END whereupon a plot legend is also constructed. Thus, for a Nyquist plot of the impedance data, the following sequence of words is required: HPPLOT { Z.REAL Z.IMAG HPPLOT.DATA } HPPLOT.END. Note that the command series enclosed by { } is repeated for each set of data to be plotted prior to executing HPPLOT.END. Note that in order to obtain equally scaled axes, the magnitude of the y-axis should be set to three-quarters of the x-axis since the plot axes are defined as 150 mm by 200 mm.

Colon definitions for plotting using an HP-LaserJet III printer are contained in HPLASER.ASY (Program A.7). In this case, the additional words HPLASER.INIT and HPLASER.END must precede and follow any sequence of plotting words.

2.3.7 Automated EIS Experiments

As can be seen from the previous sections, the entire EIS experiment involves a large number of small but crucial procedures. In order to facilitate rapid and efficient collection of EIS spectra, a number of ASYST routines were written (Programs A.8 - A.14). These are loaded along with programs from the previous sections and a new image of the ASYST system containing all these programs is saved as the IMPTEMP image. Note that the IMPTEMP image system memory must be reconfigured according to Table 2.6 in order to properly load and run all the impedance

Table 2.6 Memory configuration for IMPTEMP image of base ASYST system.

memory area	memory allocation (kbytes)
symbol table	30
string variable	7
data acquisition buffer	0
dictionary	10
unnamed array (heap)	96

programs. A list of all programs in the IMPTEMP image is given in Table 2.7.

The START.PAR colon definition (Program A.8) initiates the PAR-273 and transfers a FFT waveform which has been previously created and stored on disk by NEW.WDATA.

For the majority of EIS experiments, an adequate frequency range is 20 mHZ to 2.3 kHz. This may be measured in four separate EIS experiments using slightly overlapping frequency ranges as shown in Table 2.8 for an FFT waveform having the frequency composition listed in Table 2.2. Thus, a complete EIS spectrum will hitherto refer to a set of these four impedance experiments. Automatic calibration of the entire frequency range proceeds by inserting an appropriate calibration resistor (see Table 2.5) and running PAR.CALIBRATE (Program A.9). Should additional current range settings need to be calibrated, up to five calibrations may be stored in the multi-dimensional variables CALA, CALB, CALC, CALD and CALE contained in active RAM memory. Note, however, that these must be manually recalled whenever current ranges are changed (refer to Program A.10, CALSAVE.ASY). Corrected EIS spectra are then automatically acquired with the AUTO.EXPT colon definition (Program A.9). The entire EIS spectrum may be subsequently stored and recalled from disk by the colon definitions DATA.SAVE and DATA.READ, respectively (Programs A.11 - A.12). A summary of relevant array variables used in these automated EIS experiments is given in Table 2.9. Automatic plotting of the entire EIS spectrum is achieved with colon definitions contained in PLOT.ASY (Program A.13). The PLOT, HPLASER.PLOT and SCREEN.PLOT words direct plotting to the HP7475A plotter, HP-LaserJet III printer and computer monitor, respectively.

Additional useful abbreviated colon definitions and function key definitions are contained in FASTCMDS.ASY (Program A.14). For example, the words HWS and VWS are used to facilitate changes in axes limits for screen plotting. An entire list of all user-level colon definitions is summarized in Table 2.10.

Table 2.7 ASYST programs saved in IMPTEMP image.

Program Number	ASYST filename
A.1	NEWWDATA.ASY
A.2	RS232.PAR
A.3	COMM.PAR
A.4	IMPCALC.ASY
A.5	CORRIMP.ASY
A.6	HPPLOT.ASY
A.7	HPLASER.ASY
A.8	START.PAR
A.9	AUTOEXPT.ASY
A.10	CALSAVE.ASY
A.11	SAVE.ASY
A.12	READ.ASY
A.13	PLOT.ASY
A.14	FASTCMDS.ASY

Table 2.8 Parameter settings for EIS spectra from 20 mHz to 2.3 kHz using waveform defined in Table 2.2.

expt. no.	TMB	S/P	SWPS	frequency range
1	500	1	16	0.977 to 684 Hz
2	150	1	16	3.26 to 2279 Hz
3	500	5	16	0.195 to 137 Hz
4	500	50	10	19.5 mHz to 13.7 Hz

Table 2.9 Array variables used for automated EIS experiments.

experiment number	correction function	impedance results	
		Z.REAL	Z.IMAG
1	G1(W)	ZR1	ZI1
2	G2(W)	ZR2	ZI2
3	G3(W)	ZR3	ZI3
4	G4(W)	ZR4	ZI4

Table 2.10 Summary of user-level colon definitions in IMPTEMP image.

colon definition	ASYST program no.	colon definition	ASYST program no.
AUTO.EXPT	A.9	NYQUIST.PLOT	A.4
AUTO.RUN	A.3	PAR.CALIBRATE	A.9
BODE.PLOT	A.4	PLOT	A.13
CORR.IMP	A.5	RECALL.CALA	A.10
DATA.READ	A.12	RECALL.CALB	A.10
DATA.SAVE	A.11	RECALL.CALC	A.10
END.RUN	A.3	RECALL.CALD	A.10
EXPT1	A.9	RECALL.CALE	A.10
EXPT2	A.9	RESPONSE.C	A.5
EXPT3	A.9	RESPONSE.R	A.5
EXPT4	A.9	RUN	A.3
GET.RESPONSE	A.2	SCREEN.PLOT	A.13
HPLASER.END	A.7	SEND.COM	A.2
HPLASER.INIT	A.7	SHOW.VALUES	A.3
HPLASER.PLOT	A.13	START.PAR	A.8
HPPLOT	A.6	STORE.CALA	A.10
HPPLOT.DATA	A.6	STORE.CALB	A.10
HPPLOT.END	A.6	STORE.CALC	A.10
IMP.CALC	A.4	STORE.CALD	A.10
NEW.WDATA	A.1	STORE.CALE	A.10

2.4 Characterization of Electrochemical Impedance Spectroscopy Measurement Systems

2.4.1 Dummy Cell Circuits

Any electrochemical cell may be represented by an equivalent electronic circuit which models the observed impedance behavior. For example, an equivalent circuit representation for an ISE membrane has been given by Armstrong [9] and is shown in Figure 2.5. In order to fully characterize the accuracy and precision of the two EIS measurement systems employed in this work, "dummy" cell circuits were fabricated from electronic circuit components. The magnitudes for these components were selected so as to resemble typical expected electrical responses of the real ISE membranes that were to be investigated.

The first dummy cell circuit constructed is shown in Figure 2.6a. This circuit is used to model both blank membranes consisting of only plasticizer and polymer, and blank membranes containing low concentrations of benzoic acid or methyl benzoate (*cf.* Chapter 3). These membranes are expected to exhibit excessively large bulk (R_b) and charge-transfer (R_{ct}) resistances which potentially might not be accurately measured. The second dummy cell circuit constructed is shown in Figure 2.6b. This circuit models ISE membranes containing an ionophore such as a neutral carrier (*e.g.* valinomycin or nonactin) or an ion-exchanger (*e.g.* dialkyl phosphate or organic ammonium ions). As a result of the presence of such ion-carriers, the bulk membrane resistance (R_b) usually assumes a moderate value while the charge-transfer resistance (R_{ct}) becomes vanishingly small (*cf.* Chapter 4). Note that solution resistances (R_s) can be safely ignored in these studies since all measurements were conducted in aqueous ionic solutions.

2.4.2 Computer Modelling of Dummy Cell Circuits

As mentioned above, electrochemical cells may be represented by equivalent electronic circuits. Impedance and admittance values for

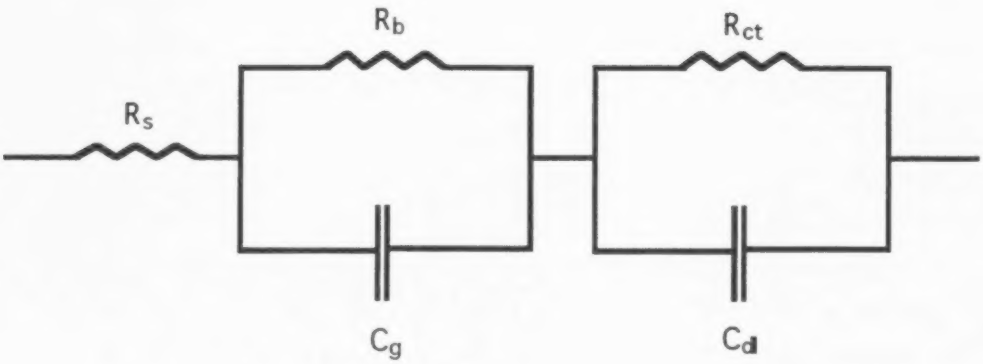
R_b
R_{ct}
R_s
C_g
C_{dl}

Figure 2.5 Equivalent circuit representation of an ISE membrane system.

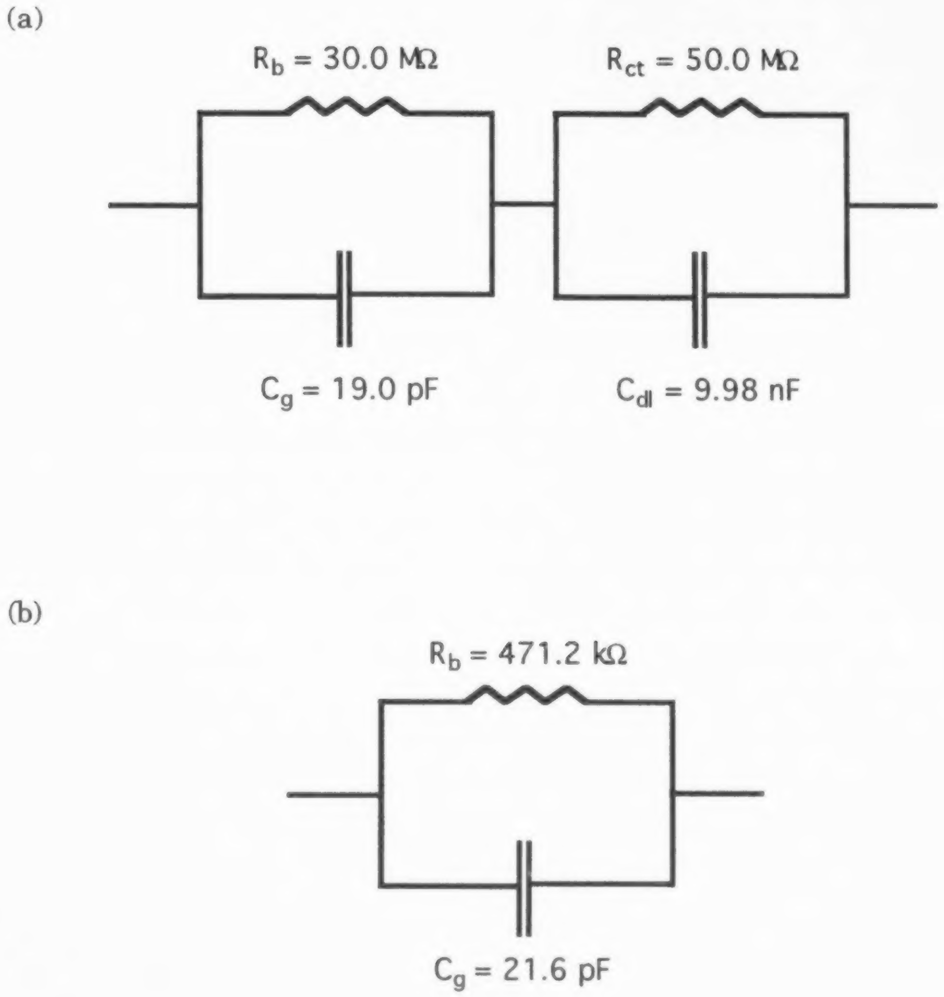
(a)
R_b = 30.0 MΩ
R_{ct} = 50.0 MΩ
C_g = 19.0 pF
C_{dl} = 9.98 nF
(b)
R_b = 471.2 kΩ
C_g = 21.6 pF

Figure 2.6 Dummy cell electronic circuits for (a) blank and (b) ionophore-containing ISE membranes.

various electric elements are given in Table 2.11. More complex circuits can be analyzed by combining individual impedances according to rules analogous to those for resistors. For impedances in series, the overall impedance is the sum of the individual impedances. For impedances in parallel, the reciprocal of the overall impedance is the sum of the reciprocals of individual impedances. As an example, the *ac* impedance equation for the equivalent circuit shown in Figure 2.5 is given by:

$$\vec{Z}_{\text{overall}} = R_s + \left[\frac{1}{R_b} + j\omega C_g\right]^{-1} + \left[\frac{1}{R_{ct}} + j\omega C_{dl}\right]^{-1} \qquad (2.14)$$

This expression is obtained by adding the series impedances for the resistor R_s and each of the RC parallel networks. The impedance of each RC parallel network is calculated as the reciprocal of its admittance given by the sum of the constituent R and C admittances. This general method may be applied to derive the impedance equation for virtually any equivalent circuit no matter how complex and will be extensively exploited in subsequent chapters. An important advantage of this procedure is that the resultant expression may be easily computer-modelled using software with complex number facility, such as ASYST. Thus, theoretically modelled EIS spectra can be generated from equation (2.14) using words contained in the ASYST file RCMODEL.ASY (Program A.15). The colon definition DOUBLE.RC.MODEL is used to generate the model spectrum in Figure 2.7 corresponding to the double parallel RC dummy circuit shown in Figure 2.6a. Similarly, SINGLE.RC.MODEL generates Figure 2.8 for the single parallel RC dummy circuit shown in Figure 2.6b.

2.4.3 Lock-In EIS System Characterization

The technique of phase-sensitive detection using a lock-in amplifier was used to obtain EIS spectra of the dummy circuits shown in Figures 2.6a and 2.6b. These spectra are shown in Figures 2.9 and 2.10, respectively.

A comparison of the EIS spectra in Figures 2.7 (model) and 2.9 (experimental) for the double parallel RC dummy circuit shows that the low

Table 2.11 *AC* impedances and admittances for circuit elements.

Impedance: $\vec{Z} = Z' - j\,Z''$

Admittance: $\vec{Y} = Y' + j\,Y''$

circuit element	**Z'**	**Z"**	**Y'**	**Y"**
resistor	R	0	1/R	0
capacitor	0	1/ωC	0	ωC
inductor	0	-ωL	0	-1/ωL

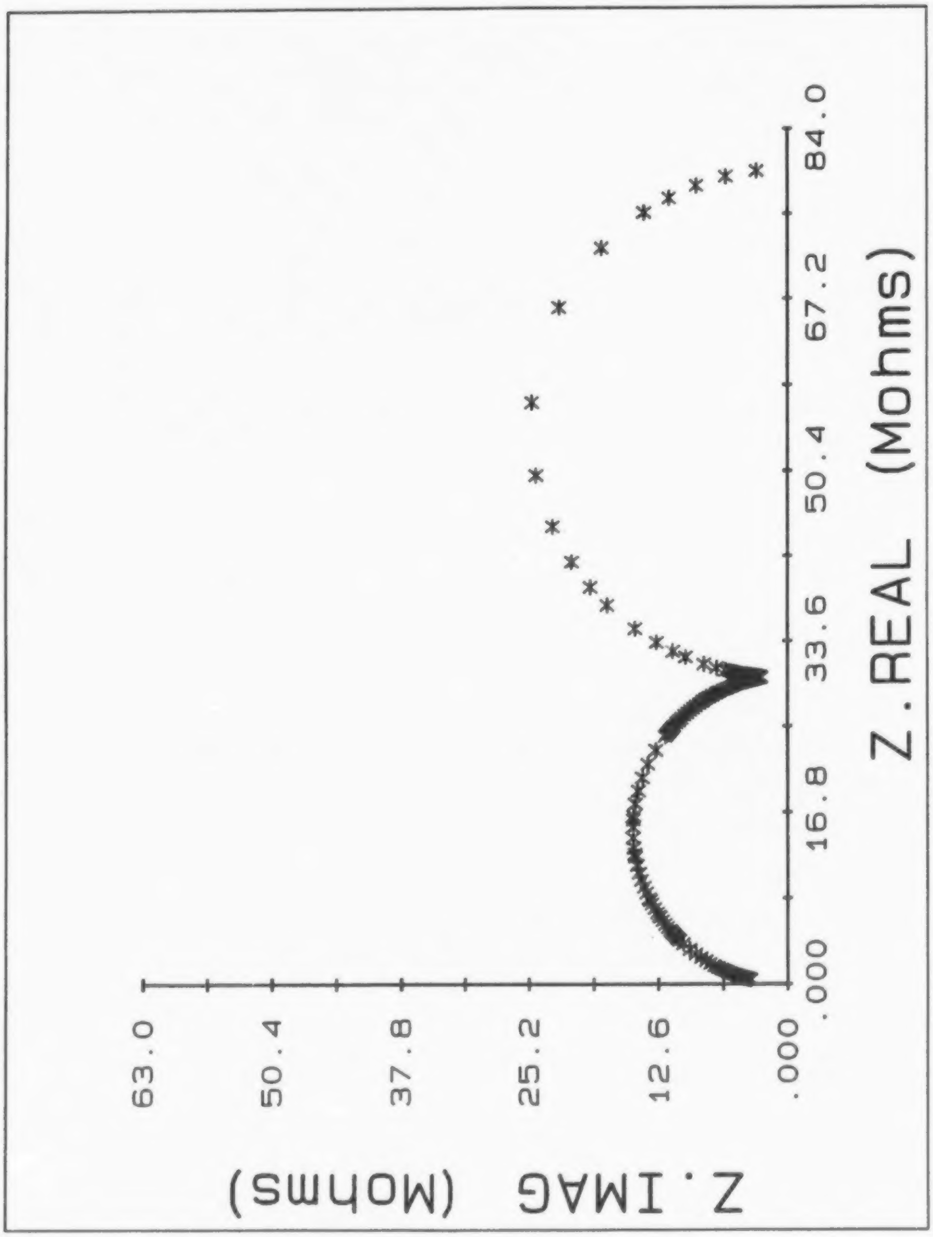

Figure 2.7 Computer-modelled EIS spectrum for double parallel RC circuit. Component values: $R_s = 0$, $R_b = 30.0$ MΩ, $C_g = 19.0$ pF, $R_{ct} = 50.0$ MΩ and $C_{dl} = 9.98$ nF. Frequency range: 19.5 mHz to 684 Hz.

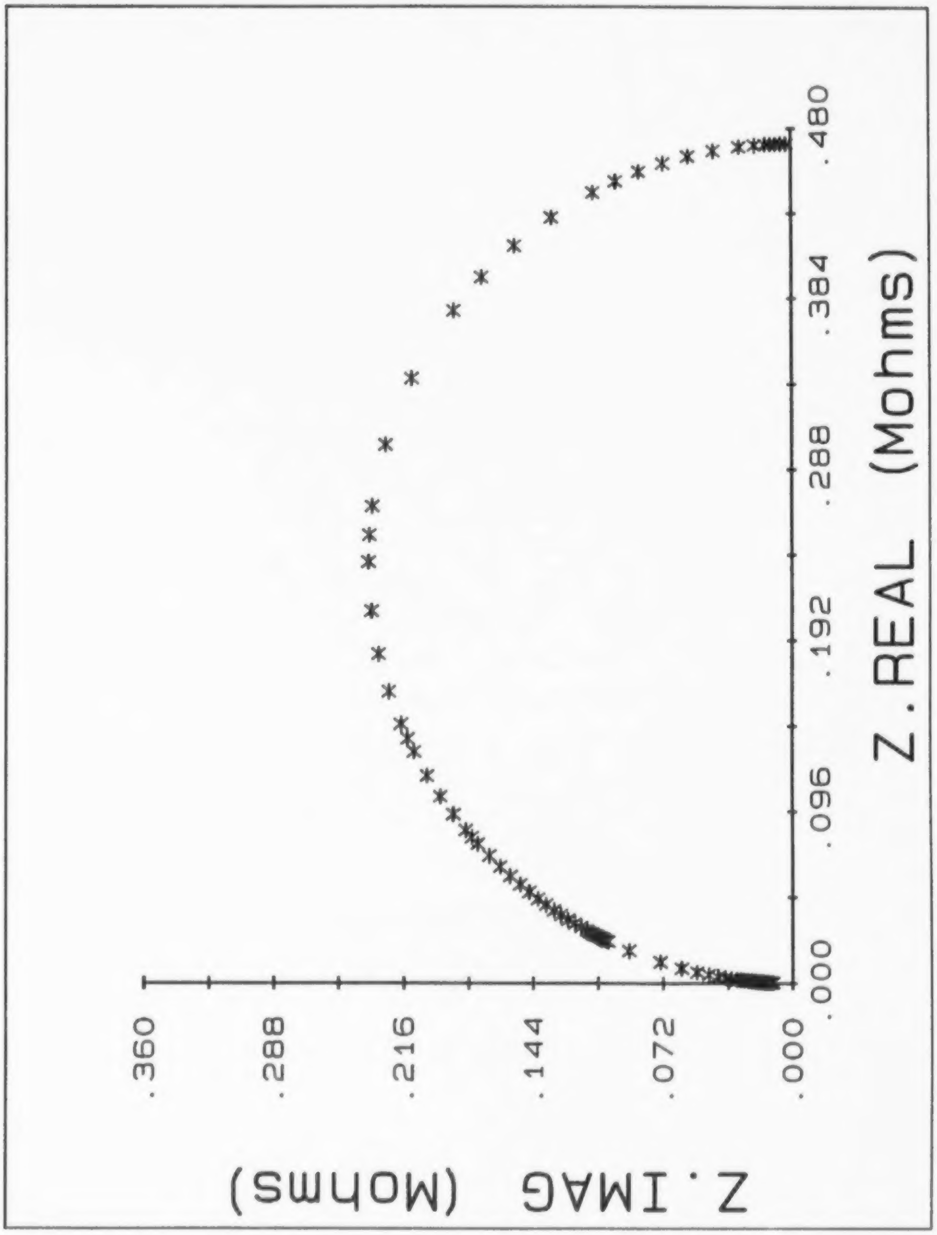

Figure 2.8 Computer-modelled EIS spectrum for single parallel RC circuit. Component values: $R_s = 0$, $R_b = 471.2\ \mathrm{k\Omega}$ and $C_g = 21.6\ \mathrm{pF}$. Frequency range: 100 Hz to 600 kHz.

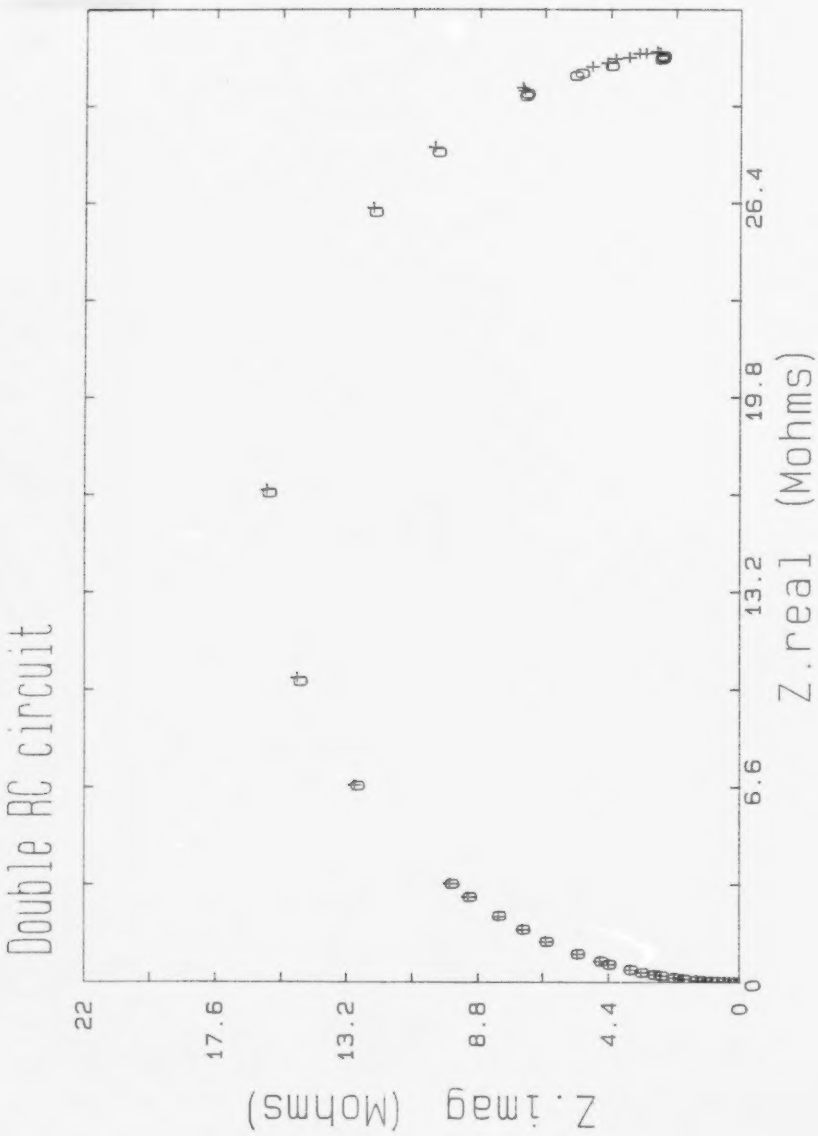

Figure 2.9 Measured lock-in EIS spectrum of a double parallel RC dummy cell circuit. Component values: $R_s = 0$, $R_b = 30.0\ M\Omega$, $C_g = 19.0\ pF$, $R_{ct} = 50.0\ M\Omega$ and $C_{dl} = 9.98\ nF$. Frequency range: 10 Hz to 40 kHz.

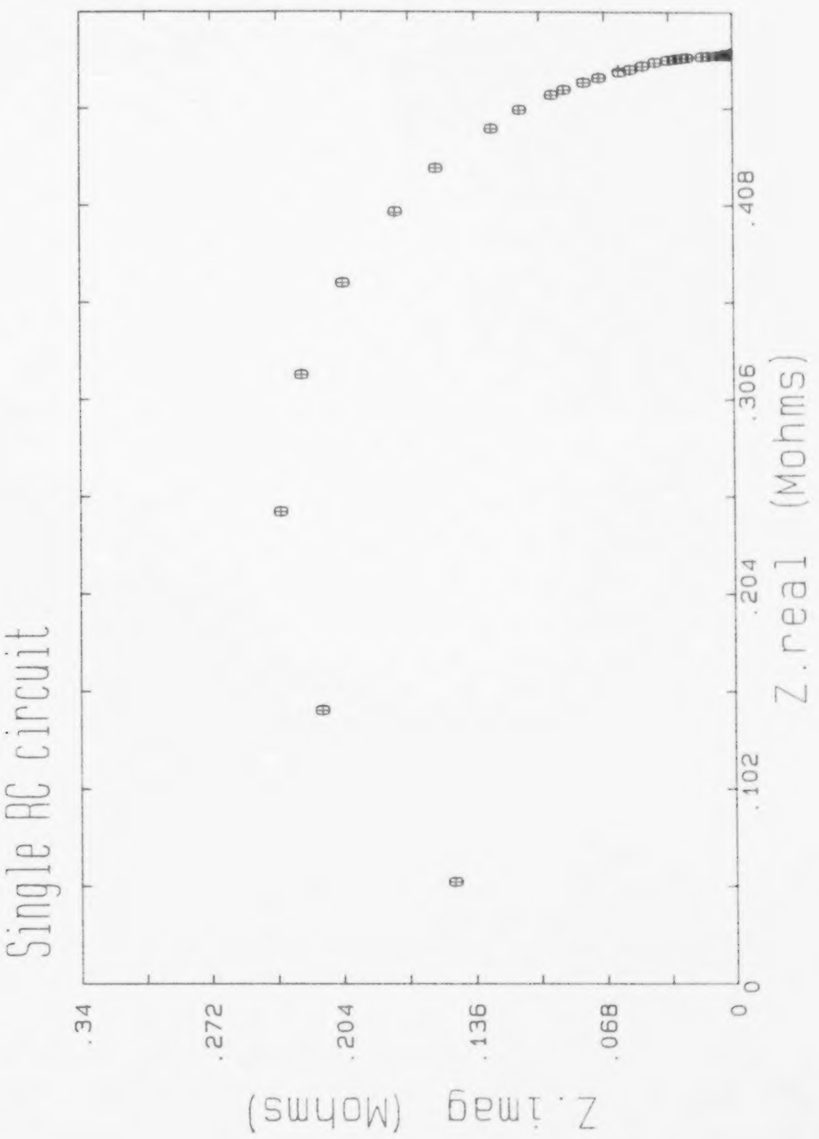

Figure 2.10 Measured lock-in EIS spectrum of a single parallel RC dummy cell circuit. Component values: $R_s = 0$, $R_b = 471.2\ \mathrm{k}\Omega$ and $C_g = 21.6$ pF. Frequency range: 10 Hz to 40 kHz.

frequency "charge transfer" semicircle is not resolved at all. As expected, the lower frequency limits accessible with the lock-in technique are too high to capture a time constant τ of 0.5 sec, where τ is calculated by $\tau = RC$. Some distortion is seen, however, in the lower frequency end of the observed faster semicircle ($\tau = 0.57$ msec) due to the presence of this slow time constant.

Resistance and capacitance values may be extracted from the EIS spectra by appropriate curve fitting to a semicircle (*cf.* Chapter 4). A plot of $1/Z_{real}$ *versus* ω^2 will yield a straight line with a slope of C^2R^2 and intercept of 1/R. Similarly, a plot of ω/Z_{imag} *versus* ω^2 will yield a straight line with a slope of C and intercept of $1/R^2C$. The former plots tend to provide more accurate fits to the observed data. The results of this curve fitting for the impedance data in Figures 2.9 and 2.10 are given in Table 2.12. The precision is better than 4% for both resistance and capacitance determinations. The accuracy for the resistance determination is ≈ 2% and 1% for the high and low impedance circuits, respectively. The large errors associated with the capacitance determination suggests the presence of a significant stray capacitance in the measurement system. This stray capacitance is estimated at ≈ 5.6 pF and 4.0 pF for the low and high current scales, respectively. These values must, therefore, be used to correct for any routine capacitance determination.

2.4.4 FFT-EIS System Characterization

The FFT-EIS measurement system developed was used to obtain EIS spectra of the dummy circuits shown in Figures 2.6a and 2.6b. These results are shown in Figures 2.11 and 2.12, respectively.

A comparison of the EIS spectra in Figures 2.7 (model) and 2.11 (experimental) for the double parallel RC dummy circuit now shows that the slow τ "charge transfer" semicircle is clearly resolved. Unfortunately, there is distortion in the high frequency experimental data as indicated by the non-zero intercept of the Z_{real} impedance at high frequencies, particularly in data from EXPT 1. This distortion is even more pronounced when the data for the single parallel RC dummy circuit are compared,

Table 2.12 Summary of lock-in EIS impedance measurement system characterization.

double RC circuit			single RC circuit		
circuit element	**true value**(a)	**meas'd value**(b)	**circuit element**	**true value**(a)	**meas'd value**(b)
R_b	30.0 MΩ	31.3 MΩ 30.1 MΩ	R_b	471.2 kΩ	475.5 kΩ 475.6 kΩ
C_g	19.0 pF	24.4 pF 24.8 pF	C_g	21.6 pF	25.6 pF 25.6 pF
R_{ct}	50.0 MΩ	(c)			
C_{dl}	9.98 nF	(c)			

(a) True resistances measured with an HP 3478A Multimeter.
True capacitances measured with an ECD capacitance meter.
(b) Measured values are given for two consecutive impedance experiments.
(c) Circuit elements not resolved.

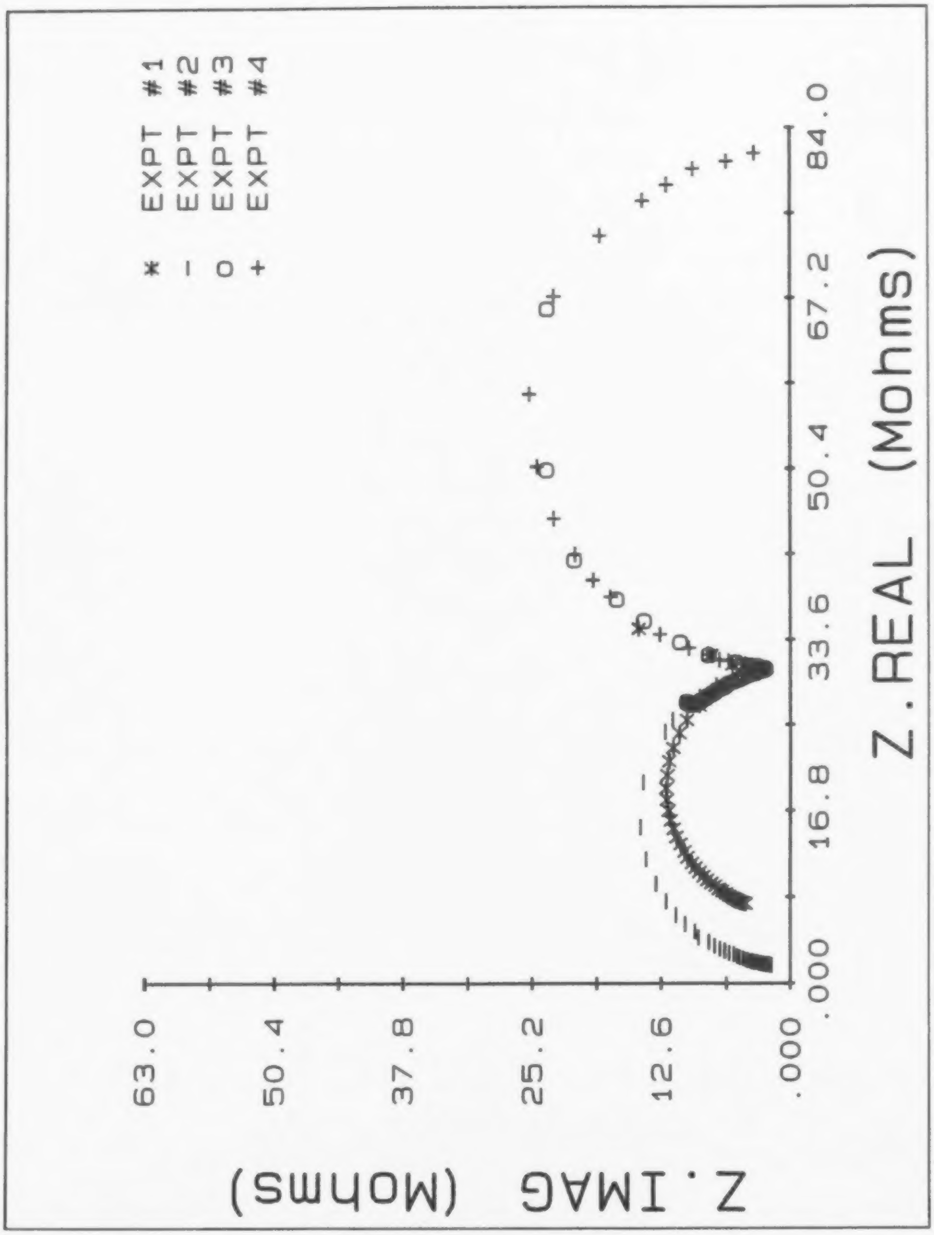

Figure 2.11 Measured FFT-EIS spectrum of a double parallel RC dummy cell circuit. Component values: $R_s = 0$, $R_b = 30.0$ MΩ, $C_g = 19.0$ pF, $R_{ct} = 50.0$ MΩ and $C_{dl} = 9.98$ nF. Frequency range: 19.5 mHz to 684 Hz.

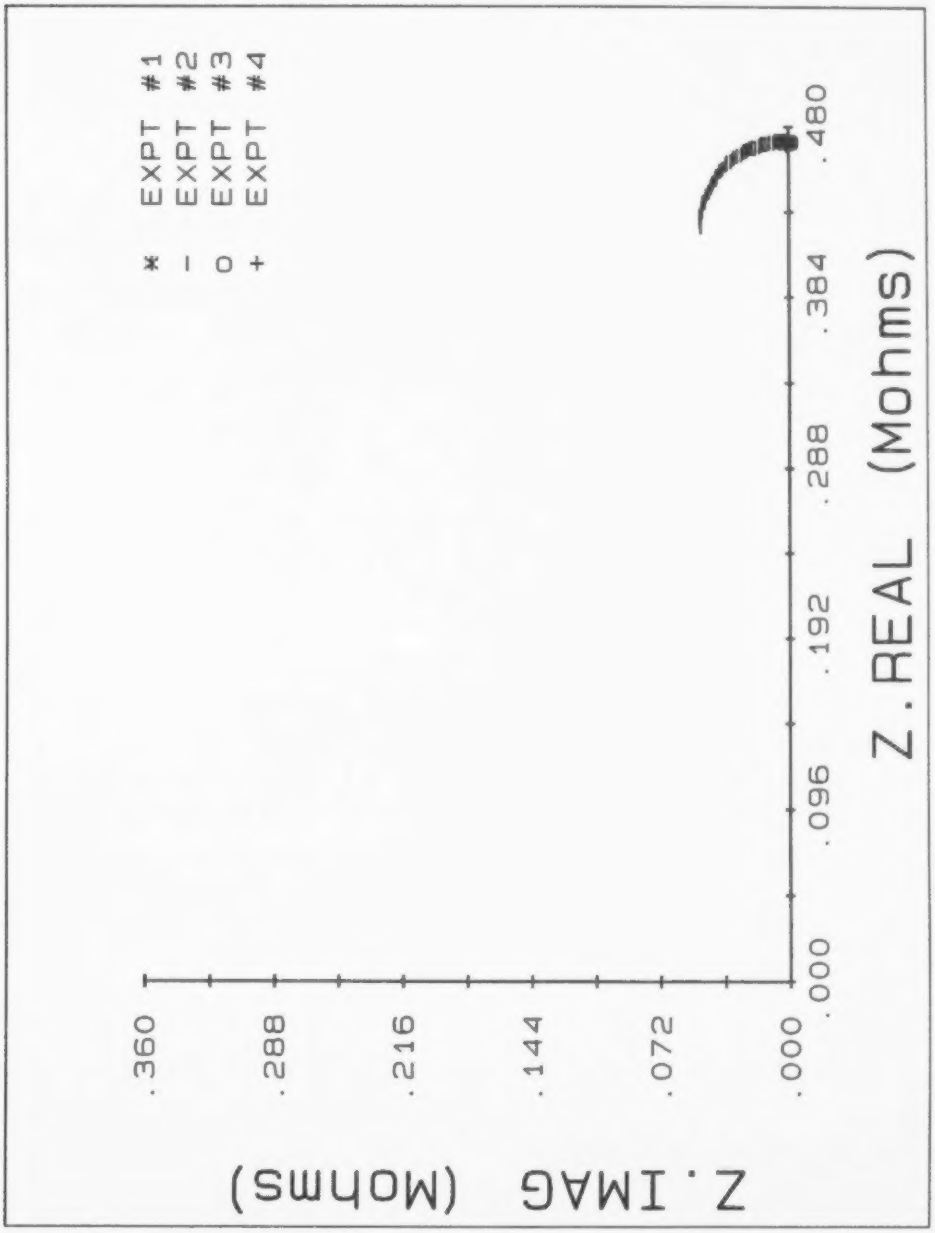

Figure 2.12 Measured FFT-EIS spectrum of a single parallel RC dummy cell circuit. Component values: $R_s = 0$, $R_b = 471.2$ kΩ and $C_g = 21.6$ pF. Frequency range: 19.5 mHz to 684 Hz.

Figures 2.8 (model) and 2.12 (experimental). This distortion most likely results from the rapid modulation rates of the FFT waveforms required in this high frequency regime, relative to the frequency response of the PAR-273 Potentiostat.

As a result of high frequency instrumental distortion of the impedance data, numerical curve fitting of the data (*vide supra*) tends not to be very satisfactory. Instead, all the data can be fitted by hand, and in this manner the Z_{real} high frequency intercept can be made to pass through zero. This curve fitting procedure proved to be quite reliable for resistance values and the extracted data are given in Table 2.13. The precision in the resistance determinations are routinely better than 1% and the accuracy is ≈ 2% and 0.05% for the high and low impedance circuits, respectively. For the low frequency ($\tau = 0.5$ sec) semicircle, the accuracy and precision for the capacitance determination is better than 0.5%. For the faster τ semicircles of 0.57 msec and 10.2 μsec, this accuracy deteriorates to 5% and 600%, respectively. This is not surprising, given the considerable distortion in the high frequency impedance data with the FFT system.

2.5 Conclusions

A system for electrochemical impedance spectroscopy has been implemented using the fast Fourier transform technique. This has been demonstrated to be precise and accurate for the determination of phenomena with slow time constants, such as membrane charge transfer. For faster time constants, such as membrane bulk transport, the data is distorted due to high frequency distortion in the associated waveforms. Although resistance determinations are still very good, capacitance determinations can be very poor.

It has also been demonstrated that the conventional phase-sensitive technique based on a lock-in amplifier perfectly complements the FFT method. The lock-in technique is essentially only capable of providing accurate and precise data from fast time constants since its restricted low frequency range does not permit slow time constants to be measured.

Table 2.13 Summary of FFT-EIS impedance measurement system characterization.

double RC circuit			single RC circuit		
circuit element	**true value**[(a)]	**meas'd value**[(b)]	**circuit element**	**true value**[(a)]	**meas'd value**[(b)]
R_b	30.0 MΩ	30.4 MΩ 30.7 MΩ	R_b	471.2 kΩ	471.6 kΩ 471.3 kΩ
C_g	19.0 pF	20.1 pF 19.9 pF	C_g	21.6 pF	154.7 pF 152.6 pF
R_{ct}	50.0 MΩ	50.6 MΩ 50.6 MΩ			
C_{dl}	9.98 nF	9.95 nF 9.95 nF			

(a) True resistances measured with an HP 3478A Multimeter.
True capacitances measured with an ECD capacitance meter.

(b) Measured values are given for two consecutive impedance experiments.

2.6 References

1. Bard, A.J.; Faulkner, L.R. *Electrochemical Methods*, John Wiley & Sons: New York, 1980.

2. Sluyters-Rehbach, M.; Sluyters, J.H. *Electroanal. Chem.* **1970**, *4*, 1.

3. Verpoorte, E.M.J. "Analysis of the Permeability and Behaviour of Dissociable Species in Ion-Selective Membranes," Ph.D. Thesis, University of Alberta, Edmonton, 1990.

4. Malmstadt, H.V.; Enke, C.G.; Crouch, S.R. *Electronics and Instrumentation for Scientists*, Benjamin/Cummings Publishing: Don Mills, Ontario, 1981.

5. Ramirez, R.W. *The FFT: Fundamentals and Concepts*, Prentice-Hall: Englewood Cliffs, N.J., 1985.

6. Cooley, P.M.; Tukey, J.W. *Math Comput.* **1965**, *19*, 297.

7. Creason, S.C.; Smith, D.E. *J. Electroanal. Chem.* **1972**, *36*, App. 1 .

8. Creason, S.C.; Hayes, J.W.; Smith, D.E. *J. Electroanal. Chem.* **1973**, *47*, 9.

9. Armstrong, R.D.; Covington, A.K.; Evans, G.P. *J. Electroanal. Chem.* **1983**, *159*, 33.

Chapter 3

AC Impedance Analysis of Neutral Species Behavior in Ion-Selective Electrode Membranes

3.1 Introduction

Ion-selective liquid membrane electrodes (ISEs) based on neutral carriers currently find wide use in analytical chemistry for the determination of a range of ions such as K^+, Na^+, Ca^{+2} and NH_4^+. These membranes typically consist of a polymer matrix such as poly(vinyl chloride) (PVC), a plasticizing, water-immiscible, organic solvent such as bis(2-ethylhexyl) adipate (DOA) and an ion carrier to induce selectivity [1-2]. It has been shown that conductivity in these membranes is due to ionic charge carriers rather than to electrons [3]. The potential response of these ISE membranes can, therefore, be adversely affected by a number of interfering species which can permeate the membrane.

The impetus for the work presented in this chapter originated from studies in our group directed towards understanding interferences in the ion sensitive field effect transistor (ISFET) incorporating these types of membranes. Fogt *et al* [4] have shown that ISFETs coated with a plasticized PVC K^+-selective membrane are subjected to what Janata [5] has termed a Severinghaus effect. Neutral forms of an acid or base such as CO_2, ascorbic acid and others can permeate the membrane coating and undergo acid-base reactions at the oxide or nitride surface of the semiconductor device. This change in charge at the surface leads to significant potential shifts at K^+-membrane coated ISFETs that an ISE prepared from the same membrane material would not produce.

Verpoorte has used *AC* impedance analysis of bulk membrane resistance to study anion interferences and the extraction of benzoic acid

(HBz), benzoate (Bz^-) and perchlorate (ClO_4^-) from aqueous sample solutions into plasticized PVC based K^+-selective membranes incorporating valinomycin [6]. These results have been used to evaluate the mechanism of this so-called Severinghaus effect. Results have shown that both the neutral species HBz and its conjugate base Bz^- permeate the membrane [7]. This result was surprising given that only the neutral acid form causes interferences at a membrane coated ISFET and that there is no response of the classical K^+ ISE to either form of benzoate. Further studies demonstrated that this was due to a more than 10,000 fold difference in concentration between these two species in the membrane [8].

The work presented in this chapter is directed towards understanding, in more detail, the role of neutral species within these ISE membrane systems. This is important since it has been shown that K^+ electrodes exposed to blood for long periods extract components into the membrane [9]. This leads to an increase in conductivity which has been correlated with a degradation in electrode performance. It was suggested that these extracted components are relatively immobile lipophilic species, both neutral and charged. In general, ISE membranes based on PVC exhibit poor performance in biological media [1,9-12]. The successful employment of liquid membrane ISEs in the analysis of physiological fluids, therefore, depends on understanding and reducing the interferences caused by the neutral species present.

Impedance studies of K^+-selective PVC membranes have been shown to be valuable in probing membrane characteristics [13-19,7-9]. This method has been proven to be a direct and sensitive method for evaluating permeation of the membranes by neutral species [7]. With this technique, it is possible to study membrane permeation at levels much lower than those required to affect electrode potentiometric response. In order to satisfactorily interpret membrane impedance changes due to permeating species from real samples, however, we require an increased base of information correlating impedance changes with deliberate, known changes in membrane composition. Towards this end, the effects on membrane bulk resistances have been discussed [7-8]. That work is extended here to include charge transfer resistance measurements in order to provide additional insight into the charge-generation phenomenon in these membranes by neutral species. Along with bulk resistance measurements, this information should discriminate between charge entering the membrane *versus* charge being generated within the membrane.

The systems examined were membrane matrices containing benzoic acid (HBz) and methyl benzoate (MeBz). The former additive may dissociate to give charged species whereas the latter additive must always remain as the neutral species. While HBz and MeBz are not common interferents, they are close homologues of the common drug metabolite salicylate. By clarifying the role of these species, we can further our understanding of the role neutral species play in determining membrane characteristics.

The ubiquitous question of reproducibility in *AC* impedance measurements of these membranes will also be addressed. A systematic study of experimental variables affecting the precision of the data is presented. As well, the effect of membrane inhomogeneity and purity of membrane matrix components on the quality of the data is investigated.

3.2 Experimental

Chemicals. Bis(2-ethylhexyl) adipate (DOA) (Fluka) was either used as received (Selectophore grade) or purified (Pract grade) under vacuum using a long path heated column packed with glass coils (b.p. 200 °C @ 0.15 Torr). Poly(vinyl chloride) (PVC) was in the form of a powder (Polysciences, chromatographic grade). Purified PVC was prepared by Alem Teclemariam by dissolution in tetrahydrofuran (THF) (BDH, distilled from potassium) followed by precipitation in methanol (BDH). Benzoic acid (Terochem) was purified by double recrystallization from cold water followed by sublimation under vacuum. Methyl benzoate (Fisher) was purified by distillation under aspirator vacuum. Solutions of these additives were prepared in distilled THF. All other chemicals were reagent grade and used as received. Water was distilled, de-ionized and re-distilled from alkaline $KMnO_4$.

Membrane preparation. Free standing membranes were fabricated by the method suggested by Craggs et al [20]. First, 800 mg of DOA were weighed into a 20 mL beaker. This was dissolved in about 8 mL of freshly distilled THF. Next, 400 mg of PVC powder were sprinkled into this solution with stirring so as to prevent coagulation of the polymer. After stirring for a few hours to effect complete dissolution, this casting solution was evenly distributed between four pre-weighed 5 mL beakers and appropriate aliquots of the additive solution were added. After stirring for another half hour, the membrane solutions were poured into Teflon rings (4 cm inner diameter, 1.5 cm deep) clamped onto a smooth Teflon surface. In order to maintain a uniform THF atmosphere during casting, pads of filter paper were placed over the rings and weighted down with glass Petri dish covers. Membranes were allowed to cure at room temperature for at least 48 hrs and then weighed to the nearest 0.1 mg. In order to account for additive-containing membrane solution inevitably left behind in the 5 mL beakers, these beakers were re-weighed 48 hrs after casting. The difference in weight was added to the mass of the cast membrane. Accurate concentrations of additive in the membrane could, therefore, be evaluated since the mass of additive added and the total mass of membrane to which the additive was added were both accurately known. Master membranes were stored on glass plates in plastic boxes at room temperature. Accurate membrane thicknesses were determined, after impedance measurements, by placing the membrane sample between square metal plates ($\approx 2\ cm^2$ area and ≈ 0.25 mm thick) and measuring this "sandwich" using a micrometer (Mitutoyo Series 193). The pressure exerted by the jaws was made reproducible by using the ratchet-slip mechanism on the micrometer. The contributions of the two metal plates were subtracted from the overall measured thickness to yield the membrane thickness to the nearest 0.002 mm.

Impedance cells. Sections of membrane to be studied were mounted between two electrolyte compartments in specially designed PTFE cells [6,8]. A diagram of one of these cells is given in Figure 3.1. The cell consists of two sections of equal length, each with a cylindrical bore 0.6 cm in diameter. Three long threaded rods are embedded at equal intervals around the perimeter of the inner face of one section. The other section has holes drilled lengthwise to allow the rods to pass through it from one end to the other. The membrane is sealed between the inner section faces by tightening small nuts on the threaded ends of each rod, after rubber and brass washers with appropriate holes are fitted between the end of the Teflon section and the nuts. Care must be taken so that torque is not applied to the membrane in tightening the cell, and the rubber washer aids in this. To ensure a proper seal and a consistent wetted surface area for the membrane, shallow, concentric grooves are machined into the inner surface of one section. Two tapered Teflon plugs serve to seal the outer ends of the central bore. Chloridized Ag wires, wound at one end into corkscrew shapes, are forced through holes in each plug and act as the electrodes in this two-electrode system. Smaller diameter holes in the top of each section allow for solution overflow. In this cell, the effective membrane surface area exposed to the bathing solution is ≈ 0.3 cm^2 (see Table 3.1), and the volume of each half cell is ≈ 1.5 mL.

The cell was thermostatted by fitting it into a brass water jacket, also shown in Figure 3.1. Water at the desired temperature was then circulated through the walls of this jacket using a circulating water bath (Ultra-Thermostat, Colora). The actual cell temperature was monitored with a thermocouple (Digi-Sense, Cole Parmer) positioned near the membrane in a shaft drilled into the Teflon cell wall along its length.

Impedance measurements. Circular sections of membrane were cut from the master membrane with a metal punch ($\approx$ 10 mm diameter) and mounted in the impedance cell. Identical electrolyte bathing solutions were then introduced into the two cell compartments and allowed to equilibrate for at least one hour before measurements at 25 ± 0.2 °C. High frequency impedance measurements were made by phase-sensitive detection. A

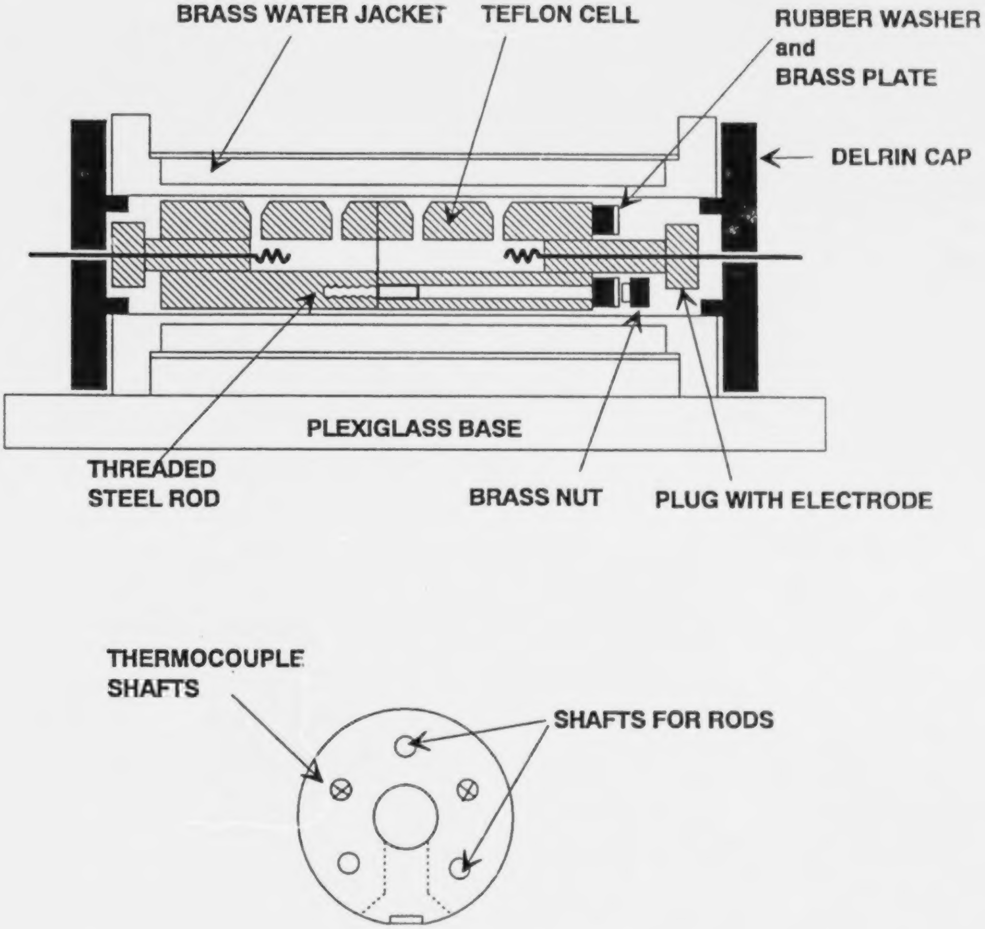
BRASS WATER JACKET
TEFLON CELL
RUBBER WASHER
and
BRASS PLATE
DELRIN CAP
PLEXIGLASS BASE
THREADED
STEEL ROD
BRASS NUT
PLUG WITH ELECTRODE
THERMOCOUPLE
SHAFTS
SHAFTS FOR RODS

Figure 3.1 Side and end views of the Teflon cell and brass water jacket used for membrane impedance measurements.

Table 3.1 Effective membrane surface area exposed to bathing solution for various impedance cells.

cell reference number	diameter of central bore (cm)$^{(a)}$	exposed membrane area (cm^2)
#1	0.660	0.3421
#2	0.658	0.3400
#3$^{(b)}$	0.622	0.3038
#4$^{(b)}$	0.618	0.3000
#5	0.633	0.3147
#6	0.638	0.3197

(a) Measured with vernier calipers.

(b) These older style cells were not used in the present study.

50 mV peak-to-peak pure sine wave was used as the applied voltage oscillation at each frequency measured. The instrument configuration and procedure employed has been previously described [7]. Low frequency impedance measurements were made by the fast Fourier transform (FFT) method as described in Chapter 2. The amplitude of the FFT waveform was ± 180 mV and consisted of 50 distinct frequencies. All electrochemical measurements were done with the impedance cells in Faraday cages.

3.3 Results and Discussion

3.3.1 Reproducibility of *AC* Impedance Membrane Data

The reproducibility of *AC* impedance measurements on ISE membrane samples is a major problem. This has been cited in several previous studies employing this method of analysis [6,8,13-14,21] and the present study is no exception. Poor reproducibility exacerbates data interpretation and directly limits the precision of the method. In this section, the problem of reproducibility of *AC* impedance membrane data will be addressed.

There are essentially two aspects of the *AC* impedance experiment on ISE membranes which lead to poor reproducibility in the data. The first can be generally categorized as measurement specific and includes all experimental variables which directly influence the actual measurement step. Although these may be subtle, they can be readily brought under control, once recognized and evaluated. The second aspect is much more problematic and can be categorized as sample specific. Membrane sample preparations may not be reproducible or variations in membrane composition may even be intrinsic to their nature through inhomogeneity. These factors can be much more difficult to control and can far outweigh the measurement specific variables.

3.3.1.1 Measurement Specific Variables

The actual measurement of a membrane impedance involves cutting a circular sample from the master membrane casting, mounting this onto one half of the impedance cell, attaching the other half of the cell, filling both compartments of each half cell with a bathing solution then finally obtaining an impedance spectrum. Each of these procedures, along with other considerations, are all prone to reproducibility problems.

The most fundamental process in an impedance experiment involves the actual impedance measurement itself with the FFT-EIS system developed (*cf.* Chapter 2). Its precision is dependent on a number of factors, including the precision of the potentiostat, the digitization errors arising from utilizing a digital waveform and the curve-fitting process used to extract bulk and charge transfer resistance values. Measurements of the impedance of dummy cells fabricated from electronic circuit components have demonstrated that the precision for all of these measurement steps is better than 1 % for both the bulk and charge transfer resistances. No effort was made to improve the impedance measurement procedures since it was anticipated that these steps would likely not limit the overall precision of membrane measurements. Additional improvements could have included, for example, increased shielding from electrical noise, digitization of the waveform with 4096 points instead of 2048 points and increased signal averaging.

The next variable to be considered is the impedance cell configuration used to make an impedance measurement on an actual membrane sample. For these studies, two impedance cell designs were available. They were very similar except for one notable difference. In the "older" style cells, the two halves of the cell were attached via threaded bolts that directly contacted the Teflon surface of the cell. Uneven tightening of the bolts can, therefore, induce a significant torque to the membrane sample since the force would be directly transmitted to the pliable membrane sample sandwiched between the two cell halves. This can often be visible just by looking through the bathing solution compartment of the cell after mounting a membrane sample. If excessive force is applied to one of the bolts, a buckling of the membrane surface can be observed. The "newer" style cells, however, incorporate a rubber spacer between the retaining nut and the Teflon surface of the cell. It can be expected that any uneven torque applied to the bolts would be dissipated through this spacer instead of simply transmitted directly to the membrane. This was indeed the case, although the membrane could still be made to buckle if enough force was applied to one of the bolts.

The results of a torque study on both types of cell designs is shown in Figures 3.2 and 3.3. Changes in the membrane bulk resistance (% ΔR_b) and in the membrane charge transfer resistance (% ΔR_{ct}) are shown relative to an average of two initial control measurements with all screws tightened to normal finger-tight torque without any visible buckling. A negative change in these values indicates a decrease in the measured resistance relative to the control. Note also that the older cell design has four screws while the newer design has only three. From the data, it can be seen that changes in the torque causes a 5 - 8 % variation in the observed membrane bulk resistances for either cell. This is not considered to be significant and most of this variation likely reflects changes in the bulk resistance with time (*vide infra*) since each individual torque experiment required about twenty minutes to complete. More significantly, however, is the observation that membrane torque results in up to a 22 % variation in the charge transfer resistance with the older cell design, but that this is reduced to only a 3 % variation with the newer cell design. Consequently, the newer cell designs incorporating the rubber spacer were used exclusively throughout this work. It is evident, therefore, that simply correcting for variations in membrane torque potentially improves the precision in the measurement by about 20%.

The above experiments do not evaluate either the uniformity of bathing solution filling or the membrane mounting procedure. Both of these factors are very important since bulk and charge transfer resistances are inversely proportional to the membrane surface area exposed to the bathing solution.

The actual membrane area exposed to the bathing solution is constrained by the physical geometry of the cell orifice. This is fixed and

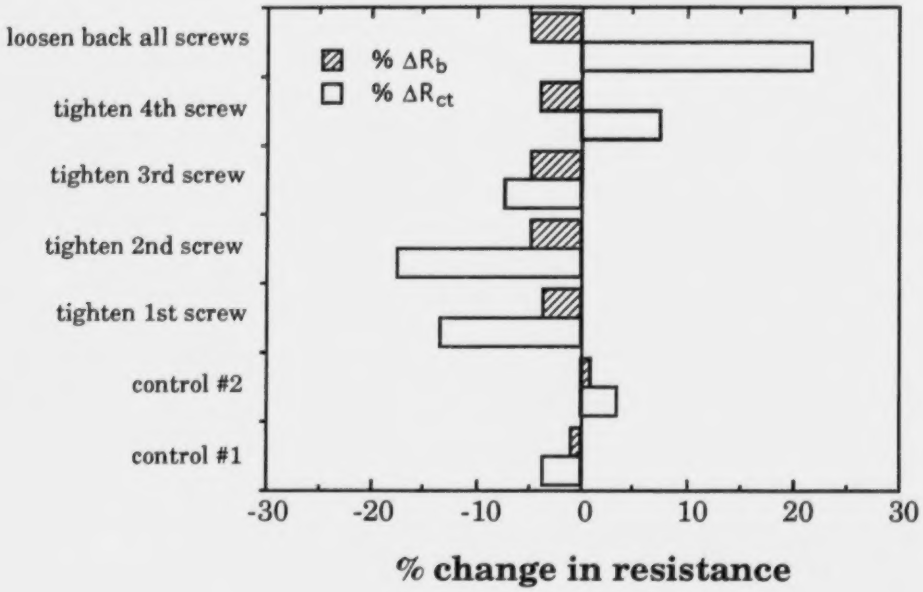

Figure 3.2 Membrane torque study on older cell design (membrane: 0.05 % valinomycin, 0.05 % $NaBPh_4$ in 66 % DOS/PVC; bathing solution: 10 mM NaCl).

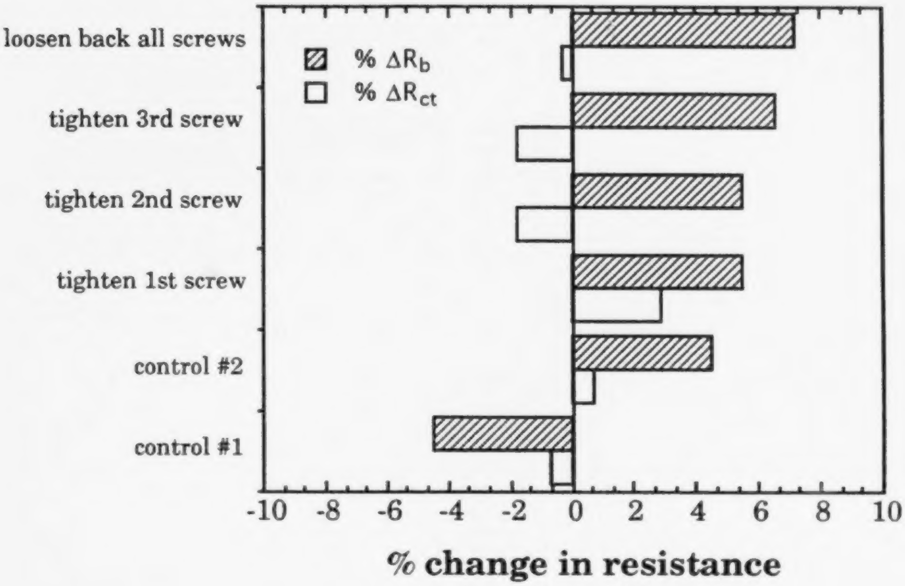

Figure 3.3 Membrane torque study on newer cell design (membrane: 0.2003 % benzoic acid in 66 % DOA/PVC; bathing solution: 10 mM KCl).

the membrane sections which are mounted are always greater than the size of this orifice. Nevertheless, buckling or stretching of the membrane can occur as the two halves of the impedance cell are brought together. This can lead to a change in the effective exposed membrane surface area. The bathing solution itself is introduced into the cell via a hypodermic syringe. The presence of air bubbles at the membrane/solution interface can also often pose a problem. A very large bubble is readily apparent from an unreasonably high measured impedance in the gigaohm range. The presence of smaller air bubbles, however, may not be as obvious. The preferred method for filling the cell was to keep the beveled edge of the needle in contact with the cell wall such that bathing solution uniformly wetted the cell interior as it flowed through the cell compartment.

The easiest way to test for variabilities in membrane sample mounting and cell filling is to disassemble the cell between two replicate experiments. In this manner, all the procedures involving the measurement setup (*ie.* mounting, torque and filling) are simultaneously evaluated along with the precision of the FFT-EIS measurement system itself. This was found to be 5 % and this now represents the overall membrane measurement procedure reproducibility.

The next consideration is the ambient laboratory environment which is not constant, especially over a calendar year. For the most part, environmental effects, such as vibrations, humidity and luminosity, are not expected to be very important. The only exception is likely to be temperature. The ambient laboratory temperature varies considerably depending on the season (most significantly between summer and winter). In order to evaluate this effect, the impedance cell containing a membrane sample was thermostatted over a range of temperatures and impedance data were acquired at each different temperature. Results are shown in Figure 3.4. This demonstrates that the measurement temperature significantly influences both the bulk and charge transfer resistances measured. Under reasonably humane variations in the laboratory temperature (20 - 30 °C), however, it can be seen that the bulk and charge transfer resistances vary by only approximately 7 % and 3 %, respectively. Nevertheless, this is sufficiently large enough to warrant adequate

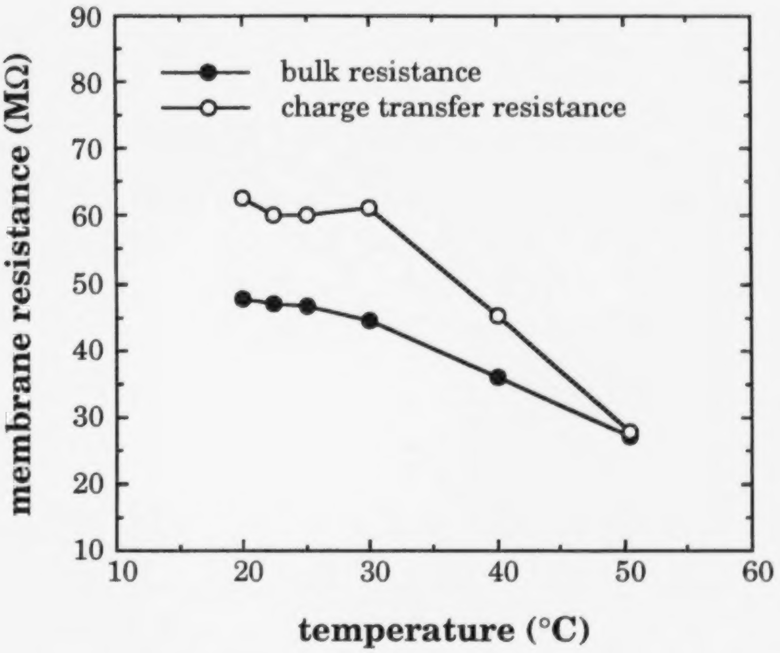

Figure 3.4 Effect of temperature for a typical impedance measurement (membrane: 0.2011 % benzoic acid in 66 % DOA/PVC; bathing solution: 10 mM KCl).

temperature control. The impedance cell was, therefore, thermostatted to 25.0 ± 0.2 °C for all measurements.

The tendency of membrane resistances to drift over time while soaked in a bathing solution has previously been reported [13-14,22-23]. This was confirmed by a study of the time course of resistance changes as summarized in Table 3.2. The plot of this data in Figure 3.5 demonstrates that membrane resistances significantly increase with soaking time. This drift presents an obvious problem for the acquisition of reproducible membrane impedances. Since the present study is not aimed towards evaluating aging processes within these membranes, a relatively short and practical duration of soaking was selected for all the experiments. From the data in Table 3.2, it can be seen that between 1 and 1.5 hrs, the bulk and charge transfer resistances change by only about 6 % and 2 %, respectively. All impedance measurements were, therefore, carried out within 1 to 1.5 hr of soaking in the appropriate bathing solution. Incidentally, this is made possible only by exploiting the multiplex advantage of the FFT implementation of *AC* impedance as described in Chapter 2. It would not be otherwise possible to attain impedance spectra rapidly enough and with sufficient resolution in this half hour time constraint using a step-wise, single frequency technique such as a lock-in analyzer method. The FFT technique, however, is ideally suited for rapidly acquiring impedance data over the entire frequency range applicable for bulk and charge transfer resistance measurements.

3.3.1.2 Sample Specific Variables

Sample specific variability is a rather broad classification which encompasses a number of different connotations. Factors which contribute to this variability may be enumerated as follows: (1) variability within a given master membrane casting, (2) variability between different master membranes cast together on the same day, and (3) variability between different master membranes cast separately on different days. The first factor directly limits the quality of impedance data from any particular

Table 3.2 Effect of soaking time for a typical impedance measurement (membrane: 0.05300 % benzoic acid in 66 % DOA/PVC; bathing solution: 10 mM KCl).

soaking time (min.)	bulk resistance (MΩ)	charge transfer resistance (MΩ)
10	36.0	63.9
26	46.5	70.5
43	51.0	70.5
65	54.2	75.2
90	57.4	74.1
120	60.9	77.4
180	64.0	77.7
240	63.6	84.8
300	64.0	85.6
360	66.4	88.8
480	70.8	89.6
750	75.2	92.7
1440	80.6	93.2

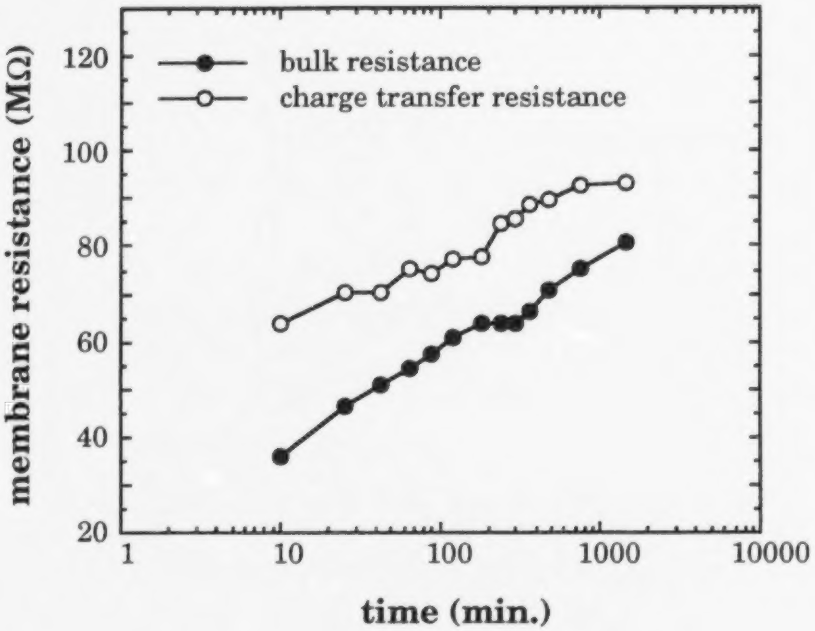

Figure 3.5 Effect of soaking time for a typical impedance measurement (membrane: 0.05300 % benzoic acid in 66 % DOA/PVC; bathing solution: 10 mM KCl).

membrane sample and ideally should be the least significant of the three factors. The second consideration is important with respect to any meaningful comparisons made between membranes of different composition. It is imperative for this to be kept as low as possible otherwise any trends in the measured impedance data could be attributed to simply indeterminate errors in the sample preparation. Finally, if results from membranes cast on different days are to be compared, factor (3) must also be either insignificant or at least controllable in the case of determinate errors. This is desirable from a practical standpoint since an impedance study may often require a large number of different samples that are most easily prepared as needed over time.

The factors which determine reproducibility between different membrane samples were evaluated by casting a series of different "identical" membranes and acquiring their impedance data. For this study, blank membranes containing only the membrane matrix components (DOA plasticizer and PVC polymer) were used without any other deliberately incorporated additive. All other experimental variables, such as source and purity of reagents, were controlled as best as possible. Blank membranes were selected since they would presumably be the most susceptible to problems with reproducibility.

Two blank master membranes #1 and #2 were first cast together on the same day. Impedance data was then acquired from four individual membrane samples (1 - 4) cut separately from each master membrane. Results from measurements of thickness (d), bulk resistance (R_b) and charge transfer resistance (R_{ct}) for all samples are presented in Tables 3.3 and 3.4 for master membranes #1 and #2, respectively. This data will permit factors (1) and (2) to be evaluated with respect to statistical criteria.

It is immediately apparent that sample thickness (d) varies considerably both within a given master membrane and between two different master membranes. As a result of the nature of the membrane casting procedure, the cured membrane thickness will always be greater towards the outer edges of the master membrane. Samples for impedance analysis were, therefore, always cut from the centers of the master membranes where the variability in thickness should be lowest.

Table 3.3 Impedance data for blank master membrane #1 cast together on the same day as blank master membrane #2 (bathing solution: 10 mM KCl).

	sample (1)	sample (2)	sample (3)	sample (4)
d (mm)	0.121	0.133	0.118	0.140
R_b (MΩ)	145.6	62.4	53.4	54.4
R_{ct} (MΩ)	399	161.4	159.6	152.4
A (cm^2)	0.3147	0.3147	0.3197	0.3197
ρ_b (MΩ•cm)	3787(a)	1476	1447	1242
ρ_{ct} (MΩ•cm^2)	125.6(a)	50.8	51.0	48.7
Average ρ_b = 1388 ± 128 MΩ • cm Average ρ_{ct} = 50 ± 1 MΩ • cm^2				

(a) Data rejected based on *Q*-test at 96 % confidence level.

Table 3.4 Impedance data for blank master membrane #2 cast together on the same day as blank master membrane #1 (bathing solution: 10 mM KCl).

	sample (1)	sample (2)	sample (3)	sample (4)
d (mm)	0.137	0.135	0.146	0.137
R_b (MΩ)	95.2	78.0	64.4	55.8
R_{ct} (MΩ)	214.4	154.2	191.8	171.0
A (cm^2)	0.3147	0.3197	0.3197	0.3197
ρ_b (MΩ•cm)	2187	1847	1410	1302
ρ_{ct} (MΩ•cm^2)	67.5	49.3	61.3	54.7

Average $\rho_b = 1686 \pm 408$ MΩ • cm
Average $\rho_{ct} = 58 \pm 8$ MΩ • cm^2

Nevertheless, it is apparent that the thickness between samples from any master membrane still differs by ≈ 8 %.

Since the measured bulk resistances are directly proportional to sample thickness, bulk data were normalized to unit thickness. The corresponding charge transfer resistance is, theoretically, independent of membrane thicknesses when this thickness is much greater than monolayer dimensions. Since the effective membrane areas (A) exposed to solution vary according to the physical geometry of the particular impedance cell used for the measurement (Table 3.1), the impedance data can also be normalized for unit membrane surface area. Resistivities can, therefore, be calculated as follows:

$$\rho_b = \frac{R_b A}{d} \tag{3.1}$$

$$\rho_{ct}' = \frac{R_{ct} A}{d'} \tag{3.2}$$

The distance, d', over which charge transfer occurs is defined by the double-layer thickness. This dimension will be approximately constant for a given type of membrane, and can be incorporated into a new variable defined by:

$$\rho_{ct} = (\rho_{ct}')(d') = R_{ct} A \tag{3.3}$$

The units for ρ_b and ρ_{ct} are, therefore, MΩ•cm and MΩ•cm^2, respectively.

The resistivity data, determined according to equations (3.1) and (3.3), for different samples within a particular master membrane were first evaluated with respect to suspect values using the *Q*-test at the 96 % confidence level. Based on this criteria, bulk and charge transfer resistivity data for sample (1) from membrane #1 can be rejected. Typically 5 - 10 % of all the impedance data acquired for these types of membranes are rejected in this manner.

From the standard deviations in the resistivity data, the precision of impedance data within a given master membrane can be estimated as 24 %

and 14 % for ρ_b and ρ_{ct}, respectively. Given the small data sets involved, these estimates may not be representative of the actual master membrane variability. Nevertheless, factors which contribute to this poor sample specific reproducibility must be examined since measurement specific variability is only about 5 % (*vide supra*).

Membrane inhomogeneity has already been alluded to and this must be the cause for the poor reproducibility. Problems of inhomogeneity in studying these types of membranes have been reported previously [6,8,13-14,21]. Horvai *et al* have noted the presence of hydrophilic impurity regions in some membrane preparations which permit enhanced water uptake and give rise to white or cloudy spots when immersed in aqueous solution [13]. As well, plastics engineers [24] have described the existence of "insoluble gels" within membranes of this type which have been attributed to the PVC not being completely dissolved by the plasticizer. These are often visible to the naked eye as colorless strands. The ISE membranes studied, however, are quite heavily plasticized and ^{13}C relaxation measurements (*cf.* Chapter 5) have shown that there is no significant macroscopic segregation between plasticizer and polymer components.

The exudation of plasticizer from plasticized PVC membranes to form "site-free resistive surface films" has also been suggested by Tóth *et al* [14]. This appeared to be an involved and almost unpredictable process. Scanning electron microscopy (SEM) has been utilized by Harrison *et al* to more thoroughly investigate the leaching process of membrane components from membrane coated n-type Si electrodes [25]. While the surfaces of freshly prepared membranes were generally smooth and featureless, exposure to solution resulted in roughening, blistering and pitting. These localized surface structures, observed in various stages of development, ranged from dimensions of 0.1 μm through to ≈ 40 μm. Energy dispersive X-ray fluorescence (XRF) analyses have suggested that these structures are extruded plasticizers. This appears more plausible than an actual surface "film" of extruded material.

Variations in membrane thickness may also contribute in part to the observed variability between measurements. The distribution of thicknesses for samples cut from the same master membrane has already been noted (Tables 3.3 and 3.4). Most likely the thickness of these individual samples also varies in a similar fashion. Sample thickness, however, is determined by a measurement of the amount by which two metal plates are displaced by the sandwiched membrane sample. As such, it is not a true measure of the mean thickness but rather more of an estimate of the maximum sample thickness. This can clearly be a problem, especially since surface bumps have been observed in dry membranes using low-angle illumination [13]. As well, surface structures resulting from aqueous storage can readily be observed using optical microscopy at 100 - 200 times magnification [25].

The bulk resistance has also been shown to be a strong, approximately exponential function of plasticizer content for both blank and normal ISE membranes [13]. This can be attributed to the sensitivity of ionic mobilities to plasticization level. Thus, if we go from a 66 % DOS/PVC membrane to a 60 % DOS/PVC membrane, the mobilities of the ions are decreased by a factor of about ten [21]. Small changes in the plasticization level may, therefore, also contribute to large changes in apparent resistivity values. This effect should not be too significant, however, since an analytical balance was used in all membrane preparations to ensure that variations in the matrix composition were well below 1 wt%.

Finally, the effect of inhomogeneous distributions of very low levels of impurities in the membranes must not be underestimated. For example, it has been suggested that small quantities of ionizable impurities in the reagents or from the environment (containers, air, *etc.*) incorporated during membrane preparation can alter membrane ion-exchange capacity [26]. In fact, it is this very sensitivity towards membrane additives that makes the impedance technique very suited for probing membrane permeation.

Having established the susceptibility of the impedance results to the portion of the membrane being sampled, the variability from one master membrane to the next can be addressed. The *t*-test can be used to evaluate whether the differences between the impedance results for the two membranes in Tables 3.3 and 3.4 are real or merely caused by statistical variation. A comparison of the means for both ρ_b and ρ_{ct} does not indicate any significant difference between the two master membranes at the 95 % confidence level.

An analysis similar to that outlined above was next carried out between master membranes cast separately on different days. (Optimum reproducibility was established for master membranes cured at room temperature for at least one week. In contrast, storing the membranes in the freezer or measuring after a 48 hr cure contributed to inferior results.) No significant difference in the measured bulk and charge transfer resistivities was suggested for most of the blank membranes at the 95 % confidence limit, except for a selected few. For membranes deliberately incorporating additives, there was almost always no significant difference between membranes prepared on different days at the 95 % confidence level. It would appear, therefore, that inhomogeneity within a given master membrane is the most significant factor out of all the sample specific variables. The exact magnitude of membrane resistivities varies just as much from portion to portion of master membrane as from one master membrane to the next.

3.3.1.3 Overall Reproducibility of *AC* Impedance Membrane Data

In order to obtain an accurate estimate for the overall reproducibility of the *AC* impedance method for blank membranes, a much larger sample population was analyzed. All the measured impedance data from a large number of experiments were pooled together and these are summarized in Table 3.5. This data reflects both measurement and sample specific variability although the latter clearly accounts for the majority of the observed scatter in the data. Based on these results, the relative standard deviation in the bulk and charge transfer resistivities for "identical" blank membranes is 16 % and 20 %, respectively. Even when additives are deliberately incorporated, this precision is generally still not better than 10 % for "identical" membrane samples.

These reproducibility studies suggest that even when proper care is paid to the preparation of the membrane matrix, membrane inhomogeneity

Table 3.5 Impedance data from pool of measured data for blank DOA/PVC membranes (bathing solution: 10 mM KCl).

ρ_b (MΩ•cm)	ρ_b (MΩ•cm)	ρ_{ct} (MΩ•cm^2)	ρ_{ct} (MΩ•cm^2)
1288	1281	39.3	48.3
1494	1259	48.3	50.7
1403	2187	52.7	67.5
1429	1847	68.5	49.3
1348	1410	37.7	61.3
1427	1302	35.6	54.7
1224	2100	38.0	46.0
1357	1381	32.1	63.0
1574	1647	37.7	42.5
1625	1223	41.4	34.4
1237	1390	43.9	48.3
1443	1354	45.9	67.8
1476	1343	42.5	61.8
1447	1273	50.8	64.8
1242	1174	51.0	58.3
1722	1109	48.7	58.1
1458	1265	33.8	46.7
		55.0	52.0
N = 34 mean ρ_b = 1434 MΩ • cm std. deviation = 236 MΩ • cm		N= 36 mean ρ_{ct} = 49.4 MΩ • cm^2 std. deviation = 10 MΩ • cm^2	

within a given master membrane casting is still a major problem. It appears that this factor directly limits the precision of the *AC* impedance data. By comparison, day-to-day variations (*e.g.* purity of the casting solvent) are not as significant. Since this is a problem intrinsic to these membranes, unfortunately there is no easy method to correct for it.

3.3.2 Impurities in Membrane Matrices

It was shown in the previous section that poor membrane reproducibility in blank ISE membranes likely results from an inhomogeneous distribution of impurities in master membrane castings. Since blank membranes contain only plasticizer and polymer components, the origin of these effects must reside in either or both of these components. In this section, the nature of impurities (charge generating or otherwise) in both the plasticizer and polymer components of the membrane matrix will be evaluated in more detail.

3.3.2.1 DOA Plasticizer Component

The plasticizer used most extensively in these impedance studies was bis(2-ethylhexyl) adipate, usually abbreviated DOA (dioctyl adipate). Blank membranes with two differing purities of this plasticizer component were cast in order to examine the effect on the measured membrane impedance. These results are summarized in Table 3.6. Matrix #1 denotes membranes cast with Fluka Pract purity grade plasticizer (≈ 85 - 90%) which was purified by vacuum distillation to ≈ 98%. Matrix #2 denotes membranes cast with Fluka Selectophore purity grade plasticizer (> 99%) marketed "for the production of reliable ion-selective electrodes".

A *t*-test on the results in Table 3.6 shows that there is no significant difference in the mean impedance results of both bulk and charge transfer resistivities for either matrix at the 95 % confidence level. The reproducibility in the data sets, however, appears to differ depending on the

Table 3.6 Impedance data for blank master membranes cast with different purities of DOA plasticizer component (bathing solution: 10 mM KCl).

	Matrix #1[a]	**Matrix #2**[b]
ρ_b (MΩ • cm)	1570 ± 298[c]	1416 ± 282[d]
ρ_{ct} (MΩ • cm^2)	59 ± 17[c]	56 ± 7[c]

[a] Distilled Fluka Pract grade (≈ 98 %).

[b] Fluka Selectophore grade (> 99 %).

[c] Average of 15 measurements.

[d] Average of 14 measurements.

source of the plasticizer. For bulk resistivity, the distilled Pract and Selectophore grades of DOA gave precisions of 19 % and 20 %, respectively. The corresponding precisions for the charge transfer resistivities are 29 % and 12 %, respectively. The *F*-test provides a statistical method for comparing the precision of the data from these two different matrices. This shows that the precision in the bulk resistivity data does not differ significantly at the 95 % confidence level with either grade of plasticizer. The precision in the charge transfer resistivity data, however, is significantly better with the Selectophore grade plasticizer at the 95 % confidence level.

It can be concluded that small amounts (≈ 2%) of impurities in the plasticizer component do not significantly affect the mean impedance results. Therefore, these impurities are most likely not charge generating. Although a constant concentration of charge generating impurities in both Pract and Selectophore grade DOA cannot be ruled out, it is reasonable to assume that the distilled Pract grade DOA contains very little, if any, of such impurities (*e.g.* salts). Since the precision in the data is significantly better for lower levels of impurities, however, for best reproducibility the Selectophore grade plasticizer is clearly the preferred choice. Unfortunately, this grade of purity was only introduced by Fluka in 1989. Some of the earlier impedance data had been acquired from membranes cast with the distilled Pract grade plasticizer. This can account, in part, for the some of the scatter observed in the impedance data.

3.3.2.2 PVC Polymer Component

ISE membranes are almost exclusively based on inert PVC polymer matrixes. A series of blank membranes were, therefore, cast with three different commercial types of this polymer. The observed impedance data is summarized in Table 3.7. A *t*-test of the bulk resistivity data demonstrates that there is no significant difference between the PVC polymer from Polysciences, Aldrich or Fluka at the 95 % confidence level. This suggests that the concentration of mobile charged impurities is the same for all these

Table 3.7 Impedance data for blank master membranes cast with various commercial types of PVC polymer (bathing solution: 10 mM KCl).

PVC	ρ_b (MΩ • cm)(a)	ρ_{ct} (MΩ • cm^2)(a)
Polysciences (chromatographic)	1470 ± 173	43 ± 2
Aldrich (reagent)	1537 ± 88	84 ± 10
Fluka (Selectophore)	1578 ± 64	57 ± 13
Polysciences (purified(b))	780 ± 99	36 ± 1

(a) Results are an average of four measurements.

(b) Purified from Polysciences (chromatographic grade) PVC by dissolution in tetrahydrofuran and precipitation in methanol.

polymer formulations. This indicates that the method of polymer synthesis must not be too different amongst these manufacturers. It appears that the Fluka Selectophore polymer gives a slightly better precision, but there is really no significant difference at the 95 % confidence level using the *F*-test. Surprisingly, the purified Polysciences PVC had a significantly lower bulk resistivity at the 95 % confidence level. This may mean that charge-generating impurities were either introduced during the purification process or charge-trapping species were removed.

Applying the *t*-test at the 95 % confidence level to the charge transfer resistivity data shows that there is a significant difference in this parameter between all the different sources of PVC. This suggests that although the concentration of mobile charged sites are the same for the various commercial sources, the chemical nature of these sites may differ. Previous studies have indicated Na^+ and K^+ to be principle counterions for the fixed anionic sites in Fluka high molecular weight (HMW) PVC [27]. For Aldrich HMW PVC, Na^+ and Ca^{+2} were the primary cations present [16]. These differences in the chemical nature of counterions and/or anionic sites in PVC can account for the observed differences in charge transfer resistivities.

3.3.2.3 Analysis of Plasticizer Impurities

The *AC* impedance results suggest that the plasticizer impurities are not charge-generating since the mean resistivity data does not depend on the concentration of impurities. The observed differences in reproducibility of the data must, therefore, be a result of some physical change in bulk membrane properties such as microviscosity or degree of plasticization. For example, it has been previously reported that membrane resistivities are a strong, approximately exponential function of plasticizer content [13]. It was of interest to further examine the nature of these impurities since this would provide insight into the effect of neutral species on membrane impedance behavior.

Various batches of DOA plasticizer were first analyzed for purity using gas chromatography (GC). These results are shown in Table 3.8. (It should be pointed out that since GC analyzes only volatiles, any salts, if present, may not be measured.) As expected, the Selectophore grade plasticizer is the purest although the Pract grade is often much purer than expected. Four major impurities were detected in the Pract grade DOA by GC analysis and these proved very difficult to remove. In fact, detectable quantities persisted despite several distillation attempts. (This is perhaps not too surprising given the cost differential of approximately 300 % between the Selectophore and Pract grades.) Analysis of the Selectophore grade plasticizer indicated the presence of only one minor impurity (< 1%) and no attempts were made to remove this.

The observed differences in precision of impedance data from membranes cast with distilled Pract grade (98%) and Selectophore grade (> 99%) DOA must, therefore, originate from the additional 2 % of impurities detected in the former. The identities of these impurity species were determined with mass spectrometry coupled with separation by gas chromatography (GC-MS). Low resolution electron impact (EI) and chemical ionization (CI) mass spectra of pure DOA are shown in Figure 3.6. Although EI is a more sensitive method of analysis, apparently it is too energetic an ionization source for these large organic plasticizer molecules. The extensive fragmentation pattern which results (*cf.* Figure 3.6a) makes interpretation very difficult. CI using NH_3 reagent gas is a significantly "softer" ionization source and strong molecular ion signals can usually be detected (*cf.* Figure 3.6b) The molecular weight of DOA is 370.6. The GC-MS results for the detected components in the Fluka Pract DOA (lot #267253986) are shown in Table 3.9. Three of the four impurities were identified as homologues of the parent DOA molecule containing one, two and four additional methylene functionalities. The identity of the fourth impurity (GC peak #4) was a bit more elusive since no obvious derivative of the parent DOA compound was suggested from the mass spectral data.

This same DOA sample was subsequently analyzed with GC-Fourier transform infrared spectroscopy (GC-FTIR). The identity of the elusive

Table 3.8 Gas chromatographic analysis of purity for Fluka DOA plasticizers (column: 6 ft. 10 % OV-1, 80/100 WHP @ 280 °C).

purity grade	assured purity(a)	lot number	actual purity(b)
Pract	85 - 90 %	239659184	97 %
Pract (distilled)(c)	-	distilled from lot #239659184	98 %
Pract	85 - 90 %	267253986	87 %
Pract (distilled)(c)	-	distilled from lot #267253986	89 %
Pract (distilled)(d)	-	distilled from lot #267253986	97 %
Selectophore	> 99 %	2505931188	> 99 %

(a) Manufacturer specification by GC analysis.

(b) Determined from integrated FID detector response.

(c) Distilled under high vacuum with a short path column.

(d) Distilled under high vacuum with a long path heated column packed with glass coils.

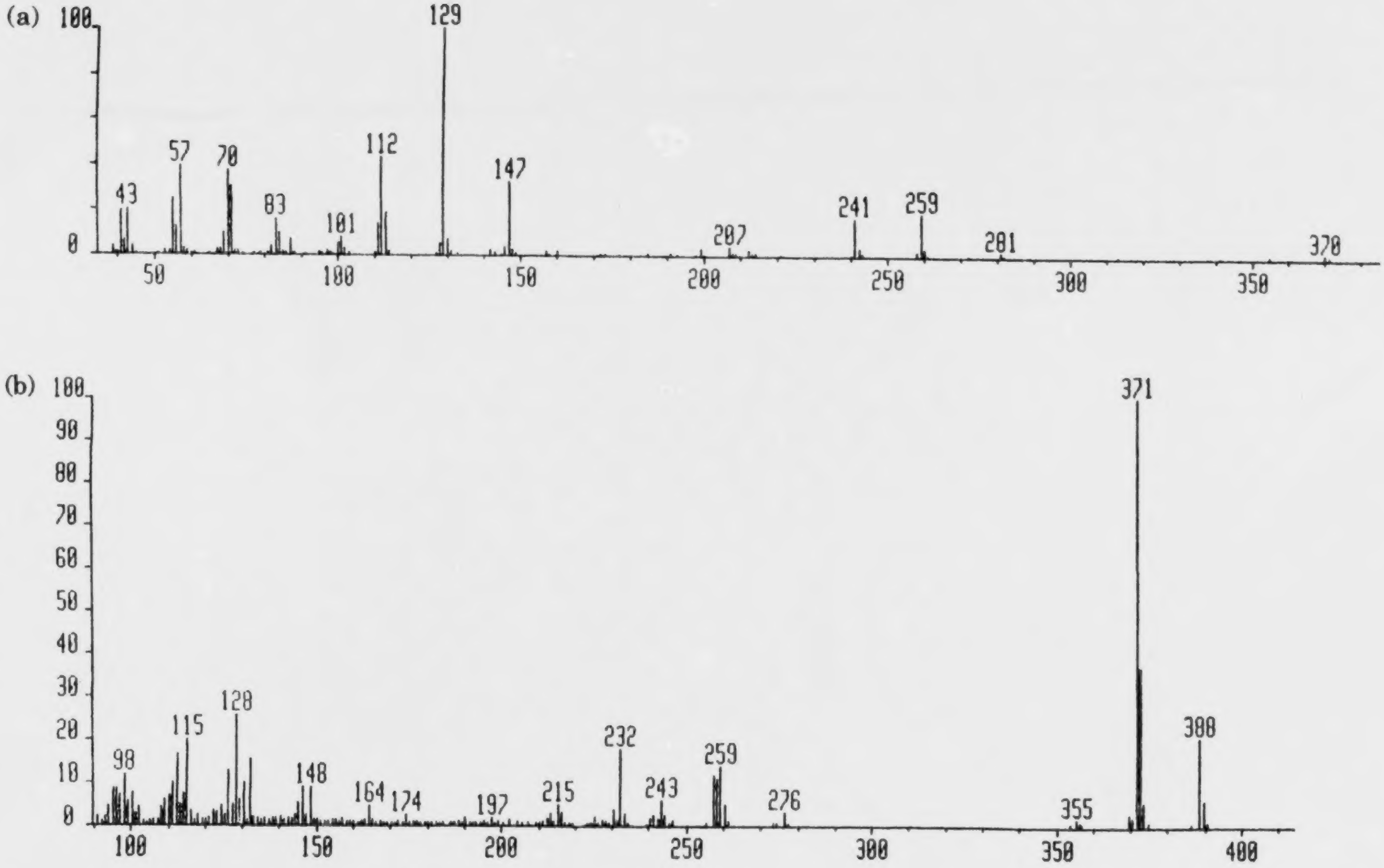

Figure 3.6 Mass spectra of DOA plasticizer: (a) electron impact source and (b) chemical ionization source.

Table 3.9 Gas chromatography-mass spectrometry analytical data for Fluka Pract DOA lot #267253986 (column: DB-5, 50 to 280 °C @ 10 °C/min.).

GC peak number	**% area**(a)	**molecular weight**(b)	**assignment**
1	88.5	371	parent DOA
2	1.5	(d)	DOA + CH_2(e)
3	6.6	399	DOA + $2CH_2$
4	(c)	419	???
5	3.4	427	DOA + $4CH_2$

(a) From integrated conventional FID signal (column: 10 % OV-1, 80/100 WHP).

(b) From molecular ion peak in chemical ionization mass spectrum.

(c) Area of peaks 3 and 4 not resolved.

(d) Not detected by chemical ionization mass spectrometry detector.

(e) Determined through comparison of electron impact mass spectral fragmentation pattern with parent DOA.

fourth impurity was clearly determined to be an ester derivative. An online spectral library search suggested a good correlation with dioctyl phthalate, but this has a molecular weight of only 390.6. FTIR spectral matching is often not too reliable between homologous series, however, and the addition of two methylene groups raises the molecular weight to 418.6. This figure then correlates very well with the mass spectral data for the unknown impurity in Table 3.9. Hence, the remaining impurity was identified as didecyl phthalate.

The FTIR method of detection also proved to be more sensitive than MS detection. An additional impurity (< 1 %) was detected prior to the DOA peak. This was identified as possibly diisobutyl adipate or some other related DOA homologue.

In contrast, Fluka Selectophore DOA contains only one significant impurity (< 1 %). Although the CI detector was not sensitive enough to detect this peak, EI detection was able to provide an EI mass spectrum of this species. From the fragmentation pattern, this impurity can also be attributed to a DOA homologue simply incorporating an additional four methylene functionalities.

The results of the preceding analysis of impurities in DOA have shown that the major impurities are merely CH_2 homologues of the parent compound, with the exception of small amounts of didecyl phthalate. Clearly these will not be charge generating in the membrane since they are all neutral species. In fact they themselves most likely will behave as plasticizers. The low concentration of these species in the plasticizer reagent (< 2 %), however, does lead to significant scatter in the impedance data. This suggests that the *AC* impedance technique is very sensitive to neutral species within the membrane phase. As previously mentioned, this must result from some physical changes in membrane properties, such as microviscosity.

Another plasticizer component frequently employed in ISE preparations is bis(2-ethylhexyl) sebacate, usually abbreviated DOS (dioctyl sebacate). The results of a similar analysis of purity are summarized in Tables 3.10 to 3.12. The data suggests that the impurities present in this plasticizer are also merely homologues of the parent DOS plasticizer.

Table 3.10 Gas chromatographic analysis of purity for DOS plasticizers (column: 6 ft. 10 % OV-1, 80/100 WHP @ 280 °C).

manufacturer	**purity grade**	**assured purity**	**actual purity**[(a)]
Fluka	Pract	95 %	98 %
Aldrich	reagent	97 %	95 %
Aldrich	reagent (distilled)	-	96 %

(a) Determined from integrated FID detector response.

Table 3.11 Gas chromatography-mass spectrometry analytical data for Aldrich reagent grade DOS (column: DB-5, 50 to 280 ^{o}C @ 10 ^{o}C/min.).

GC peak number	% area(a)	molecular weight(b)	assignment
1	95	427	parent DOS
2	3	441	DOS + CH_2
3	2	455	DOS + $2CH_2$

(a) From integrated conventional FID signal (column: 10 % OV-1, 80/100 WHP).

(b) From molecular ion peak in chemical ionization mass spectrum.

Table 3.12 Gas chromatography-mass spectrometry analytical data for Fluka Pract grade DOS (column: DB-5, 50 to 280 °C @ 10 °C/min.).

GC peak number	**% area**[(a)]	**molecular weight**[(b)]	**assignment**
1	98	427	parent DOS
2	2	371	DOS - $4CH_2$

(a) From integrated conventional FID signal (column: 10 % OV-1, 80/100 WHP).

(b) From molecular ion peak in chemical ionization mass spectrum.

3.3.3 Neutral Species Behavior

Neutral additives can affect electrical and physical properties of the membrane matrix. These include charge carrier concentrations, dielectric strength, viscosity and water content. The initial impetus for studying membranes containing known amounts of additives was to develop calibration curves of bulk resistance as a function of concentration in the membrane. This would then permit an estimation of the amount of permeation by these interfering species from an external bathing solution into normal membranes [6,8]. Several neutral species, however, demonstrated peculiar non-monotonic calibration curves [6]. Since the changes induced by the additive may affect the bulk and the charge transfer resistivities in different ways, measurement of these two parameters can be used to sort out the mechanisms by which neutral species affect ISE membrane characteristics.

Benzoic acid was the first additive investigated. Since this may dissociate to give charged species, its effects could be due to ionic reactions, such as acid-base chemistry, in addition to physical effects, such as viscosity and dielectric changes. Methyl benzoate additive was, therefore, also studied since this cannot directly participate in any of the ionic reactions.

The membrane matrix used was 66 % DOA/PVC without any addition of lipophilic salts. The primary role of these lipophilic salts is to simply introduce additional fixed sites into the membrane in order to enhance Donnan exclusion of anions [28-31]. They will also affect ionic strength and, in turn, dissociation reactions. Generally, the influence of impurities in plasticized PVC membranes is somewhat diminished when these salts are deliberately used in the membrane [21]. Additionally, the presence of a high concentration of anionic sites in the membrane is known to greatly facilitate interfacial exchange reactions, and thereby reduce the charge transfer resistance [1,18]. For these reasons, the salt-free matrix was chosen in order to best observe any changes in impedance behavior caused by the additives studied. The scatter in impedance measurements from the ISE membrane matrix has already been determined to be large enough to make interpretation of effects on resistivity difficult.

In order to interpret the effects of neutral species additives on the observed impedance behavior, the origins of bulk (ρ_b) and charge transfer (ρ_{ct}) resistivities in the membrane must first be discussed.

3.3.3.1 Origins of Membrane Bulk and Charge Transfer Resistivities

The bulk resistivity is inversely related to the specific conductivity of the membrane (σ):

$$\sigma = \frac{1}{\rho_b} = F \sum_i |z_i| C_i u_i \qquad (3.4)$$

where z_i, C_i and u_i represent the charge, concentration and mobility of the ith charge carrying species [32].

When the membrane is at equilibrium with an aqueous bathing electrolyte solution, there will be an exchange of ions across the membrane/solution interface. This can be characterized by an exchange current (i_o). The relationship between potential and exchange current density is given by the Butler-Volmer equation. If the interfacial potential is perturbed from its equilibrium value, a net current (i) will flow which is proportional to the deviation of the interfacial potential from its equilibrium value, provided that this overpotential (η) is sufficiently small. The ratio of overpotential to current density (η/i) has dimensions of resistance and is designated as the charge transfer or polarization resistance (R_{ct}) [32-33]. It is this parameter which is directly determined from impedance measurements and this serves as a convenient index of the kinetic facility of charge transfer. Given the presence of a double-layer in both the aqueous phase and the membrane phase, there is not a simple relationship between R_{ct} and i_o [21]. The following relationship, however, is a good approximation:

$$R_{ct} = \frac{RT}{zFi_o} \tag{3.5}$$

where R, T, z and F have their usual meaning. If the exchange current is normalized to unit area to provide the exchange current density (j_o):

$$\rho_{ct} = \frac{RT}{zFj_o} \tag{3.6}$$

For selective charge transfer of M^{+z} ions across an interface, the exchange current density should follow [18]:

$$j_o = z\, F\, k_{M^{+z}} \left(C_{M^{+z}}\right)_{aq}^{\alpha} \left(C_{M^{+z}}\right)_{m}^{1-\alpha} \tag{3.7}$$

where $k_{M^{+z}}$ is the heterogeneous rate constant for the exchange process and α is the transfer coefficient which is normally expected to be near 0.5. The subscripts (aq) and (m) refer to the concentrations of the M^{+z} ion in the aqueous and membrane phases, respectively. Expanding equation (3.7) to the non-selective charge transfer of ions in the absence of ionophore gives:

$$j_o = F \sum_{i} |z_i|\, k_i \left(C_i\right)_{aq}^{\alpha} \left(C_i\right)_{m}^{1-\alpha} \tag{3.8}$$

where the summation is over all the exchangeable ions in the system. For our membrane system, it is anticipated that:

$$\rho_{ct} \propto \frac{1}{\left(C_{K^+}\right)_{m}^{1-\alpha}} \tag{3.9}$$

since the membranes under study can only exchange with K^+ ions in the 10 mM KCl bathing solution. Indeed, increases in membrane ion content have been reported to lead to corresponding decreases in charge transfer resistivities [1,18].

3.3.3.2 Benzoic Acid-Containing Membranes

A series of membranes were cast containing various concentrations of benzoic acid (HBz) additive. The bulk and charge transfer resistances were measured for each membrane after soaking in 10 mM KCl for 1 to 1.5 hrs. The resistance data was then normalized for thickness and area to yield resistivities according to equations (3.1) and (3.3). The resulting calibration curves of % $\Delta\rho_b$ and % $\Delta\rho_{ct}$ *versus* concentration of HBz are presented in Figure 3.7. Resistivities are expressed as percent changes in resistivity between membranes with additive and those without any additive. Each point in Figure 3.7 represents an average of four samples taken from different portions of each master membrane.

The data in Figure 3.7 shows that the presence of HBz in the membrane has a complex effect on the bulk and charge transfer resistivities. We observe, however, that the behavior of ρ_b and ρ_{ct} track one another quite well throughout the HBz concentration range studied. As shown by equations (3.4), (3.6) and (3.8), ρ_b and ρ_{ct} are both inversely related to the ion concentration in the membrane phase. Therefore, this suggests that the observed changes in impedance result from an electrical effect of some kind whereby the neutral additive alters the charge carrier concentration within the membrane phase. These effects may be understood by considering the behavior of the HBz additive in the membrane and its interaction with the fixed ion exchange sites present in these types of membranes. Consideration of alternative effects by which HBz could alter ρ_b and ρ_{ct} is reserved until after presentation of the data for MeBz.

It is generally accepted that plasticized PVC-based membranes contain endogenous, weakly dissociable fixed sites capable of ion exchange [2,29,34]. The concentration of these sites is small and can vary from about 0.05 mM to 0.6 mM. These sites have been associated primarily with the PVC polymer component and are believed to arise from adventitious impurities introduced in the synthesis of this polymer [1,13,27]. A study on the chemical identification of these sites using X-ray photoelectron spectroscopy (XPS), secondary ion mass spectrometry (SIMS) and X-ray

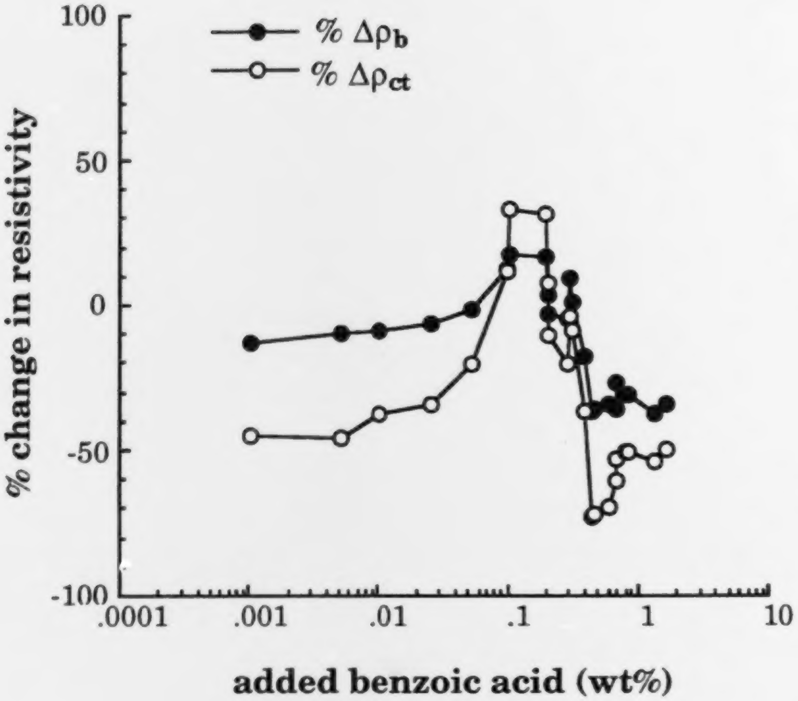

Figure 3.7 Calibration curves for the change in membrane bulk and charge transfer resistivities as a function of weight percent of benzoic acid additive incorporated into the membrane during its preparation (membrane matrix: 66 % DOA/PVC; bathing solution: 10 mM KCl). Clearly, changes in resistivity are 0 for membranes prepared without additive. The solid lines in these plots are for clarity only.

fluorescence (XRF) was recently reported [27]. It was suggested that these anionic sites might be polymer-bound sulfate ($ROSO_3^-$) or sulfonate (RSO_3^-) groups generated by a metal persulfate anion radical initiator. Although some of these sites will be relatively mobile within the membrane matrix, the majority are assumed to be fixed. It is the presence of these impurities that makes these membranes permselective for cations and ensures that hydrophilic anions are excluded from the membrane [2]. In fact, anionic lipophilic salts, such as potassium tetraphenylborate ($KBPh_4$), are usually deliberately added to the membrane at ≈ 1 mM [21,29,35,36]. The BPh_4^- anions act as nearly fixed sites in the membrane, effectively improving Donnan exclusion of anions. In the K^+ membrane, preferential extraction of the K^+ cation from solution occurs because of the presence of valinomycin ionophore in the membrane phase.

The fixed ion exchange sites in these membranes can be represented by X^-. Studies have shown that the counterions for these anionic sites are primarily Na^+, K^+ and Ca^{+2} depending on the preparation of the PVC polymer, particularly additives used in manufacture by suspension or by emulsion methods [16,27]. For simplicity, these counterions will be generically represented as univalent M^+ ions.

In blank membranes without any additive, dissociated counterions from the corresponding fixed and mobile charged sites in the polymer give rise to the intrinsic bulk conductivity in the membrane:

$$(X^-M^+)_{(m)} \rightarrow X^-_{(m)} + M^+_{(m)} \tag{3.10}$$

Charge transfer of K^+ ions occurs by ion exchange between these fixed sites and the external bathing solution:

$$(X^-K^+)_{(m)} + \mathbf{K}^+_{(aq)} \rightarrow (X^-\mathbf{K}^+)_{(m)} + K^+_{(aq)} \tag{3.11}$$

When HBz is initially introduced into the membrane, ρ_b values are decreased compared to membranes without the additive present. This is consistent with the expected effect of addition of a weakly dissociable species such as HBz to the membrane:

$$HBz_{(m)} \rightarrow H^{+}_{(m)} + Bz^{-}_{(m)} \tag{3.12}$$

The acid dissociation constant (K_a) governing this process might be expected to be very small, however, given that the membrane is a low dielectric medium. The pK_a for HBz is generally only in the range from 10 to 21 for most non-aqueous solvents [37]. The observed pK_a for HBz in these organic membranes, however, were estimated to be between 5 and 6 depending on the particular membrane matrix [6]. This degree of dissociation is not that much smaller than the pK_a in water of 4.2. This has been attributed to the presence of water in the membrane phase which assists the dissociation process [6]. Hence, the observed initial drop in ρ_b must result from the increased numbers of additional charge carrying species, $H^{+}_{(m)}$ and $Bz^{-}_{(m)}$, according to equation (3.4).

The effect of acid dissociation of HBz may also be regarded as augmenting the number of weakly dissociable sites in the membrane. This would facilitate the charge transfer of K^+ ions via equation (3.11) and can account for observed initial drop in ρ_{ct} values once HBz is added to the membrane. In fact, the considerable reduction in charge transfer resistance has been cited as one of the additional benefits of incorporating lipophilic salts, such as potassium tetraphenylborate, into ISE membrane preparations based on plasticized PVC [1,28].

As the concentration of HBz in the membrane is increased, the bulk and charge transfer resistivities gradually begin to increase. Maximum resistivity values are attained at ≈ 0.1 to 0.2 wt% HBz that are actually significantly higher than the original resistivities for membranes without the additive. This observed increase in bulk resistivity implies a net loss of charge carriers in the membrane which suggests a mechanism by which the added HBz gradually removes ions from participation in current conduction.

The fixed X^- sites ($ROSO_3^-$ or RSO_3^-) in the membrane are weakly acidic ion exchange sites in the low dielectric of the membrane. Hence, these will have a relatively strong affinity for protons. The gradual incorporation of the HBz into the membrane in Figure 3.7 can, therefore, be regarded as a titration of these fixed sites by the weak acid additive:

$$(X^-M^+)_{(m)} + HBz_{(m)} \rightarrow (X^-H^+)_{(m)} + M^+Bz^-_{(m)} \qquad (3.13)$$

This protonation of fixed sites can produce counterions $M^+_{(m)}$ along with $Bz^-_{(m)}$ through ion-pair dissociation.

$$M^+Bz^-_{(m)} \rightarrow M^+_{(m)} + Bz^-_{(m)} \qquad (3.14)$$

Equation (3.10) shows that $(X^-M^+)_{(m)}$ can also dissociate, as can $(X^-H^+)_{(m)}$. However, due to the weakly acidic nature of the $(X^-H^+)_{(m)}$ group, its extent of dissociation is expected to be much smaller relative to the dissociation of $(X^-M^+)_{(m)}$. The effect on the concentration of charge carriers in the membrane will, therefore, depend on the relative dissociation equilibria between $(X^-M^+)_{(m)}$ and $(M^+Bz^-)_{(m)}$.

The dissociation constants (K_d) of sodium, potassium and tetraethylammonium benzoate salts have been evaluated in the membrane through use of the Fuoss equation of conductance for associated electrolytes [6]. Low K_d's of these salts were reported in the range of 1.9×10^{-5} to 3.5×10^{-5}. This is significantly smaller than the K_d's for tetraphenylborate salts of Na^+, K^+ and NBu_4^+ which ranged from 2.3×10^{-3} to 5.0×10^{-4}, as estimated by Armstrong *et al* in a similar DOS/PVC membrane matrix [19,21]. (Activity coefficients were neglected by using the Ostwald limiting law, however, and this results in an overestimate of K_d [6].) In fact, it is even reasonable to assume that at higher concentrations of HBz additive, the low dielectric membrane medium will not be able to support the higher amounts of benzoate salt produced and these will begin to precipitate out:

$$M^+_{(m)} + Bz^-_{(m)} \rightarrow M^+Bz^-_{(s)} \qquad (3.15)$$

In support of this hypothesis, a previous analysis of conductance *versus* concentration curves for various benzoate salt additives has indicated low solubility of NaBz in the membrane [6].

Thus, the net effect of initial increases in HBz concentration is protonation of membrane sites with a concomitant overall reduction in membrane charge carriers. According to equation (3.4), this can account for the observed increase in bulk resistivity.

The parallel increase in charge transfer resistivity can also be understood by this titration phenomenon. Protonation of fixed ion-exchange sites occurs via equations (3.13). Ion pair association or precipitation of these newly formed $M^+Bz^-_{(m)}$ sites can then subsequently occur. These processes all serve to reduce the concentration of available sites for K^+ exchange. This can give rise to the observed increase in charge transfer resistivity as HBz is added to the membrane.

As the concentration of HBz is increased beyond ≈ 0.1 - 0.2 wt%, the resistivities are seen to rapidly drop off in magnitude. In this concentration regime, all of the fixed sites have already been protonated and can be represented as $(X^-H^+)_{(m)}$. Additional HBz then only affects charge carrier concentration through simple acid dissociation:

$$HBz_{(m)} \rightarrow H^+_{(m)} + Bz^-_{(m)} \qquad (3.16)$$

This generation of charge carriers in the membrane would account for the observed decrease in bulk resistivity according to equation (3.4).

Acid dissociation of HBz will also provide more weakly dissociable sites (Bz^-) in the membrane for K^+ ion exchange:

$$(K^+Bz^-)_{(m)} + \mathbf{K}^+_{(aq)} \rightarrow (\mathbf{K}^+Bz^-)_{(m)} + K^+_{(aq)} \qquad (3.17)$$

This would account for the observed reduction in charge transfer resistivity.

Beyond ≈ 0.82 wt% HBz, it can be seen that further increases in HBz concentration appear to have little effect on the measured impedance. Bulk and charge transfer resistivities remain more or less constant. At higher concentrations, the dissociated fraction of any weak acid will decrease. Therefore, further additions of the HBz additive will not significantly alter charge carrier concentrations. There will no longer be any effect on the electrical properties of the membrane and ρ_b and ρ_{ct} should remain constant.

We can make the approximation that all of the added HBz contributes to the protonation of X^- membrane sites. This assumes that the equilibrium constant for the protonation of X^- is large enough such that at the equivalence point all the available membrane sites are protonated by the added HBz, *i.e.* $[X^-] = [HBz]$. This is likely to be a poor assumption since all the acidic sites are weak in the organic membrane matrix. Additionally, at least some of the X^- sites are $ROSO_3^-$ and RSO_3^- groups which should have stronger proton affinities than Bz^-. Nevertheless, by interpretation of Figure 3.7 as a direct titration of active membrane sites X^- by HBz additive, we can make an estimate of the equivalent site concentration. The "equivalence point" in this titration corresponds to the HBz concentration which results in the maximum membrane resistivity, and this occurs at *ca.* 0.1 to 0.2 wt% HBz. The corresponding volume concentrations of HBz in the membrane can be estimated as 8.8 to 17.7 mM, based on an additive molecular weight of 122.12 g/mol and a membrane density of about 1.08 g/cm^3 (*cf.* Chapter 7). This suggests that the effective membrane site concentration is ≈ 8.8 to 17.7 mM. In actuality, cation-selective membranes based on PVC are thought to contain only ≈ 0.05 to 0.6 mM negative fixed sites, depending on polymer molecular weight and mode of polymerization [13,16]. The discrepancy likely arises from the approximation that the titration reaction goes to completion at the equivalence point.

3.3.3.3 Methyl Benzoate-Containing Membranes

The role of methyl benzoate (MeBz) additive in DOA/PVC membranes was evaluated in an analogous fashion to the preceding HBz study. The observed calibration curves of % $\Delta\rho_b$ and % $\Delta\rho_{ct}$ *versus* concentration of MeBz are presented in Figure 3.8. It is apparent from this data that the ρ_b and ρ_{ct} data for the MeBz additive do not track one another very well. This implies that the observed changes in the impedance behavior do not simply reflect changes in membrane charge carrier concentration.

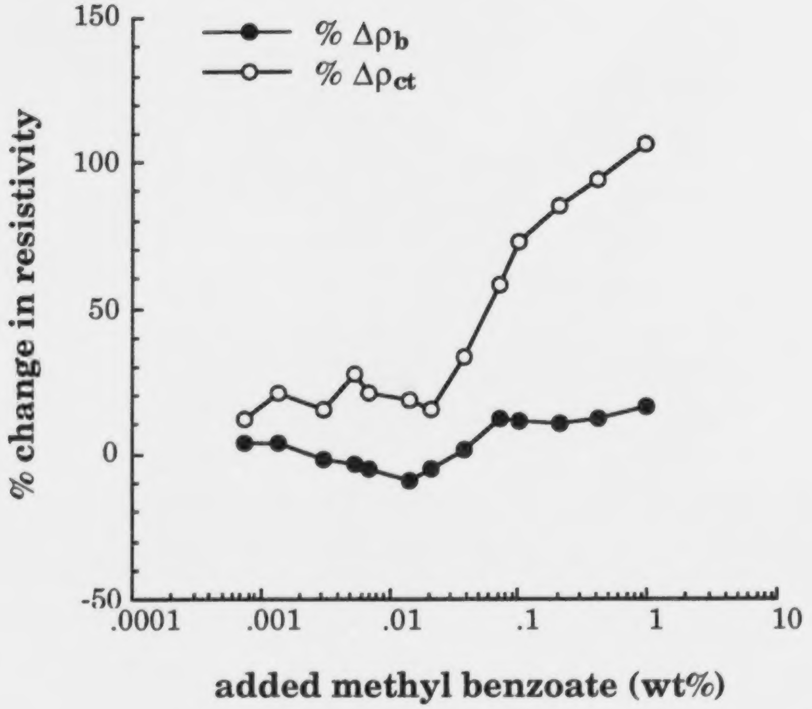

Figure 3.8 Calibration curves for the change in membrane bulk and charge transfer resistivities as a function of weight percent of methyl benzoate additive incorporated into the membrane during its preparation (membrane matrix: 66 % DOA/PVC; bathing solution: 10 mM KCl). Clearly, changes in resistivity are 0 for membranes prepared without additive. The solid lines in these plots are for clarity only.

Initially, the bulk resistivity decreases as MeBz is added. Then at ≈ 0.01 wt%, further additions of MeBz begin to cause a gradual increase in the observed bulk resistivity. The overall magnitude for these bulk resistivity changes is quite small. In contrast, changes in the charge transfer resistivity are more complex. Small fluctuations in the charge transfer resistivity appear to occur in an unpredictable fashion below concentrations of ≈ 0.02 wt%. At higher concentrations of the additive, however, this parameter then begins to rapidly increase to quite a large value. There are many factors which can contribute to this observed impedance behavior and these will be discussed in the following few sections.

Unlike the HBz additive, MeBz is not dissociable so it is unable to directly change the charge carrier concentration in the membrane (C_i). Hence, other more subtle effects must account for the observed trends in the resistivity data. The presence of MeBz in the membrane is capable of altering significant physical properties of the membrane. It must be these physical changes which are indirectly affecting the electrical behavior in the membrane phase.

In a study of solvent properties of PVC membranes, Armstrong *et al* [38] have reported a minimum in bulk resistivity similar to the one seen in Figure 3.8. In that study, DOS/PVC membranes containing 1 mM $NaBPh_4$ were studied as the PVC content was varied. The membrane bulk resistivity went through a minimum in spite of the fact that the mobilities of Na^+ and BPh_4^- decrease monotonically with increasing PVC level. This was explained by a competition between the reduction of ionic mobilities and the increased dissociation of the salt with additions of PVC. In a related fashion, the minimum in the % $\Delta\rho_b$ data observed in Figure 3.8 can be also attributed to a competition between the mobility and the dissociation of anionic PVC impurity sites. The expected changes to these two parameters, as MeBz is added to the membrane, is outlined in the following paragraphs.

The dielectric constant (ε_r) for a membrane can be determined by assuming that it is well-represented by a parallel combination of a geometric capacitor (C_g) and a bulk resistor (R_b). The ε_r of the membrane can then be calculated using [38]:

$$C_g = \frac{\varepsilon_0 \varepsilon_r A}{d} \tag{3.19}$$

where ε_0 is the permittivity of free space (8.854×10^{-12} F/m), A is the membrane area, and d is the membrane thickness. For blank DOA/PVC membranes without any additive $\varepsilon_r = 8.2$ (Appendix C); for pure MeBz additive $\varepsilon_r = 6.59$ [39]. Therefore, it can be expected that incorporation of MeBz additive will lead to a decrease in the membrane dielectric strength.

Accurate values for ε_r are best calculated from high frequency impedance data using a lock-in analyzer technique. All of the impedance data in the present study, however, were acquired with the fast Fourier transform technique (*cf.* Chapter 2). Nevertheless, evaluation of the data yields $\varepsilon_r \approx 7.7$ for blank membranes and $\varepsilon_r \approx 7.3$ for membranes containing a high concentration of MeBz (> 1 wt%). This suggests that a modest decrease in ε_r does occur as MeBz is added. This effect should decrease the extent of dissociation of membrane sites via equation (3.10) which would lead to an increase in bulk resistivity according to equation (3.4).

Decreased dissociation of membrane sites should also lead to an increase in the charge transfer resistivity. According to equation (3.11), decreasing the number of sites will hinder charge transfer of K^+ ions across the membrane/solution interface. Since the difference in dielectric constants is very small, however, this effect on the degree of dissociation of membrane sites should also be very small. There must, therefore, be other mechanisms operative by which the addition of MeBz causes the observed large increases in the % $\Delta\rho_{ct}$ data.

It is possible that MeBz additive, with its polar ester functionality, may act as a chelating agent and complex cations within the membrane. In a study of the dependence of conductivity on temperature for MeBz in a similar membrane matrix, however, it has been shown that this is not a significant effect [6]. Nevertheless, a limited solvation of cations still might occur:

$$xMeBz_{(m)} + M^+{}_{(m)} \rightarrow [M^+(MeBz)_x]_{(m)} \qquad (3.20)$$

By acting as a coordinating ligand, the presence of MeBz would probably facilitate charge transfer of ions. Hence, this would contribute to a decrease in ρ_{ct}.

Any solvation of counterions by MeBz would also facilitate the dissociation of membrane sites by preventing the formation of direct contact ion pairs, $(X^-M^+)_m$, and favoring the formation of additive-separated ion pairs, $[X^-M^+(MeBz)_x]_m$. Since the latter are inherently more thermally unstable, the degree of site dissociation would, therefore, tend to increase with increasing MeBz content [38]. This should lead to a decrease in ρ_b according to equation (3.4). Also, the site dissociation reaction given by equation (3.10) would tend to proceed in the forward direction if stabilization of the $M^+{}_{(m)}$ product occurred by solvation, and so decrease ρ_b.

If solvation of cations is occurring, this could alter charge carrier mobilities (u_i). Mobilities may be increased or decreased, relative to the uncomplexed counterions, thereby producing corresponding changes in ρ_b according to equation (3.4). The mobilities of ionic species in any medium also depend on frictional drag according to Stokes law. The incorporation of significant concentrations of any additive may change the membrane viscosity, for example by altering plasticizer-polymer interactions (*cf.* Chapter 5). Any changes in the membrane viscosity will, therefore, also contribute to changes in the ionic mobilities, and hence ρ_b.

Another cause for the increase in charge transfer resistivity observed when MeBz is added may be the formation of site-free resistive surface films of MeBz by exudation of this additive from the membrane interior. This leaching out of neutral substances can be followed by impedance measurements, however, it is an involved process which cannot always be rationalized [21,14,9]. An interesting example of this is the exudation of plasticizer and/or valinomycin from K^+-sensitive membranes [14]. Apparently this leads to the formation of surface resistive films of different composition from the membrane interior. These films can be removed when the membrane is removed from the bathing solution or when air or argon is bubbled onto the membrane surface.

Finally, the complex role of water in the membrane must not be underestimated. The presence of the MeBz additive may change the concentration and/or distribution of water in the membrane. For example, the addition of $KBPh_4$ significantly increases the uptake of water in the membrane (*cf.* Chapters 5 and 6). Irregular white or cloudy water drops in soaked membranes have also been traced to filterable impurities in the membrane [13]. Furthermore, it has been demonstrated that a water rich surface region exists in these membranes whose thickness depends on the hydrophilicity of the additives [40].

Water in the membrane may have many diverse effects. It can significantly alter the membrane dielectric constant since $\varepsilon_r(H_2O) = 78.5$. Its role in determining the dissociation constants in the membrane has already been implicated [6]. Immobile anionic sites capable of ion exchange have been suggested to originate from proton exchange reactions involving water which trap OH^- ions in water clusters [41]. Aqueous regions of the membrane are also able to immobilize dissociated charge carriers and impurities in the membrane by forming colloidal inclusions [26]. Ion exchange can subsequently occur between these inclusions and the bulk aqueous phase [21].

It can be seen that the effect of the MeBz additive is most likely to alter any of several physical properties of the membrane. Changes in these properties, in turn, can indirectly affect the electrical properties of the membrane.

3.3.3.4 Comparison Between Benzoic Acid and Methyl Benzoate Behavior

The ability of these nominally neutral species to effect changes in the membrane resistivities is perhaps surprising. This impedance study, therefore, provides insight into the complex nature of neutral species interference in these plasticized PVC membranes. It must be emphasized that some, if not all, of the effects attributed to the presence of the MeBz additive are equally valid for the HBz system.

For the bulk resistivity behavior, it appears that the effects of the HBz additive on physical membrane properties, such as viscosity and dielectric strength, are much less pronounced relative to the acid dissociation effects of HBz. Acid dissociation directly introduces charge carriers into the membrane phase. In fact, we can see that the changes in bulk resistivity are much larger for HBz than for MeBz. The % $\Delta\rho_b$ values range from -38 % to +17 % and from -9 % to +16 %, respectively. For the charge transfer resistivity, these indirect physical effects appear to be quite significant for both types of additives. The % $\Delta\rho_{ct}$ values range from -73 % to +32 % and from +12 % to +106 %, respectively. However, the fact that ρ_b and ρ_{ct} track each other for HBz, but not for MeBz, strongly suggests that acid dissociation is also the dominant effect in changes in ρ_{ct} for the HBz additive. For these reasons, we conclude that the "titration" based interpretation is the best able to explain the non-monotonic behavior of resistivity when HBz is added.

3.4 Conclusions

The permeation of an ISE membrane by neutral species from a sample solution is a real problem. This work attempts to clarify the role that these extractable neutral species play in determining membrane characteristics. The applicability of the impedance method in studying membrane permeation has been confirmed. It has been shown that the impedance characteristics of membranes are very sensitive to neutral impurities, either intentionally or unintentionally incorporated.

The incorporation of neutral species into an ISE membrane matrix was concluded to significantly alter the kinetics of ion exchange across the membrane/solution interface. This has been attributed to the mediation of physical properties of the membrane with addition of the neutral species. If the neutral species itself is dissociable, this can also lead to significant changes in the bulk membrane resistance. A clearer understanding of neutral species behavior within these membranes may ultimately lead to a better understanding of the mechanism by which some nominally neutral compounds in physiological fluids interfere with electrode response and affect lifetime.

3.5 References

1. Ammann, D.; Morf, W.E.; Anker, P.; Meier, P.C.; Pretsch, E.; Simon, W. *Ion-Selective Electrode Rev.* **1983**, *5*, 3.

2. Morf, W.E.; Simon, W. *Helv. Chim. Acta* **1986**, *69*, 1120.

3. Carmack, G.D.; Freiser, H. *Anal. Chem.* **1975**, *47*, 2249.

4. Fogt, E.J.; Untereker, D.F.; Norenberg, M.S.; Meyerhoff, M.E. *Anal. Chem.* **1985**, *57*, 1995.

5. Janata, J. *Biosensor Technology, Fundamentals and Applications* Buck, R.P.; Hatfield, W.E., Umaña, M., Bowden, E.F., Ed.; Marcel Dekker: New York, Chapter 2, 1990.

6. Verpoorte, E.M.J. "Analysis of the Permeability and Behaviour of Dissociable Species in Ion-Selective Membranes", Ph.D. Thesis, University of Alberta, Edmonton, 1990.

7. Li, X.; Verpoorte, E.M.J.; Harrison, D.J. *Anal. Chem.* **1988**, *60*, 493.

8. Verpoorte, E.M.J.; Harrison, D.J. "Calibration of Anion Permeation in K^+-Ion Selective Electrode Membranes Using Impedance Methods", in press.

9. Harrison, D.J. *J. Electroanal. Chem.* **1990**, *278*, 193.

10. Oesch, U.; Dinten, O.; Ammann, D.; Simon, W. In *Ion Measurements in Physiology and Medicine*; Kessler, M., Harrison, D.K., Hoeper, J., Eds.; Springer-Verlag: Berlin, p. 42, 1985.

11. Jenny, H.-B.; Riess, C.; Ammann, D.; Magyar, B.; Asper, R.; Simon, W. *Mikrochim. Acta* **1980**, *II*, 309.

12. Koch, D.D.; Ladenson, J.H. *Anal. Chem.* **1983**, *55*, 1807.

13. Horvai, G.; Gráf, E.; Tóth, K.; Pungor, E.; Buck, R.P. *Anal. Chem.* **1986**, *58*, 2735.

14. Tóth, K.; Gráf, E.; Horvai, G.; Pungor, E.; Buck, R.P. *Anal. Chem.* **1986**, *58*, 2741.

15. Iglehart, M.L.; Buck, R.P.; Pungor, E. *Anal. Chem.* **1988**, *60*, 290.

16. Lindner, E.; Gráf, E.; Niegreisz, Z.; Tóth, K.; Pungor, E.; Buck, R.P. *Anal. Chem.* **1988**, *60*, 295.

17. Armstrong, R.D.; Nikitas, P. *Electrochim. Acta* **1985**, *30*, 1627.

18. Armstrong, R.D.; Lockhart, J.C.; Todd, M. *Electrochim. Acta* **1986**, *31*, 591.

19. Armstrong, R.D.; Todd, M. *Electrochim. Acta* **1987**, *32*, 155.

20. A. Craggs, G.J. Moody, J.D.R. Thomas, J. Chem. Ed., 51, 541 (1974).

21. Armstrong, R.D.; Horvai, G. *Electrochim. Acta* **1990**, *35*, 1.

22. Armstrong, R.D.; Todd, M. *Electrochim. Acta* **1987**, *32*, 1403.

23. Abu Samrah, M.M.; Bitar, R.A.; Zihlif, A.M. *Appl. Phys. Comm.* **1983**, *3*, 225.

24. Sears, J.K.; Darby, J.R. *The Technology of Plasticizers*, John Wiley and Sons: New York, 1982.

25. Harrison, D.J.; Cunningham, L.L.; Li, X.; Teclemariam, A.; Permann, D. *J. Electrochem. Soc.* **1988**, *135*, 2473.

26. Horvai, G.; Horváth, V.; Farkas, A.; Pungor, E. *Anal. Lett.* **1988**, *21*, 2165.

27. van den Berg, A.; van der Wal, P.D.; Skowronska-Ptasinska, M.; Sudhölter, E.J.R.; Reinhoudt, D.N.; Bergveld, P. *Anal. Chem.* **1987**, *59*, 2827.

28. Meier, P.C.; Morf, W.E.; Läubli, M.; Simon, W. *Anal. Chim. Acta* **1984**, *156*, 1.

29. Buck, R.P.; Tóth, K.; Gráf, E.; Horvai, G.; Pungor, E. *J. Electroanal. Chem.* ***1987***, *223*, 51.

30. Morf, W.E.; Kahr, G.; Simon, W. *Anal. Letters* **1974**, 7, 9.

31. Morf, W.E.; Ammann, D.; Simon, W. *Chimia* **1974**, *28*, 65.

32. Bard, A.J.; Faulkner, L.R. *Electrochemical Methods*; John Wiley & Sons: New York, 1980.

33. Linder, E.; Tóth, K.; Pungor, E. *Dynamic Characteristics of Ion-Selective Electrodes*; CRC Press: Boca Raton, 1988.

34. Perry, M.; Löbel, E.; Bloch, R. *J. Membr. Sci.* **1976**, *1*, 223.

35. Armstrong, R.D. *Electrochim. Acta* **1987**, *32*, 1549.

36. Morf, W.E.; Ammann, D.; Simon, W. *Chimia* **1974**, *28*, 65.

37. Laitinen, H.A.; Harris, W.E. *Chemical Analysis, 2nd Ed.*; McGraw-Hill: New York, 1975.

38. Armstrong, R.D.; Covington, A.K.; Proud, W.G. *J. Electroanal. Chem.* **1988**, *257*, 155.

39. *CRC Handbook of Chemistry and Physics, 62nd Ed.*; Weast, R.C., Astle, M.J., Eds.; CRC Press: Boca Raton, 1981.

40. Harrison, D.J.; Li, X. *IEEE Int. Conf. on Solid-State Sensors and Actuators, Tech. Digest*, p.777, San Francisco, June 1991.

41. Thoma, A.P.; Viviani-Nauer, A.; Arvanltis, S.; Morf, W.E.; Simon, W. *Anal. Chem.* **1977**, *49*, 1567.

Chapter 4

AC Impedance Study of a Plasticized Poly(vinyl chloride) Ca^{+2} Ion-Exchanger Electrode

4.1 Introduction

AC impedance analysis was first used to study Faradaic processes in electrochemistry in the 1960s by Sluyters [1-2]. Applications can now be found in the study of semiconductors, corrosion, batteries, electrodeposition, electroorganic synthesis and coatings evaluation [3]. Recently, the *ac* impedance method has been applied to investigate ion transport in ion-selective electrode (ISE) membranes plasticized with poly(vinyl chloride). Key papers have been contributed by research groups at the University of North Carolina (Buck), the Technical University of Budapest (Pungor and Tóth), the University of Newcastle-upon-Tyne (Armstrong) and the University of Alberta (Harrison). Extensive literature citations can be found in references [4-10].

Up to now, these impedance studies have focussed primarily on K^+-sensitive membranes based on the neutral carrier valinomycin. For these systems, the impedance behavior has always been restricted to the first quadrant of the complex plane. In fact, depending on specific experimental conditions, generally only three features are ever observed: 1) a high frequency semicircle arising from bulk membrane resistance and geometric capacitance, 2) a low frequency semicircle arising from charge transfer resistance and double-layer capacitance, and 3) a low frequency 45° straight line arising from Warburg diffusional impedance.

In the present study, impedance analysis is applied to a Ca^{+2}-selective membrane based on a diarylphosphate liquid ion-exchanger ligand. For this system, impedance characteristics corresponding to inductive behavior has been observed in the fourth quadrant of the complex plane. This marks the first time for which such behavior has ever been reported for an ion-selective membrane. A detailed theoretical basis for this behavior is presented along with an analysis of the factors which contribute to its existence. Preliminary studies have also found inductive behavior in NH_4^+-sensitive membranes based on the nonactin ionophore and plasticized with tris(2-ethylhexyl) phosphate (TEHP). Additional studies, however, are required to fully characterize this ISE membrane system.

4.2 Theoretical Treatment

4.2.1 Background

Very often data from *ac* impedance measurements are simply analyzed by defining an equivalent electronic circuit which models the observed impedance behavior of the electrochemical cell. The constituent circuit elements (resistors, capacitors and inductors) are then interpreted as various discrete steps in the overall electrochemical behavior (*e.g.* charge transfer resistance, double-layer capacitance, diffusional impedance, *etc.*). A more fundamental and rigorous method of analysis, however, is based on kinetic theory [11-14]. In this approach, the experimentally observed impedance behavior is correlated with that theoretically derived for a proposed reaction mechanism in terms of rate constants and other kinetic parameters. The resultant kinetic variables (R_t, a, m, b, B below) are generally much easier to interpret than their corresponding equivalent circuit elements. In fact, mechanistic significance can always be attributed to all the kinetic variables even though an equivalent circuit cannot always be built from real components. Although the concept of an equivalent circuit is not a necessary part of this kinetic type of analysis, it is usually still useful to adopt a convenient circuit to which mechanistic significance may be attached.

Inductive behavior has been reported over the years in the study of the corrosion behavior of metals [15-23]. This usually arises under conditions of a negative Tafel slope for an anodic reaction and corresponds formally to a negative reaction resistance. An example of this is the passivation of iron oxidation by inhibitors [21]. Inductive behavior, however, is also manifested in processes exhibiting normal positive reaction resistance. This situation is more complex and as of 1991: "The origin of this behavior is difficult to identify, and there is no direct or clear explanation in the literature" [24]. Most commonly this behavior has been attributed to some kind of relaxation in the surface coverage of the electrode by an adsorbed intermediate species following a potential perturbation [16,17,19,23]. By analogy, we can interpret the observed inductive behavior in the Ca^{+2} ion-exchanger membrane through the adsorption kinetics of an analogously adsorbed intermediate species. The impedance for the corresponding proposed mechanism of Ca^{+2} ion transport can subsequently be derived by following related treatments from the corrosion literature [12-14].

4.2.2 Proposed Transport Model

Ion-selective membranes based on liquid ion-exchangers exhibit a strong tendency towards permselectivity. This permselectivity occurs despite the fact that the plasticizer employed typically has a high dielectric constant which leads to a high salt extraction coefficient. For neutral carrier membranes, this would normally be conducive to Donnan failure. For the ion-exchanger membranes, however, good permselectivity results from counterions being attracted by ion-exchange sites and oppositely charged coions being repelled by these sites. Furthermore, large values for the free energy of hydration for divalent cations prevent these species from being extracted as free ions into the liquid ion-exchanger membranes. Morf [25] has thus suggested that the following species predominate within divalent-ion-selective membranes based on negatively charged ligands (R^-) when contacted with aqueous solutions of J^{+2} cations: JR_2, JR^+ and R^-.

In Figure 4.1, a model for the transport of ions through the Ca^{+2} ion-exchanger membrane is proposed which involves these species. In this

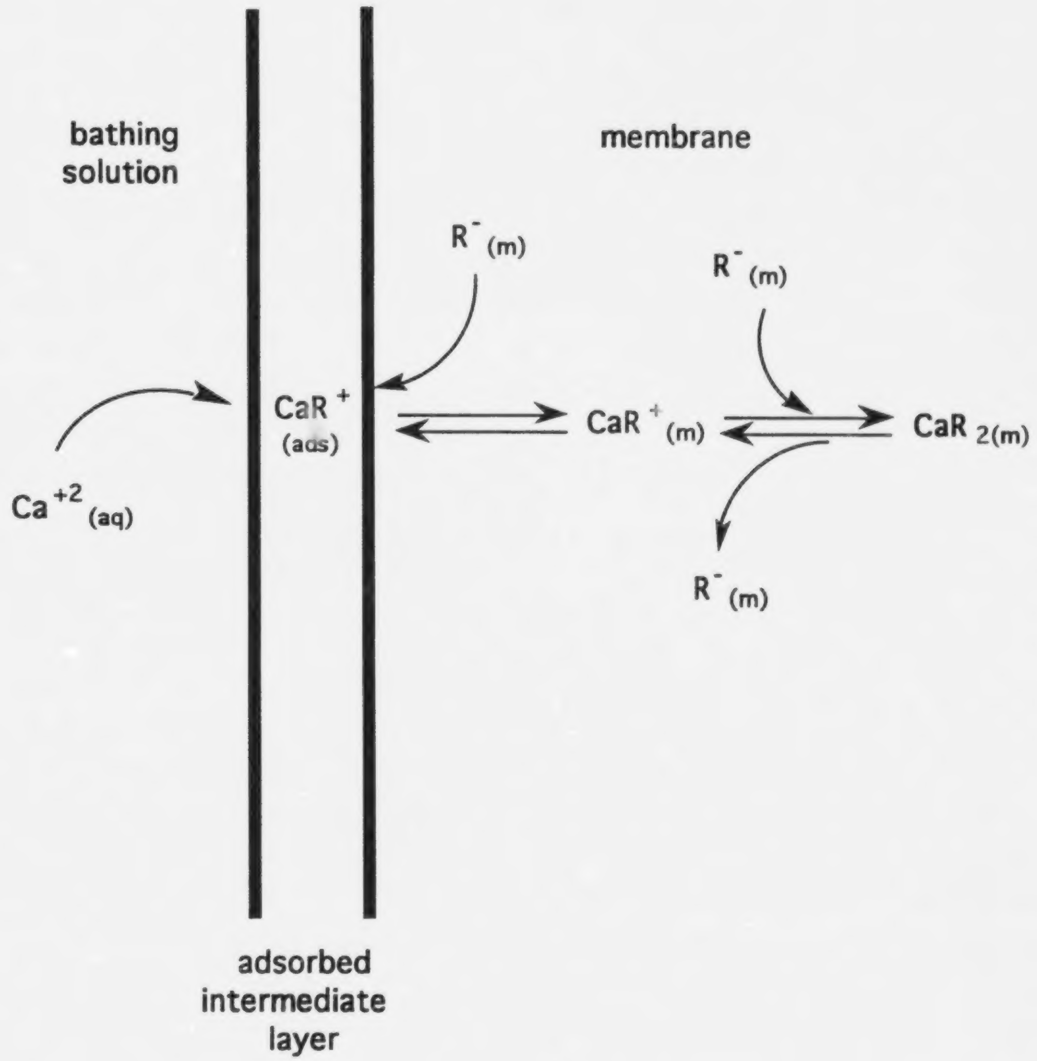
bathing solution
membrane
R⁻ (m)
R⁻ (m)
CaR⁺ (ads)
CaR⁺ (m)
CaR 2(m)
Ca+2 (aq)
R⁻ (m)
adsorbed intermediate layer

Figure 4.1 Proposed model for the transport of Ca^{+2} ions through the membrane (scales exaggerated).

model, transport proceeds via a modified closed-circuit shuttle mechanism [26] involving an adsorbed intermediate at the membrane interface in order to account for the inductive characteristics observed in the impedance spectra. At the entering interface, Ca^{+2} ions enter the membrane in a two-step process:

$$\text{STEP \#1:} \qquad Ca^{+2}_{(aq)} + R^{-}_{(m)} \rightarrow CaR^{+}_{(ads)} \tag{4.1}$$

$$\text{STEP \#2:} \qquad CaR^{+}_{(ads)} \rightarrow CaR^{+}_{(m)} \tag{4.2}$$

where (aq), (m) and (ads) denote the aqueous, membrane and adsorbed phases, respectively. The neutral 1:2 complex can then be formed by a third step:

$$\text{STEP \#3:} \qquad CaR^{+}_{(m)} + R^{-}_{(m)} \rightarrow CaR_{2(m)} \tag{4.3}$$

At the exiting interface, Ca^{+2} ions are liberated from the membrane by the reverse of steps #2 and #1 for the 1:1 complex. For the 1:2 complex, this is preceded by step #3. In the steady-state, free R^- migrates from the exiting to the entering interface with a flux that exactly balances the current carried by CaR^+.

4.2.3 Derivation of the Impedance

In this section, the impedance is derived for a general transport mechanism involving one adsorbed intermediate in which diffusion of the participating species is not rate-limiting [12-14].

We let θ be the fractional surface coverage of the adsorbed intermediate species on the membrane surface, *i.e.* $CaR^+_{(ads)}$. If it is assumed that θ is the only state variable (other than electrode potential) which affects the impedance behavior, then the current in the steady-state will be a function of E and θ:

$$I = f\left(E\,,\theta\right) \tag{4.4}$$

For the *ac* impedance method, a small sinusoidal perturbation of potential at frequency ω/2π is applied across the membrane/solution interface. This applied potential consists of an *ac* component applied on top of a *dc* or steady-state potential:

$$E = E_{ss} + E_{max}\exp(j\omega t) \tag{4.5}$$

where E_{ss} = steady-state potential
E_{max} = amplitude of the sinusoid

This leads to a corresponding perturbation of θ.

$$\theta = \theta_{ss} + \theta_{max}\exp(j\omega t) \tag{4.6}$$

We can define deviations from the steady-state values caused by this *ac* modulation as follows:

$$\Delta E = E - E_{ss} \tag{4.7}$$

$$\Delta I = I - I_{ss} \tag{4.8}$$

$$\Delta \theta = \theta - \theta_{ss} \tag{4.9}$$

For small perturbations from the steady-state, a linearized approximation of the current can be found from a Taylor series expansion [27] of equation (4.4) from the steady-state value:

$$I = I_{ss} + \left(\frac{\partial I}{\partial E}\right)_{\theta}\Delta E + \left(\frac{\partial I}{\partial \theta}\right)_{E}\Delta\theta \tag{4.10}$$

where the second and higher order terms have been neglected and the derivatives are evaluated at the steady-state point. Using vector notation, the admittance of the interface is given by:

$$\vec{Y}_{int} = \frac{\Delta I}{\Delta E} = \frac{1}{R_t} + m\frac{\Delta\theta}{\Delta E} \tag{4.11}$$

where

$$\frac{1}{R_t} = \left(\frac{\partial I}{\partial E}\right)_\theta \qquad m = \left(\frac{\partial I}{\partial \theta}\right)_E$$

The variation rate of θ will also be a function of the related state variables:

$$\frac{d\theta}{dt} = \dot{\theta} = g\left(E, \theta\right) \tag{4.12}$$

For small $\Delta\theta$, a Taylor series expansion can also be given:

$$\frac{d\theta}{dt} = \left(\frac{d\theta}{dt}\right)_{ss} + \left(\frac{\partial\dot{\theta}}{\partial E}\right)_\theta \Delta E + \left(\frac{\partial\dot{\theta}}{\partial\theta}\right)_E \Delta\theta$$

$$\frac{d\theta}{dt} - \left(\frac{d\theta}{dt}\right)_{ss} = \frac{d\Delta\theta}{dt} = b\Delta E - a\Delta\theta \tag{4.13}$$

where

$$b = \left(\frac{\partial\dot{\theta}}{\partial E}\right)_\theta, \qquad a = -\left(\frac{\partial\dot{\theta}}{\partial\theta}\right)_E$$

From equations (4.6) and (4.9),

$$\frac{d\Delta\theta}{dt} = j\omega\theta_{max}\exp\left(j\omega t\right) = j\omega\Delta\theta \tag{4.14}$$

Thus, from equations (4.13) and (4.14),

$$b\Delta E - a\Delta\theta = j\omega\Delta\theta$$

$$\frac{\Delta\theta}{\Delta E} = \frac{b}{a + j\omega} \tag{4.15}$$

And from equations (4.11) and (4.15),

$$\vec{Y}_{int} = \frac{1}{R_t} + \frac{B}{a + j\omega} \tag{4.16}$$

where

$$B = mb = \left(\frac{\partial I}{\partial \theta}\right)_E \left(\frac{\partial \dot{\theta}}{\partial E}\right)_\theta$$

Equation (4.16), therefore, represents a generalized admittance for an interface at which there is an adsorbed intermediate species. The real and imaginary components of the interfacial admittance may be extracted from equation (4.16) as follows:

$$\vec{Y}_{int} \equiv Y'_{int} + jY''_{int} \tag{4.17}$$

$$Y'_{int} = \frac{1}{R_t} + \frac{aB}{a^2 + \omega^2} \tag{4.18}$$

$$Y''_{int} = -\frac{\omega B}{a^2 + \omega^2} \tag{4.19}$$

Since inductive behavior implies $Y''_{int} < 0$, the condition for inductive characteristics must be $B > 0$.

The actual signs of the various kinetic parameters defined above will depend on the signs of their partial derivatives of rates with respect to θ and E. R_t represents the charge transfer resistance of ions across the membrane/solution interface. At constant θ, I will always increase with increasing overpotential. Thus, R_t will always take on a positive value.

For a Langmuir type process, which assumes no interaction between adsorbed sites, the rate of desorption is proportional to θ while the rate of adsorption to (1 - θ). Thus, the rate of a step which produces adsorbate, *e.g.* step #1, will generally decrease as θ increases since the back reaction will be promoted and the forward reaction will be inhibited. With the Temkin and Frumkin models, however, the interactions between adsorbed molecules must be considered. These interactions can be either attractive or repulsive so that the enthalpy of adsorption will depend on θ. Generally, interactions are repulsive or negligible and, as a result, the a-parameter will usually assume a positive value.

The remaining two parameters, m and b, may assume either positive or negative values. Thus, m and b (or more simply B) are sign dependent parameters. Harrington and Conway [13] have shown that equation (4.16) is a general expression which corresponds to a number of different equivalent circuits often reported in the literature. Since all the circuit elements (R, C, L) should naturally be positive, it is suggested that the sign of the B-parameter essentially dictates which of the various possible equivalent circuits should be selected.

For $B < 0$, equation (4.16) may be rewritten as:

$$\vec{Y}_{int} = \left[R_t + \frac{1}{1/R_p + j\omega C_p}\right]^{-1} \tag{4.20}$$

where

$$R_p = \frac{-BR_t^2}{a + BR_t}, \qquad C_p = -\frac{1}{BR_t^2}$$

The equivalent circuit corresponding to this equation is shown in Figure 4.2a. If all the circuit elements are positive then simulations show that the impedance plane plot for this case is restricted to the first quadrant.

For $B > 0$, equation (4.16) may be rewritten as:

$$\vec{Y}_{int} = \frac{1}{R_t} + \frac{1}{R_o + j\omega L_s} \tag{4.21}$$

where

$$R_o = a/B$$
$$L_s = 1/B$$

The equivalent circuit corresponding to this equation is shown in Figure 4.2b. If all the circuit elements are again positive then simulations show that the impedance plane display in this case is restricted to the fourth quadrant.

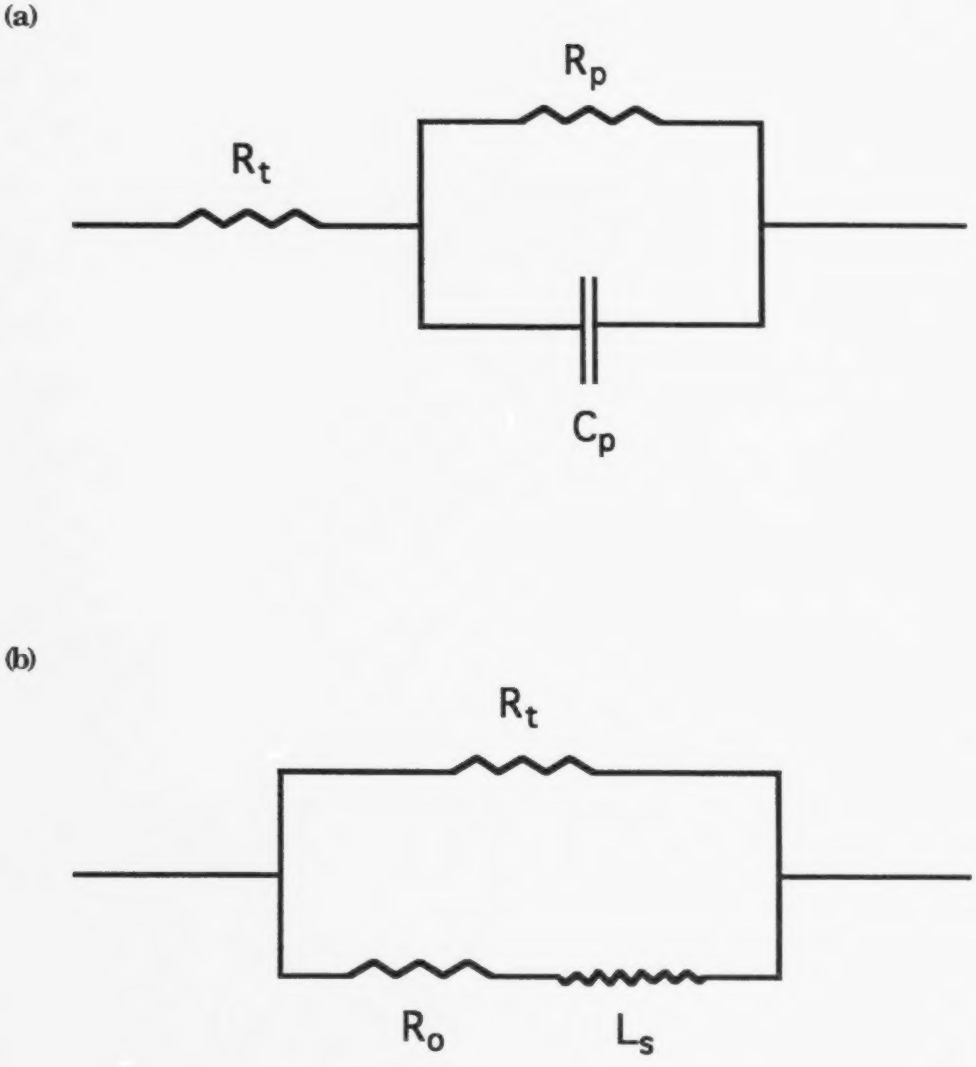
(a)
R_p
R_t
C_p
(b)
R_t
R_o
L_s

Figure 4.2 Equivalent circuits for the interfacial adsorption: (a) $B < 0$ condition, and (b) $B > 0$ condition.

From the preceding analysis, it can be seen that the mathematical condition for an inductive component to be observed in the impedance plane plot is for the kinetic parameters m and b to both act in the same direction, *i.e.* $B > 0$. Physically this implies that the current response to changes in the surface coverage must be in the same direction as the surface coverage relaxation response to changes in the applied potential.

4.2.4 Proposed Overall Membrane Equivalent Circuit

The overall impedance for an actual ISE membrane system must incorporate additional elements for the electrical double-layer and the membrane bulk. If it is assumed that the adsorption of the intermediate species does not alter the charge of the electric double-layer then this simply introduces a parallel double-layer capacitance (C_{dl}). The total interfacial admittance of the membrane can, therefore, be expressed as follows:

$$\vec{Y}_{int(mem)} = j\omega C_{dl} + \vec{Y}_{int} \tag{4.22}$$

Furthermore, the membrane bulk is in series with the membrane interface. Thus, the overall admittance for the entire membrane system is given by:

$$\frac{1}{\vec{Y}_{overall}} = \frac{1}{\vec{Y}_{bulk(mem)}} + \frac{1}{\vec{Y}_{int(mem)}} \tag{4.23}$$

Since the membrane bulk is generally represented as a parallel RC network consisting of a bulk resistance (R_b) and a geometric capacitance (C_g), the final impedance equation proposed for the overall membrane system can be given by:

$$\vec{Z}_{overall} = \frac{1}{\vec{Y}_{overall}} = \left[\frac{1}{R_b} + j\omega C_g\right]^{-1} + \left[j\omega C_{dl} + \frac{1}{R_t} + \frac{1}{R_o + j\omega L_s}\right]^{-1} \tag{4.24}$$

The corresponding equivalent circuit for this overall membrane impedance is shown in Figure 4.3. A diffusional, or Warburg, impedance (W) has also been added to this circuit representation in order to represent resistance to mass transfer.

4.2.5 Impedance Behavior of Proposed Overall Membrane Equivalent Circuit

The easiest method to analyze the impedance characteristics of the proposed overall membrane equivalent circuit, shown in Figure 4.3, is to consider limiting behavior under certain conditions. These limits will include fast and slow kinetics of interfacial adsorption/desorption and high and low frequencies of excitation.

In the limit of very rapid adsorption/desorption kinetics, the surface coverage of the adsorbed intermediate species will remain at a relatively constant and low value. Small changes in E or θ will, therefore, not significantly perturb the variation rate of the surface coverage and small changes in θ will likewise not significantly affect the current response. Thus, the parameters m, a, b, hence B, will all tend to assume relatively small magnitudes. This, in turn, will lead to a very large equivalent circuit value for the inductive circuit component L_s. Since a large inductance represents a large impedance, in this limit the R_oL_s series branch of the membrane equivalent circuit is effectively shorted out by the other circuit elements. Hence, in the limit of fast interfacial kinetics, the overall membrane equivalent circuit reduces to a parallel RC combination of bulk resistance (R_b) and geometric capacitance (C_g) in series with another parallel RC combination of charge transfer resistance (R_t) and double-layer capacitance (C_{dl}). This leads to the familiar double semicircles in the impedance plane plot with the higher frequency arc taken to represent the bulk membrane process and the lower frequency arc representing the charge-transfer process across the membrane/solution interface [28].

In the limit of very slow adsorption/desorption kinetics, however, the inductive component of the membrane equivalent circuit becomes

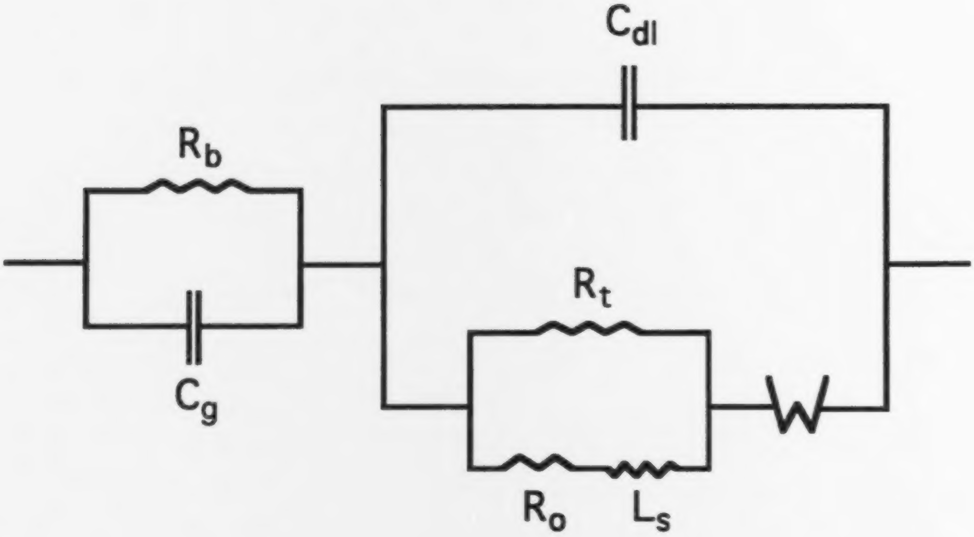
C_{dl}
R_b
R_t
C_g
R_o
L_s

Figure 4.3 Proposed equivalent circuit for the overall ISE membrane system.

important. The relevant constituent elements may be isolated from the rest of the overall membrane circuit and analyzed separately. This results in the simpler equivalent circuit as shown in Figure 4.2b for which the corresponding impedance equation is given by equation (4.21):

$$\vec{Z}_{ads} = \left[\frac{1}{R_t} + \frac{1}{R_o + j\,\omega\,L_s}\right]^{-1} \tag{4.25}$$

This equation may be separated into individual expressions for the real and imaginary components of impedance as follows:

$$Z'_{ads} = \frac{R_t\left[R_o\,(R_o + R_t) + (\omega L_s)^2\right]}{(R_o + R_t)^2 + (\omega L_s)^2} \tag{4.26}$$

$$Z''_{ads} = \frac{-\,\omega R_t^2 L_s}{(R_o + R_t)^2 + (\omega L_s)^2} \tag{4.27}$$

As previously mentioned, computer modelling of these expressions leads to the appearance of another semicircle which lies below the Z' axis in the fourth quadrant. Intercepts on the real axis occur at the frequency limits $\omega = \infty$ and $\omega = 0$ and the diameter of the inductive loop can be calculated as follows:

$$\begin{aligned} \text{loop diameter} &= Z'_{ads}(\infty) - Z'_{ads}(0) \\ &= R_t - \frac{R_t R_o}{R_o + R_t} \\ &= \frac{R_t^2}{R_o + R_t} \end{aligned} \tag{4.28}$$

Furthermore, at an angular frequency of ω_{max} for which Z''_{ads} attains its maximum value:

$$Z'_{ads}(\omega_{max}) = Z'_{ads}(\infty) - \frac{1}{2}\,\text{loop diameter} \tag{4.29}$$

Substituting equations (4.26) and (4.28) into equation (4.29) yields:

$$\frac{R_t\left[R_o\,(R_o + R_t) + (\omega_{max} L_s)^2\right]}{(R_o + R_t)^2 + (\omega_{max} L_s)^2} = R_t - \frac{1}{2}\left(\frac{R_t^2}{R_o + R_t}\right) \tag{4.30}$$

From this relation, ω_{max} may be isolated:

$$\omega_{max} = \frac{R_o + R_t}{L_s} \tag{4.31}$$

These results are summarized in the model impedance plot for the inductive branch of the overall membrane equivalent circuit as shown in Figure 4.4.

When the overall membrane equivalent circuit (Figure 4.3) is considered in the limit of slow interfacial kinetics, the resulting model impedance plot yields three semicircles as shown in Figure 4.5. These correspond to: 1) bulk electrical relaxation, 2) charge transfer kinetics, and 3) surface coverage relaxation. Therefore, the effect of slow interfacial adsorption kinetics has been shown to add a third "surface coverage relaxation" semicircle to the two more familiar bulk and kinetic semicircles in the complex plane. The time constants (τ) for each of these processes may be defined as follows:

$$\tau_b = R_b\, C_g \tag{4.32}$$

$$\tau_k = R_t\, C_{dl} \tag{4.33}$$

$$\tau_r = \frac{L_s}{R_o} \tag{4.34}$$

The physical significance of these various equivalent circuit parameters will be discussed in a later section.

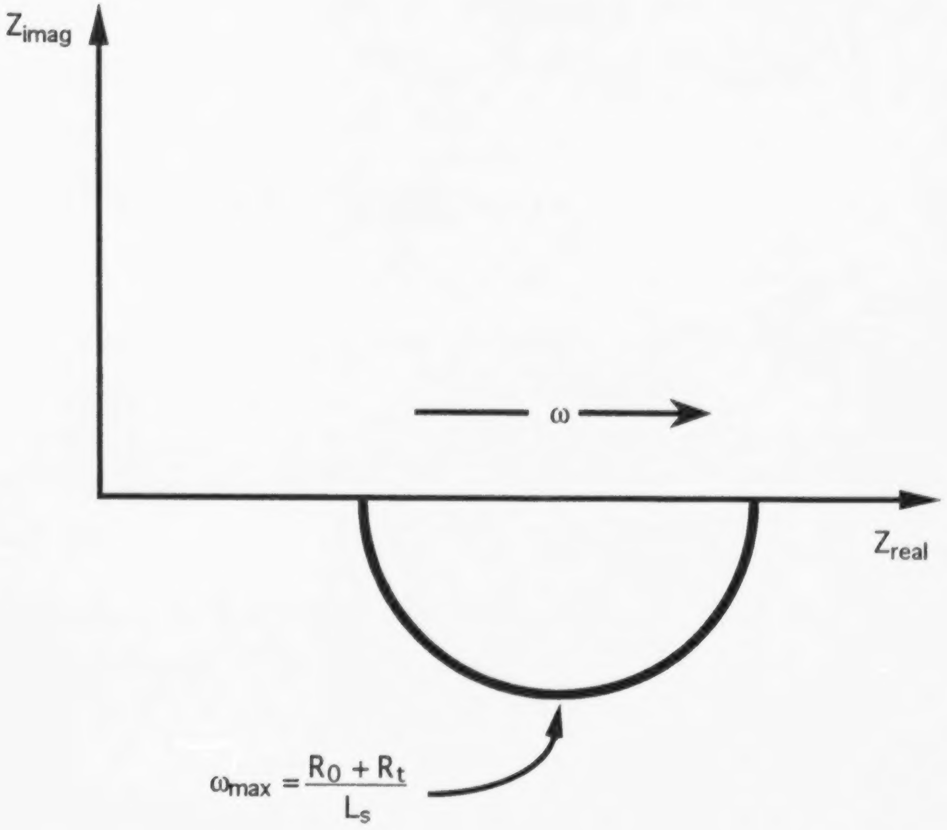

high frequency limit: $Z'' \rightarrow 0,\ Z' \rightarrow R_t$

low frequency limit: $Z'' \rightarrow 0,\ Z' \rightarrow \frac{R_t R_o}{R_o + R_t}$

Figure 4.4 Model impedance plot for the inductive branch of the overall membrane equivalent circuit (*cf.* Figure 4.2b).

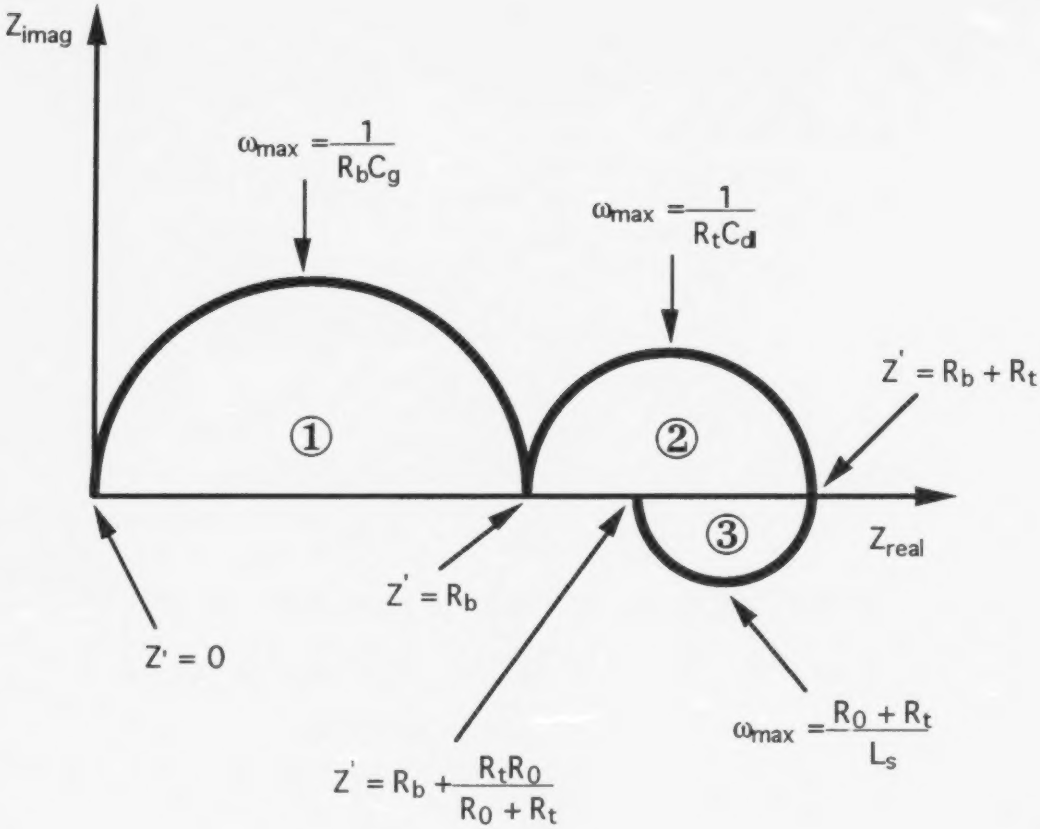
Z_{imag}
$\omega_{max} = \frac{1}{R_b C_g}$
$\omega_{max} = \frac{1}{R_t C_{dl}}$
$Z' = R_b + R_t$
①
②
③
Z_{real}
$Z' = R_b$
$Z' = 0$
$\omega_{max} = \frac{R_0 + R_t}{L_s}$
$Z' = R_b + \frac{R_t R_0}{R_0 + R_t}$

Figure 4.5 Model impedance plot for the overall membrane equivalent circuit (*cf.* Figure 4.3). ① bulk electrical relaxation, ② charge transfer kinetics, and ③ surface coverage relaxation.

4.3 Experimental

Membrane preparation. The Ca^{+2} ion-exchanger ligand di-[4-(2,2-dimethylhexyl)phenyl]phosphate (R^-) was synthesized according to reference 29 by Paul Glavina. Free standing master ISE membranes were fabricated by the method suggested by Craggs *et al* [30]. Freshly distilled tetrahydrofuran (BDH, distilled from potassium) was used as the casting solvent. Compositions of the membranes studied are designated as follows: (1) "normal", 29.5 % poly(vinyl chloride) (PVC) (Polysciences, chromatographic grade), 66 % dioctyl phenylphosphonate (DOPP) (Aldrich, 98 %), 4.5 % CaR_2, and (2) "blank", 34 % PVC, 66 % DOPP.

Calcium-buffering solution. Standard free calcium ion concentrations from 10^{-8} M to 10^{-3} M were obtained by titrating a mixture of calcium-buffering ligands with a calcium solution according to reference [31]. The recommended titrand was composed of $5x10^{-4}$ M ethylene glycol bis(β-aminoethyl ether)-N,N,N',N'-tetraacetic acid (EGTA), $5x10^{-4}$ M N-(2-hydroxyethyl)ethylene-diaminetriacetic acid (HEDTA) (G.F. Smith Chem. Co.), $5x10^{-4}$ M nitrilotriacetic acid (NTA) (Terochem) and $1x10^{-2}$ M tris(hydroxymethyl)aminomethane (Tris) (Terochem), adjusted with hydrochloric acid to pH 7.4. KCl (Mallinckrodt) was added to adjust the ionic strength of the titrand to 0.1 M. The titrant used was 0.02 M $CaCl_2$ (Fisher).

Impedance measurements. Sections of membrane to be studied were cut from a master membrane and mounted between two electrolyte compartments in a specially designed PTFE cell, as previously described in Chapter 3. Identical bathing solutions were then introduced into the two compartments and allowed to equilibrate for at least one hour before measurements. The active membrane area in contact with the bathing solution was 0.32 cm^2 and average membrane thickness was approximately 120 μm as measured according to the procedure previously described in Chapter 3. All electrochemical measurements were done with the cell in a

Faraday cage and thermostatted to 25.0 ± 0.2 °C in a water jacket with a Colora Ultra-Thermostat circulating bath.

High frequency impedance measurements were made by phase-sensitive detection [32]. A 50 mV peak-to-peak pure sine wave was used as the applied voltage oscillation at each frequency measured. The instrument configuration and procedure employed was as described previously by us [8].

Low frequency impedance measurements were made by the fast Fourier transform (FFT) method as described in reference [33]. A PAR Model 273 Potentiostat/Galvanostat used in three electrode configuration provided potentiostatic control and current measurement. A 2048-point waveform consisting of 50 superimposed sine waves of various frequencies was used as the perturbation signal. The amplitude of this FFT waveform was ± 180 mV, unless otherwise noted. The admittance was computed from fast Fourier transformations of the resultant potential and current waveforms from which the real and imaginary components of impedance were obtained. Instrumental phase shifts were compensated by replacement of the electrochemical cell with a resistor (450 kΩ to 10 MΩ) then deconvolution of an instrument response function from the measured response. This function was used to correct all subsequent measurements. Experiment control, data acquisition and subsequent processing were all done with an interfaced IBM PC-XT computer using ASYST (Macmillan) routines written in this laboratory.

Current-voltage curves. Current-voltage (I-V) curves were determined by stepwise increases or reductions of the applied voltage beginning at 0 V and continuing to a maximum of 60 V or beginning at a maximum of 60 V and continuing to a minimum of 0 V. At each voltage, the steady-state current was recorded once it changed by no more than 0.5 % per minute. Voltages were applied with the PAR-273 up to its maximum of 10 V. Higher voltages were then provided by Hewlett-Packard 6216B power supplies in series with the PAR-273. Currents were measured with the current monitor of the PAR-273. Voltages were measured with a

Hewlett-Packard 3478A digital multimeter in parallel with the rest of the circuit.

4.4 Results and Discussion

4.4.1 General Impedance Characteristics

4.4.1.1 Blank *versus* Normal Membranes

An impedance plane plot for a blank Ca^{+2} membrane (DOPP/PVC) soaked in a 1 mM $CaCl_2$ symmetric bathing solution is given in Figure 4.6. A high frequency semicircle associated with bulk characteristics of the membrane system is observed. This is joined on the low frequency side by a 45° line arising from Warburg impedance.

A typical impedance plane plot for a normal Ca^{+2} ion-exchanger membrane, also bathed symmetrically in 1 mM $CaCl_2$, is shown in Figure 4.7. Compared with the blank membrane in Figure 4.6, two significant differences are apparent. The high frequency bulk semicircle exhibits a lower resistance and an inductive behavior is observed in the intermediate frequency region. At low frequencies, Warburg behavior is again demonstrated. A detailed discussion of these impedance characteristics will follow.

4.4.1.2 Bulk Impedance Behavior

The high frequency semicircle corresponds to bulk characteristics of the membrane system, namely the bulk resistance (R_b) and the geometric capacitance (C_g). This behavior has already been well characterized [28]. The observed reduction in bulk resistance upon going from a dummy membrane to a normal Ca^{+2}-sensitive membrane must, therefore, result from the incorporation of the dissociable ion-exchanger ligand $Ca^{+2}(R^-)_2$ into the membrane. This serves to increase the concentration of charge

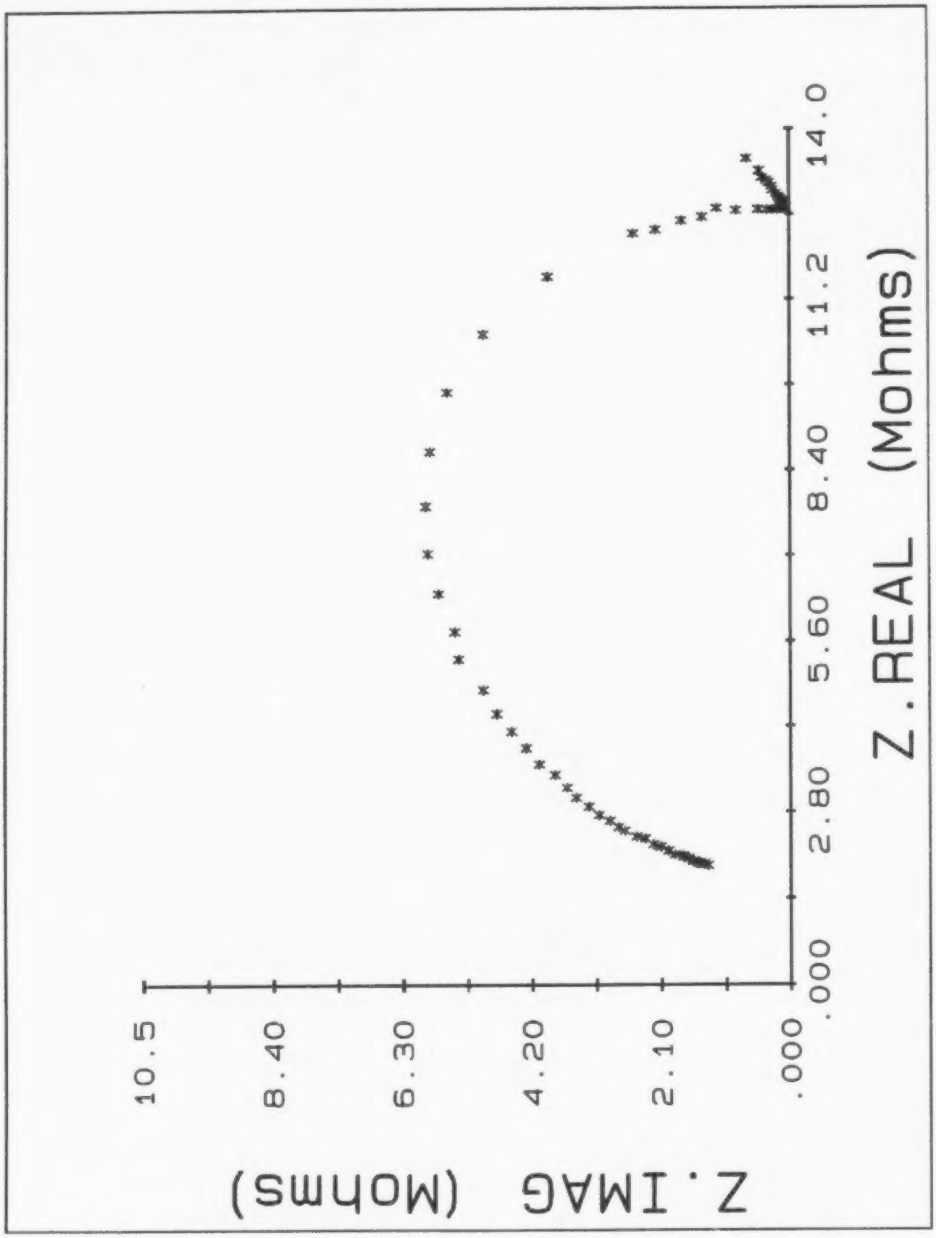

Figure 4.6 Impedance plane plot of a blank Ca^{+2} membrane (DOPP/PVC) in 1 mM $CaCl_2$. Frequency range 2280 Hz to 0.98 mHz. (membrane thickness: 0.133 mm).

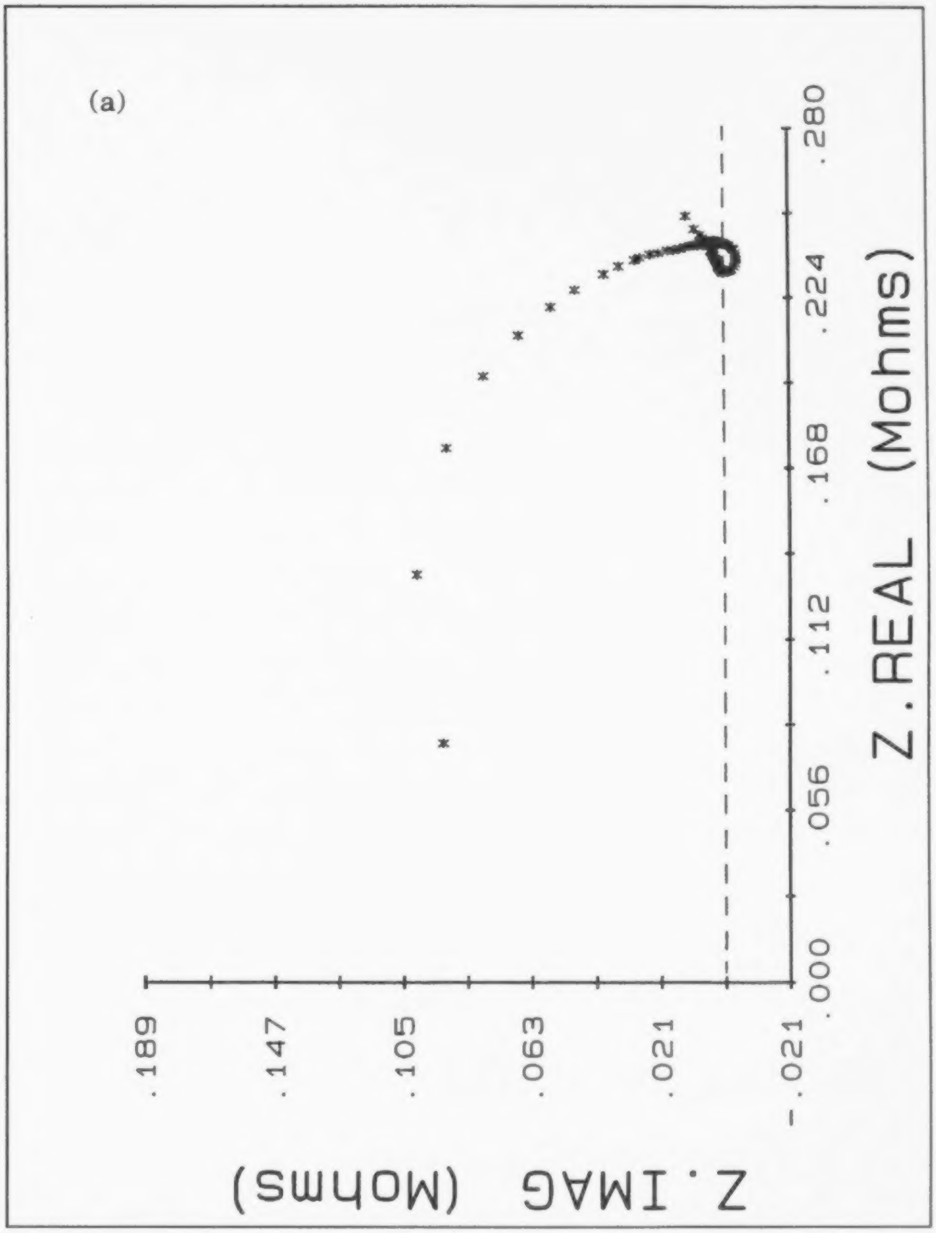

Figure 4.7 Impedance plane plot of a normal Ca^{+2} membrane in 1 mM $CaCl_2$: (a) Frequency range 40 kHz to 0.98 mHz, and (b) frequency range 2280 Hz to 0.98 mHz. (membrane thickness: 0.126 mm).

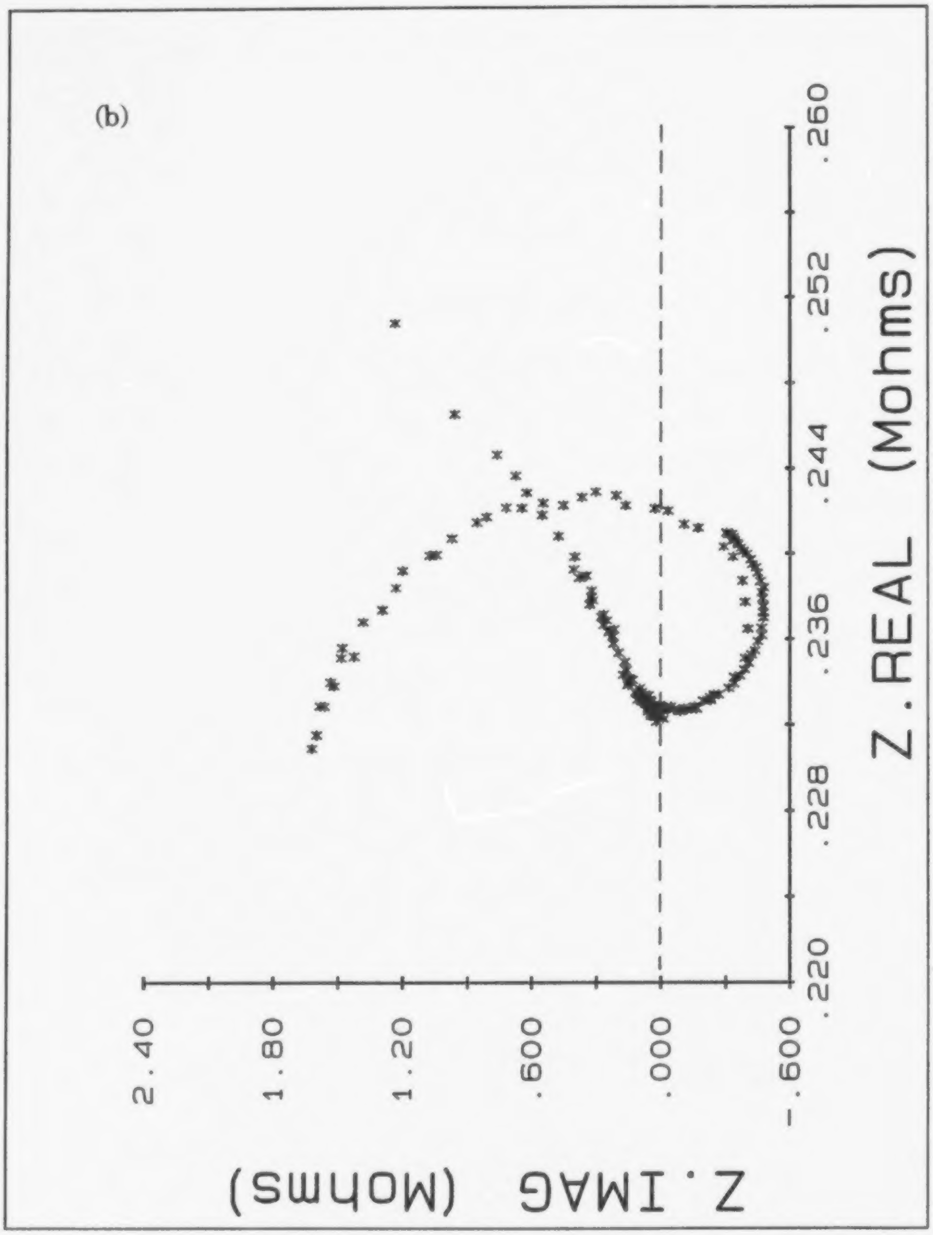

Figure 4.7 Impedance plane plot of a normal Ca^{+2} membrane in 1 mM $CaCl_2$: (a) Frequency range 40 kHz to 0.98 mHz, and (b) frequency range 2280 Hz to 0.98 mHz (continued).

carrying species in the membrane phase which leads to a lower bulk resistance.

4.4.1.3 Warburg Impedance Behavior

Warburg diffusional impedance behavior has been previously reported in other ISE membrane systems. Armstrong [34] observed Warburg impedance for K^+-sensitive membranes at low carrier loadings. This was thought to result from the simple one-step direct exchange of K^+ from the K^+-$val_{(m)}$ complex becoming a two-step process with insufficient valinomycin present. Thus, an initial dissociation of the K^+-$val_{(m)}$ complex was postulated to occur prior to transfer across the membrane interface. The Warburg impedance was consequently attributed to the diffusion of this resulting low concentration intermediate $K^+_{(m)}$ species to the interface. By analogy, we interpret the Warburg behavior in the Ca^{+2} ion-exchanger membrane by an initial dissociation of the $CaR_{2(m)}$ and $CaR^+_{(m)}$ complexes:

$$CaR_{2(m)} \rightarrow CaR^+_{(m)} + R^-_{(m)} \tag{4.35}$$

$$CaR^+_{(m)} \rightarrow Ca^{+2}_{(m)} + R^-_{(m)} \tag{4.36}$$

and a low rate of transport of at least one of these species in the membrane phase. This is then followed by transfer of Ca^{+2} ions across the interface:

$$Ca^{+2}_{(m)} \rightarrow Ca^{+2}_{(aq)} \tag{4.37}$$

As mentioned in the introduction, the concentration of free divalent ions will be very low in the membrane phase. Thus, it is most likely that it is the diffusion of this low concentration $Ca^{+2}_{(m)}$ intermediate to the interface which leads to the observed Warburg diffusion behavior.

For the blank membrane, Warburg behavior can be attributed to diffusion of trapped, mobile anionic sites within the membranes. The origin of these sites is thought to be from the manufacturing process for the polymer [35]. This was also used to interpret Warburg behavior observed for blank dibutyl sebacate (DBS)/PVC membranes [6].

4.4.1.4 Inductive Impedance Behavior

In the intermediate frequency region for the normal Ca^{+2} ion-exchanger membrane, inductive behavior is observed. This is the first time such behavior has ever been reported for an ion-selective membrane. As outlined in the theoretical treatment of the impedance, this inductive behavior can be expected under conditions for which the B kinetic parameter given in equation (4.16) is positive. In this section, the specific proposed transport mechanism, depicted by equations (4.1) - (4.3) as steps #1 - #3, is evaluated with respect to this criterion. This will allow theoretical predictions of the experimental factors which can contribute to the inductive behavior. A subsequent comparison of these predictions with actual experimental observations allows the validity of the proposed mechanism to be evaluated.

The rate of any reaction is given by basic heterogeneous kinetic rate theory. The net rate (v) of a chemical reaction can be expressed as the difference in the rates of the forward and backward processes. In order to introduce the potential dependence on electrode reactions, the Butler-Volmer formulation of electrode kinetics can be utilized [27]. This can be applied to each of the constituent steps of the proposed transport mechanism, except step #3 which should be potential independent since it is just an association reaction. Therefore:

$$\begin{aligned} v_1 &= k_1\,[Ca^{+2}_{(aq)}]\,[R^{-}_{(m)}] - k_{-1}\,\theta \\ &= k_1'\,[Ca^{+2}_{(aq)}]\,[R^{-}_{(m)}]\exp(+\alpha f\Delta E) - k_1'\,\theta\exp(-\beta f\Delta E) \end{aligned} \tag{4.38}$$

$$\begin{aligned} v_2 &= k_2\,\theta - k_{-2}\,[CaR^{+}_{(m)}] \\ &= k_2'\,\theta\exp(+\alpha f\Delta E) - k_2'\,[CaR^{+}_{(m)}]\exp(-\beta f\Delta E) \end{aligned} \tag{4.39}$$

$$v_3 = k_3\,[CaR^{+}_{(m)}]\,[R^{-}_{(m)}] - k_{-3}\,[CaR_{2(m)}] \tag{4.40}$$

where the shorthand notation $f \equiv F/RT$ has been employed and F, R, T are the Faraday constant, gas constant and absolute temperature, respectively. The overpotential, ΔE, has been previously defined according to equation (4.7). The forward and backward rate constants are denoted by k_1, k_2, k_3 and k_{-1}, k_{-2}, k_{-3} , respectively. Primed values refer to the standard rate constant for each step. This is also often referred to as the intrinsic rate constant. Furthermore, it is assumed that these rate constants follow a Tafel-type relation with transfer coefficients α and β, where $\alpha + \beta = 1$. Note that the signs in the exponential terms are opposite to those normally seen. The Butler-Volmer equation is usually written for a faradaic process in which the charge carriers are electrons. As a result, sign reversal is required to maintain consistency with the manner in which ΔE is defined. Thus, if the electrode potential is changed to a more positive value (*i.e.* greater ΔE), then the net rate of charge transport must also increase.

The rate of change in adsorbed intermediate species is controlled by the rate of its formation (step #1) and disappearance (step #2). Hence,

$$\dot{\theta} = v_1 - v_2 \tag{4.41}$$

and

$$\begin{aligned} a &= -\left(\frac{\partial\dot{\theta}}{\partial\theta}\right)_E = -\left[\left(\frac{\partial v_1}{\partial\theta}\right)_E - \left(\frac{\partial v_2}{\partial\theta}\right)_E\right] \\ &= -\left[-k_1^{'}\exp\left(-\beta f\Delta E\right) - k_2^{'}\exp\left(+\alpha f\Delta E\right)\right] > 0 \end{aligned} \tag{4.42}$$

Thus, in this case the a-parameter does indeed assume a positive value.

Current in the ISE system results from ion flow [36]. Every unit of charge transported will lead to the flow of one electron in the external circuit. In step #1, there is a net movement of +1 charge corresponding to the transport of Ca^{+2} ion from the aqueous phase and R^- ion from the membrane phase to the interface region. In step #2, there is also a net movement of +1 charge corresponding to transport of CaR^+ intermediate from the interface region into the membrane phase. Step #3, however, is not current producing since there is no net charge transport between any of the phases. The overall current flow resulting from the proposed transport mechanism is, therefore, given by:

$$I = v_1 + v_2 \tag{4.43}$$

Thus,

$$\begin{aligned} \frac{1}{R_t} &= \left(\frac{\partial I}{\partial E}\right)_\theta = \left(\frac{\partial v_1}{\partial E}\right)_\theta + \left(\frac{\partial v_2}{\partial E}\right)_\theta \\ &= \begin{bmatrix} \alpha f k_1' \ [Ca^{+2}_{(aq)}]\,[R^-_{(m)}] \exp(+\alpha f \Delta E) + \beta f k_1' \,\theta \exp(-\beta f \Delta E) \\ + \alpha f k_2' \ \theta \exp(+\alpha f \Delta E) + \beta f k_2' \,[CaR^+_{(m)}] \exp(-\beta f \Delta E) \end{bmatrix} > 0 \end{aligned} \tag{4.44}$$

and the R_t parameter is indeed also positive.

The remaining two kinetic parameter, m and b, can be evaluated as follows:

$$\begin{aligned} m &= \left(\frac{\partial I}{\partial \theta}\right)_E = \left(\frac{\partial v_1}{\partial \theta}\right)_E + \left(\frac{\partial v_2}{\partial \theta}\right)_E \\ &= \left[-k_1' \exp(-\beta f \Delta E) + k_2' \exp(+\alpha f \Delta E)\right] \end{aligned} \tag{4.45}$$

and

$$\begin{aligned} b &= \left(\frac{\partial \dot{\theta}}{\partial E}\right)_\theta = \left(\frac{\partial v_1}{\partial E}\right)_\theta - \left(\frac{\partial v_2}{\partial E}\right)_\theta \\ &= \begin{bmatrix} \alpha f k_1' \ [Ca^{+2}_{(aq)}]\,[R^-_{(m)}] \exp(+\alpha f \Delta E) + \beta f k_1' \,\theta \exp(-\beta f \Delta E) \\ - \alpha f k_2' \ \theta \exp(+\alpha f \Delta E) - \beta f k_2' \,[CaR^+_{(m)}] \exp(-\beta f \Delta E) \end{bmatrix} \end{aligned} \tag{4.46}$$

From these two equations, it can be seen that the signs of the m and b parameters depend in a complex fashion on the relative magnitudes of various parameters. For a fixed set of experimental conditions, the signs depend only on the relative magnitudes of the adsorption/desorption standard rate constants. If $k_2' >> k_1'$, *i.e.* the adsorption process is rate limiting, then $m > 0$ and $b < 0$. In this case $B \equiv mb < 0$ and inductive behavior results. If $k_2' << k_1'$, *i.e.* the desorption process is rate limiting, then $m < 0$ and $b > 0$. In this case $B \equiv mb < 0$, as well, and inductive behavior also results. In the remaining cases when $k_2' \approx k_1'$, *i.e.* neither adsorption nor desorption are rate limiting, then the actual signs of m and b can be mediated by the overpotential (ΔE) and concentrations of the various reaction species ($Ca^{+2}_{(aq)}$, $R^{-}_{(m)}$ and $CaR^{+}_{(m)}$). Therefore, under these conditions, the existence and magnitude of the inductive feature should be amenable to experimental manipulation.

4.4.2 Equivalent Circuit Analysis

4.4.2.1 Extraction of Equivalent Circuit Elements

Equivalent circuit parameters may be extracted from the experimental membrane impedance plots by analyzing the results according to Figure 4.5. Since the charge transfer semicircle is too small to be resolved from the bulk semicircle, however, equivalent circuit values R_b and R_t for these processes are not readily accessible from the real axis intercepts. But, values for either of these two resistances are required in order to apply the derived equations needed to calculate the remaining circuit element parameters (*vide supra*). In this case, an alternative method of determining R_b or R_t is required.

One method of obtaining a value of R_b is by considering the impedance in the high frequency regime measured by phase-sensitive detection. At sufficiently high frequencies, $\omega > 1/R_bC_g$, the impedance will be dominated by the bulk process and the presence of other processes will not influence the observed impedance. Therefore, by analyzing the observed impedance at high enough frequencies, R_b may be calculated. For a simple bulk RC process, the impedance is given by:

$$Z'_{bulk} = \frac{R_b}{1 + (\omega R_b C_g)^2} \tag{4.47}$$

$$Z''_{bulk} = \frac{\omega R_b^2 C_g}{1 + (\omega R_b C_g)^2} \tag{4.48}$$

Thus, a plot of 1/Z' *versus* ω^2 will provide a straight line having a slope of $R_b C_g^2$ and intercept of $1/R_b$. This allows values for R_b and C_g to be calculated.

From the low frequency impedance measurements made by the FFT method, circuit values for all the remaining elements in the overall membrane equivalent circuit may then be extracted from the relations shown in Figure 4.5. Note that C_{dl} cannot be determined, however, since the second charge-transfer semicircle was not resolved in the impedance plane. Nevertheless, a maximum allowable value for C_{dl} can be calculated on the basis that the time constants for two separate processes must differ by a factor of around ten in order to be resolved [4]. Thus,

$$\frac{\tau_k}{\tau_b} < 10$$

$$R_t\, C_{dl} < 10\,(\, R_b\, C_g\,)$$

$$C_{dl} < \frac{10\,(\, R_b\, C_g\,)}{R_t} \tag{4.49}$$

Extracted values for the equivalent circuit elements of a Ca^{+2} ion-exchanger membrane bathed in symmetric 0.1 M $CaCl_2$ are summarized in Table 4.1.

4.4.2.2 Significance of Equivalent Circuit Elements

In this section, mechanistic significance is attributed to the various equivalent circuit elements (*cf.* Figure 4.3). The physical ramifications of the magnitudes of the various elements will also be considered.

The electrical relaxation time, τ_b, is given by equation (4.32). The resistor R_b represents the membrane bulk resistance and the capacitor C_g

Table 4.1 Equivalent circuit values for a Ca^{+2} ion-exchanger membrane bathed in symmetric 0.1 M $CaCl_2$ bathing solution.

equivalent circuit element	**equivalent circuit value**
R_b	429 kΩ
C_g(a)	16.8 pF
C_{dl}	< 2.4 nF
R_t	30 kΩ
R_o	5.3 kΩ
L_s	10.9 H

(a) Corrected for 4.0 pF instrumental stray capacitance.

represents the geometric capacitance as defined by the membrane dielectric constant [4]. τ_b is typically ≈ 0.3 msec for the blank membrane and ≈ 7 μsec for the normal membrane. Much of this difference can be accounted for by the observed change in the bulk membrane resistance. For example, in Figures 4.6 and 4.7, it can be seen that R_b decreases from ≈ 12.3 MΩ to ≈ 0.24 MΩ between blank and normal membranes of comparable thicknesses. Charge transport in the blank membrane relies solely upon the low concentration of impurity sites [5]. The significantly lower bulk resistance observed for the normal membrane, therefore, suggests that there must be considerable dissociation of the incorporated ion-exchanger salt, CaR_2. The presence of these additional charge carriers also serves to lower the membrane dielectric constant resulting in a decrease in C_g values from ≈ 28 pF to ≈ 17 pF upon going from a blank to a normal membrane.

The kinetic charge transfer time constant, τ_k, is given by equation (4.33). Since a second low frequency semicircle was never resolved from the bulk process, this indicates $\tau_k < 10\ \tau_b$ for both the blank and normal membranes. For the normal Ca^{+2} membrane, $\tau_k < 70$ μsec. This shows that the time constants for these two processes are comparable and difficult to resolve.

This rapid charge transfer observed for the blank DOPP/PVC membranes contrasts with results for other blank membranes plasticized with dibutyl sebacate (DBS), dioctyl sebacate (DOS) or dioctyl adipate (DOA). In the latter membranes, the charge transfer and bulk processes are usually clearly resolved in the impedance plane [6,37]. It is believed that the greater charge density for the DOPP plasticizer facilitates ion-transfer across the membrane interface leading to greater exchange currents and subsequently lower charge transfer resistances. As a result, the charge transfer resistances become too small to measure and are lost in the low frequency part of the bulk resistances. An analogous situation also exists for membranes plasticized with the high dielectric 2-nitrophenyl octyl ether (NPOE) plasticizer [37]. Increases in exchange current can be induced in the blank DBS, DOS or DOA membranes, however, by incorporating an ionophore such as valinomycin [34]. In this case, a very rapid exchange of

K^+ ions now occurs at both interfaces. There is a direct release of K^+ from the $Kval^+$ complex in the membrane phase into the aqueous phase and a corresponding direct crossing of K^+ from the aqueous phase into empty valinomycin molecules in the membrane phase.

An equivalent circuit value for R_t in the normal Ca^{+2}-sensitive membrane is given in Table 4.1. The R_t element is associated with the charge transfer part of the current response which occurs without change in surface coverage. As indicated in the equivalent circuit (Figure 4.3), the current response of this part of the interfacial admittance is purely resistive since the system responds immediately to potential changes if the surface coverage does not have to change. The relatively small magnitude of $\approx 30\ k\Omega$ reported for the R_t circuit element is also in agreement with the interpretation of rapid exchange currents.

The C_{dl} capacitor represents the double-layer capacitance in the membrane at the membrane/solution interface. An absolute value for this element could not be determined since there was insufficient resolution between the τ_k and τ_b time constants, however, an upper limit of $C_{dl} < 2.4$ nF was established. This is significantly smaller than double-layer capacitances typically associated with ISE membranes, especially considering the higher dielectric strength of the DOPP matrix ($\varepsilon_r = 11.9$) compared to DOS or DOA ($\varepsilon_r = 8.2$). For example, $C_{dl} \approx 8.8$ nF for a DOA/PVC matrix [37]. This discrepancy can be rationalized by the adsorption of the CaR^+ intermediate species.

The electric double-layer at an electrode surface may generally be described by a compact (Helmholtz) double-layer in series with a diffuse (Gouy-Chapman) double-layer [27]:

$$\frac{1}{C_{dl}} = \frac{1}{C_H} + \frac{1}{C_{GC}} \tag{4.50}$$

As a result of the relatively low dielectric strength in all these plasticized PVC membranes [37], the concentration of membrane charge carriers will be quite low. Physically, this means that the observed double-layer capacitance approaches that of the diffuse double-layer model. In this case,

$$\frac{1}{C_{dl}} \approx \frac{1}{C_{GC}} \tag{4.51}$$

For the Ca^{+2} ion-exchanger membrane, however, specific adsorption of CaR^{+} intermediate species occurs. This adsorption must take place in the compact double-layer, often at the inner Helmholtz plane. This should introduce an appreciable C_H contribution, and C_{dl} must be instead described using the more complete model given by equation (4.50). If this C_H is of comparable magnitude to C_{GC}, then this can clearly result in a smaller overall C_{dl}. Unfortunately, there is no easy way to determine the relative magnitudes of these two terms.

The relaxation time constant, τ_r, is given by equation (4.34) and is a measure of how rapidly the surface coverage relaxes to its new value after the potential has been changed. The R_0L_s branch in the equivalent circuit is, therefore, associated with that part of the current response which occurs as the surface coverage changes. Unlike the R_t branch, however, the current response for this part of the interfacial admittance is not purely resistive. R_0 is related to the resistance due to relaxation of surface coverage following potential perturbation, while L_s is related to the reciprocal difference in rates for the adsorption and desorption processes. For the normal Ca^{+2} ion-exchanger membrane, $\tau_r \approx 2000$ μsec. This indicates that the adsorption kinetics for this membrane system are extremely slow relative to electrical relaxation ($\tau_b \approx 7.2$ μsec) and charge transfer ($\tau_k < 72$ μsec) processes. It is for this very reason that the adsorption semicircle can be resolved.

4.4.3 Specific Impedance Characteristics

In this section, a number of specific variables are varied in order to observe their effects on the observed impedance behavior. These can then be compared to the predictions based on the kinetic method of analysis of the proposed transport mechanism. For these studies, the FFT impedance method was used exclusively since the low frequency inductive behavior was of primary interest. Unfortunately, this technique is limited to a maximum frequency of about 2.3 kHz (*cf.* Chapter 2) and, therefore, accurate values for R_b will not be able to be extracted. For this reason, the reported impedance behavior is characterized in this section only by the sum (R_b + R_t), as determined by the mid-frequency Z_{real} intercept, and by the diameter of the inductive loop feature. The (R_b + R_t) parameter represents the θ-independent part of the overall impedance and the loop diameter represents the θ-dependent component.

4.4.3.1 Effect of Amplitude of Potential Perturbation

The low frequency impedance measurements are usually carried out in our laboratory using an FFT waveform perturbation with a maximum potential amplitude, ΔE_{max}, of about ± 180 mV. In order to evaluate the effect of the amplitude of this perturbation on the impedance characteristics, ΔE_{max} was varied from ± 1.8 mV to ± 1.8 V in decade steps. The observed impedance behavior at each ΔE_{max} is summarized in Table 4.2. From this data, it appears that the loop diameter decreases drastically at higher amplitudes, but the effect on the (R_b + R_t) parameter does not appear to be as significant.

As ΔE is increased, there is a general decrease observed in the value for the (R_b + R_t) parameter. This effect is not too large, however, since a change of only about 10 % is observed when ΔE_{max} changes by a factor of 1000 from ± 1.8 mV to ± 1800 mV. This suggests that the changes in (R_b + R_t) probably result primarily from changes in the R_t component, since R_t usually represents about 6 % of the (R_b + R_t) total (*cf.* Table 4.1). Conversely, if changes due to the 1000-fold increase in ΔE_{max} were reflected in the R_b component, a proportionately larger effect on the (R_b + R_t) total would be expected.

The kinetic expression for the parameter $1/R_t$ is given by equation (4.44). This clearly shows a dependence on the magnitude of the ΔE variable. Specifically, the prediction is that R_t, and hence (R_b + R_t), should decrease as ΔE is increased. The data in Table 4.2 in fact does demonstrate that there is a modest decrease observed in the value for the

Table 4.2 Effect of amplitude of waveform perturbation on impedance behavior.

ΔE_{max} (± mV)	1 mM $CaCl_2$		0.1 M $CaCl_2$	
	(R_b+R_t) (MΩ)	loop diameter (kΩ)	(R_b+R_t) (MΩ)	loop diameter (kΩ)
1.8	0.234	26.4	0.230	34.5
18	0.234	14.0	0.225	27.6
180	0.224	12.8	0.216	18.4
1800	0.210	0.3	0.197	0.6

total ($R_b + R_t$) parameter as ΔE_{max} is increased. If most of the change in ($R_b + R_t$) is attributed to the R_t component, however, then the effect of ΔE becomes considerable. Assuming that R_b does not change significantly with ΔE and that R_t represents about 10 % of the total ($R_b + R_t$) value at $\Delta E_{max} = \pm 1.8$ mV, then it can be seen that the value of R_t essentially drops to zero by $\Delta E_{max} = \pm 1.8$ V. This considerable effect is not unexpected given the exponential dependence of R_t on ΔE in equation (4.44). The exact theoretical dependence of R_t on ΔE, however, cannot be predicted since values for most of the parameters in equation (4.44) are not readily accessible.

It has been noted that the effect of ΔE on the R_b component of the ($R_b + R_t$) total does not appear to be very significant. Considering that the peak-to-peak amplitude is changed from 3.6 mV to 3.6 V, this suggests that the system must remain within the linear region throughout this range of experimental amplitudes, and that linear expansion of the Taylor series is also appropriate. This result is not surprising, however, since an FFT waveform does indeed subject an electrochemical test system to much less severe perturbations than, for example, a series of simple sine waves. The rms excitation of an FFT waveform is approximately 35% of the peak amplitude while the corresponding rms value for a simple sine wave is approximately 70% of the peak amplitude.

From Table 4.2, it can be seen that the magnitude of the inductive loop is significantly dependent upon ΔE_{max}. As ΔE_{max} is increased the loop diameter rapidly decreases, and at $\Delta E_{max} = \pm 1.8$ V it is barely resolved at all. It can be postulated that perhaps this large effect results from a breakdown in linearity through failure in the Taylor series approximations used in the derivation of the impedance for the proposed reaction mechanism. Linearity, however, was demonstrated at the higher frequencies and frequency does not factor into the Taylor series expansions. Thus, it can be expected that the Taylor series approximation should hold throughout the entire frequency spectrum.

The effect of ΔE on the inductive loop diameter can instead be analyzed according to the kinetic analysis of the proposed transport model. The loop diameter is given by $R_t^2/(R_o+R_t)$ according to equation (4.28). Since

R_t decreases significantly as ΔE is increased, as outlined above, this will tend to decrease the loop diameter. The effect of R_o, however, is not so obvious since this element depends in a complex manner upon ΔE. $R_o \equiv a/mb$ and the a, m and b parameters all depend on ΔE according to equations (4.42), (4.45) and (4.46), respectively. Since numeric values for most of the variables involved are not readily accessible, these effects cannot be properly modelled.

The dependence of ΔE on the inductive behavior can, nevertheless, be qualitatively understood through a consideration of the adsorption-desorption kinetics of the membrane system. Large ΔE potential excursions from the steady-state will be expected to result in large swings in the surface coverage, θ, according to equations (4.5) and (4.6). Consequently, slow adsorption/desorption kinetics will mean that over a given time period, θ will not be able to respond proportionately as ΔE is increased. The relaxation of surface coverage (τ_r) has already been established to be very slow compared to both the bulk electrical relaxation (τ_b) and the charge transfer kinetics (τ_k). In effect, as ΔE increases, the θ-dependent part of the impedance will begin to contribute to a smaller and smaller fraction of the overall impedance, *i.e.* the inductive characteristics gradually disappear.

4.4.3.2 Effect of Bathing Solution Concentration

The impedance data for identical experiments on Ca^{+2} membranes bathed in 1 mM and 0.1 M symmetric $CaCl_2$ solutions are presented in Table 4.2. Two effects are observed upon increasing the bathing solution concentration: ($R_b + R_t$) drops slightly and the size of the inductive loop is increased. These effects may be rationalized by considering the effects of $[Ca^{+2}_{(aq)}]$ on the kinetic parameters.

Values for the bulk resistance of K^+-sensitive membranes based on valinomycin have been shown to decrease with increasing concentration of aqueous KCl [5]. An analogous effect appears to occur in the Ca^{+2} ion-exchanger membrane. From steps #1 and #2 of the proposed transport mechanism, it can be seen that an increase of Ca^{+2} ions in the aqueous phase should contribute to a greater number of membrane charge carriers, $CaR^{+}_{(m)}$. This would subsequently lead to a reduction in R_b and, hence, the value $(R_b + R_t)$. As long as the desorption kinetics of the $CaR^{+}_{(abs)}$ complex do not become rate limiting (Step #2), this dependence of R_b on the bathing solution concentrations will be quite general.

The R_t element also depends on $[Ca^{+2}_{(aq)}]$ as shown by equation (4.44). An increase in the Ca^{+2} ion concentration in the aqueous phase is predicted to lead to a decrease in the charge transfer resistance. This will, therefore, also contribute to the observed decrease in the $(R_b + R_t)$ total with increasing bathing solution concentration. Since the relative changes in the overall $(R_b + R_t)$ values are quite small, it appears that a reduction in R_t is the primary effect of increasing bathing solution concentration.

The effect of bathing solution concentrations on the magnitude of the inductive component of the impedance can also be understood through the kinetic analysis of the proposed transport mechanism. The loop diameter is given by equation (4.28) as $R_t^2/(R_o+R_t)$. As outlined above, R_t depends inversely on $[Ca^{+2}_{(aq)}]$ and this dependence will tend to decrease loop diameters as concentration is increased. The R_o element, however, also depends on $[Ca^{+2}_{(aq)}]$. $R_o \equiv a/mb$ and an examination of equations (4.42), (4.45) and (4.46) will show that only the b-kinetic parameter is directly dependent on $[Ca^{+2}_{(aq)}]$. In fact, as $[Ca^{+2}_{(aq)}]$ is increased, it is predicted that b will also increase. This would serve to decrease R_o and consequently contribute to an increase in the loop diameter through $R_t^2/(R_o+R_t)$. Unfortunately, the exact dependence of the loop diameter on $[Ca^{+2}_{(aq)}]$ cannot be modelled since values for all of the various kinetic parameters defining R_t and R_o are not readily accessible.

4.4.3.3 Surface Active Reagents

During one investigation of the impedance of normal membranes, Ca^{+2} buffered bathing solutions were used. In that study, it was observed that the concentration dependence of the magnitude of the inductive loop disappeared. Loop diameters did not vary by more that 5 % despite a change in free Ca^{+2} concentration of over five orders of magnitude (Table 4.3). This observation can be attributed to the well-known surface active properties of the Ca^{+2} ligands present in the aqueous bathing solution. Apparently, these ligands can adsorb onto the membrane surface and mediate the adsorption/desorption kinetics of Ca^{+2} ions from the bathing solution. These results, therefore, provide additional support that the inductive behavior originates from a surface-related phenomenon.

4.4.3.4 Voltage Effects

4.4.3.4.1 Current-Voltage Curves

Steady-state current-voltage (I-V) curves have previously been used to evaluate ion transport properties of neutral carrier-containing membranes [38]. Three distinct regions are usually observed: low-voltage ohmic, medium-voltage limiting and high-voltage Donnan breakdown. These have been interpreted according to the "closed circuit shuttle" carrier mechanism [39].

I-V curves for symmetrically bathed blank and normal Ca^{+2} ion-exchanger membranes using 1 mM $CaCl_2$ are given in Figure 4.8. The blank membrane, as expected, exhibits only high resistance I-V behavior since it relies upon the presence of membrane-trapped impurities for transport of current. These impurities, believed to originate from the PVC polymer, are present only at low concentrations of typically 0.05 - 5 mM [40]. In contrast, ion-exchanger ligand, $Ca^{+2}(R^-)_2$, is added to the normal composition membrane at a concentration of around 50 mM. Although the ion-exchanger ligand is not expected to fully dissociate, Figure 4.8 demonstrates that a significant reduction in the membrane resistance does occur. This is in agreement with the *ac* impedance measurements (*vide supra*).

Table 4.3 Dependance of inductive loop diameter on [$Ca^{+2}_{(aq)}$] for Ca^{+2} buffered bathing solutions.

[$Ca^{+2}_{(aq)}$] (M)	**inductive loop diameter (kΩ)**
7×10^{-5}	18.6
5.8×10^{-4}	18.0
1×10^{-3}	16.8
2×10^{-2}	17.4
1×10^{-1}	17.4

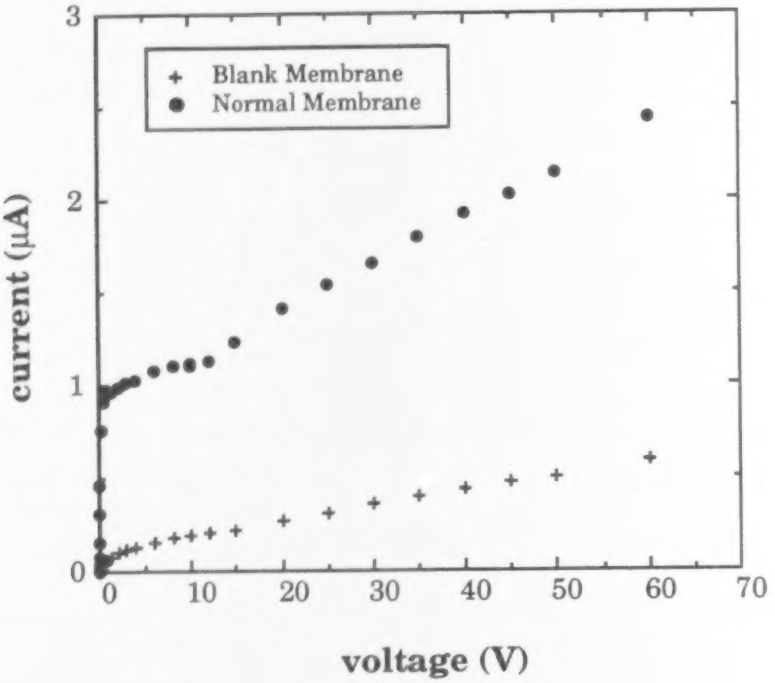

Figure 4.8 Steady-state current-voltage curves in 1 mM $CaCl_2$ bathing solution (+ blank membrane, • normal membrane).

For the normal membrane in the low-voltage region, 0 - 200 mV applied, the I-V curves are perfectly ohmic. This agrees with the bulk *ac* impedance data which was observed to be linear for FFT perturbations up to $\Delta E_{max} = \pm 1.8$ V. In the steady-state of this voltage regime, the current is determined only by the membrane resistance since the R^- flux is able to increase to accommodate increased currents. There is a concentration polarization of the R^- ligand in which the R^- concentration is higher at the interface where Ca^{+2} leaves the membrane and lower at the side where Ca^{+2} enters the membrane, but this polarization is not rate limiting.

Table 4.4 gives *dc* specific resistivities (ρ_{dc}), calculated from the low-voltage ohmic region of I-V curves, as a function of $CaCl_2$ bathing electrolyte concentration. The observed trend in ρ_{dc} is in agreement with ρ_{ac} values, calculated from $(R_b + R_t)$ values from impedance plots. The differences in the absolute magnitudes of the *dc* and *ac* resistivities may be attributed to the significant Warburg impedance behavior present in these membranes. The *dc* point occurs at frequencies much lower than the Z' intercept from which the $(R_b + R_t)$ values are calculated. From Figure 4.7, it can be seen that at these much lower frequencies, high impedances are observed as a result of the Warburg impedance. Thus, ρ_{dc} is generally larger than ρ_{ac}. A difference between ρ_{dc} and ρ_{ac} is also consistent with mobile site behavior [38-39].

As the voltage is increased, the current eventually reaches a limiting plateau region for neutral carrier type membranes [38]. At these voltages, the neutral carrier concentration is believed to be zero at the entering interface and current is then controlled solely by back diffusion of the neutral carrier. The medium-voltage behavior for the Ca^{+2} ion-exchanger membrane, however, is not really flat and is not well-defined for bathing solution concentrations beyond $\approx$ 10 mM $CaCl_2$. In this case back diffusion of free R^- is believed to be compounded by electrical migration of the charged ligand. Since this migration increases as voltage increases, the "plateau" region will no longer be flat. As well, the higher dielectric of the DOPP plasticizer, compared to DOS or DOA for neutral carrier membranes, tends to decrease the window for the "plateau" region through a more rapid onset of Donnan failure.

Table 4.4 *DC* and *AC* specific resistances as a function of bathing solution concentrations.

$[CaCl_2]$ (M)	ρ_{ac} (kΩ•cm)(a)	ρ_{dc} (kΩ•cm)(b)
0.001	6954	7136
0.01		7071
0.1	5793	6475
1		6190

(a) Calculated from (R_b + R_t) values at the high frequency Z_{real} intercepts in the *ac* impedance plane plots.

(b) Calculated from the low-voltage ohmic regions in the I-V plots.

In the high-voltage ohmic region, beyond ≈ 15 V applied, ρ_{dc} decreases dramatically compared to the medium-voltage region. It is believed that at these high applied voltages, field-induced Donnan exclusion failure occurs [39]. This involves loss of cation permselectivity through encroachment and transport of additional ions in the membrane (*e.g.* Cl^-). This Donnan failure is corroborated by the experimental observation that the transparent membranes become opaque after high voltage application. This is consistent with increased light scattering from water droplets which form around hydrophilic impurity sites in rubbers [41]. Also, hysteresis current loops were observed when I-V curves were taken in reverse from high to low voltages immediately after high voltage polarization. These time and scan direction dependences on the I-V behavior are consistent with a modification of membrane compositions through voltage-assisted salt extraction.

4.4.3.4.2 Effect of Electrolysis

It was of interest to examine the effect of polarization on the inductive behavior. Normal membranes were, therefore, electrolyzed at *dc* potentials corresponding to the different voltage regions then subsequently their impedance spectra were recorded as a function of time. The time duration for the initial electrolysis was also varied from between 5 min and 2 hrs. This did not appear to significantly influence the observed results.

Electrolysis at 100 mV, in the low-voltage ohmic region, had no effect whatsoever on the impedance characteristics. Ideal membrane behavior is observed at this low applied potential. The flux of ions required to sustain the current is readily accommodated by the R^- concentration [26].

After the membranes were electrolyzed at higher *dc* potentials, the impedance changed rapidly in the initial few minutes due to rapid re-equilibration. Electrolysis at 6 V, in the medium-voltage region, was observed to initially decrease the magnitude of the inductive loop, but the original magnitude was rapidly restored within ≈ 10 min. It is believed that the R^- concentration profile is tipped very steeply upon electrolysis and a finite amount of time is required for it to return to the steady-state condition [26]. Since inductive behavior depends on $[R^-_{(m)}]$, through the b-parameter according to equation (4.46), this re-equilibration will affect the impedance characteristics.

Electrolysis at 50 V, in the high-voltage Donnan breakdown region, had the most influence on the inductive behavior. The inductive loop disappeared entirely and only reappeared ≈ 45 min after electrolysis. It subsequently required at least 2 hrs for the original impedance to be restored. The injection of charge, which accompanies Donnan failure, must somehow interfere with the processes which contribute to inductive behavior. Once permselectivity is restored, however, the inductive behavior returns. This demonstrates that the possibility of Donnan exclusion failure occurring during *ac* impedance measurements, as suggested by Buck [42], must not be the origin of the observed inductive behavior. This is further supported by the fact that inductance disappears as ΔE is increased to 1.8 V (*vide supra*). Since higher ΔE is more likely to induce Donnan failure, this argues against Donnan failure as the source of the inductance.

4.5 Tendency Towards Inductive Impedance Behavior

Inductive impedance behavior has never been previously reported in any other ISE membrane system. In this section, factors which can contribute to the tendency towards inductive behavior in the impedance plane are assessed through comparisons with the Ca^{+2} ion-exchanger membrane system.

In the present membrane system studied, the analyte ion (Ca^{+2}) is divalent and the ion-exchanger ligand (R^-) is univalent. Direct transport of Ca^{+2} ions across the membrane/solution interface as the neutral CaR_2 species probably does not occur since this requires an unlikely trimolecular reaction at the interface:

$$Ca^{+2}_{(aq)} + R^-_{(m)} + R^-_{(m)} \rightarrow CaR_{2(m)} \qquad (4.52)$$

Instead, the formation of the neutral species most likely involves an intermediate species such as CaR^+ which forms via a bimolecular reaction at the interface:

$$Ca^{+2}_{(aq)} + R^-_{(m)} \rightarrow CaR^+_{(ads)} \tag{4.53}$$

Whether or not this charged interfacial intermediate remains adsorbed at the interface or desorbs depends upon thermodynamic as well as kinetic considerations. If desorption is favored then the formation of the neutral complex proceeds in the membrane phase as follows:

$$CaR^+_{(m)} + R^-_{(m)} \rightarrow CaR_{2(m)} \tag{4.54}$$

Alternatively, if desorption is not favored then the formation of the neutral species involves a second bimolecular reaction at the interface:

$$CaR^+_{(ads)} + R^-_{(m)} \rightarrow CaR_{2(m)} \tag{4.55}$$

In any case, the stoichiometry for this particular ion-exchange process favors the formation of a surface adsorbed intermediate species. Since charged species are involved, this will lead to a potential dependence on the surface coverage of this adsorbed intermediate. As outlined in the theoretical section, this is a basic requirement for inductive behavior.

The presence of an adsorbed charged intermediate species, however, is not a sufficient condition for inductive behavior. It can be argued that finite, albeit low, concentrations of intermediates exist at all ISE interfaces. Thus, for any generic ISE membrane:

$$M^{+z}_{(aq)} + L_{(m)} \rightarrow M^{+z}L_{(ads)} \tag{4.56}$$

where M^{+z} represents the analyte ion and L is the ion-selective carrier (neutral or charged). In the kinetic analysis for the Ca^{+2} ion-exchanger membrane, however, it was demonstrated that inductive behavior may result only if the parameter $B \equiv mb$ is negative. The actual mathematical sign for this B-parameter, however, depends in a complex manner upon a number of variables. These include bathing solution, membrane and surface concentrations of several chemical species as well as standard rate constants. Most of these variables will vary considerably between different membrane systems. Therefore, inductive impedance behavior is not some fundamental characteristic of ISE membranes with adsorbed charged intermediate species.

Additionally, the dependence on the particular overpotential range employed must not be underestimated, as demonstrated in the studies of inductive behavior as a function of ΔE. In fact, a theoretical study on the dependence of electrode overpotential on pseudoinductive behavior of faradaic reactions involving electrosorbed intermediates has recently been reported by Bai and Conway [24]. In that study, theoretically derived three-dimensional ΔE-Z'-Z" complex plane plots were presented and these clearly demonstrate that the magnitude of the inductive semicircle is reduced exponentially with increasing electrode potential, especially at potentials substantially displaced from the equilibrium value. Furthermore, it was concluded that inductive behavior in their model system was manifested only over a narrow potential range. Therefore, even for ISE membrane which kinetically favor inductive behavior, it may be that the overpotentials employed for their impedance studies are not within the region where the surface coverage of the intermediate is changing appreciably. Under these conditions, inductive behavior would never be observed.

Finally, all real electrode systems must include a double-layer capacitance. A theoretical treatment of the proposed transport mechanism was used to establish a criterion for inductive behavior, *viz.* $B > 0$. In this derivation, however, the effect of C_{dl} was not considered. Thus, the $B > 0$ criterion applies if only the contribution of the adsorption process to the interfacial admittance is considered. The unavoidable influence of C_{dl} in any real system, however, is that the impedance behavior resulting from the adsorption process tends to become obscured and the criteria for inductive behavior changes [24].

From equations (4.22) and (4.16), the overall interfacial admittance of the membrane is given by:

$$\vec{Y}_{int(mem)} = j\omega C_{dl} + \frac{1}{R_t} + \frac{B}{a + j\omega} \qquad (4.57)$$

The real and imaginary components of this admittance may be calculated as follows:

$$Y'_{int(mem)} = \frac{1}{R_t} + \frac{aB}{a^2 + \omega^2} \qquad (4.58)$$

$$Y''_{int(mem)} = -\frac{\omega B - \omega C_{dl}\left(a^2 + \omega^2\right)}{a^2 + \omega^2} \qquad (4.59)$$

The condition for inductive behavior (*i.e.* fourth quadrant behavior) is for the imaginary component of admittance to be negative. Thus,

$$B > C_{dl}\left(a^2 + \omega^2\right) \qquad (4.60)$$

This represents the new criterion for the appearance of an inductive behavior in the overall interfacial impedance once the effect of C_{dl} is included.

Values for ω vary considerably in *ac* impedance analyses and they can range from 10^{-4} to 10^6 radians/s. Thus, even if there exists a tendency for inductive behavior in a given system, the time constant (τ_r) for the relaxation process must be large enough that it occurs in the lower ω range. Otherwise, any inductive characteristic will be obscured by the presence of τ_k due to C_{dl}. Once C_{dl} dominates the total interfacial impedance, then inductive behavior may never even be observed at all. Therefore, inductive impedance behavior in actual systems appears possible only at sufficiently low frequencies and small C_{dl}. The relatively small value of C_{dl} observed for the Ca^{+2} ion-exchanger membrane, compared to other ISE membranes, is conducive towards observing inductive impedance behavior.

It has been demonstrated that there are many conditions which must be fulfilled before inductive behavior in an ISE membrane system transpires. Some of these are amenable to experimental control while others are intrinsic. As a result, inductive impedance behavior is not intrinsic to all membrane systems. This is analogous to the charge-transfer impedance whose observation depends on kinetic, concentration and frequency considerations.

4.6 Conclusions

The observed inductive impedance character displayed by the Ca^{+2} ion-exchanger membrane has been successfully attributed to an adsorbed intermediate species using a modified closed-circuit shuttle mechanism. Good correlation was found between theoretical predictions from this model and actual experimental observations. A general analysis of inductive behavior in other ISE membrane systems was also presented.

4.7 References

1. Sluyters, J.H. *Recl. Trav. Chim. Pays-Bas* **1960,** *79,* 1092.
2. Sluyters-Rehbach, M.; Sluyters, J.H. *Electroanal. Chem.* **1970,** *4,* 1.
3. *EG&G PARC Application Note AC-1,* "Basics of AC Impedance Measurements," 1984.
4. Buck, R.P. *Ion-Selective Electrode Rev.* **1982,** *4,* 3.
5. Horvai, G.; Gráf, E.; Tóth, K.; Pungor, E.; Buck, R.P. *Anal. Chem.* **1986,** *58,* 2735.
6. Tóth, K.; Gráf, E.; Horvai, G.; Pungor, E.; Buck, R.P. *Anal. Chem.* **1986,** *58,* 2741.
7. Armstrong, R.D. *Electrochim. Acta* **1987,** *32,* 1549.
8. Li, X.; Verpoorte, E.M.J.; Harrison, D.J. *Anal. Chem.* **1988,** *60,* 493.
9. Harrison, D.J. *J. Electroanal. Chem.* **1990,** *278,* 193.
10. Verpoorte, E.M.J. "Analysis of the Permeability and Behaviour of Dissociable Species in Ion-Selective Membranes", Ph.D. Thesis, University of Alberta, Edmonton, 1990.
11. Armstrong, R.D.; Edmondson, K. *Electrochim. Acta* **1973,** *18,* 937.
12. Armstrong, R.D.; Henderson, M. *J. Electroanal. Chem.* **1972,** *39,* 81.
13. Harrington, D.A.; Conway, B.E. *Electrochim. Acta* **1987,** *32,* 1703.
14. Cao, C.-N. *Electrochim. Acta* **1990,** *35,* 831.
15. Cole, K.S.; Baker, R.F. *J. Gen. Physiol.* **1941,** *24,* 771.
16. Epelboin, I.; Keddam, M. *J. Electrochem. Soc.* **1970,** *117,* 1052.
17. Epelboin, I.; Morel, P.; Takenouti, H. *J. Electrochem. Soc.* **1971,** *118,* 1282.
18. Epelboin, I.; Keddam, M.; Takenouti, H. *J. Appl. Electrochem.* **1972,** *2,* 71.

19. Epelboin, I.; Keddam, M.; Lestrade, J.C. *Faraday Disc. Chem. Soc.*, **1973** *56*, 264.

20. Bressan, J.; Wiart, R. *J. Electroanal. Chem.* **1980**, *107*, 233.

21. Lorenz, W.J.; Mansfeld, F. *Corrosion Sci.* **1981**, *21*, 647.

22. Bai, L.; Conway, B.E. *J. Electrochem. Soc.* **1990**, *137*, 3737.

23. Barcia, O.E.; Mattos, O.R. *Electrochim. Acta* **1990**, *35*, 1601.

24. Bai, L.; Conway, B.E. *J. Electrochem. Soc.* **1991**, *138*, 2897.

25. Morf, W.E. *The Principles of Ion-Selective Electrodes and of Membrane Transport*, Elsevier: New York, 1981.

26. Morf, W.E.; Wuhrmann, P.; Simon, W. *Anal. Chem.* **1976**, *48*, 1031.

27. Bard, A.J.; Faulkner, L.R. *Electrochemical Methods*; John Wiley & Sons: New York, 1980.

28. Linder, E.; Tóth, K.; Pungor, E. *Dynamic Characteristics of Ion-Selective Electrodes*; CRC Press: Boca Raton, 1988.

29. Craggs, A.; Delduca, P.G.; Keil, L.; Key, B.J.; Moody, G.J.; Thomas, J.D.R. *J. Inorg. Nucl. Chem.* **1978**, *40*, 1483.

30. Craggs, A.; Moody, G.J.; Thomas, J.D.R. *J. Chem. Ed.* **1974**, *51*, 541.

31. Otto, M.; May, P.M.; Murray, K.; Thomas, J.D.R. *Anal. Chem.* **1985**, *57*, 1511.

32. MacDonald, D.D. *Transient Techniques in Electrochemistry*, Plenum Press: New York, 1977.

33. Creason, S.C.; Smith, D.E. *J. Electroanal. Chem.* **1972**, *36*, App. 1.

34. Armstrong, R.D.; Lockhart, J.C.; Todd, M. *Electrochim. Acta* **1986**, *31*, 591.

35. van den Berg, A.; van der Wal, P.D.; Skowronska-Ptasinska, M.; Sudhölter, E.J.R.; Reinhoudt, D.N.; Bergveld, P. *Anal. Chem.* **1987**, *59*, 2827.

36. Carmack, G.D.; Freiser, H. *Anal. Chem.* **1975**, *47*, 2249.

37. Appendix C.

38. Iglehart, M.L.; Buck, R.P. *Talanta* **1989**, *36*, 89.

39. Iglehart, M.L.; Buck, R.P.; Pungor, E. *Anal. Chem.* **1988**, *60*, 290.

40. Lindner, E.; Gráf, E.; Niegreisz, Z.; Tóth, K.; Pungor, E.; Buck, R.P. *Anal. Chem.* **1988**, *60*, 295.

41. Thomas, A.G.; Muniandy, K. *Polymer* **1987**, *28*, 408.

42. Stover, F.S.; Buck, R.P. *J. Electroanal. Chem.* **1980**, *107*, 165.

Chapter 5

Carbon-13 Spin-Lattice Relaxation Studies of Ion-Selective Membranes

5.1 Introduction

There have been extensive studies directed towards understanding the fundamental electrical behavior of ion-selective electrode liquid membranes and membrane transport [1-3]. There have not been, however, many studies on the physical characteristics of the bulk membrane system itself, which is typically a polymer matrix. An understanding of the physical and chemical phenomena occurring in these membranes at both the microscopic and molecular level is of great importance to ongoing research on chemical sensors, particularly for systems that are to be integrated with solid state devices [4]. The development of electrochemically based sensors requires new polymeric materials and the modification of present materials to improve sensitivity, chemical selectivity and durability. An increased knowledge of the physical structure and chemical equilibria occurring in polymeric films and membranes used with sensors is needed to guide this effort.

Liquid membranes for ion-selective electrodes (ISEs) are usually fabricated with plasticized polymer matrices [5]. Typical compositions are 33 wt% polymer, 66 wt% plasticizer and 1 wt% ion carrier (ionophore), where the polymer is almost exclusively poly(vinyl chloride) (PVC). The polymer should be an inert matrix that gives structural integrity to the liquid membrane. The plasticizer is normally a low dielectric constant, water-immiscible solvent such as the ester bis(2-ethylhexyl) adipate (DOA) which functions as a solvent for the ion carrier. This contrasts with the traditional function of a plasticizer which according to the ASTM-D-883 definition is a material incorporated in a polymer to increase its workability and flexibility or distensibility [6]. PVC destined for general commercial use is plasticized at a range of levels, but the most common concentration is only around 30 wt% plasticizer [7]. Thus, the ISE membrane is clearly plasticized at an unusually high level; the physical properties of this composition have not been studied extensively.

Optical studies of the PVC/DOA membrane matrix have shown that the behavior of water is very complex. Freely dissolved H_2O is present at very low concentrations, while at higher concentrations phase separation of the water into droplets occurs. This second process is associated with significant changes in the apparent diffusion coefficient of water as a function of concentration, time and position in the membrane. These observations indicate large perturbations are induced by the uptake of water, but it is unclear whether the changes in the measured parameters for water reflect changes in the matrix properties as a whole. Nuclear magnetic resonance (NMR) studies of the membrane matrix components can provide insight into the effect of H_2O on their environment.

It is well-known and understood that molecular motions give rise to relaxation or decay of NMR magnetization [8-10]. NMR relaxation studies have proven to be an important experimental technique for the study of conformational mobilities of polymers by providing a direct probe of molecular motions. The spin-lattice or longitudinal relaxation time T_1 is a time constant used to quantify the first-order rate process of the transfer of energy from the nuclear spin system to its surroundings or lattice. It describes the rate of return of the M_z component of the total magnetization to equilibrium after a perturbation. The measurement of ^{13}C T_1 values on long-chain molecules can be used to provide information on the relationship between the motion of the molecule as a whole and the individual chain segments.

Studies on polymer motions by NMR have focussed largely on pure solid polymer or copolymer blends [11-17]. An NMR relaxation rate study has been reported for tricresyl phosphate plasticized PVC, but only for the more typical plasticization levels from 0 to 40 wt% [18]. Similarly, PVC plasticized with di-isodecyl phthalate at 0 to 17 wt% has been studied and this showed evidence of inhomogeneity in the plasticized material [19]. Studies on the effects of different plasticizers present at 0 to 25 wt% on bisphenol-A-polycarbonate [20] and a glassy polymer blend [21] have also been reported. Simon and coworkers [22] have previously reported T_1 data for *o*-nitrophenyl octyl ether (NPOE) plasticizer in $CDCl_3$, in neat solution and in a "membrane" phase. Molecular motions were not analyzed specifically and only the general conclusion that this "membrane" phase behaved more like a liquid than a solid phase was given. Moreover, these "membrane" phases were actually 32 wt% ionophore, 35 wt% NPOE plasticizer and 33 wt% PVC polymer since these NMR studies were focussed on the coordinating behavior of the ionophore components [22-23]. Clearly, such samples are not representative of the usual ISE membrane composition. Up to now there have been no reported studies of molecular motion at the high plasticization levels used with ISE membranes. A system which can somewhat model the membrane system is found in dilute polymer solutions whereby the solvent may be regarded as the "plasticizer". Obviously this represents an approximation, but the results can be used to interpret the effect of low polymer concentrations on solvent motion. Such studies on solvent-polymer interactions have been reported for poly(ethyl methacrylate) in 50 to 100 wt% chloroform [24] and poly(methyl methacrylate) in 80 to 100 wt% acetone [25].

The majority of the above mentioned studies on molecular motions have focussed on the behavior of the polymer molecules themselves [11-20]. In the present study we have examined both the polymer and plasticizer behavior as a function of DOA and PVC composition, as well as H_2O and salt content. The molecular mobility of the plasticizer molecules can also probe plasticizer-polymer interactions and changes to the membrane as a whole. Such changes may be critical, since the plasticizer also serves as the solvent for the ionic species. Additionally, the plasticizer resonances are easily resolved by a conventional NMR spectrometer at the high plasticization levels associated with these ISE membranes. This obviates the necessity for more sophisticated solid state NMR techniques.

5.2 Experimental Section

Sample preparation. Membrane samples for NMR analysis were prepared by dissolving appropriate amounts of bis(2-ethylhexyl) adipate (DOA) (Fluka, Selectophore grade) and poly(vinyl chloride) (PVC) (Polysciences, chromatographic grade) in 3 mL of freshly distilled tetrahydrofuran (THF) (BDH, distilled from potassium). Potassium tetraphenylborate ($KBPh_4$) was added to this membrane solution as an appropriate aliquot of a $KBPh_4$/THF solution. $KBPh_4$ was prepared by a precipitation method from sodium tetraphenylborate (Terochem) [26]. After stirring for one hour to effect complete dissolution, small aliquots of this casting solution were added to a 5 mm NMR tube. Between each addition the sample tube was dried in a 60 °C oven for 24 hours in order to ensure a uniform casting and complete solvent evaporation. Final dried membranes were about 2 cm in height and 225 mg in weight. Paramagnetic molecular oxygen was then removed from the NMR tube by repeated purging and filling of the interior with argon gas. Exposure of the membrane to aqueous solution was effected by soaking the sample in nanopure H_2O (Barnstead) for several days.

NMR measurements. ^{13}C NMR experiments were performed at ambient temperature, with a probe temperature of about +25 °C, on a Bruker WH-200 spectrometer operating at 50 MHz with complete proton noise decoupling. A ^2D-lock was established using a DOA/$CDCl_3$ sample with tetramethylsilane (TMS) providing the chemical shift reference. Actual membrane samples were then measured with the spectrometer unlocked. Spin-lattice relaxation measurements were made by using a $180°$-τ-$90°$-$5T_1$ inversion-recovery pulse sequence [27]. The peak intensities from sets of spectra representing 10 - 15 values of τ were then used to calculate T_1 from a non-linear least-squares fit to the three-parameter equation suggested by Kowalewski *et al* [28].

5.3 Results

The molecular structure of DOA plasticizer is given in Figure 5.1. As shown, there are two peripheral chain segments (C-5,4,3,2,1 and C-5,7,8) and one central chain segment (C-5,6,9,10,11). These will be referred to as segments 1, 2, and 3, respectively.

A representative fully relaxed ^{13}C NMR spectrum of a 66 % DOA/PVC membrane is shown in Figure 5.2. The chemical shifts, and the corresponding assignments, are presented in Table 5.1 (averaged from three spectra). Carbon assignments for the DOA component were made with the aid of an attached proton test (APT) measurement on neat DOA and reference to spectral tables. (The APT experiment converts ^{13}C NMR spectra into sign information that can be used for multiplicity determinations [29].) Assignment of the PVC resonances were made according to reference 30.

^{13}C spin-lattice relaxation times (T_1) were measured for the neat DOA plasticizer and for a 66 % DOA/PVC membrane. These are presented in Table 5.2 as NT_1 values where N is the number of hydrogens directly attached to the carbon. For nonprotonated carbons, T_1 values are given. NT_1 values for membranes cast at various levels of plasticization were also obtained and representative results for various resonances are given in Figures 5.3 - 5.5. For the DOA component, these values have been normalized by calculating the ratio for the NT_1 value for a particular carbon at a given plasticization level to the NT_1 value for the same carbon in the neat liquid. NT_1 measurements were also made on membranes containing various amounts of $KBPh_4$ before and after exposure to aqueous solutions. Results are summarized in Table 5.3 for 66 % DOA/PVC membranes containing 0, 0.01 and 0.1 wt% $KBPh_4$ where ΔNT_1 refers to the change in NT_1 in going from a dry membrane to the same membrane after equilibration with water. A negative ΔNT_1 indicates a decrease in the NT_1 value. Note that ΔNT_1 data is presented only for the DOA plasticizer resonances. Corresponding data for the effect of water on the PVC polymer resonances are too scattered to be meaningfully interpreted.

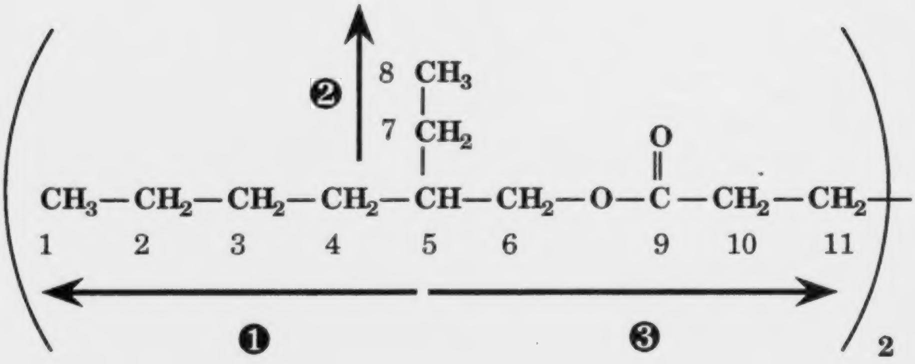

➋
8
CH3
7
CH2
O
CH3—CH2—CH2—CH2—CH—CH2—O—C—CH2—CH2
1
2
3
4
5
6
9
10
11
➊
➌
2

Figure 5.1 Molecular structure of bis(2-ethylhexyl) adipate (DOA) showing peripheral (➊ and ➋) and central chain (➌) segments.

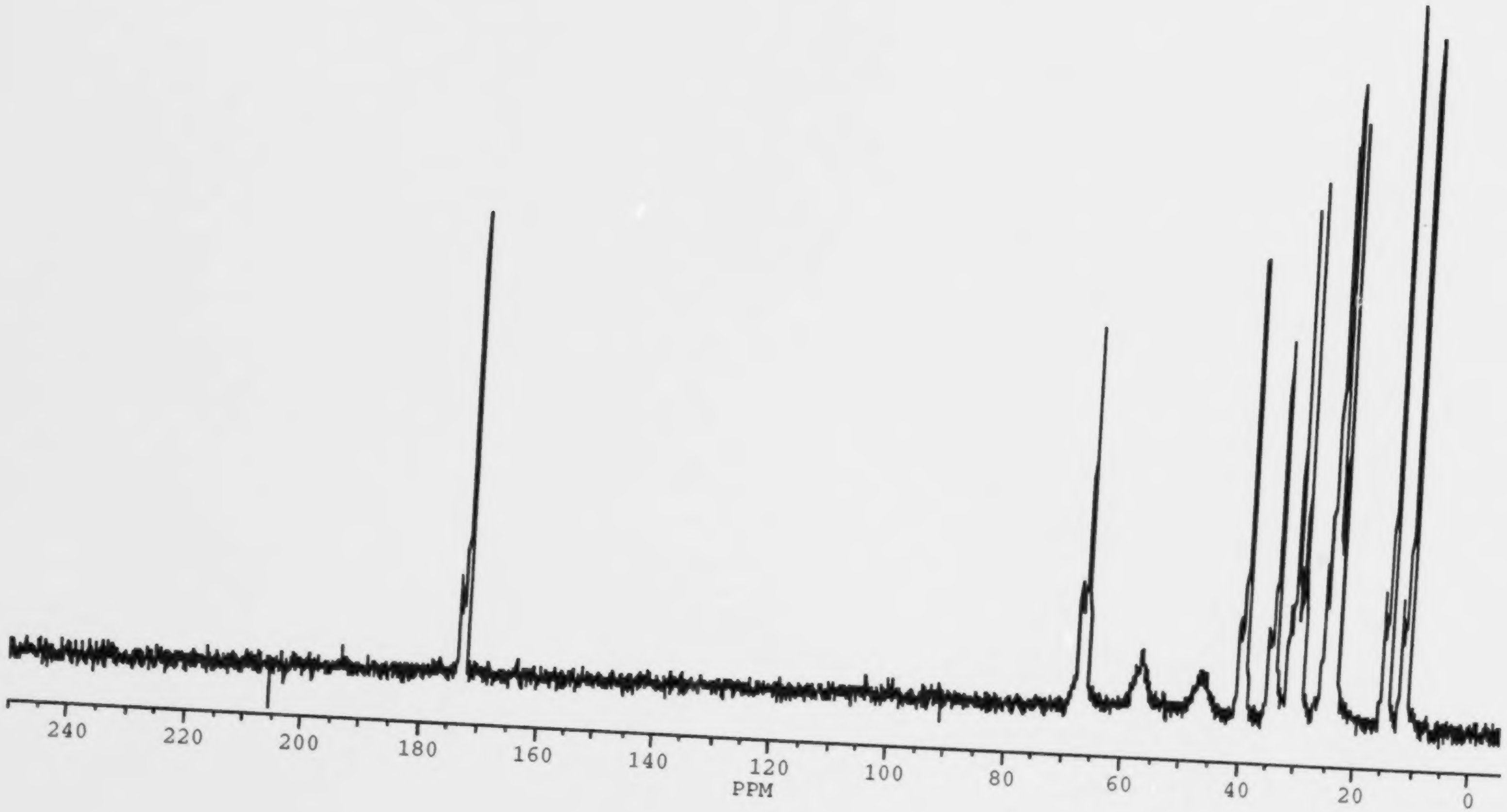

Figure 5.2 Fully relaxed ^{13}C NMR spectrum of a 66 % DOA/PVC membrane.

Table 5.1 ^{13}C NMR chemical shift data for a 66 % DOA/PVC membrane.

δ_c (TMS, external)	assignment
172.3	DOA C-9
66.4	DOA C-6
56.8	PVC CHCl methine
46.6	PVC CH_2 methylene
39.2	DOA C-5
33.9	DOA C-10
30.8	DOA C-11
29.2	DOA C-7
24.7	DOA C-4
24.2	DOA C-3
23.2	DOA C-2
14.1	DOA C-8
11.1	DOA C-1

Table 5.2 ^{13}C NMR spin-lattice relaxation times for neat DOA plasticizer and for a 66% DOA/PVC membrane.

Carbon Resonance	NT$_1$ (sec.)	
	Neat DOA	66% DOA/PVC
DOA C-1	5.79	4.03
DOA C-2	2.54	1.16
DOA C-3 *	1.00	0.69
DOA C-4 *	0.91	0.69
DOA C-5	0.54	0.26
DOA C-6	0.62	0.31
DOA C-7	1.51	0.80
DOA C-8	7.72	5.38
DOA C-9	5.73	2.74
DOA C-10	0.75	0.42
DOA C-11	0.99	0.56
PVC CHCl	-	0.15
PVC CH_2	-	0.14

* Relaxation times not resolved for the DOA/PVC matrix.

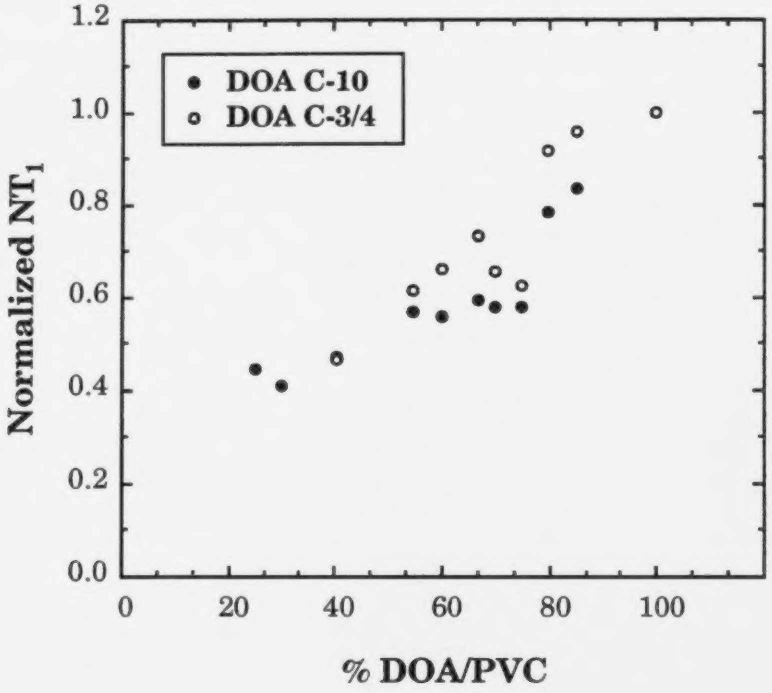

Figure 5.3 Plasticization level dependence of the DOA methylene (C-3/4 and C-10) ^{13}C relaxation times.

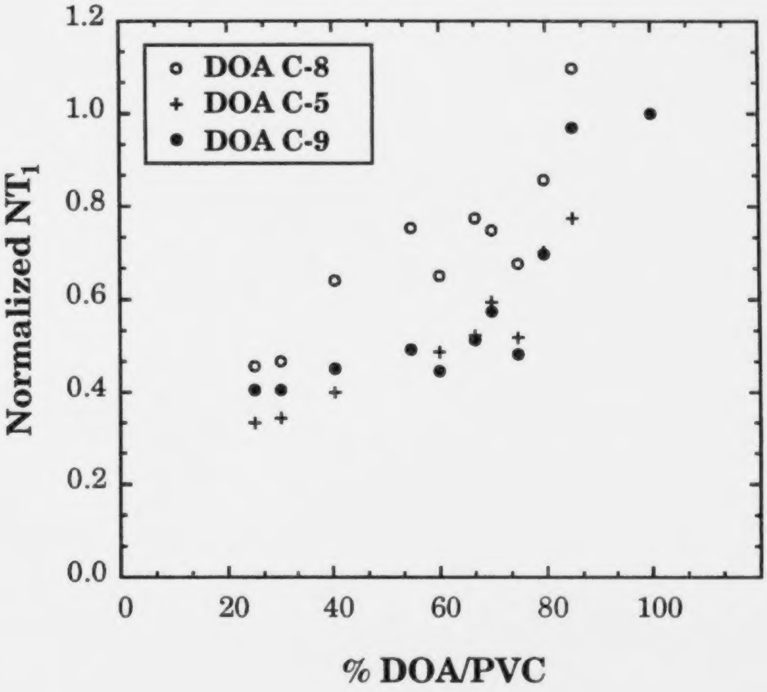

Figure 5.4 Plasticization level dependence of the DOA methyl (C-8), methine (C-5) and carbonyl (C-9) ^{13}C relaxation times.

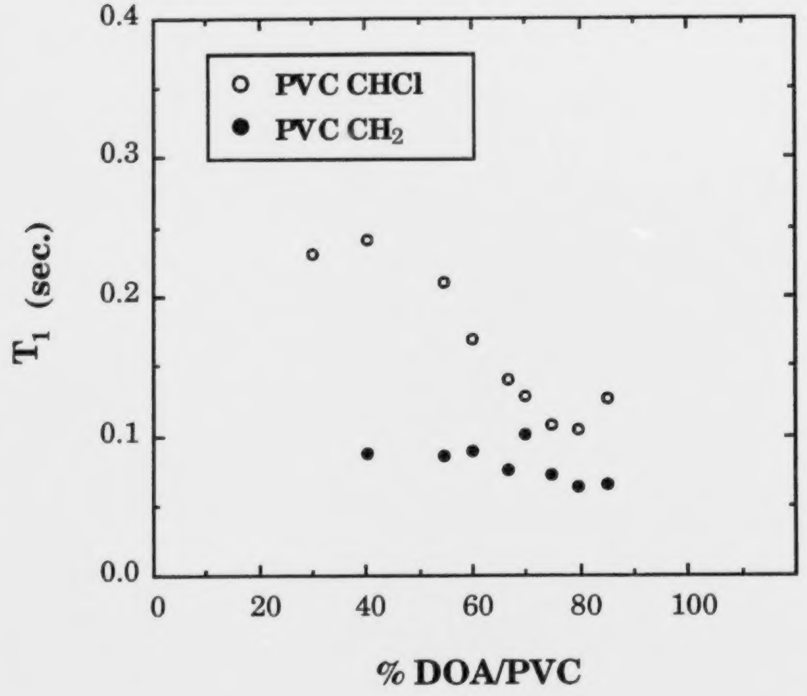

Figure 5.5 Plasticization level dependence of the PVC polymer ^{13}C relaxation times.

Table 5.3 Changes in ^{13}C NMR spin-lattice relaxation times for 66 % DOA/PVC membranes containing $KBPh_4$ equilibrated with water.

DOA carbon	ΔNT_1 (sec.)		
	0 % $KBPh_4$	**0.01 % $KBPh_4$**(a)	**0.1 % $KBPh_4$**
C-1	-0.3 ± 0.1	-1.40	+0.3 ± 0.1
C-2	-0.07 ± 0.04	-0.68	+0.20 ± 0.08
C-3,4(b)	-0.08 ± 0.03	-0.18	+0.06 ± 0.04
C-5	+0.01 ± 0.02	0.00	-0.01 ± 0.02
C-6	+0.01 ± 0.02	0.00	+0.01 ± 0.01
C-7	-0.06 ± 0.03	-0.14	+0.06 ± 0.03
C-8	-0.1 ± 0.2	-1.18	+0.1 ± 0.3
C-9	-0.1 ± 0.4	-0.43	+0.11 ± 0.05
C-10	+0.02 ± 0.05	+0.01	0.00 ± 0.02
C-11	-0.01 ± 0.05	-0.06	+0.03 ± 0.01

(a) Only one 0.01 % $KBPh_4$ sample was studied.

(b) Relaxation times not resolved.

5.4 Discussion

Spin-lattice relaxation only occurs if there is some specific interaction between the nucleus and its environment which results in energy exchange. Nuclei of small magnetic moment such as ^{13}C are relaxed predominantly by intramolecular interaction with nearby nuclei of large magnetogyric ratio such as ^{1}H. This is in fact the main ^{13}C spin-lattice relaxation mechanism, particularly in proton-decoupled ^{13}C NMR experiments [9]. Molecular motions modulate the localized magnetic fields arising from these ^{13}C-^{1}H internuclear dipolar interactions. Molecular motions and interactions can, therefore, be evaluated through interpretation of the T_1 relaxation times.

It is customary to represent molecular motions by correlation times. The correlation times for both tumbling and internal motions correspond to the time intervals required for their respective molecular reorientations. These correlation times are related by the following expression:

$$\tau^{-1} = \tau_c^{-1} + \tau_e^{-1} \tag{5.1}$$

where τ, τ_c and τ_e are the composite, molecular tumbling and internal motion correlation times, respectively [31]. An increase in molecular mobility corresponds to a shorter time period between different molecular rearrangements, and thus a shorter τ value. Conversely, an increase in molecular mobility results in less effective dipolar relaxation and a longer spin-lattice relaxation time. It has been shown that for carbons bearing N protons, NT_1 is approximately inversely proportional to the period between different molecular rearrangements, that is, the composite correlation time, τ [8]. Longer NT_1 values therefore indicate greater conformational mobility, and relaxation times are frequently used as motional parameters [8-9]. Changes in solution viscosity have a significant effect on molecular tumbling, τ_c, and NT_1 tends to be proportional to viscosity when τ_c is the dominant contributor to τ. While τ for small molecules is dominated by τ_c, larger, more flexible molecules show a significant contribution from τ_e [27].

For the latter molecules, changes in internal motion due to molecular conformation are also signalled by changes in NT_1. For these compounds viscosity changes may have a much reduced effect if $\tau_e \gtrsim \tau_c$.

5.4.1 Neat DOA Plasticizer

An examination of the spin-lattice relaxation times for neat DOA presented in Table 5.2 reveals continuous increases in NT_1 values along chain segments 1, 2, and 3. Qualitatively this can be understood in terms of greater motional freedom for carbons near the ends of a chain, such that each carbon has a different effective correlation time. Such localized internal motions along molecular substructures are referred to as segmental motions [8]. The NT_1 minimum observed for the tertiary carbon (C-5) suggests that the segmental motions for the three branches radiate from this point. This interpretation is analogous to that from earlier ^{13}C T_1 measurements of lecithin models for which motion was most restricted near the junction of the alkyl side chains [32-34]. We conclude that the composite correlation time for the tertiary carbon (C-5) in DOA contains the least contribution from the internal motion correlation time, although τ_e may still be greater than τ_c. Conversely, the contribution of internal segmental motions to NT_1 values increases rapidly from this point in all directions.

The quaternary carbonyl (C-9) has a long T_1 value, as expected. This slow dipolar relaxation is a result of the large internuclear distance to the nearest proton on the α-carbon [9]. Relaxation of the carbon nuclei of carbonyls often is dominated by shielding anisotropies, and these effects too can be dependent on molecular motions [10]. The extremely long NT_1 values for the methyl carbons (C-1 and C-8) are due to their free internal rotation, independent of other molecular motions [8].

5.4.2 DOA and PVC Mixtures

To understand the effect on T_1 relaxation times in standard 66 wt% plasticized PVC membranes, a series of plasticization levels was studied. Relaxation times for the plasticizer and polymer were measured for PVC membrane samples with plasticization levels varying from 25 to 100 wt%. The upper limit is neat plasticizer, while the lowest plasticization level studied was determined by the limit of detection and resolution of the solution state NMR spectrometer. The NT_1 data for some representative plasticizer resonances, normalized to the value in neat DOA, are shown in Figures 5.3 - 5.4 as a function of plasticizer content. Figure 5.5 shows the changes in T_1 for the polymer resonances.

The general decrease in NT_1 for all of the plasticizer carbons suggests an increasing restriction in the overall molecular mobility of the DOA. The various local molecular motions expressed by the values of NT_1 reflect a solution's microviscosity. For small molecules, there is a direct proportionality between a decrease in NT_1 values and a decrease in macroscopic shear viscosity [35]. However, for larger molecules and macromolecules the relationship is much weaker. For example, ^{13}C T_1 values for neat 1-octanol are decreased by a factor of only 1.1 when measured in a 10 wt% solution of poly(vinyl pyrrolidone), despite a 1000-fold reduction in viscosity [36]. An analogous result is seen for the DOA/PVC mixtures. The macroscopic viscosity is reduced by over four orders of magnitude between neat DOA (14.4 centipoise (cP)) [37] and a 66 % DOA/PVC membrane (2×10^5 cP) [38]. Within this same interval the NT_1 values for DOA carbons decrease by an average of only 1.6, as shown in Table 5.2.

The relatively weak correlation between DOA NT_1 values and macroscopic viscosities can be attributed to the significant contribution of segmental motions relative to molecular tumbling towards the overall correlation time, τ [27]. In light of equation (5.1), this weak trend indicates that τ_e is definitely greater than τ_c. Viscosity effects that increase molecular tumbling correlation times appear to contribute only a small part to the observed decrease in plasticizer NT_1 values.

The data in Table 5.2 for a 66 % plasticized membrane show a pattern of segmental motion similar to that for neat DOA. Continuous increases in NT_1 along the various chain segments 1 to 3 are in fact seen at all plasticization levels, indicating the segmental motions still originate from the methine (C-5) carbon. Furthermore, the slopes in the plots of normalized NT_1 *versus* % DOA are essentially the same, except for the carbonyl (C-9), so the relative change in NT_1 is the same for each carbon. This indicates there is no strong interaction between the polymer chains and the plasticizer. Strong, specific intermolecular interactions are known to alter the segmental motions of long chain molecules, and to modify their characteristic pattern of spin-lattice relaxations [8]. The data show that specific interactions between DOA and PVC must be weak, if present at all.

The carbonyl carbon (C-9) does exhibit a greater change than the other carbons in the region of high plasticization (75 to 100 % DOA). This may indicate a weak interaction of this polar site with the PVC, however, there is sufficient scatter in the data that this is not conclusive. If there is an interaction it must be sufficiently weak that the overall motion of the DOA is not affected.

The decrease in plasticizer NT_1 values with increasing PVC content can be attributed to increased entrapment of the plasticizer molecule within the polymer matrix. This hindrance would lead to an overall reduction in the motions of the alkyl chains without severely compromising the nature of their characteristic segmental motions. Previously, broadband NMR studies of the spin-spin relaxation time, T_2, and the spin-lattice relaxation time in the rotating frame, $T_{1\rho}$, have been used to characterize some plasticized PVC systems [11,13,18,19,39]. A broadband ^1H NMR T_2 study of dibutyl phthalate (DBP) molecules in plasticized PVC reported by Maklakov *et al* provides a similar interpretation of plasticizer-polymer interactions [39]. Increased DPB correlation times were attributed to increased hindrance at lower concentrations of plasticizer. At room temperature Maklakov *et al* report a single time constant for DPB in PVC, when plasticized with the same mole fraction of DPB as the 60% DOA/PVC mixture. At lower temperatures, or lower plasticizer content, the motion of the plasticizer was reportedly resolved into a slowly and a rapidly relaxing component, suggested to be due to different extents of interaction of DPB with the PVC. However, we do not see any evidence for this at 25 °C for the DOA/PVC compositions studied.

The effect of plasticizer content on NT_1 values provides insight into the spatial homogeneity of the ISE membrane system. The uniform change in relaxation times as plasticizer concentration is varied, shown in Figures 5.3 - 5.4, suggest that the plasticizer is homogeneously distributed throughout the membrane. Any significant segregation of the DOA component would have led to a discontinuous variation in the NT_1 data or to the observation of two time constants. We therefore conclude that there is a homogeneous solution of DOA and PVC components throughout the 25 to 100 wt% plasticization range. The presence of a small density of inhomogeneous regions cannot be ruled out due to the limits of experimental error. In fact, differences in the transparency of ISE membranes seen by visual inspection suggest some regions of inhomogeneity do exist. For significantly lower plasticization levels of 0 to 17 wt% di-isodecyl phthalate in PVC, $T_{1\rho}$ and T_2 relaxation studies indicate heterogeneous mixtures [19]. This difference likely arises from the very limited extent of plasticization in those materials.

The observed T_1 values for the PVC resonances, shown in Figure 5.5, are comparable to literature values of 120 and 140 msec for the CH and CH_2 carbons, respectively, for PVC dissolved in dimethyl-d_6 sulfoxide (DMSO-d_6) at 50 °C [40]. This agreement is reasonable given the differences in solvents, temperatures and concentrations, as well as experimental error. It should be pointed out that both the methine carbon and the methylene carbon, to a smaller extent, have additional sources of relaxation due to dipolar coupling to the ^{35}Cl and ^{37}Cl quadrupolar nuclei. This leads to relaxation by scalar coupling which causes these ^{13}C PVC polymer nuclei to relax relatively fast [9].

Figure 5.5 shows that the PVC T_1 values, particularly for the methylene carbon, are quite insensitive to the amount of DOA present, and hence to the macroscopic viscosity. This behavior has been reported for other polymer systems, and is attributed to segmental motion of the polymer being dominant relative to molecular tumbling [40]. This is analogous to the weak dependence of DOA NT_1 values on changes in the macroviscosity. Since the same segmental motions of the polymer chain should affect the relaxation of the methylene and methine carbons equally, their dependence on plasticizer content should be the same [40]. However, the clear difference in behavior shown in Figure 5.5 indicates specific interactions involving the PVC carbons are present. This is best interpreted in terms of a polar interaction of the more polar CHCl group, since it is this T_1 that is most affected. The effect must be relatively weak since the methylene carbon of the PVC remains unaffected, indicating the characteristic segmental motions of the chain are unchanged. The interaction may be with the ester functionality of the DOA, which would be consistent with the trend in T_1 discussed above for the carbonyl. Alternatively, an increase in polar polymer-polymer interactions as the DOA content decreased could lead to changes in T_1 of the PVC methine carbon.

It must be noted that the inverse relationship between correlation times and T_1 values is valid only in the "extreme narrowing limit" region, where correlation times are very short relative to the reciprocal of the resonance frequency [27,40]. Dipole-dipole interactions must also make the dominant contribution to spin-lattice relaxation. These conditions hold for most ^{13}C nuclei of organic compounds, but they may be violated for highly restricted polymers or polymers in viscous solutions [27]. Measurement of the nuclear Overhauser enhancement (NOE) factors can be used to evaluate the relative contribution of ^{13}C-^{1}H dipole-dipole relaxation mechanism [27] to the overall relaxation process. Unfortunately, for the DOA/PVC system the noise in the polymer resonances prevented determination of their NOE. As a result we cannot be certain that polymer mobility in the DOA/PVC system is within the extreme narrowing limit. However, we note that the

NOE factors for dilute solutions of PVC in DMSO-d_6 indicate dipole-dipole coupling is the dominant relaxation mechanism [40].

5.4.3 Effect of Water Exposure

The variation of NT_1 values when a normal 66 wt% DOA/PVC membrane was soaked in aqueous solution was determined to obtain some insight into the influence of water on these systems. Table 5.3 shows the change in NT_1 (ΔNT_1) observed for membranes following exposure to water for several days. The magnitude of ΔNT_1 is typically less than 10% of NT_1, and this is within the range of precision obtained for T_1 data. However, while the deviation in NT_1 values for a given carbon can be 10% between different runs we found this was a systematic effect. That is, NT_1 for all the carbon nuclei are shifted by about the same amount. Consequently, while the absolute values of ΔNT_1 relative to NT_1 in a dry membrane may not be significant, differences in ΔNT_1 between each of the nuclei may be significant. To improve confidence in the data, multiple measurements on several samples were made. The average values of ΔNT_1 and the absolute standard deviations for each carbon are given in Table 5.3. For all but the fastest relaxing nuclei the relative error is about ± 4 %.

Table 5.3 shows that for membranes without additives there is a decrease in NT_1 for the peripheral carbons in segments 1 and 2 relative to the central carbons in segment 3. The effect is modest but statistically significant. Overall, the characteristic segmental motions continue to diverge from C_5, radiating along the three segments. However, the differences in ΔNT_1 signal some changes in the pattern or amplitudes of these motions. For membranes with the lipophilic salt potassium tetraphenylborate ($KBPh_4$) added at 0.1 wt% to enhance Donnan exclusion, differences in ΔNT_1 are also observed. In this case, though, the peripheral carbon nuclei relax more slowly than the central carbons in segment 3, indicating motion of the periphery is enhanced relative to the centre. For membranes with a lower $KBPh_4$ loading of 0.01 wt%, the trend observed was similar to that with no salt added. However, only one sample was studied and the confidence in the data is lower.

Previous studies have shown that the presence of salt within a polymer increases the uptake and distribution of water [41]. As a result, there is significantly more water absorbed in membranes containing 0.1% $KBPh_4$ than for those containing 0 or 0.01% $KBPh_4$. This is suggested even by a casual visual observation, which reveals a much greater degree of opacity in the 0.1% $KBPh_4$ membranes due to light scattering from internal water droplets. Our optical studies [42] have shown that water exists in at least two states in the membrane, a form freely dissolved in the membrane at very low concentrations, and "droplets" of varying size at higher concentrations. In all of these experiments reported here the water uptake was sufficient to produce "droplets". ^1H and ^2D NMR studies [43] of water uptake in normal 66 wt% DOA/PVC membranes show that the character of the "droplets" changes considerably with the amount of salt in the membrane. Small clusters are believed to be formed when there is little or no salt added, while larger droplets form at higher salt content. These differences in the state of water clearly correlate with the differences in NT_1 behavior upon addition of salt.

Our data show that uptake of water at low membrane salt content decreases the mobility of the periphery of the plasticizer. This corresponds to antiplasticization, or at least to a decrease in the efficiency of DOA as a plasticizer. In contrast the greater water content induced by adding more salt has the opposite affect. Again, only the periphery of the DOA is noticeably affected, but the microviscosity is apparently decreased, leading to greater mobility. Studies of hydrated polymers have suggested that water may act as a plasticizer or antiplasticizer, depending on concentration and temperature [44-45]. A detailed study of the phenomena of antiplasticization by Liu shows clearly that small amounts of di-*n*-butyl phthalate result in decreased local motions of the backbone of glassy bisphenol-A-polycarbonate [46]. Typically, antiplasticizing behavior is observed at low concentrations of diluent in a glassy or crystalline polymer. It is believed to result from improved local packing of the polymer arising from the diluent's role in decreasing the energy barrier to molecular rearrangement. However, the PVC membranes studied here are already strongly plasticized, and polymer interactions are highly disrupted by the plasticizer. Consequently, the antiplasticizing behavior observed more likely arises from a decrease in the efficiency of the plasticizer's action, not from the more classical antiplasticizer action.

It is possible to interpret the changes in NT_1 with water uptake in terms of the free volume theory of plasticization [47]. Robeson [48] demonstrated that the apparent densities of various low molecular weight diluents increased at lower levels of addition in several polymer systems. He concluded that the diluent must initially fill polymer free volume, and this was correlated with the elimination of the secondary low temperature mechanical loss transitions for the polymers. These transitions are generally considered to be due to molecular flexibility of side chain groups and main chain rotations, that is, to segmental motion of the polymer.

For membranes with 0 or 0.01 % $KBPh_4$ added, the small water clusters formed may be associated with filling free volume in the membrane. Since plasticizing action can be interpreted as increasing the free volume this would lead to a decrease in the plasticizer efficiency. Alternatively, the components of the membrane may be forced to order or pack better to accommodate these small water entities. This could also lead to a decrease in free volume and mobility.

For membranes with 0.1 % $KBPh_4$, the increase in mobility due to water uptake can also be understood through free volume considerations. The increased concentration of water in these membranes can eventually begin to create more free volume in the membrane system [47]. Also, the higher concentration of salt introduces additional nucleation sites for the formation of larger water droplets. These would not be as readily accommodated within the membrane phase and, as a result, local order in the membrane would be disrupted. This would again lead to an increase in free volume through swelling the polymer. According to the free volume theory this would lead to increased mobility in the membrane.

We noted earlier that the peripheral motions of DOA are affected by water to a much greater extent than the central carbons. The simplest interpretation of free volume theory would suggest that both molecular tumbling and segmental motions would change as the free volume is changed. Indeed, Figures 5.3 - 5.4 show that changing the amount of plasticizer in the polymer, which should affect free volume, causes uniform changes in mobility for all the DOA carbons. The uptake of water causes relatively small changes in NT_1 values, indicating only a modest change in free volume has occurred. Under such circumstances the segmental motions may be more strongly affected than molecular tumbling, and the periphery may be more sensitive to this subtle effect.

The original lubricity theory for plasticizers, along with more recent clarification [47], provides another interpretation of the observed water behavior. At low concentrations of water, hydrophobic interactions can lead to increased cohesion of the DOA additive to the polymer chains through dipole-dipole interactions. This would result in reduced cooperative main-chain molecular motions [18]. Thus, the presence of water can be thought to increase friction within the membrane system. Since plasticizer and polymer chains would not move as easily, this could lead to the observed decrease in DOA mobility following low water uptake (0 and 0.01 % $KBPh_4$ membranes). At higher water concentrations, the physical separation of the polymer chains by the water would reduce the energy necessary to separate the polymer chains. This would overcome any increased cohesion effects due to H_2O at low concentrations. Thus, the water acts as an internal lubricant to reduce intermolecular friction and facilitate movement of the polymer chains. This would result in the observed increase in DOA mobility (0.1 % $KBPh_4$ membrane). Such behavior for low molecular weight diluents has been noted previously. Belfiore *et al* have reported on the behavior of four diluent molecules that may act as lubricants and reduce interchain interactions in bisphenol-A-polycarbonate, thus allowing for more polymer chain motion [20].

The lubricity theory helps understand the greater sensitivity of the periphery carbon T_1's to the effect of H_2O. The high viscosity in the

DOA/PVC mixtures significantly reduces the contribution of tumbling compared to internal segmental motions towards the overall DOA motion. As a result, lubrication effects should be more pronounced at the molecular periphery, which involves segmental motions, compared to the molecular interior, which involves primarily tumbling motions.

As an alternative to these theories based on plasticizing action, it is possible that the pattern of segmental motions is altered due to direct interactions of DOA and H_2O. Dipole interactions of the ester functionality with H_2O would be the most likely site for this. However, this could be expected to have a larger effect on the carbonyl (C-9) than is observed. Also, it seems likely that the effect on the central fragment relative to the side chains would not differ with the amount of salt present. As a result we do not favor this interpretation, but the evidence is not sufficient to rule it out.

5.5 Conclusions

There do not appear to be strong, specific interactions between the DOA and PVC membrane components throughout the range of plasticization levels studied (25 to 100 wt%). Instead, it appears that entrapment of the plasticizer molecules within the polymer matrix leads to the observed changes in plasticizer motions. Within the plasticization range studied, there also does not appear to be any segregation of the DOA plasticizer. This suggests that the DOA and PVC components are uniformly distributed throughout this ISE membrane system, but, given other evidence available about inhomogeneity, this may simply indicate the method is insensitive to minor components. The particular composition of PVC/plasticizer (~33/66 wt%) used for most ISE compositions exhibits no unique properties in terms of mobility *versus* % plasticizer. A monotonic trend is observed with mobility decreasing as % plasticizer decreases. This contrasts with the conductivity of membranes which shows a non-monotonic dependence on composition [49].

Equilibration of H_2O with the membrane is known to cause significant changes in the apparent rate of its diffusion in the membrane [42]. It is not clear whether this behavior reflects changes in the state of H_2O in the membrane, or more general changes in the membrane itself. This NT_1 study shows that water does affect the properties of the membrane matrix, in particular the mobility of DOA. The changes in relaxation times for the periphery of DOA relative to its central carbons show that H_2O does affect the pattern of segmental motion. The fact that these effects differ with the added salt content of the membrane is significant, since other work has established that added salt affects the distribution of water between various chemical states in the membrane. These results show that water does affect the behavior of other membrane components. The effects on NT_1 indicate that water causes measurable changes in segmental mobilities, but these are not large compared to the overall molecular mobility. Consequently, water uptake does not strongly perturb the microviscosity of the membrane matrix.

5.6 References

1. Morf, W.E. *The Principles of Ion-Selective Electrodes and of Membrane Transport*; Elsevier: New York, 1981.

2. Morf, W.E.; Simon, W. *Helv. Chim. Acta* **1986**, *69*, 1120.

3. Armstrong, R.D.; Horvai, G. *Electrochim. Acta* **1990**, *35*, 1.

4. Janata, J.; Huber, R.J. (editors) *Solid State Chemical Sensors*; Academic Press: Orlando, Fl., 1985.

5. Band, D.M.; Kratochvil, J.; Treasure, T. *Proc. Physiol. Soc.* **1976**, *265*, 5P.

6. ASTM D-883 Plastics Nomenclature, *1966 Book of ASTM Standards*, Part 27; Philadelphia, 1966.

7. Bolker, H.I. *Natural and Synthetic Polymers*; Marcel Dekker: New York, 1974.

8. Breitmaier, E.; Spohn, K.-H.; Berger, S. *Angew. Chem. Internat. Edit.* **1975**, *14*, 144.

9. Breitmaier, E.; Voelter,W. *Carbon-13 NMR Spectroscopy, 3rd ed.*; VCH Publishers: New York, 1987.

10. Kalinowski, H.-O.; Berger, S.; Braun, S. *Carbon-13 NMR Spectroscopy*; Becconsall, J.K., Trans.; John Wiley & Sons: Toronto, 1988.

11. Sefcik, M.D.; Schaefer, J. *J. Polym. Sci. Polym. Phys. Ed.* **1983,** *21*, 1055.

12. Schaefer, J.; Stejskal, E.O.; Buchdahl, R. *Macromolecules* **1977**, *10*, 384.

13. Sefcik, M.D.; Schaefer, J.; Stejskal, E.O.; McKay, R.A. *Macromolecules* **1980**, *13*, 1132.

14. Jelinski, L.W.; Schilling, F.C.; Bovey, F.A. *Macromolecules* **1981**,*14*, 581.

15. Menger, E.M.; Veeman, W.S.; de Boer, E. *Macromolecules* **1982**, *15*, 1406.

16. Albert, B.; Jerome, R.; Teyssie, P.; Smyth, G.; Boyle, N.G.; McBrierty, V.J. *Macromolecules* **1985**, *18*, 388.

17. Boyle, N.G.; McBrierty, V.J.; Eisenberg, A. *Macromolecules* **1983**, *16*, 80.

18. Sefcik, M.D.; Schaefer, J.; May, F.L.; Raucher, D.; Dub, S.M. *J. Polym. Sci. Polym. Phys. Ed.* **1983**, *21*, 1041.

19. McBrierty, V.J. *Faraday Discuss. R. Soc. Chem.* **1980**, *68*, 78 .

20. Belfiore, L.A.; Henrichs, P.M.; Massa, D.J.; Zumbulyadis, N.; Rothwell, W.P.; Cooper, S.L. *Macromolecules* **1983**, *16*, 1744 .

21. Kambour, R.P.; Kelly, J.M.; McKinley, B.J.; Cauley, B.J.; Inglefield, P.T.; Jones, A.A. *Macromolecules* **1988**, *21*, 2937.

22. Büchi, R.; Pretsch, E.; Simon, W. *Helv. Chim. Acta* **1976**, *59*, 2327.

23. Büchi, R.; Pretsch, E.; Simon, W. *Tetrahedron Letters* **1976**, *20*, 1709.

24. Hedlund, L.J.; Riddle, R.M.; Miller, W.G. *ACS Symp. Ser. (C-13 NMR in Polym. Sci.)* **1979**, *103*, 143.

25. Heatley, F.; Scrivens, J.H. *Polymer* **1975**, *16*, 489.

26. Bassett, J.; Denney, R.C.; Jeffery, G.H.; Mendham, J. *Vogel's Textbook of Quantitative Inorganic Analysis, 4th ed.*; Longman: London, 1978.

27. Levy, G.C. *Acc. Chem. Res.* **1973**, *6*, 161.

28. Kowalewski, J.; Levy, G.C.; Johnson, L.F.; Palmer, L. *J. Magn. Reson.* **1977**, *26*, 533.

29. Patt, S.L.; Shoolery, J.N. *J. Magn. Reson.* **1982**, *46*, 535.

30. Komoroski, R.A. *J. Polym Sci. Polym. Phys. Ed.* **1983**, *21*, 1569.

31. Bull, L.M.; Gillies, D.G.; Matthews, S.J.; Sutcliffe, L.H.; Williams, A.J. *Magn. Reson. Chem.* **1991**, *29*, 273.

32. Metcalfe, J.C.; Birdsall, N.J.M.; Feeney, J.; Lee, A.G.; Levine, Y.K.; Partington, P. *Nature* **1971**, *233*, 199.

33. Levine, Y.K.; Birdsall, N.J.M.; Lee, A.G.; Metcalfe, J.C. *Biochemistry* **1972**, *11*, 1416.

34. Lee, A.G.; Birdsall, N.J.M.; Metcalfe, J.C. *Chem. Brit.* **1973**, *9*, 116.

35. Wright, D.A.; Axelson, D.E.; Levy, G.C. *Top. Carbon-13 NMR Spectrosc.* **1979**, *3*, 103.

36. Lyerla, J.R.; Levy, G.C. *Top. Carbon-13 NMR Spectrosc.* **1974**, *1*, 79.

37. Oesch, U.; Simon, W. *Anal. Chem.* **1980**, *52*, 692.

38. Unpublished data, personal communication, Kavassalis, T.; Xerox Research Centre of Canada, Mississauga, Ontario.

39. Maklakov, A.I.; Maklakov, A.A.; Temnikov, A.N.; Teplov, B.F. *Polymer Sci. USSR* **1979**, *20*, 1492.

40. Inoue, Y.; Nishioka, A.; Chujo, R. *J. Polym. Sci. Polym. Phys. Ed.* **1973**, *11*, 2237.

41. Southern, E.; Thomas, A.G. *ACS Symp. Ser. (Water Polym.)* **1980**, *127*, 375.

42. Li., X; Petrovic, S; Harrison, D.J. *Sensors and Actuators* **1990**, *B1*, 275.

43. Chan, A.D.C.; Harrison, D.J., in preparation.

44. Starkweather, H.W. Jr. *ACS Symp. Ser. (Water Polym.)* **1980**, *127*, 433.

45. Moy, P.; Karasz, F.E. *ACS Symp. Ser. (Water Polym.)* **1980**, *127*, 505.

46. Liu, Y.; Roy, A.K.; Jones, A.A.; Inglefield, P.T.; Ogden, P. *Macromolecules* **1990**, *23*, 968.

47. Sears, J.K; Darby, J.R. In *Encyclopedia of PVC*, 2nd ed., Vol. 1; Nass, L.I., Heiberger, C.A., Eds.; Marcel Dekker: New York, 1986.

48. Robeson, L.M. *Polym. Eng. Sci.* **1969**, *9*, 277.

49. Armstrong, R.D.; Covington, A.K.; Proud, W.G. *J. Electroanal. Chem.* **1988**, *257*, 155.

Chapter 6

An Investigation of Water Absorbed Inside an Ion-Selective Membrane

6.1 Introduction

Neutral carriers (ionophores) are uncharged, hydrophobic complexing agents which form the basis of a class of liquid membrane ion-sensitive electrodes (ISEs). Typical compositions of these membranes are 66 wt% plasticizer, 33 wt% polymer and 1 wt% neutral carrier. The plasticizer functions as a low dielectric constant solvent for the neutral carrier and is typically a water-immiscible ester such as bis(2-ethylhexyl) adipate (DOA). The polymer is almost exclusively poly(vinyl chloride) (PVC) and this simply provides structural integrity to the liquid membrane. Various lipophilic salts, such as potassium tetraphenylborate ($KBPh_4$), are also often added at 0.01 wt% in order to enhance Donnan exclusion [1]. Over the years, considerable effort has been directed towards elucidating the operation of these devices, particularly with regards to the development of membrane potentials [2-4]. Water is known to play an important role, however, the behavior and distribution of water in these liquid membranes has not been extensively examined.

In any study of water in polymers, there is always the difficulty of characterizing the different types of water which may be present. Most of the earlier literature has distinguished two different states, described variously as "bound" or "imbibed" or "associated" and "bulk" or "free". The first state ("bound" water) is that water in the vicinity of a macromolecule which manifests thermodynamic properties essentially different from those observed in the second more normal "bulk" state. These properties include vapor pressure, melting point, boiling point, and hence partial molar free energy, enthalpy, entropy, heat capacity and volume [5]. There likely is no sharp physical division, however, which separates "bound" from "bulk" water. Rather, a range of states likely exists from the most tightly bound to free, bulk-like water. This purely operational definition is a problem, however, since each measurement technique determines a different physical property of the system and these may not always be interrelated. Furthermore, the time-scales associated with many measurements may be very long compared to the times for molecular motion. In this case, some measurements may only provide an average value for all types of water in the system. Clearly, a more refined definition of the state of water must include considerations of actual molecular organization.

Water which is miscible in another medium (*e.g.* ethyl alcohol) is molecularly dispersed and can be categorized as "dissolved" water. If the water is specifically associated to another molecule then this can be described as "bound" water. Examples of these include waters of hydration and water H-bonded to a polar functionality. Since "dissolved" or "bound" water will not freeze, these states will give rise to the so-called "non-freezable" states of water.

If the physical state is such that water molecules tend to favor the vicinity of other water molecules then they will aggregate. This type of water will be "freezable" since freezing and melting transitions are cooperative phenomena. Large quantities of water, on the order of one mole of molecules, will definitely aggregate and this form of water is usually termed "bulk" water. "Bulk" water will obviously exhibit all the usual properties of normal water. It is also possible to induce freezing and melting for much smaller aggregates of water molecules (*e.g.* fine droplets in aerosols and emulsions of water in oils), but these will often exhibit properties that are significantly modified from normal "bulk" water [6].

Freezable water that can be distinguished from "bulk" water is often referred to as water "clusters" or "droplets". Unfortunately, the use of these terms is not very clear. The literal definition of a cluster is "a collection of objects of the same kind growing or fastened together" while a droplet is "a small quantity of liquid" [7]. Clearly, these definitions are not too useful. In the present study, "cluster" will refer to aggregates of water molecules in the size range from microns downwards. (This should not be confused with "clusters" in cluster chemistry which involve only a handful of molecules. A 0.01 μm diameter water cluster actually contains ≈ 17,500 molecules [6].) A "droplet" will be used to refer to larger clusters, which may or may not be visible to the naked eye, but are clearly not in the bulk state.

Bulk water itself is a fairly well-documented system although still not fully understood [8-9]. Both ice and liquid water consist of space-filling networks of H-bonds. In ice, these H-bonds are regular and static with each molecule participating in exactly four bonds spatially disposed so as to form polygons with only an even number of sides. On the other hand, in liquid water there is indefinite coordination varying from one to five. The energy of interaction between water molecules in bulk is significant, the absolute value of the H-bond being about 5 kcal/mol.

When small amounts of water are absorbed in a restrictive environment such as a polymeric solid, however, we might expect that the H-bonding requirements for these water molecules might not be completely satisfied. Still, rather than being absorbed separately without H-bonding to each other, the water molecules will tend to form mobile clusters of mutually H-bonded water molecules [10]. The water in polymers, in fact, is generally perceived to be clustered [11]. Specific associations between the water molecules and the polar groups in the polymer can also lead to non-random mixing of water within a polymer. Evidence for this clustering can be found from peculiarities in the sorption isotherm. If the polymer contains water soluble impurities (*e.g.* emulsifiers and initiator residues) then this clustering can also lead to the development of opacity ("blushing") upon immersion in water. This observation is due to light scattering from individual water droplets. Clustering of water in plasticized PVC may also be described in an analogous fashion.

In bulk water, there are an enormous number of interacting molecular degrees of freedom which give rise to dramatic changes in various intensive quantities upon freezing and melting (*e.g.* volume, heat capacities, viscosity, *etc.*). The finite size effects of water clusters, however, reduce the number of molecular degrees of freedom. Also, the increased proportion of water molecules present in the interfacial surface region will disrupt the natural order of the H-bond network in the bulk phase. These effects are expected to cause modifications in the sharp, first-order phase transitions characteristic of normal bulk water. This is manifested, for example, by phase transition rounding and freezing point depression [6].

Recent spectroscopic studies in our group using a spatial imaging photometer have attempted to probe the internal concentration profile of water in an ISE membrane [12-13]. These results have demonstrated that water movement within the membrane is a complicated progression of events. Water permeates the membrane in a two stage process. The first initial stage involves a fast uptake with a diffusion coefficient of around 10^{-6} cm^2/s and leads to a uniform distribution of water throughout the membrane. This first step appears to cause little perturbation. It can be attributed to water being dissolved throughout the membrane phase. The second stage involves a slower uptake with an apparent diffusion coefficient of around 2×10^{-8} cm^2/s that is time and concentration dependent. This stage leads to some physical or structural change in the membrane as evidenced by the generation of light scattering centers and a decreased apparent diffusion coefficient. It has been postulated that these light scattering centers are the result of water droplet formation in the membrane. Other effects such as phase segregation of the plasticizer, however, can also produce the observed light scattering. Therefore, it is of interest to investigate the nature and state of water within these membranes in more detail.

Methods of study of water in polymers have primarily involved thermodynamic methods (*e.g.* heat capacity measurements, differential scanning calorimetry), kinetic methods (*e.g.* ^1H NMR relaxation, dielectric relaxation), spectroscopic methods (*e.g.* IR, Raman, ^1H NMR) and diffraction techniques (*e.g.* low-angle X-ray scattering) [5,10]. Spectroscopic methods are generally very useful since they will reflect solvent and H-bonding effects of the water molecules. ^1H NMR, in particular, should be ideal for identifying the various forms of water in a fixed membrane matrix because chemical shifts of ^1H nuclei are very sensitive to their surrounding environment. This technique has previously been used to study water in several natural and synthetic polymers [14-17]. There have not been any reports, however, of the technique being used to study water in the heavily plasticized polymers that are typically found in ISE formulations.

In this study, ^1H and ^2D NMR are used to investigate the nature of water within both neat DOA plasticizer and 66 wt% plasticized DOA/PVC membranes. The effect of adding lipophilic $KBPh_4$ salt to the membrane is also considered. These NMR observations are supplemented by some infrared (IR) spectroscopic measurements.

6.2 Experimental

Sample preparation. Membrane samples for NMR analysis were prepared by dissolving 150 mg of bis(2-ethylhexyl) adipate (DOA) (Fluka, Selectophore grade) in 3 mL of freshly distilled tetrahydrofuran (THF) (BDH, distilled from potassium). Next, 75 mg of poly(vinyl chloride) (PVC) powder (Polysciences, chromatographic grade) were sprinkled into this DOA/THF solution followed by potassium tetraphenylborate ($KBPh_4$) as an appropriate aliquot of a $KBPh_4$/THF solution. $KBPh_4$ was prepared by precipitation from sodium tetraphenylborate (Terochem) as outlined in reference [18]. After stirring for one hour to effect complete dissolution, small aliquots of this casting solution were added to a 5 mm NMR tube. Between each addition, the sample tube was dried in a 60 ^{0}C oven for 24 hours in order to ensure a uniform casting and complete solvent evaporation. Final dried membranes were about 2 cm in height. Membranes were allowed to equilibrate for several days with either nanopure H_2O (Barnstead) or 99.8 % D_2O (General Intermediates) before NMR experiments.

Membrane samples for IR analysis were prepared by dissolving 200 mg of DOA in 3 mL of THF followed by 100 mg of PVC powder. After complete dissolution, these solutions were cast into Teflon rings (inner diameter 4 cm) clamped onto a Teflon sheet to form master membranes according to the method of Craggs *et al* [19]. A flexible membrane of *ca.* 120 μm thickness remained after complete evaporation of the THF solvent. Actual samples for FTIR analyses were in the form of 1.5 cm diameter disks cut away from the master membrane.

Plasticizer samples saturated with water were prepared by shaking equal volume portions of DOA and water for one hour with a Wrist-Action Shaker (Burrell Corp.). The two bulk phases were then separated by either gravity or centrifugation.

Potassium ion-selective electrodes were prepared from membranes cast onto glass slides according to procedures published by Craggs *et al* [19]. The following membrane composition was used: 66 % DOA, 33 % PVC, 1 % valinomycin (Sigma) and 0.01 % $KBPh_4$. For calibration, 10^{-2} to 10^{-6} M KCl solutions were prepared by serial dilutions of a 10^{-1} M KCl stock solution.

Apparatus. ^1H, ^2D and ^{13}C NMR measurements were made on a Bruker WH-200 spectrometer operating in the pulsed Fourier transform mode at Larmor frequencies of 200 MHz, 30 MHz and 50 MHz, respectively. For the ^1H and ^{13}C measurements, a ^2D-lock was established using a $DOA/CDCl_3$ sample with TMS providing the chemical shift reference. Actual membrane samples were then measured with the spectrometer unlocked. For the ^2D measurements, a sample of pure D_2O provided both the initial lock and chemical shift reference. Since the membrane samples were of small volume, they were centered around the *rf* receiver coil for all experiments in order to minimize magnetic inhomogeneities. Temperature was regulated with a Bruker B-VT-1000 Temperature Controller using nitrogen gas boiled from a liquid nitrogen dewar. Actual probe temperatures were measured to within ± 1 °C with an Analogic AN2572 thermocouple. The spectrometer was re-locked and re-shimmed at each different temperature using the $DOA/CDCl_3/TMS$ or D_2O samples. Membrane samples were accordingly stored in the refrigerator or freezer in order to minimize extreme temperature modulations during this procedure.

Fourier transform infrared (FTIR) spectroscopic measurements were made on a Nicolet 7199 Fourier transform spectrometer with a resolution capability of 0.06 cm^{-1}.

EMF measurements were made with a Fisher 825 MP meter. A saturated NaCl calomel electrode was used as the reference electrode. The temperature of the calibration solutions (10^{-6} to 10^{-2} M KCl) was adjusted with a Lauda K-4/RD circulator bath (Brinkmann Instruments) using a 50 % methanol/water mixture as the thermostatic medium.

6.3 Results and Discussion

6.3.1 Water in Neat DOA Plasticizer

A ^1H NMR spectrum of pure neat DOA plasticizer is given in Figure 6.1. An expansion of the 4.8 ppm region characteristic for H_2O resonance, did not reveal any water signal. Shaking the plasticizer with H_2O resulted in a "milky" white suspension due to light scattering from H_2O droplets suspended in the DOA plasticizer. These large water droplets were clearly visible with the naked eye. When the two bulk phases were allowed to settle by gravity, the water droplets were no longer visible. Since the DOA sample was translucent, however, this indicates that there was still a phase separation between the H_2O and DOA components. In this case, the light scattering centers are most likely smaller water clusters suspended in the DOA phase. Only when the sample was centrifuged did it return to its original clear and colorless state. This suggests that the H_2O indeed had originally phase separated into water clusters in the DOA plasticizer.

^1H NMR spectra were obtained for the various phase separations described above. The wt% of H_2O in the DOA plasticizer can be determined by comparing the integral for the observed water resonance with the integral for all the peaks due to the DOA component. Results from these calculations are summarized in Table 6.1. The data shows that, within the

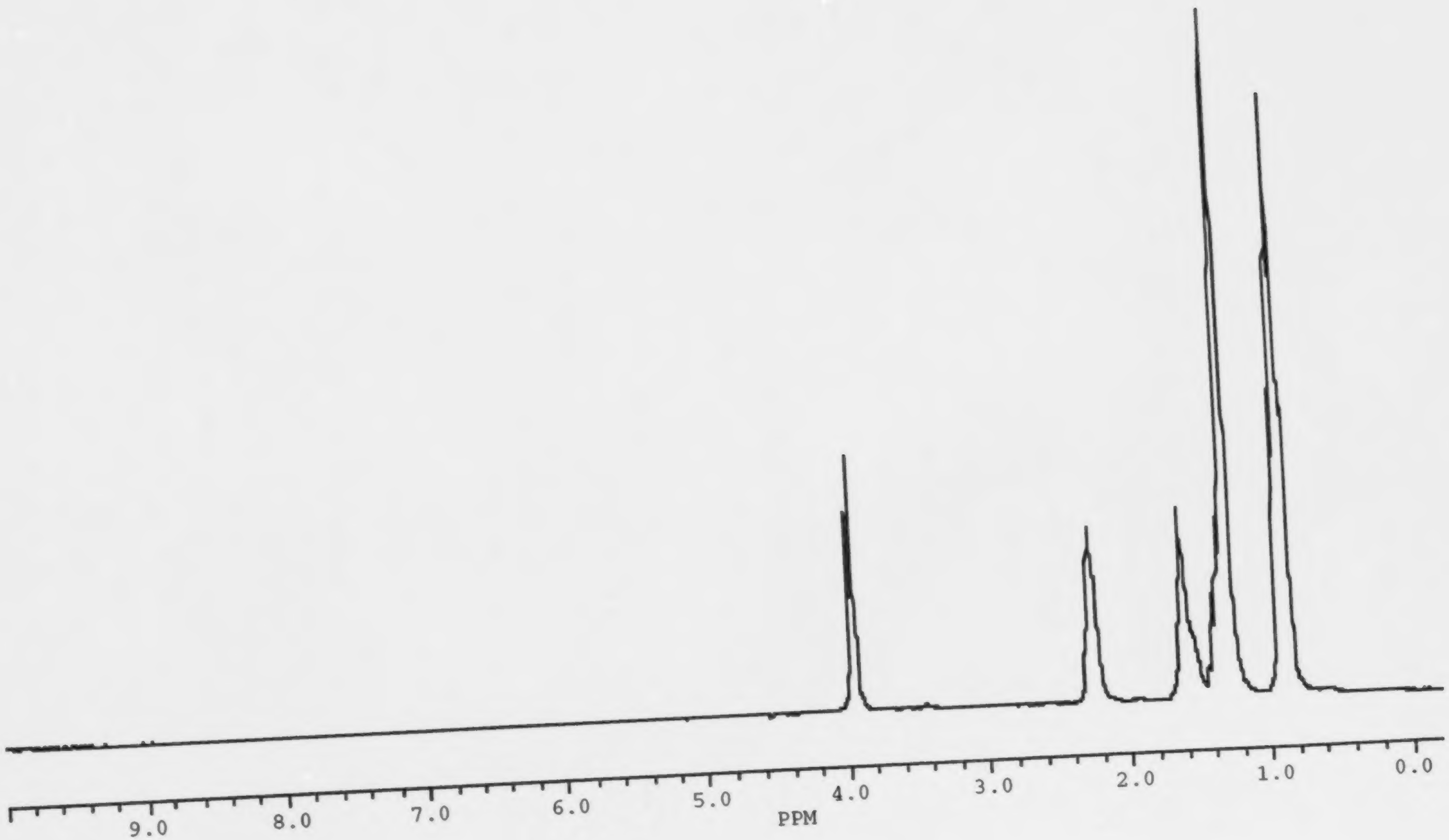

Figure 6.1 ^{1}H NMR spectrum of pure neat DOA plasticizer.

Table 6.1 ^1H NMR integrations of H_2O-saturated DOA samples.

sample	sample treatment	H_2O integral	DOA integral	wt% H_2O(d)
1(a)	< 1 min.	829.1	728.8	53.7 ± 0.1
2(a)	15 min.	6.5	361.4	1.8 ± 0.3
3(a)	1 hr	2.5	371.4	0.7 ± 0.3
4(b)	centrifuge	< 1.0	403.5	< 0.2
5(c)	no water	< 1.0	408.0	< 0.2

a) Samples 1-3 were shaken with H_2O for one hour then separated by gravity for the times indicated.

b) Sample 4 was shaken with H_2O for one hour then separated by centrifugation for five minutes.

c) Sample 5 was neat DOA with no deliberate exposure to H_2O.

d) Errors indicated for the wt% H_2O are based on the precision of calculating the water integral. This was estimated to be ± 1 integration unit.

limits of detection by NMR, water does not dissolve in the plasticizer. A H_2O-DOA emulsion can be produced, however, with phase separation of small water clusters which gives rise to a significant NMR water signal. The disappearance of this water signal upon centrifugation provides additional evidence that water can exist in the plasticizer only primarily in the form of phase-separated small water clusters.

An FTIR spectrum of neat DOA plasticizer, sampled directly out of the reagent bottle, is shown in Figure 6.2a. A low intensity, broad band corresponding to an O-H stretching vibration can be seen at 3450 cm^{-1}. This suggests that the pure plasticizer is contaminated by trace amounts of atmospheric moisture. When the plasticizer is saturated with water, and isolated by centrifugation, the resulting FTIR spectrum is shown in Figure 6.2b. It can be seen that the OH band at 3450 cm^{-1} has noticeably increased in intensity. Also, changes are observed in the fingerprint region between 1200 and 1400 cm^{-1}. This most likely corresponds to O-H bending mode vibrations from the increased water content in the plasticizer sample. Hence, unlike ^1H NMR, FTIR appears to be more sensitive to the presence of low concentrations of water. These results demonstrate that water does in fact dissolve to an appreciable extent in the DOA plasticizer. We notice, however, that the amount of dissolved water is not too large as evidenced by the relatively low intensity for the OH band in the water saturated sample.

We can conclude from these studies that water can exist in the plasticizer phase in two forms. It can be dissolved in very small amounts or phase separated into small water clusters. Next, we now focus our attention on the more practical consideration of water in an actual ISE membrane phase.

6.3.2 Water in 66 % DOA/PVC Membranes

Water in a 66 % DOA/PVC ISE membrane matrix was first studied by IR spectroscopy. Diffuse reflectance IR measurements have been shown to be quite useful for the analysis of plastics and other solid samples. A

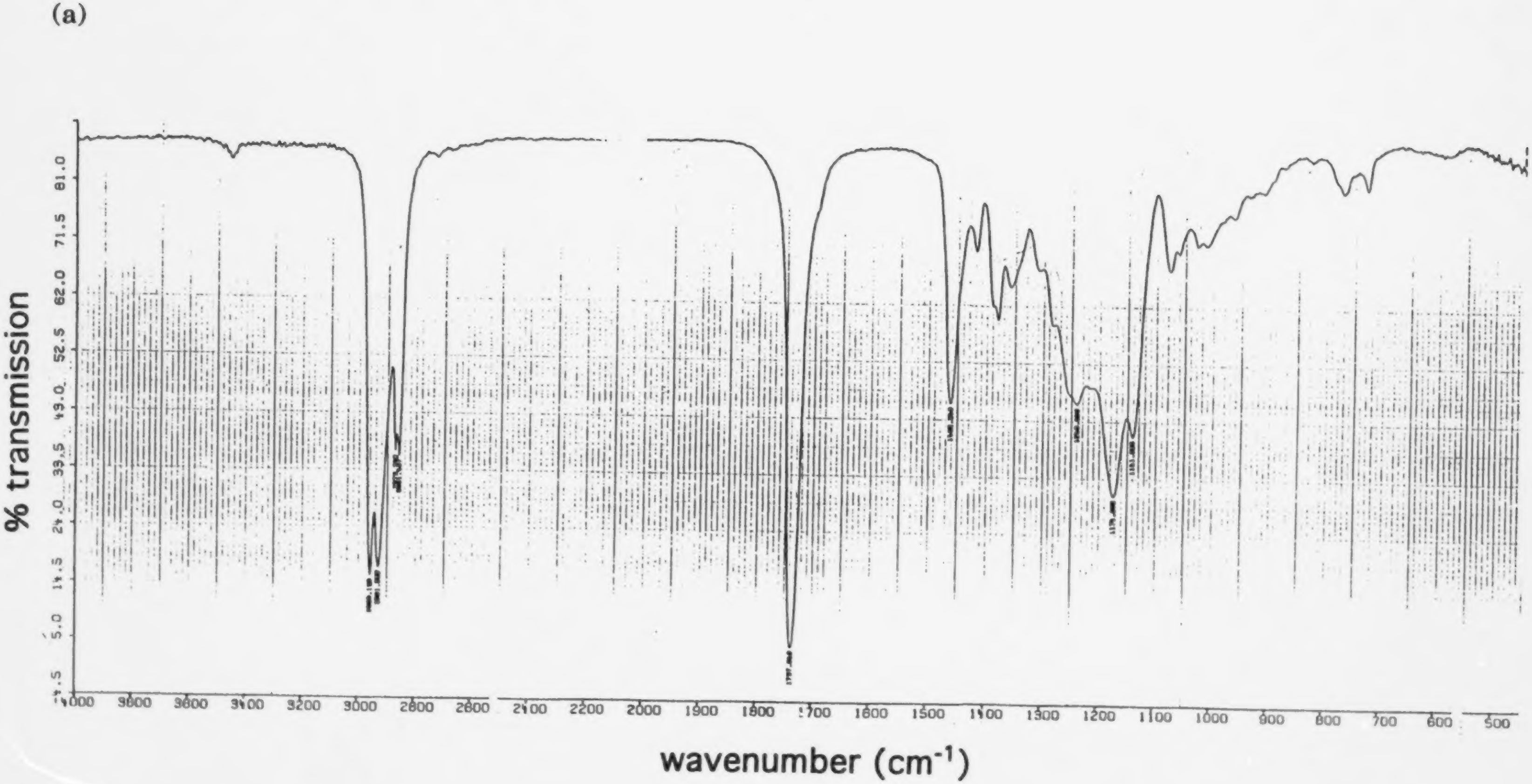

Figure 6.2 FTIR spectra of neat DOA plasticizer: (a) pure and (b) saturated with H_2O.

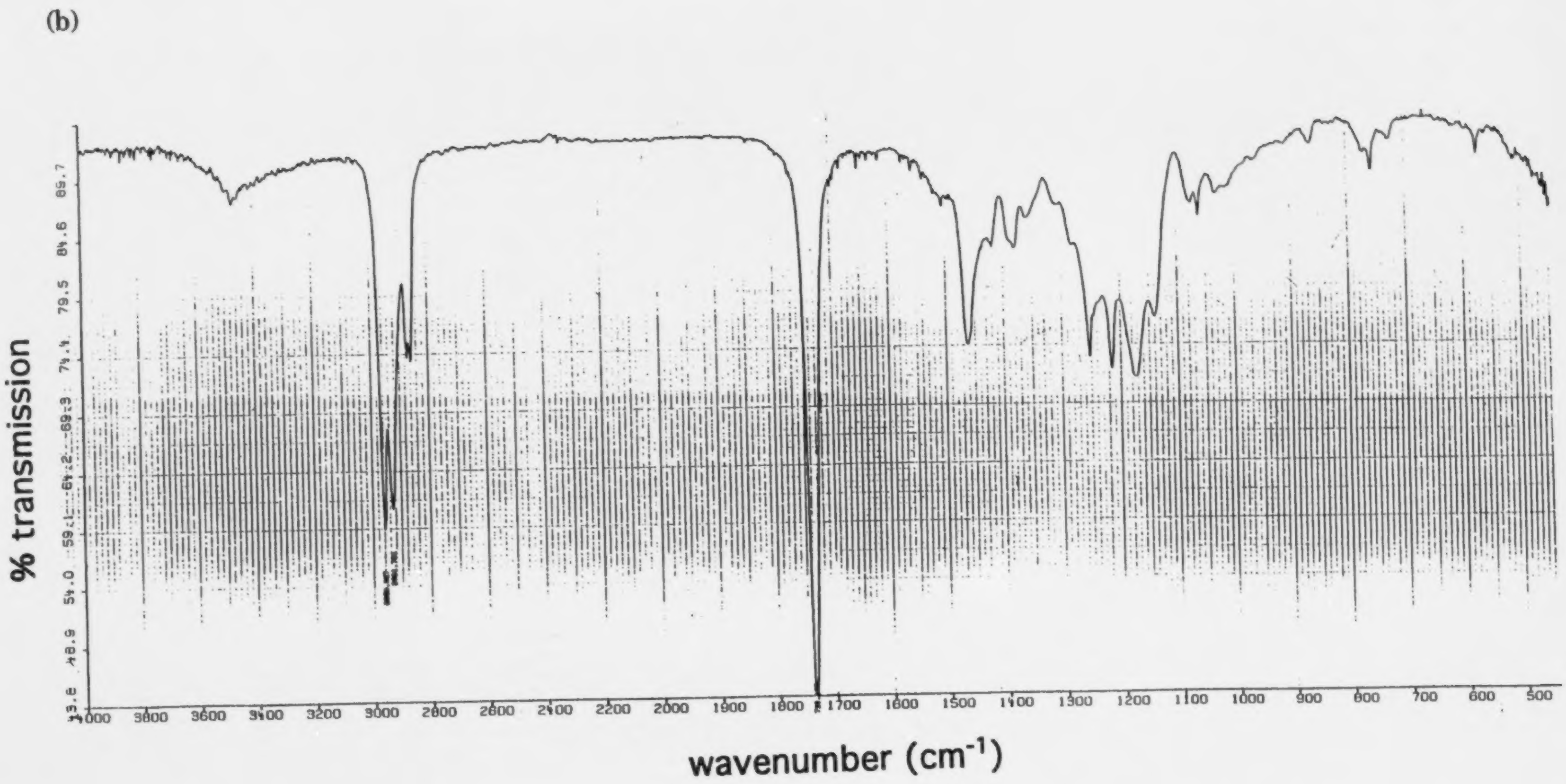

Figure 6.2 FTIR spectra of neat DOA plasticizer: (a) pure and (b) saturated with H_2O (continued).

diffuse reflectance FTIR spectrum of a 66 % DOA/PVC membrane sample soaked in H_2O is shown in Figure 6.3. Peak resolution is quite good and this spectrum shows typical features of superimposed PVC and DOA spectra without additional bands or significant band shifts [20-21]. Since this is an inherently surface sensitive technique, however, it unfortunately proved not to be sensitive enough for probing water in the bulk membrane phase. It can be seen that any O-H stretching vibrations due to water at the membrane surface cannot be discriminated from the noise in the spectrum.

A normal transmission FTIR spectrum of the same membrane sample is shown in Figure 6.4a. It can be seen that the radiation is completely attenuated for the major vibrational modes of the membrane components. These include C-H stretching (2900 cm^{-1}), C=O stretching (1750 cm^{-1}), and C-C stretching and C-H bending (1100 - 1500 cm^{-1}) modes of the DOA plasticizer. Nevertheless, a well-defined O-H stretching vibration at 3450 cm^{-1} can clearly be seen. This most likely results from the water originally present in the pure plasticizer component. A normal transmission FTIR spectrum is shown in Figure 6.4b for the membrane now equilibrated for 7 days in water. In order to properly evaluate differences in water uptake, the relative intensity of the OH band at 3450 cm^{-1} was calculated for the dry and wet samples by using the 490 cm^{-1} membrane band as a pseudo internal standard band. Such interpretation shows that the band ratio, I_{3450}/I_{490}, increases by approximately 18 % upon exposure to water. This can be taken, however, as only a very crude estimate for the increased water uptake. Band intensities, not areas, were measured on a strongly sloping spectral baseline. A more reliable quantitative estimate of water uptake can be determined from gravimetric water desorption or adsorption experiments (*cf.* Chapter 7).

The relative sharpness of the water O-H stretching band observed in the membrane phase is quite surprising (Figure 6.4). O-H stretching modes characteristically give rise to broad absorption bands such as those observed for the neat DOA plasticizer (Figure 6.2). The usual breadth of the O-H stretch in water results from H-bonds of varying strength which gives

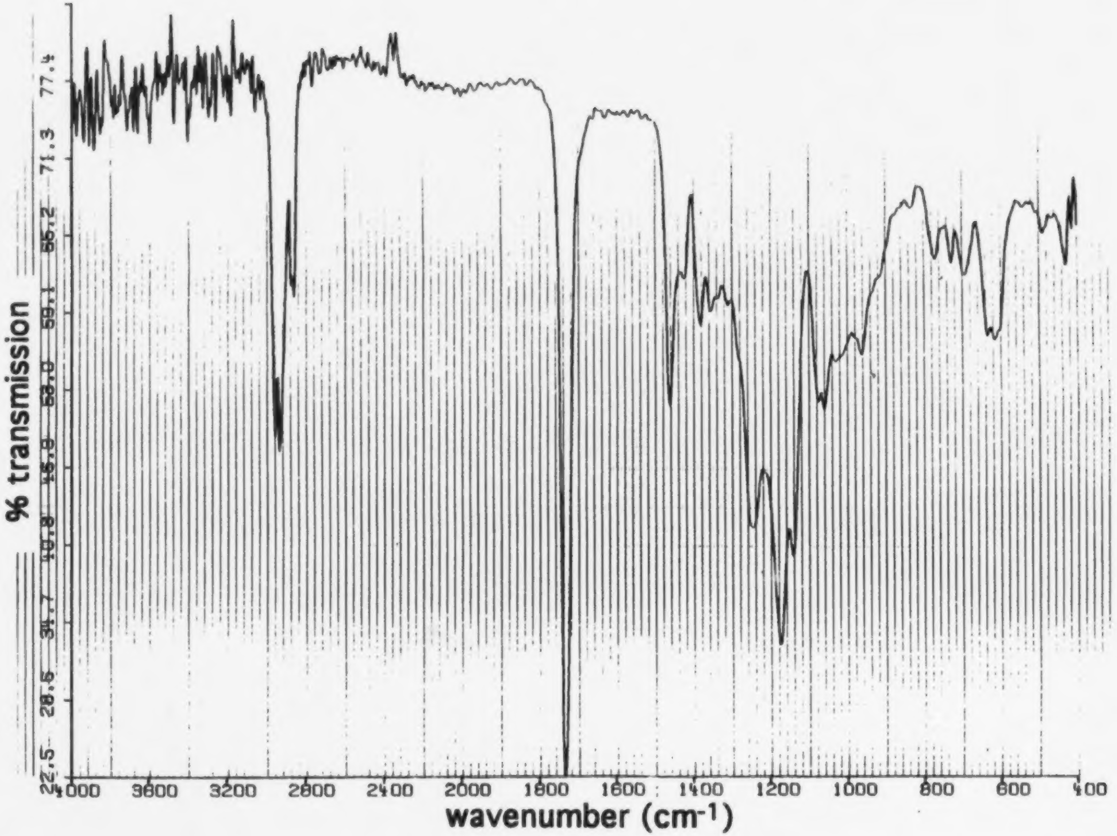

Figure 6.3 Diffuse reflectance FTIR spectrum of a H_2O-soaked 66% DOA/PVC membrane sample.

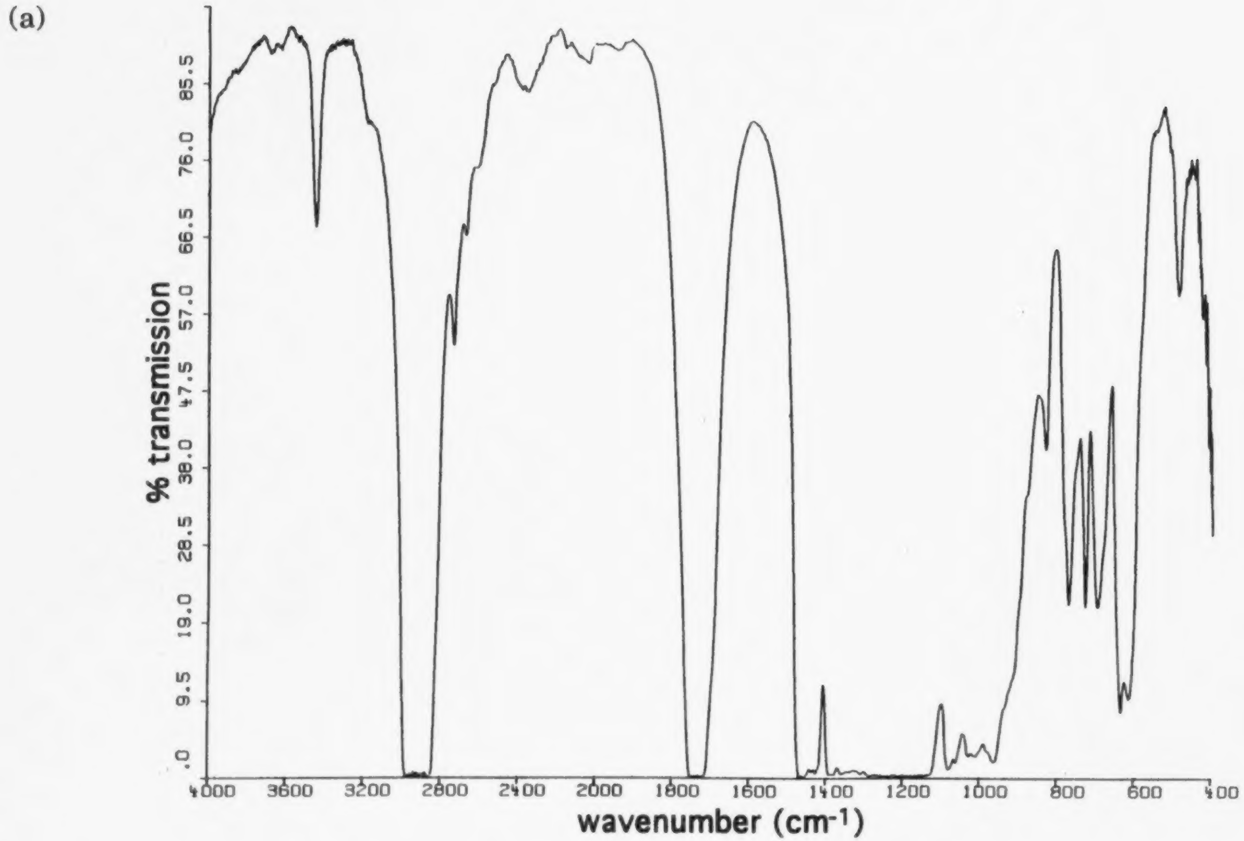

Figure 6.4 Normal transmission FTIR spectra of a 66% DOA/PVC membrane sample: (a) dry and (b) H_2O-soaked.

(b)

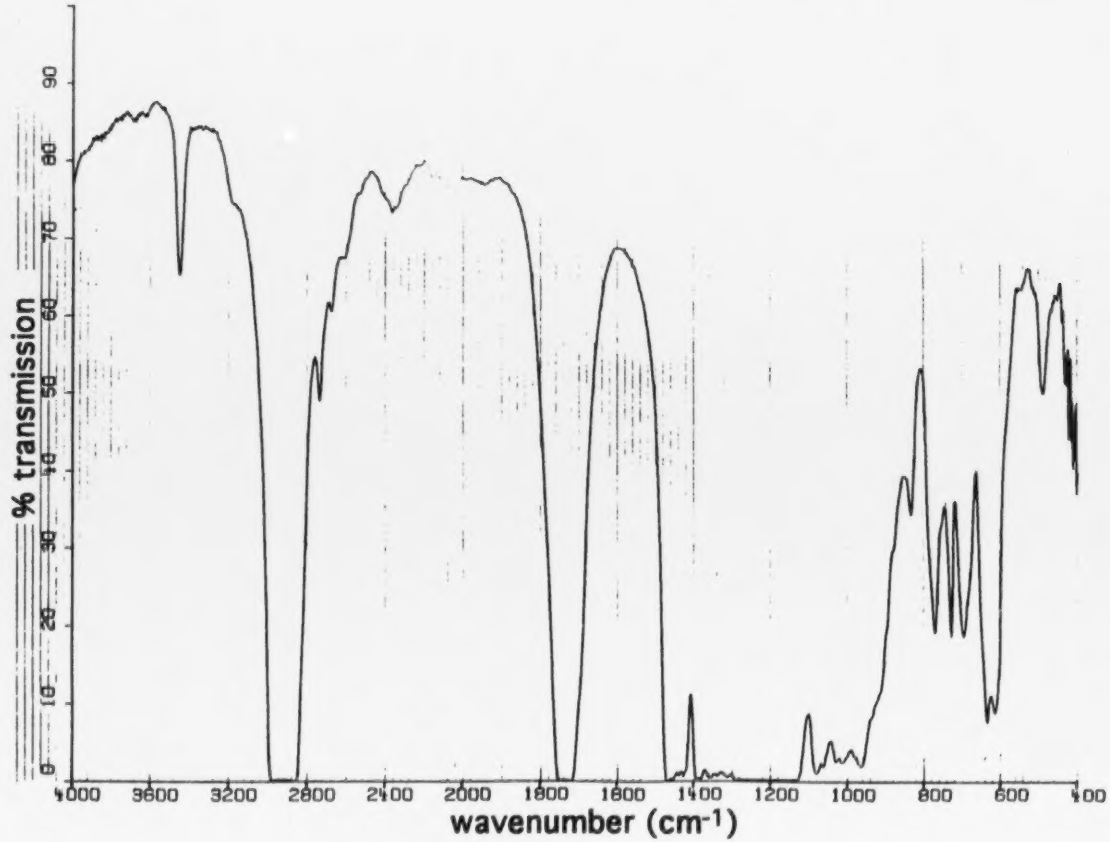

Figure 6.4 Normal transmission FTIR spectra of a 66% DOA/PVC membrane sample: (a) dry and (b) H_2O-soaked (continued).

rise to varying O-H frequencies. Very narrow O-H stretching bands for water, however, have been observed for isolated dimers in rare gas matrices. These have been attributed to the absence of intermolecular couplings [22]. Therefore, the reduced breadth of the O-H stretch for water in the membrane phase indicates that intermolecular coupling is reduced in an analogous fashion. This suggests that the water absorbed in the membrane must exist as compact entities which gives rise to a more restrictive H-bonding environment.

This chemical form of water within the membrane phase is unexpected in light of recent optical studies of the internal concentration profile of water in the membrane reported by Harrison and Li [12]. These studies have shown that, although water is generally uniformly distributed throughout the membrane phase, there is a water rich surface region which develops whose thickness depends on membrane additives. The presence of such a water region should lead to the usual broad O-H stretching bands in the FTIR, but this was not in fact observed. Harrison and Li have also noted, however, that this water rich region at the surface disappears very rapidly. The region requires about 24 hrs to develop, yet it disappears within 15 min once the membrane is allowed to dry. We conclude, therefore, that a correspondingly rapid evaporation of this surface region must have occurred during sample preparation prior to the actual acquisition of the FTIR data.

The FTIR experiments have demonstrated that water exists in the membrane phase as small entities with reduced intermolecular couplings. We will refer to these entities as small "water clusters" which are on the order of sub-micrometer dimensions (*vide infra*). The FTIR data, however, cannot provide any specific information regarding the nature of these water clusters themselves in the membrane phase.

^{1}H and ^{2}D NMR spectroscopies were used to investigate the state of water in the membrane phase in more detail. Now, the ISE membranes under study are more "solid" than "liquid" in appearance despite the fact that they contain twice as much organic plasticizer solvent than solid PVC polymer. Characterization of these membrane systems as "solid membranes", however, is misleading and the term "liquid membranes" or "liquid polymer membranes" has been suggested by Simon [23]. This distinction is an important consideration for their NMR studies and more than a matter of semantics. While solution state NMR is capable of high resolution and a wealth of structural information, this conventional NMR measurement on solids gives only broad, featureless bands of little use. This is a result of the restricted molecular motion in a solid which leads to dipolar broadening. Elaborate refinements involving magic-angle spinning and cross-polarization techniques are required to obtain really useful solid state NMR spectra. Fortunately, ISE membranes plasticized at the normal 66 wt% level are sufficiently liquid-like to be studied by conventional solution state NMR techniques. This is not true, however, for membranes with lower levels of plasticization (*cf.* Chapter 5).

A ^{13}C NMR spectrum of a dry 66 % DOA/PVC membrane is shown in Figure 6.5. Considering the solid physical nature of the membrane sample, the resolution observed in this spectrum is quite surprising. Linewidths are only about 20 Hz and 100 Hz for the plasticizer and PVC resonances, respectively. ^{13}C relaxation studies can readily be performed on these samples to provide information on plasticizer-polymer interactions (*cf.* Chapter 5). On the other hand, the ^{1}H NMR spectrum shown in Figure 6.6 is relatively broad and the features are poorly resolved. ^{1}H NMR, however, should still be useful for studying water absorption within these membranes since the liquid water resonances should be relatively sharp compared to the membrane signals. Alternatively, ^{2}D NMR measurements of D_2O-soaked membranes can also be employed. In this case, only the D_2O signals would be observed. This should completely eliminate spectral interferences from the other membrane components and greatly simplify spectral interpretation.

Membrane samples for NMR analysis were treated by filling the sample tube with water. An initial NMR spectrum showed no water resonances. This demonstrates that the "head" of water resting on top of the membrane sample was not detected by the spectrometer. After a couple

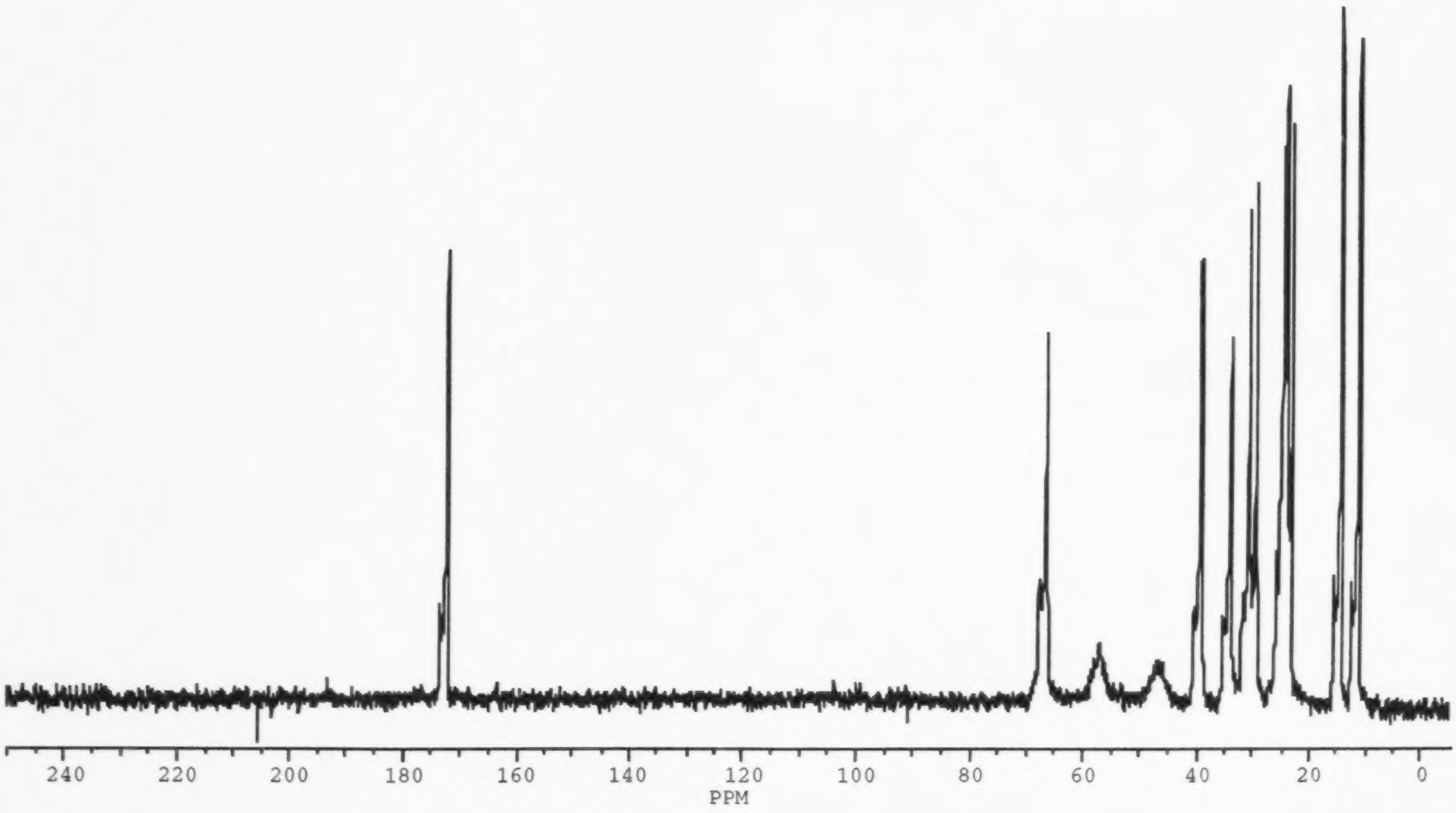

Figure 6.5 ^{13}C NMR spectrum of a dry 66% DOA/PVC membrane sample.

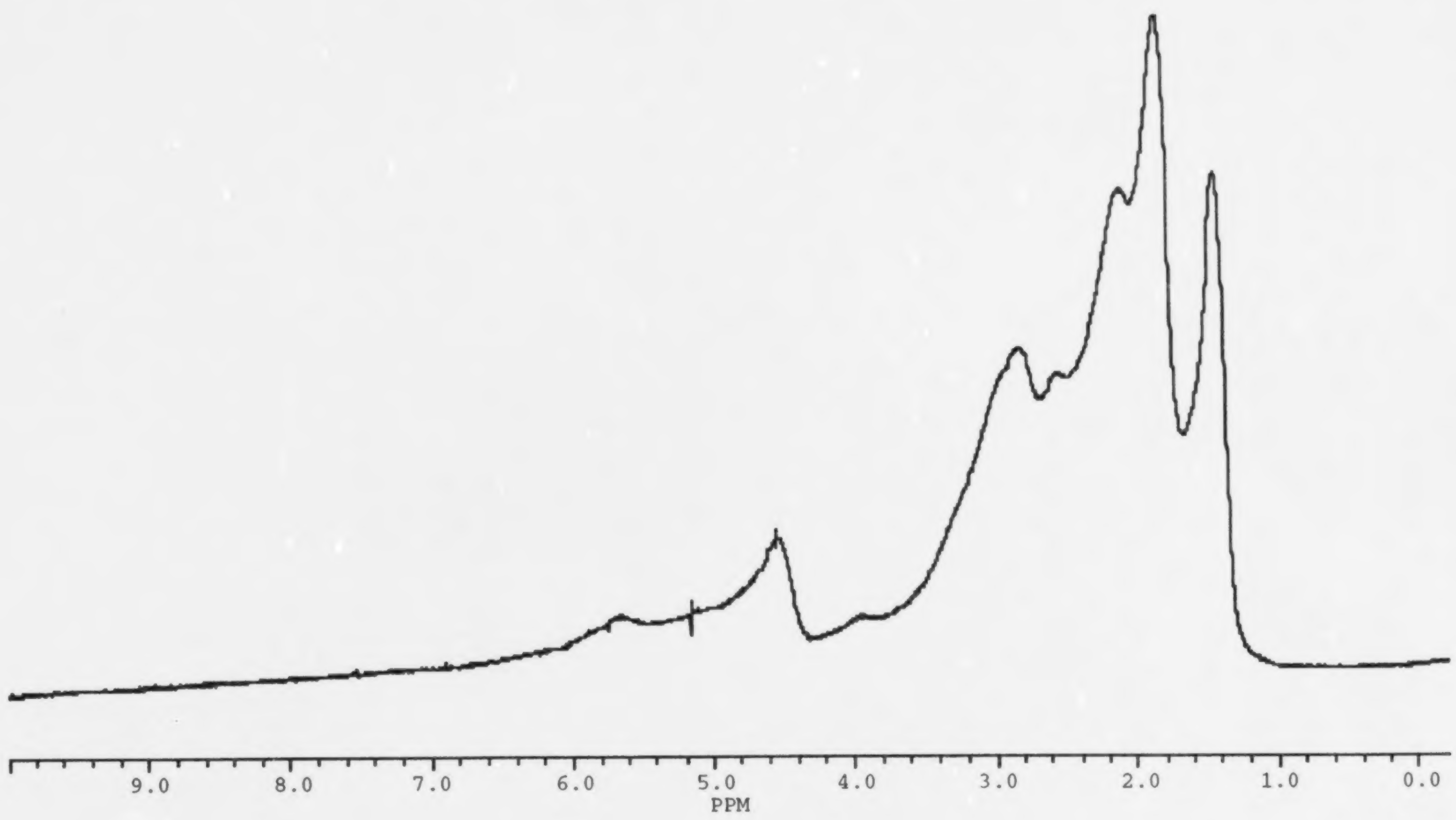

Figure 6.6 ^{1}H NMR spectrum of a dry 66% DOA/PVC membrane sample.

of days, a stable water signal was observed indicating that equilibration with the water phase had been achieved.

The physical nature of the membrane matrix, however, raises concern with regards to magnetic inhomogeneities of the solution state ^1H NMR method. This could lead to broadening and distortion in the chemical shift data between different samples. To evaluate this, 10 wt% tetramethylammonium chloride (Me_4NCl) was incorporated into the aqueous soaking solutions of various membrane samples. The Me_4NCl resonance was not observed to vary by more than ± 0.1 ppm from its usual value of ≈ 2.9 ppm in pure D_2O solvent. Additionally, it was also observed that a soaking period of ≈ 24 hrs was required before the Me_4NCl resonance was detectable. This important observation also demonstrates that it is the aqueous phase within the membrane which is probed and not merely the "head" of solution above the sample.

6.3.2.1 Low $KBPh_4$ Membranes

A ^1H NMR spectrum of a 66 % DOA/PVC membrane containing 0.01 % $KBPh_4$ salt soaked in H_2O is shown in Figure 6.7. The absorbed water gives rise to the observed spread of chemical shifts between 4.9 and 5.3 ppm. Analogous ^2D NMR measurements on D_2O-soaked membranes have confirmed that these signals are indeed water resonances and not a manifestation of some physical change to the membrane itself. From the ^1H NMR experiments on water-saturated DOA plasticizer in the previous section, we can additionally conclude that these large water resonances do not originate from water being simply dissolved in the membrane phase. Instead, water also phase separates into small water clusters in the membrane. Unlike the neat DOA system, however, we can expect these water clusters to be much less mobile in the more entangled and viscous membrane matrix. Hence, the water clusters cannot, for example, settle out under gravitational forces. These concepts of water cluster formations

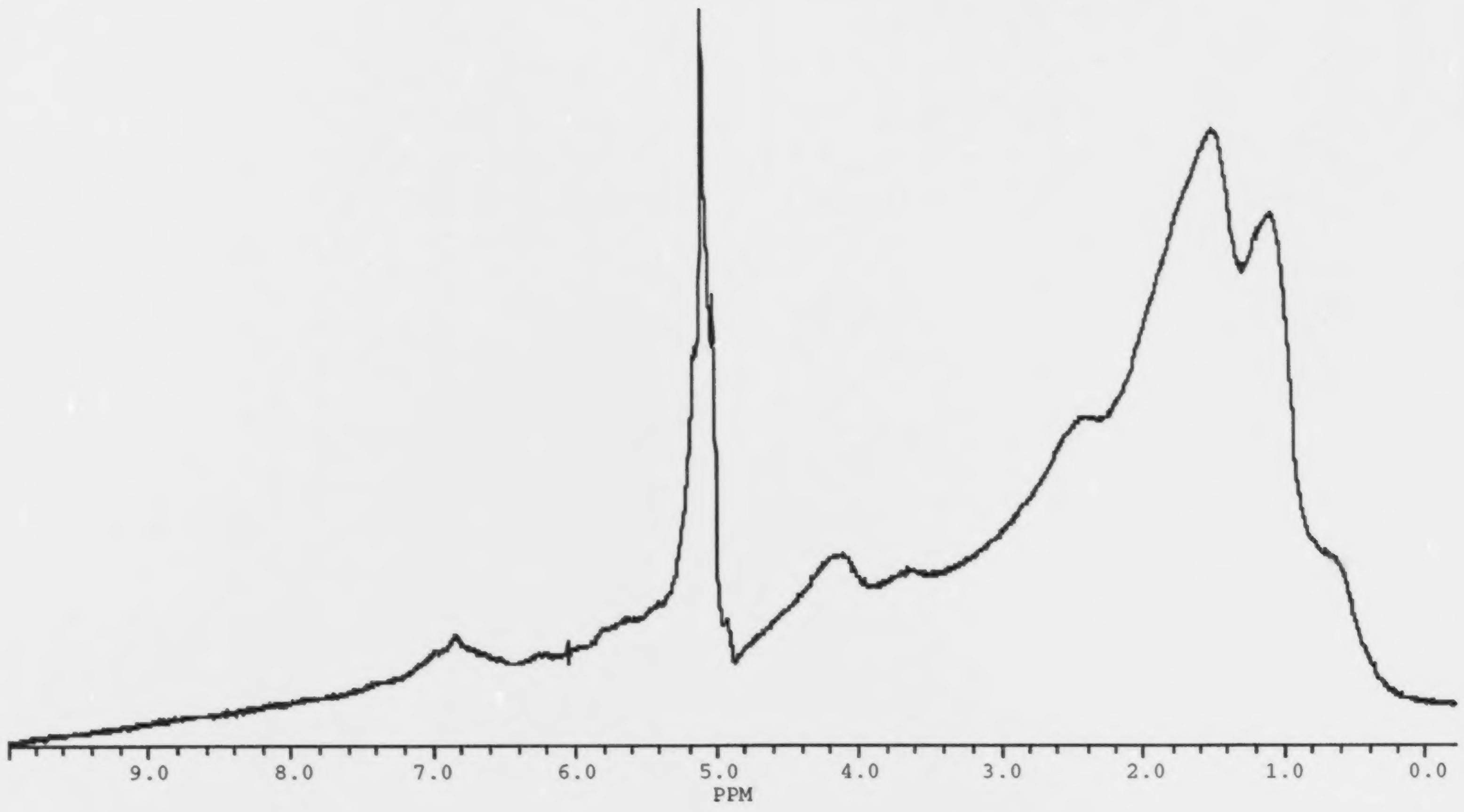

Figure 6.7 ^{1}H NMR spectrum of a H_2O-soaked 66% DOA/PVC membrane containing 0.01% $KBPh_4$ salt.

in the membrane phase are in agreement with the conclusions reached from the IR studies discussed previously.

The water clusters in the neat plasticizer led to a single sharp resonance, yet the presence of the water clusters in the membrane phase gives rise to quite a spread of signals. This observation, however, should not be too surprising. Water in the membrane phase must exist in a more restrictive geometry than in the neat DOA phase. Unlike bulk water, we thus do not expect the environments of all the absorbed water molecules to be identical. The water may be exclusively H-bonded to each other and/or to one or more of the membrane components. We have observed, however, that the particular underlying fine structure of the water signal is not reproducible between different H_2O-soaked membrane samples. This would seem to suggest that the absorbed water molecules do not exist in well-defined, static environments. It is likely that water clusters of various sizes exist and that these are randomly distributed throughout the membrane phase. These will present an assortment of different chemical environments and can account for the observed spread in the water signals.

Low temperature NMR measurements have proven useful in the study of bound water in protein and polypeptide systems [5,24-25]. Variable-temperature (VT) NMR studies can, therefore, provide further insight to the nature and behavior of the water in these membranes. ^2D NMR spectra of a D_2O-soaked membrane measured at various probe temperatures are shown in Figure 6.8. Analogous ^1H NMR VT spectra of H_2O-soaked membranes have also been acquired, but these are complicated by the broad membrane resonances.

It should be pointed out that the absolute peak intensities of the VT spectra shown in Figure 6.8 depend on the placement of the sample relative to the *rf* receiver coil. Measurement at each temperature, however, involves a repositioning of the membrane sample in the spectrometer (*cf.* Experimental). Furthermore, vertical expansions are shown for some of the spectra. Hence, relative peak intensities between spectra obtained at different temperatures are not too meaningful.

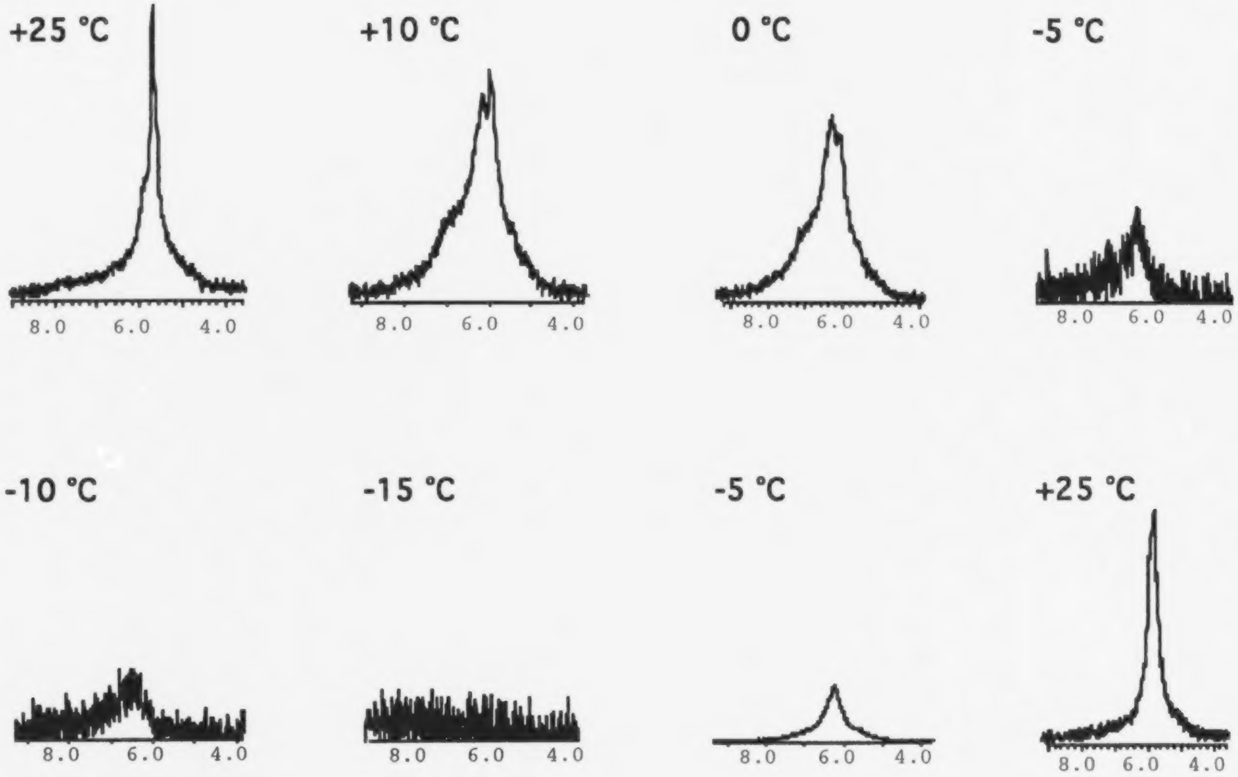

Figure 6.8 Variable temperature ^{2}D NMR spectra of a D_2O-soaked 66% DOA/PVC membrane containing 0.01% $KBPh_4$ salt.

From the VT spectra in Figure 6.8, it is evident that the absorbed D_2O eventually freezes out in the membrane. That is, it begins to freeze at -5 °C, and by -25 °C it is completely frozen as evidenced by the disappearance of the D_2O signal at the liquid to solid transition. We have indicated that the absorbed water exists in the membrane primarily as clusters of various different sizes. Unlike water which is dissolved or simply dispersed throughout the membrane on a molecular scale, these will eventually freeze out at sufficiently low temperatures. Note that the sensitivity of the NMR technique does not allow observation of any unfrozen dissolved water at low temperatures. This is consistent with the lack of sensitivity observed for dissolved water in pure DOA plasticizer (*vide supra*).

When the water freezes out, it does so at a temperature significantly below the normal freezing point of the bulk liquid. The normal freezing point of D_2O is +3.78 °C yet a significant amount of D_2O still retains appreciable mobility below this temperature. This water is sufficiently mobile to provide a relatively sharp NMR signal at even -10 °C (linewidth *ca.* 20 Hz). Water frozen into ice has a linewidth on the order of 10^5 Hz and would make very little contribution to the observed signal. A freezing point depression of this magnitude cannot be due to simple colligative effects of the added $KBPh_4$ salt since the molal freezing-point-depression constant for water is only 1.86 K kg/mol. This supercooling effect, whereby a considerable fraction of water remains unfrozen below its normal freezing point, is not unique to these membranes but has been observed in other polymer-water systems as well. Freezing point depressions of up to 35 °C are not uncommon [24].

The restricted environment of the water clusters within these membranes likely prevents the full development of those properties so characteristic of bulk water. This can result if the membrane is able to trap water in sufficiently small channels or pores [26-27]. Space restrictions within these cavities may then preclude the formation of 3-D ice crystals for the absorbed water. Thus, whereas ice is the stable phase in bulk below the normal freezing point, a lower free energy state can be achieved if the water clusters remained in the interstices in liquid form. In addition to these thermodynamic considerations, there are also kinetic difficulties presented in nucleating the crystal phase of water clusters of limited size [6]. Furthermore, between -10 °C and 0 °C, the surface of ice is believed to be covered by a mobile liquid-like layer containing bifurcated H-bonds and odd-sided polygons [28]. The increased number of water molecules in the surface region due to these small clusters will also contribute to a proportionately greater amount of "liquid" fraction below the normal freezing point.

From Figure 6.8, we can also see that the process of crystallization and subsequent thawing does not appear to significantly affect the distribution of water in the membrane. The similarity of the D_2O resonances at +25 °C both before and after freezing suggests that similar small water clusters are present under both conditions.

Analogous ^1H NMR VT experiments on H_2O-soaked membranes shows that the absorbed H_2O does not freeze until about -15 °C. We can use this result to calculate the radius of the water cluster required to cause a freezing point depression of this magnitude. Higuti [29] has thermodynamically derived a correlation between the freezing point depression (ΔT) and the radius of pore (r) in which a liquid is condensed. This is given by the following equation:

$$\frac{\Delta T}{T_o} = \frac{2\gamma M}{\rho r \Delta H_{fus}} \tag{6.1}$$

where T_o, M and ΔH_{fus} are the normal freezing point, the molecular weight and the heat of fusion for the bulk liquid, respectively, and γ and ρ are the surface tension and the density of the supercooled liquid. Numeric values for the various physical constants can be approximated by room temperature values for a small range of ΔT. Thus, we can apply equation (6.1) to our observation by substituting the following parameters:

$\Delta T = 15\ \mathrm{K}$

$T_o = 273\ \mathrm{K}$

$\gamma = 71.97$ dynes/cm @ 25 °C
$M = 18.01$ g/mol
$\rho = 0.99707$ g/cm^3 @ 25 °C
$\Delta H_{fus} = 6.0082 \times 10^{10}$ erg/mol

From this calculation, the radius (r) of the water clusters may be estimated as 0.0078 μm. The diameter of these water clusters in the membrane phase is, therefore, approximately 0.016 μm.

This size estimate correlates very well with a study of the volumetric behavior of liquid water in clusters by Stillinger [6]. It was supposed that the outer 5 Å for a spherical water cluster behaves as a "normal" nonaqueous liquid with thermal expansion of 10^{-3}/°C, and the remainder as bulk water. This leads to a crude size estimate of 0.01 μm for the cluster diameter required to depress the well-known density maximum of bulk water from +3.98 °C to -12.88 °C. This is roughly a 17 °C depression for this particular intensive quantity. It would be reasonable to assume that supercooling anomalies of similar magnitude for this cluster size might also result for other intensive quantities, such as freezing point. Stillinger has further calculated that the content of spherical water clusters of 0.01 μm diameter is 1.75×10^4 water molecules of which 4.74×10^3, or 27.1 %, are within 5 Å of the surface. Clearly such a significant fraction of water in the surface region can account for the observed deviation in the IR and NMR spectroscopies from normal bulk water.

6.3.2.2 High $KBPh_4$ Membranes

When the level of $KBPh_4$ incorporated into the membrane is increased ten-fold to 0.1 wt%, there is a significant difference in the distribution of water. This is evident through a comparison of the ^1H NMR spectra for H_2O-soaked 0.01 % and 0.1 % $KBPh_4$ membranes shown in Figures 6.7 and 6.9, respectively. The structural organization of absorbed water is known to be quite sensitive to polymer mobility [16-17]. We have

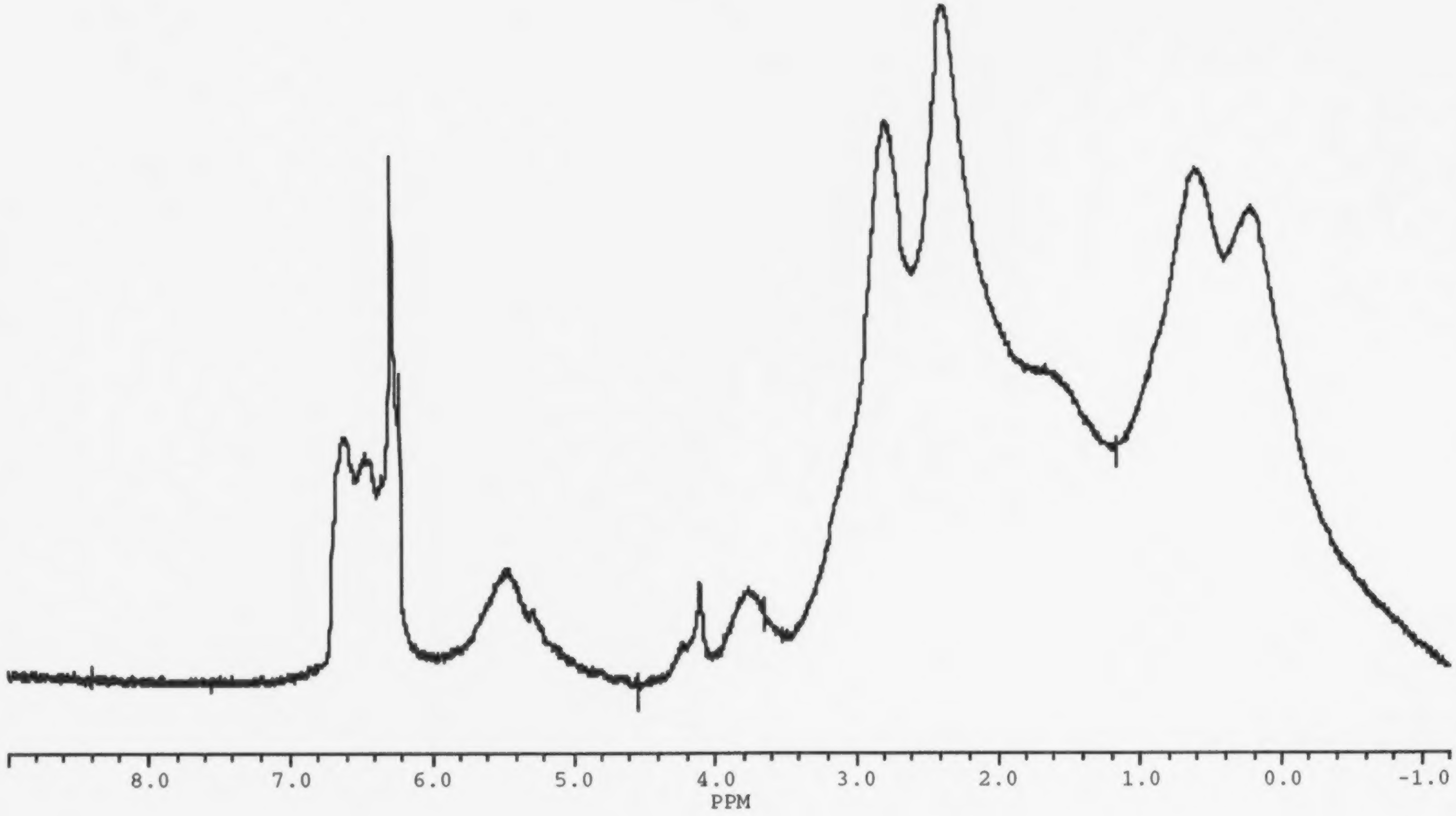

Figure 6.9 ^1H NMR spectrum of a H_2O-soaked 66% DOA/PVC membrane containing 0.1% $KBPh_4$ salt.

shown that the mobility of the plasticizer component in ISE membranes with low and high salt concentrations is different when soaked in water (*cf.* Chapter 5). This can, therefore, lead to the observed changes in the organization of absorbed water upon going from a 0.01 % to 0.1 % $KBPh_4$ membrane.

Previous studies have also shown that the presence of salt within a polymer increases the uptake and distribution of water [5,30]. As a result, there is significantly more water absorbed in membranes containing 0.1 % $KBPh_4$ than for those containing 0.01 % $KBPh_4$. This is suggested even by a casual visual comparison of the opacity developed through water exposure. Initially transparent 0.01 % $KBPh_4$ membranes become translucent as water diffuses in and the individual water clusters uniformly scatter light. In contrast, 0.1 % $KBPh_4$ membranes, while initially transparent as well, become white and opaque upon soaking in water. This is indicative of a much greater degree of light scattering from greater numbers of water clusters and/or larger internal water droplets. The differences in the NMR water signals for membranes with low and high concentrations of $KBPh_4$ must therefore be related to the amount of water within the membrane, and the extent of phase transformation, which is evidenced by the formation of light scattering centers [13].

The large spread of chemical shifts for the water in the 0.1 % $KBPh_4$ membrane reflects an increased distribution of water environments. Multiple water peaks have previously been reported for different states of water within polymer and protein phases [5]. This arises from the high sensitivity of the ^1H chemical shifts to solvent and H-bonding effects. For example, certain ion-exchange resins in bead form can trap water within the beads so that two sets of water peaks are observed. One corresponds to bulk solvent and the other represents solvent in the hydration sphere of the counter-ion inside the resin [31].

As seen in Figure 6.9, the chemical shift differences for the various water environments observed in the membrane are about 2 ppm downfield from bulk water (*ca.* 4.8 ppm). This is a relatively small shift since, for example, the shift from water liquid to water vapor is +6 ppm at room temperature. Hence, this implies that the water environments do not have radically different H-bonding patterns from each other and from bulk water [5]. It is rationalized that the higher concentration of water in the 0.1 % $KBPh_4$ membrane leads the formation of small water droplets in addition to water clusters. The higher concentration of salt in the membrane can also assist in this process by acting as nucleation sites. Thus, water can exist in the 0.1 % $KBPh_4$ membrane in a range of environments from small water clusters to larger water droplets. This can lead to the multitude of chemical shifts for the water resonances observed in Figure 6.9. Furthermore, since these environments are resolved on the NMR time scale, this indicates that any exchange process between the different environments must not be too rapid. This suggests that the water clusters and droplets are isolated entities.

^{2}D NMR VT spectra for a 0.1 % $KBPh_4$ membrane soaked in D_2O are shown in Figure 6.10. We again see a supercooling effect for the freezing of the D_2O. In this membrane, however, the process of freezing and thawing is shown to have a pronounced effect on the distribution of water in the membrane. Whereas the original spectrum at +25 °C demonstrated a range of water environments, after freezing it would appear that there is one preferred environment as indicated by the dominance of the peak at 4.9 ppm. Hysteresis effects in hydrated polymers are often observed on heating and cooling [16-17]. It appears that the process of crystallization leads to the aggregation of some of the small water clusters into the larger water droplets. This is consistent with that fact that when water begins to freeze, it acts as nucleating centers for the formation of more ice. Thus, subsequent to freezing, most of the water will exist in these larger water entities and a significantly lower fraction will exist in the smaller water clusters.

Support for this hypothesis is found from sorption studies of polycarbonate and polyethylene which indicated that water clusters formed when the polymer, initially saturated with water, was rapidly cooled [32]. This was a result of a lowering of the solubility of water in the polymer such that some of the water condensed in the form of microscopic water-filled

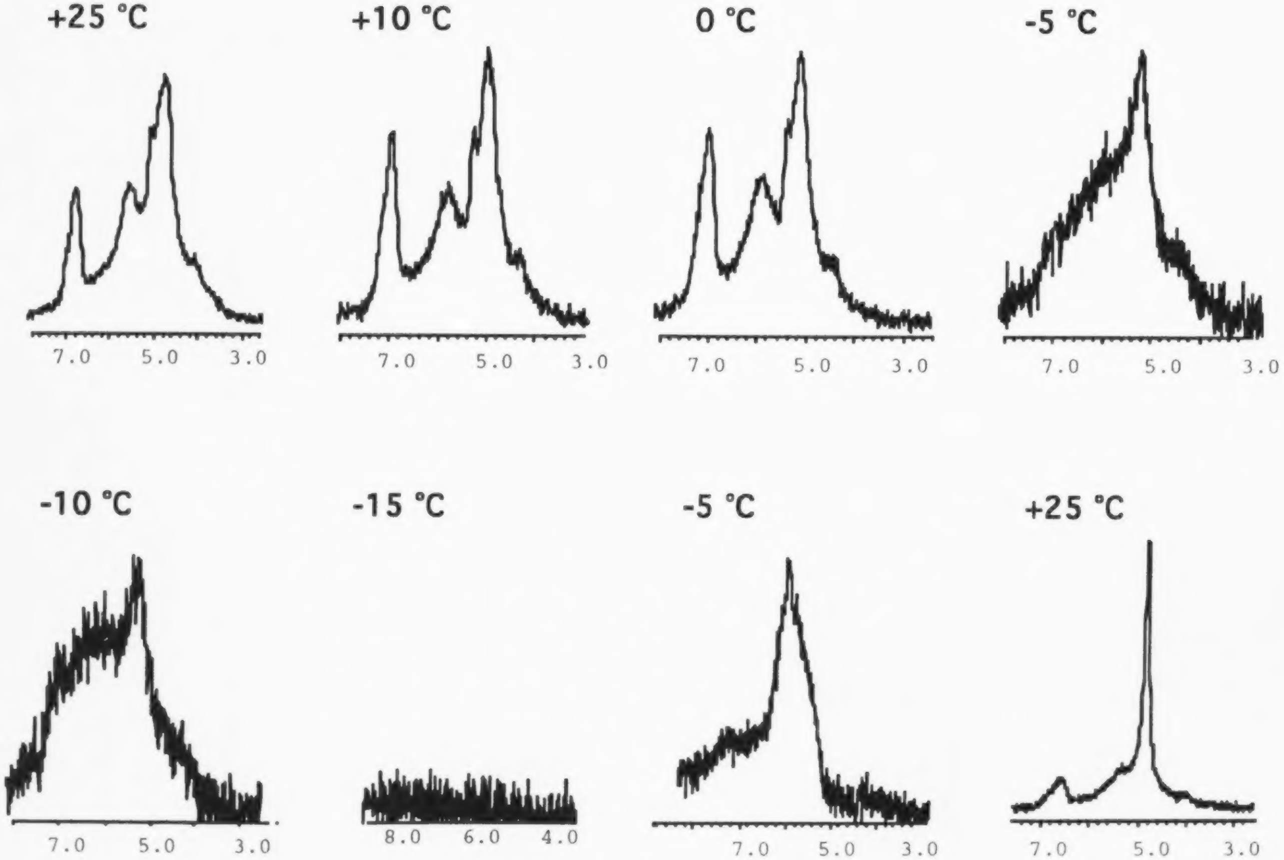

Figure 6.10 Variable temperature ^{2}D NMR spectra of a D_2O-soaked 66% DOA/PVC membrane containing 0.1% $KBPh_4$ salt.

cavities. The internal pressure generated by the excess water, however, must clearly exceed the strength of the polymer interactions. The liquid-like nature of the ISE membranes studied should be conducive to the formation of such cavities. Plasticizer-polymer, plasticizer-plasticizer and polymer-polymer interactions for these membrane systems are all rather weak (*cf.* Chapter 5).

6.3.3 Effect of Temperature on EMF Measurements

There is a significant reorganization in the distribution of water within an ISE membranes at temperatures close to the freezing point. This is particularly pronounced for those membranes containing the typical 0.01 % concentration of $KBPh_4$ lipophilic salt, as evidenced by the considerable change in the NMR water spectra at temperatures between +25 °C and +10 °C (*cf.* Figure 6.8). In these membranes, the water exists as randomly dispersed small water clusters (*vide supra*). It is important to understand what effect, if any, this water reorganization has on the electrochemical performance of these membranes as ISE devices.

In order to evaluate the effect of temperature on ISE performance, potentiometric data were acquired over a range of temperatures. ISE calibration slopes and standard potentials measured relative to the saturated NaCl reference electrode are shown in Figure 6.11 as a function of temperature. We do not see any anomalous behavior for either of these two potentiometric parameters between +25 °C and +10 °C where the water distribution is rapidly changing. Rather, gradual changes in the data are observed throughout the entire temperature range studied. From this we can conclude that the observed changes in the water distribution in these membranes apparently do not appear to significantly influence their electrochemical behavior.

(a)

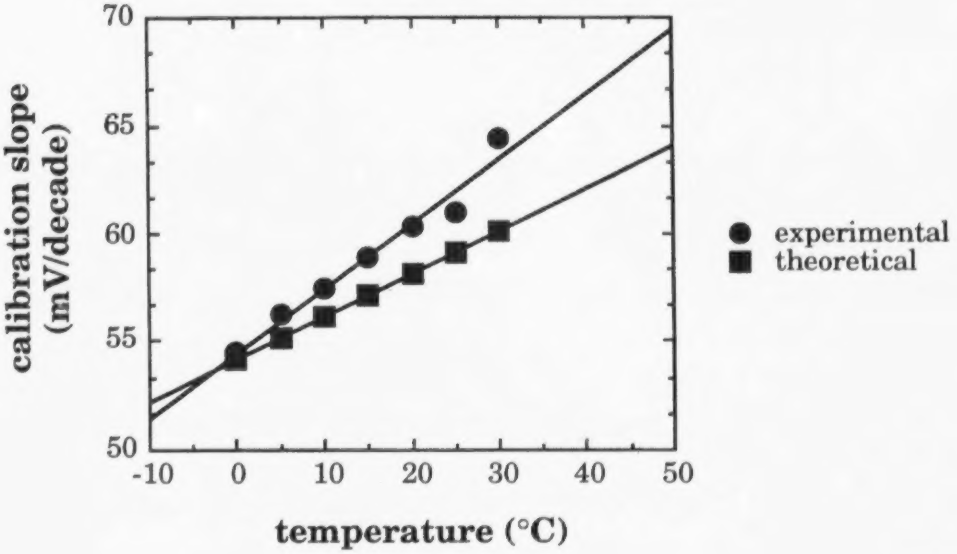

Figure 6.11 Potentiometric data for K+-sensitive ISE membrane as a function of temperature: (a) calibration slopes and (b) standard potentials.

(b)

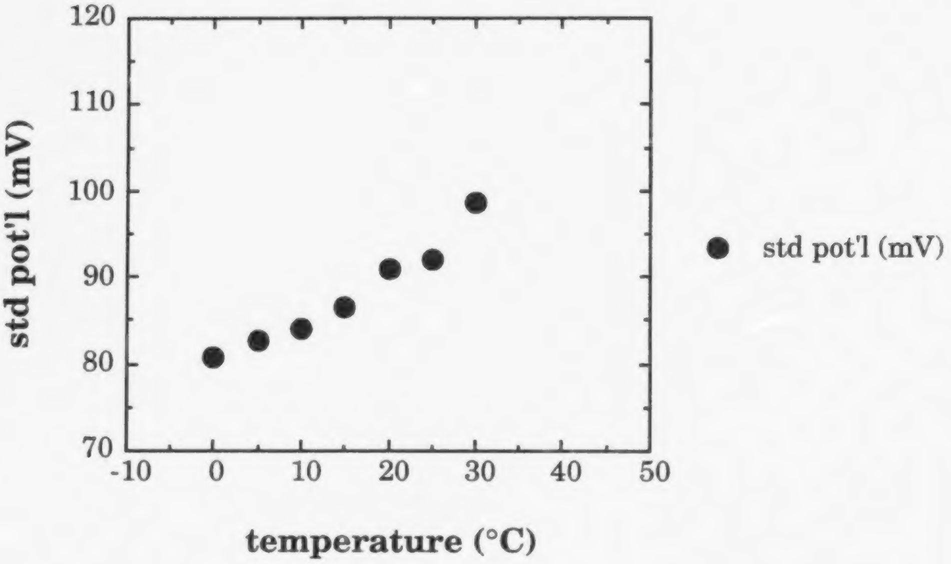

Figure 6.11 Potentiometric data for K+-sensitive ISE membrane as a function of temperature: (a) calibration slopes and (b) standard potentials (continued).

6.4 Conclusions

It has been shown that water dissolves to a small extent in neat DOA plasticizer, however, most of it phase separates. In a 66 % DOA/PVC membrane containing 0.01 % $KBPh_4$ salt, the absorbed water phase separates into small water clusters randomly distributed throughout the membrane phase. This observation confirms that water droplets or clusters form the light scattering centers observed in membranes equilibrated with water. The diameter of these water clusters was estimated to be approximately 0.016 μm. At higher salt concentration, the water also phase separates into larger water droplets. The performance of these membranes as ISE devices does not appear to be significantly affected by the distribution of the absorbed water.

6.5 References

1. Band, D.M.; Kratochvil, J.; Treasure, T. *J. Physiol. (London)* **1976**, *265*, 2P.

2. Morf, W.E. *The Principles of Ion-Selective Electrodes and of Membrane Transport*, Elsevier: New York, 1981.

3. Morf, W.E.; Simon, W. *Helv. Chim. Acta* **1986**, *69*, 1120.

4. Armstrong, R.D.; Horvai, G. *Electrochim. Acta* **1990**, *35*, 1.

5. Kuntz, I.D.; Kauzmann, W. *Adv. Protein Chem.* **1974**, *28*, 239.

6. Stillinger, F.H. *ACS Symp. Ser. (Water Polym.)* **1980**, *127*, 11.

7. *Funk & Wagnalls Canadian College Dictionary*; Avis, W.S., Ed.; Fitzhenry & Whiteside: Toronto, 1989.

8. Eisenberg, D.; Kauzmann, W. *The Structure and Properties of Water*, Oxford Univ. Press: London, 1969.

9. Franks, F., ed. *Water: A Comprehensive Treatise*, vol. 1 - 7, Plenum Press: New York, 1972 - 1982.

10. Hoeve, C.A.J. *ACS Symp. Ser. (Water Polym.)* **1980**, *127*, 135.

11. Brown, G.L. *ACS Symp. Ser. (Water Polym.)* **1980**, *127*, 441.

12. Harrison, D.J.; Li, X.; *IEEE Int. Conf. on Solid-State Sensors and Actuators, Tech. Digest*, p.777, San Francisco, June 1991.

13. Li., X; Petrovic, S; Harrison, D.J. *Sensors and Actuators* **1990**, *B1*, 275.

14. Boyle, N.G.; McBrierty, V.J.; Douglass, D.C. *Macromolecules* **1983**, *16*, 75.

15. McCall, D.W.; Douglass, D.C.; Blyler, L.L.Jr.; Johnson, G.E.; Jelinski, L.W.; Bair, H.E. *Macromolecules* **1984**, *17*, 1644.

16. Quinn, F.X.; Kampff, E.; Smyth, G.; McBrierty, V.J. *Macromolecules* **1988**, *21*, 3191.

17. Smyth, G.; Quinn, F.X.; McBrierty, V.J. *Macromolecules* **1988**, *21*, 3198.

18. Bassett, J.; Denney, R.C.; Jeffery, G.H.; Mendham, J. *Vogel's Textbook of Quantitative Inorganic Analysis*, 4th ed., Longman: London, 1978.

19. Craggs, A.; Moody, G.J.; Thomas, J.D.R. *J. Chem. Ed.* **1974**, *51*, 541.

20. Kellner, R.; Fischböck, G.; Götzinger, G.; Pungor, E.; Tóth, K.; Polos, L.; Lindner, E. *Fresenius Z. Anal. Chem.* **1985**, *322*, 151.

21. Kellner, R.; Zippel, E.; Pungor, E.; Tóth, K.; Lindner, E. *Fresenius Z. Anal. Chem.* **1987**, *328*, 464.

22. Kollman, P.A.; Allen, L.C. *Chem. Rev.* **1972**, *72*, 283.

23. Büchi, R.; Pretsch, E.; Simon, W. *Helv. Chim. Acta* **1976**, *59*, 2327.

24. Kuntz, I.D.; Brassfield, T.S.; Law, G.D.; Purcell, G.V. *Science* **1969**, *163*, 1329.

25. Kuntz, I.D. *J. Amer. Chem. Soc.* **1971**, *93*, 514.

26. Resing, H.A.; Thompson, J.K.; Krebs, J.J. *J. Phys. Chem.* **1964**, *68*, 1621.

27. Dransfeld, K.; Frisch, H.L.; Wood, E.A. *J. Chem. Phys.* **1962**, *36*, 1574.

28. Fletcher, N.H. *The Chemical Physics of Ice*, Cambridge U.P.: Cambridge, 1970.

29. Higuti, I.; Iwagami, Y. *J. Phys. Chem.* **1952**, *56*, 921.

30. Southern,E.; Thomas, A.G. *ACS Symp. Ser. (Water Polym.)* **1980**, *127*, 375.

31. Pesek, J.J.; Pecsok, R.L. *Anal. Chem.* **1972**, *44*, 620.

32. Bair, H.E.; Johnson, G.E.; Merriweather, R. *J. Appl. Phys.* **1978**, *49*, 4976.

Chapter 7

Water Desorption From An Ion-Selective Electrode Membrane

7.1 Introduction

Liquid membrane ion-selective electrodes (ISEs) are typically composed of 66 wt% plasticizer, 33 wt% polymer and 1 wt% neutral ion carrier. The plasticizer functions as a low dielectric constant solvent for the neutral carrier and is typically a water-immiscible ester such as bis(2-ethylhexyl) adipate (DOA) or bis(2-ethylhexyl) sebacate (DOS). The polymer is almost exclusively poly(vinyl chloride) (PVC) and this simply provides structural integrity to the liquid membrane. Over the years, considerable effort has been directed towards elucidating the operation of these devices, particularly with regards to the development of membrane potentials [1-3]. The presence of water is known to be of great importance, however, the behavior and distribution of water in these liquid membranes has not been as extensively examined.

There is little information in the literature on the role of water in these plasticized PVC membranes and quantitative data is not in good agreement. Marian *et al* have estimated the diffusion coefficient of water to be 1.0×10^{-6} cm^2/s in PVC membranes plasticized with 70% 1,4-dihydroxyphenyl-bis(dibutylphosphate) using radiotracer measurements with tritiated water [4]. Thoma *et al* have also used radiotracer studies on 66% DOA/PVC membranes prepared with valinomycin [5]. A water concentration of 0.15 M and a flux of 1.7×10^{-8} mol cm^{-2} s^{-1} was reported for 200 μm thick membranes. Applying Fick's first law of diffusion to this data yields a diffusion coefficient of $\approx 2.3 \times 10^{-6}$ cm^2/s. Armstrong *et al* have used Karl Fischer water analyses to determine water concentrations in 66% DOS/PVC membranes [6]. When the membranes were exposed to water, an equilibrium water concentration corresponding to 0.43 wt% or 0.38 M was determined. The water permeation through the membranes was determined gravimetrically to be 1.2×10^{-8} mol cm^{-2} s^{-1} and, through Fick's first law of diffusion, a diffusion coefficient of 0.4×10^{-6} cm^2/s was reported. Harrison *et al* have developed a spatial imaging photometer used to measure ISE membranes incorporating various water-sensitive dyes [7,8]. They observed that the water uptake in a 66% DOA/PVC membrane is actually a complicated two stage process involving a first rapid stage with a diffusion coefficient of $\approx 10^{-6}$ cm^2/s, and a second stage with an apparent diffusion coefficient of 2×10^{-8} cm^2/s.

Recent Fourier transform infrared (FTIR) and ^1H and ^2D nuclear magnetic resonance (NMR) spectroscopic measurements have provided a more detailed study of the microscopic nature of water in an ISE membrane (*cf.* Chapter 6). These have suggested that the absorbed water phase separates into small clusters (*ca.* 0.016 μm) within the membrane. Neither NMR nor FTIR, however, were able to provide reliable determinations of the actual amounts of water which enter the membrane. Accurate integrations of the absorbed H_2O ^1H NMR signals are difficult due to imprecise placement of the sample relative to the rf receiver coil in the spectrometer. Furthermore, the broad resonances from the membrane components are not reproducibly integrated and complicate the H_2O integrations through spectral overlap. FTIR analysis was able to indicate only relative changes in water content, and it also suffers from poor reproducibility.

In the present study, water desorption experiments were carried out in order to provide a quantitative estimate of water uptake in the ISE membrane. This was accomplished gravimetrically with an ordinary analytical balance. Additionally, a detailed investigation of the kinetics of water desorption from the membrane is presented through measurements of the weight loss as a function of time.

7.2 Experimental

Sample preparation. For water desorption experiments, large cylindrical membrane samples were prepared. Leftover pieces of various master membranes cast for a previous impedance study (*cf.* Chapter 3 and reference [9]) were first collected. These consisted of 33 wt% poly(vinyl chloride) (PVC) (Polysciences, chromatographic grade) and 66 wt% bis(2-ethylhexyl) adipate (DOA) (Fluka, Practical grade) and contained < 0.01 wt% of various alkali metal benzoate salts. Membrane casting solutions were obtained by dissolving these pieces in freshly distilled tetrahydrofuran (THF) (BDH, distilled from potassium). These were then cast into Teflon rings (inner diameter 4 cm) resting on glass plates according to the method of Craggs *et al* [10]. The dimensions of the dried membranes were approximately 4 cm diameter and 3 cm thick, as measured with vernier calipers. (Note that membranes cut for ISE electrodes in our lab are usually only *ca.* 0.6 cm diameter and 120 μm thick.) For the desorption studies, these "giant" membranes were soaked in nanopure water (Barnstead) for several weeks. Surplus water was blotted off the membrane surfaces with a tissue just prior to the desorption measurements.

Desorption measurements. Water desorption from a membrane sample was measured by weighing it as a function of time as the water-soaked membrane sample was allowed to dry at ambient conditions in motionless air. The sample weight was monitored with a Mettler AE200 electronic analytical balance equipped with an Option 011 Data Output Interface. Data acquisition was controlled with an IBM-XT computer using in-house software routines. The experimental configuration is shown in Figure 7.1. Measurements were obtained every 15 sec for the first 40 hrs and every 60 sec thereafter until a constant weight was obtained. Longterm drift of the balance was approximately ± 0.7 mg over a 24 hr period as determined from measurements with 25.0000 g calibration weights (Ainsworth, Denver Instrument Co.). The precision for replicate weight measurements was determined to be ± 0.1 mg.

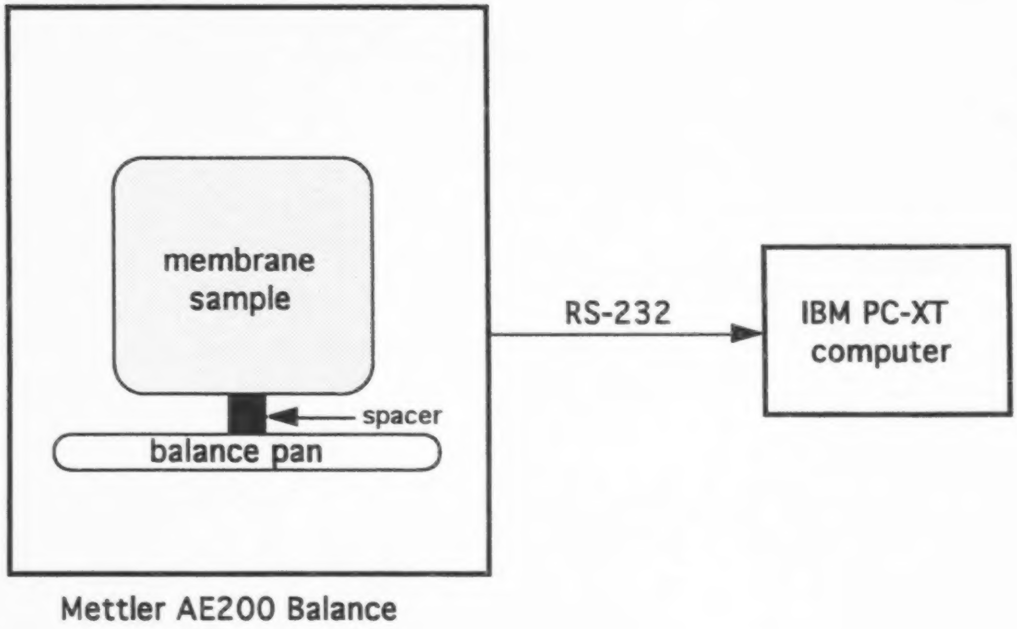
membrane
sample
spacer
balance pan
Mettler AE200 Balance
RS-232
IBM PC-XT
computer

Figure 7.1 Experimental configuration for water desorption employing a gravimetric method of measurement.

Software considerations. Weight data from the balance is provided according to the format shown in Table 7.1. This can be collected through a serial RS-232 interface to an IBM-XT computer using software routines written in either ASYST (Macmillan, version 1.5) or BASIC (Microsoft, version A2.10). These are given in Appendix B as Program B.1 (BALANCE.ASY) and Program B.2 (BALANCE.BAS), respectively. The ASYST routine was found to be unreliable for long term data acquisition due to intermittent system crashes, but the BASIC routine proved to be much more dependable. BASIC was, therefore, used exclusively for all data acquisition. The collected experimental data was subsequently transferred to ASYST via Program B.3 (READBAS.ASY) for additional data processing. Routines for theoretically modelling the diffusion process are contained in Program B.4 (DIFFUS.ASY).

7.3 Results and Discussion

7.3.1 General Effects of Water Exposure

The giant membrane samples were initially transparent, but rapidly became cloudy in appearance when exposed to water. After immersion for a few days, they then became completely white and opaque. When the membrane samples were allowed to dry at room temperature, it was observed that the original transparency was eventually restored, beginning at the outermost regions and progressing gradually towards the center of the membrane. Finally, after a few days, the entire membrane sample was completely restored to its original transparent state. A typical water desorption curve is shown in Figure 7.2. Desorption data are summarized in Table 7.2 for experiments on two separate giant membrane samples denoted by #1 and #2.

Table 7.1 Weight data format from Mettler AE200 balance with Option 011 Data Output Interface.

character block	contents
1-2	identification block(a)
3	space
4-12	weight data(b)
13	space
14	weight unit(c)
15	carriage return
16	line feed

(a) "S " stable result
"SD" unstable result
"SI" invalid result

(b) Data train is flush right and includes decimal point and sign.

(c) Units for weight data, namely "g".

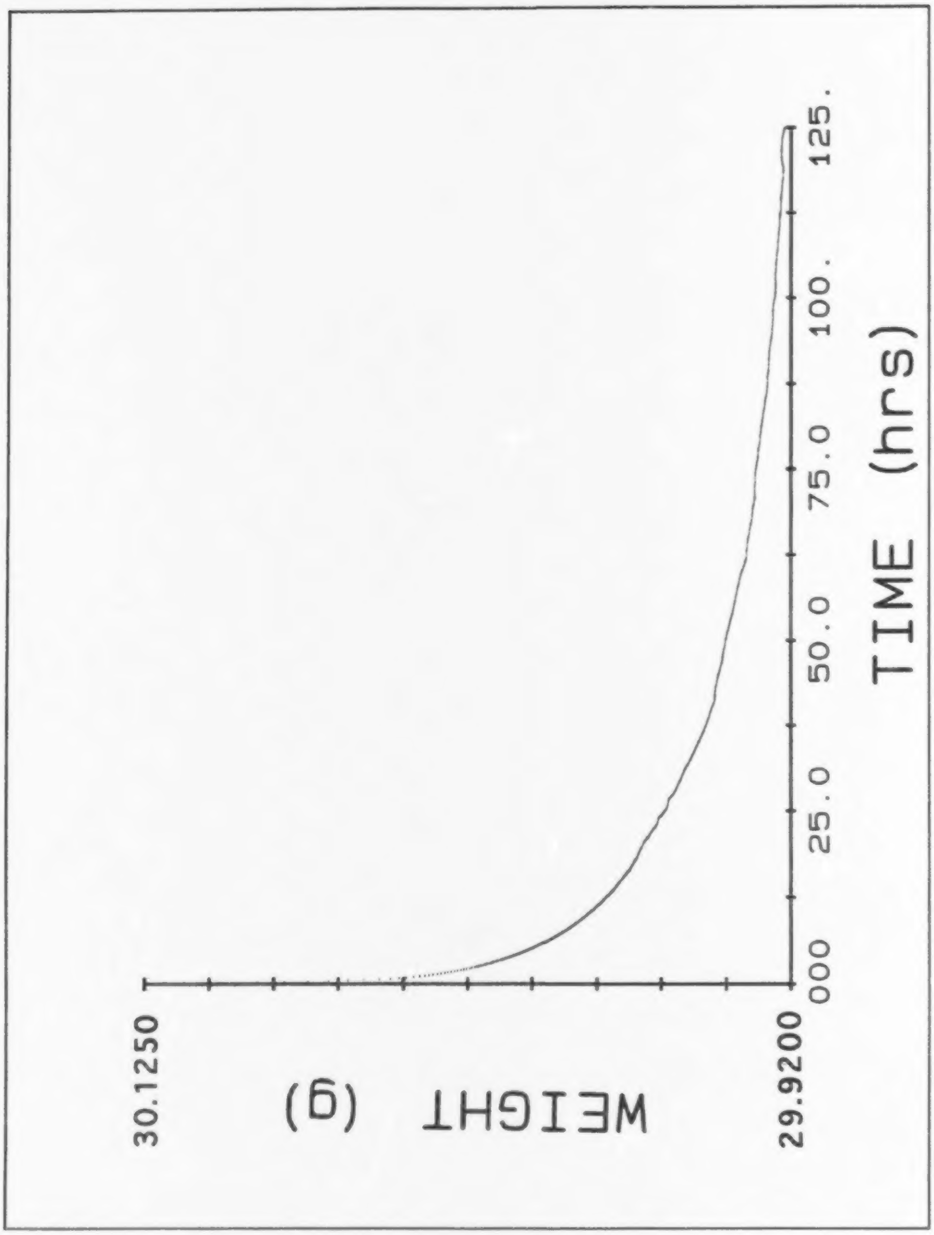

Figure 7.2 Typical water desorption curve for a 66% DOA/PVC membrane.

Table 7.2 Summary of water desorption data from 66% DOA/PVC membranes.

	membrane sample #1	**membrane sample #2**
height	2.292 cm	2.808 cm
diameter	3.556 cm	3.564 cm
surface area(a)	45.47 cm^2	51.39 cm^2
volume(b)	22.76 cm^3	28.01 cm^3
dry weight	24.8287 g	30.1241 g
H_2O absorbed	0.1354 g	0.2020 g

(a) surface area = 2π radius (radius + height)

(b) volume = π $radius^2$ height

7.3.2 Determination of Membrane Density

An accurate estimate of the density (ρ) of an ISE membrane is usually difficult to determine as a result of their small physical dimensions. This is a useful parameter, however, especially for calculating volume concentrations of deliberately incorporated additives, such as neutral carriers or lipophilic salts. From the physical measurements made on the giant membranes used in this study (Table 7.2), we can calculate an accurate density of $\rho(\text{mem}) = 1.08 \pm 0.01$ g/cm^3. The density for neat DOA is $\rho(\text{DOA}) = 0.922$ g/cm^3 [11] and the apparent bulk density of pure PVC is $\rho(\text{PVC}) \approx 1.4$ g/cm^3 [12]. Since the membranes are two-thirds plasticizer by weight, the expected density can be estimated as 2/3 ρ(DOA) plus 1/3 ρ(PVC) or 1.08 g/cm^3. This is in excellent agreement with the actual observed density for the plasticized membrane.

7.3.3 Determination of Equilibrium Water Concentration

The amount of aqueous sample solution transported through an ISE membrane is an important consideration. This is governed by the permeability of the membrane to the solution which is characterized by the product of its solubility and diffusion coefficient in the membrane.

The solubility of water in the membrane determines the total amount of water absorbed at equilibrium. From Table 7.2, we can calculate this solubility to be approximately 6.1 ± 0.9 mg of water per g of membrane or approximately 0.6 wt%. Based on $\rho(\text{mem}) = 1.08$ g/cm^3, this corresponds to a volume concentration of 0.36 ± 0.05 M. This compares favorably with values in the literature of 0.15 M [5] and 0.38 M [6] for similar 66% plasticized PVC membranes. The discrepancy for the 0.15 M value can likely be attributed to the 1% valinomycin ionophore incorporated in this particular membrane preparation. The amount of water absorbed by rubbers, for example, is strongly influenced by impurities present in the rubber [13]. Therefore, it is observed that the water solubility is very low in these heavily plasticized ISE membrane matrices. In contrast, rubber exposed to water for extended periods may absorb very large amounts of water, as much as several times the original specimen weight [14].

7.3.4 Kinetics of Water Desorption

The rate of movement of the absorbed water is characterized by its diffusion coefficient (D) in the membrane. Diffusion coefficients of liquids in solids may be determined from absorption and/or desorption data [13-16]. For example, McCall has studied the diffusion of benzene and *n*-hexane in ethylene polymers by weight loss from thin polymer slabs [16].

The mathematical aspects of diffusion have been reported and the diffusion equation has been solved for a variety of simple geometric shapes (*e.g.* cube, rod, sphere, sheet) [17]. For many purposes, such as diffusion of liquids through rubbers, a simplified approach using the simplest mathematical solution for a semi-infinite medium is adequate [13]. In this case, it is assumed that the liquid extends to infinity on one side of the boundary interface and that the sample extends to infinity on the other side. Although this approximation works well for sheets of finite thickness, however, it is not so good for rods, spheres or blocks.

7.3.4.1 Initial Interpretation of Desorption Behavior

7.3.4.1.1 Overall Desorption from a Solid Cylinder

Vergnaud [18] has recently compiled a useful treatment of diffusion in a plane sheet, in a cylinder (solid and hollow) and in a sphere. For our particular system, we are interested in diffusion from a solid cylinder of finite length, under non-steady state conditions, in which transport is both radial and longitudinal. The corresponding equation for this type of diffusion is given by:

$$\frac{\partial C}{\partial t} = D\left[\frac{\partial^2 C}{\partial z^2} + \frac{\partial^2 C}{\partial r^2} + \frac{1}{r}\frac{\partial C}{\partial r}\right] \tag{7.1}$$

where C = concentration of diffusing substance
t = time
D = diffusion coefficient
z = longitudinal diffusion axis
r = radial diffusion axis

The rate of loss of diffusing substance from a solid cylinder of finite length may be determined from solution of this diffusion equation by assuming that D is constant. We can define the dimensions of this cylinder with a radius R and a length 2L. If initially the cylinder is at a uniform concentration of C_0 throughout, and the surface concentration is kept constant at C_1, then the initial condition is:

$$C = C_0, \qquad -L < z < +L, \qquad 0 < r < R, \qquad t = 0$$

and the boundary condition is:

$$C = C_1, \qquad z = \pm L, \qquad r = R, \qquad t > 0.$$

It can be shown that the total amount of diffusing substance remaining in the cylinder, M_t, after time t can be expressed as [18]:

$$\frac{M_t}{M_\infty} = \frac{32}{\pi^2}\sum_{m=1}^{\infty}\frac{1}{\alpha_m{}^2}\exp\left[-\frac{\alpha_m{}^2}{R^2}Dt\right]\sum_{n=0}^{\infty}\frac{1}{(2n+1)^2}\exp\left[-\frac{(2n+1)^2\pi^2}{4L^2}Dt\right] \tag{7.2}$$

where $M_\infty = 2\pi R^2 L C_0$, *i.e.* the total amount of diffusing substance initially in the cylinder, and α_m are the roots of the Bessel function of the first kind of order zero given in mathematical tables [19]. These roots may also be approximated as:

$$\alpha_m = \pi\,(m - 0.25) \tag{7.3}$$

In the case of short times, equation (7.2) is reduced to [18]:

$$\frac{M_t}{M_\infty} = 1 - 4\left(\frac{Dt}{\pi}\right)^{1/2}\left(\frac{1}{R} + \frac{1}{2L}\right) \tag{7.4}$$

Thus, D can be determined by plotting M_t/M_∞ *versus* $t^{1/2}$ for the early stages of the diffusion process.

For our system, C_0 and M_∞ are the initial concentrations and amounts of water, respectively, in the soaked membranes and these may be calculated from the data in Table 7.2. M_t is the mass of water which remains in the membrane after time t. This may be calculated from the following relationship:

$$M_t = w(t) - w(\infty) \tag{7.5}$$

where $w(t)$ = weight of soaked membrane after time t
$w(\infty)$ = weight of dry membrane

A plot of M_t/M_∞ *versus* $t^{1/2}$ at short times can, subsequently, be used to calculate the average diffusion coefficient (D) from the slope according to equation (7.4).

A plot of M_t/M_∞ *versus* $t^{1/2}$ for water desorption from one of the 66% DOA/PVC membranes is given in Figure 7.3. There is an initial linear region observed up to about 30 min. This region is expanded in Figure 7.4 and the slope, from a linear regression analysis, can be used to calculate an initial diffusion coefficient ($D_{initial}$) from the short time relationship given by equation (7.4). This value for $D_{initial}$ may be then used to model the desorption behavior over the entire desorption experiment using the more general relationship for the desorption at all times given by equation (7.2). This theoretical fit to the overall experimental data using a diffusion coefficient of $D_{initial}$ is shown in Figure 7.5. Clearly, the behavior at the later stages of desorption is not at all well described by $D = D_{initial}$. By selecting a smaller value for the diffusion coefficient (D_{later}), through a

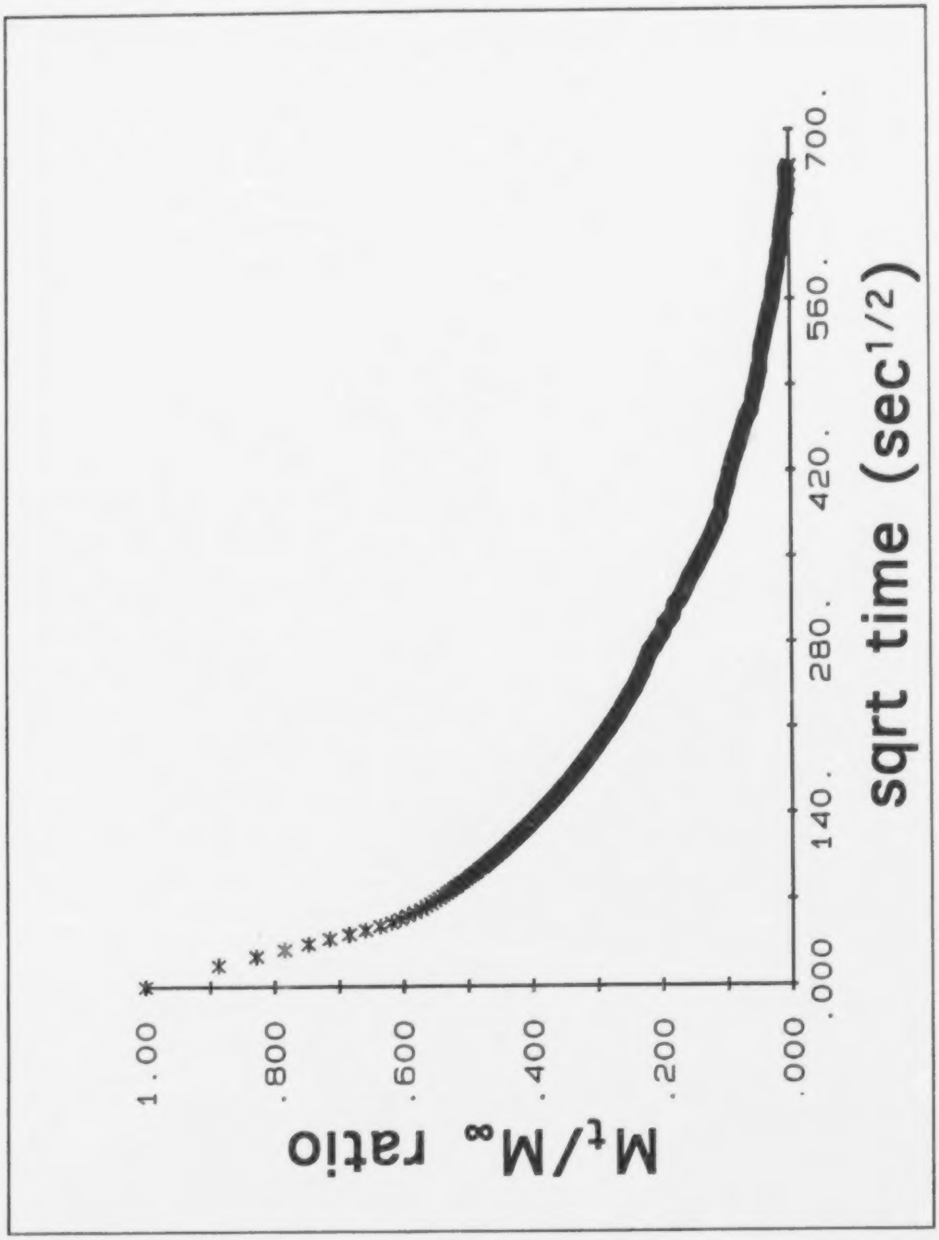

Figure 7.3 Plot of M_t/M_∞ *versus* square root of time for overall water desorption from membrane sample #2. Every tenth data point is plotted.

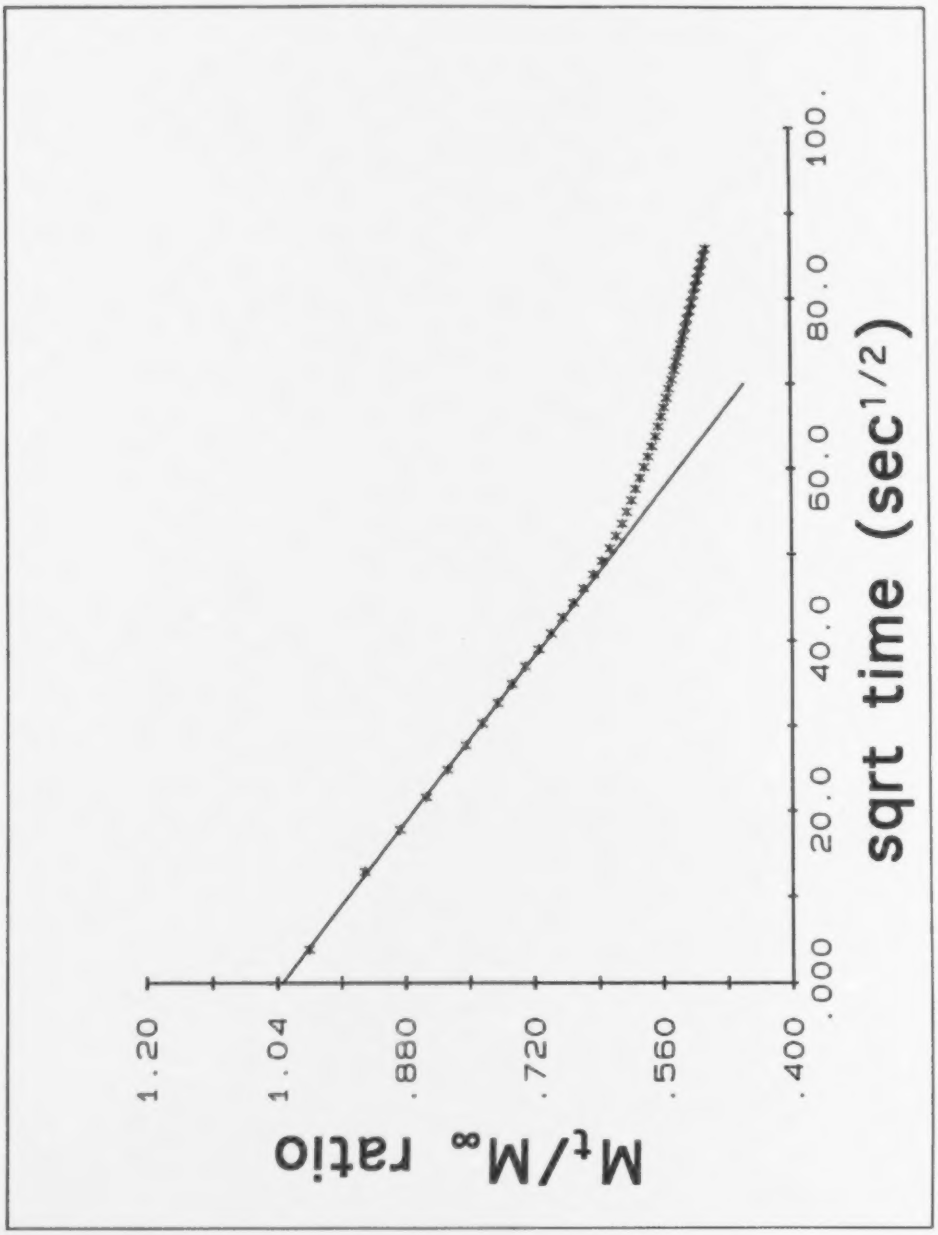

Figure 7.4 Expanded plot of M_t/M_∞ *versus* square root of time for overall water desorption from membrane sample #2. Every tenth data point is plotted. The solid line results from linear regression of the early data.

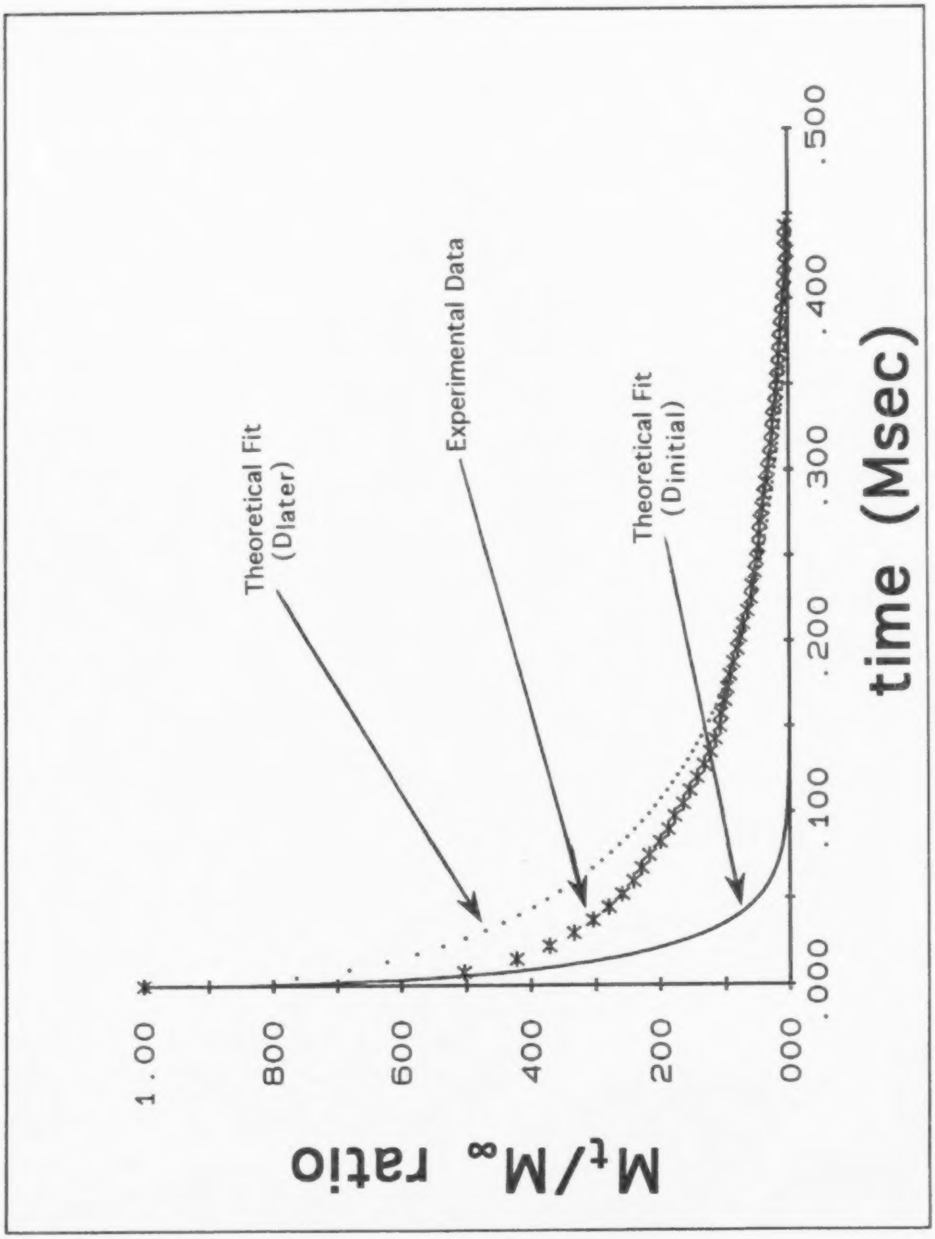

Figure 7.5 Theoretical and experimental data for overall water desorption from membrane sample #2. Points (*) represent every tenth experimental data point, solid line is theoretical fit using $D_{initial} = 1.58 \times 10^{-5}$ cm^2/s, and dotted line is theoretical fit using $D_{later} = 3.0 \times 10^{-6}$ cm^2/s.

trial and error procedure, a reasonable theoretical fit to the later stages of water desorption can be established as shown also in Figure 7.5. The use of this smaller value of $D = D_{later}$, however, can be seen to provide a very poor theoretical fit for the shorter initial stages of desorption. Calculated values for these $D_{initial}$ and D_{later} diffusion coefficients are summarized in Table 7.3 for both membrane samples.

The desorption data, therefore, suggest that water desorption from the membrane is a complex process involving two distinct stages. There is an initial rapid loss of water which occurs in the first half hour whereby water leaves the membrane with an apparent diffusion coefficient of around 1.6×10^{-5} cm^2/s. The remainder of the water in the membrane then leaves at a much slower rate with an apparent diffusion coefficient of around 3.2×10^{-6} cm^2/s. This slower diffusion coefficient, D_{later}, correlates quite well with other values for the diffusion coefficient of water reported in the literature: 1.0×10^{-6} cm^2/s [4], 2.3×10^{-6} cm^2/s [5], 0.4×10^{-6} cm^2/s [6] and $\approx 10^{-6}$ cm^2/s [7,8]. Again, differences in the data may be attributed to the presence of additives, deliberately or unintentionally incorporated into the membrane. The observed complex water desorption behavior may be correlated with related optical studies on the behavior and distribution of water by Xizhong Li in our group as outlined in the following section.

7.3.4.1.2 Correlation with Related Optical Studies

Li *et al* have developed an optical instrument that allows the concentration profiles inside an ISE membrane to be determined [7,8,20]. The distribution of water can be determined as a function of position inside the membrane, measured from the water interface, as a function of time. These results have demonstrated that water movement within the membrane is indeed a complicated progression of events which can be understood in terms of there being at least two chemical states of water within the membrane. The first type of water enters the membrane rapidly with a diffusion coefficient of around 10^{-6} cm^2/s and leads to a uniform

Table 7.3 Summary of calculated results for water desorption from overall membrane.

	membrane sample #1	**membrane sample #2**
M_∞	0.1354 g	0.2020 g
volume	22.76 cm^3	28.01 cm^3
[H_2O]	0.33 M	0.40 M
$D_{initial}$	1.57 x 10^{-5} cm^2/s	1.58 x 10^{-5} cm^2/s
D_{later}	3.5 x 10^{-6} cm^2/s	3.0 x 10^{-6} cm^2/s
desorption time	83.3 hrs	125.0 hrs

distribution of water throughout the membrane. This first rapid ingress of water appears to cause little perturbation and can be attributed to the uptake of water dissolved in the membrane matrix. The second form is associated with a phase transformation leading to the formation of light scattering centers, presumed to be water droplets. This moves much slower with an apparent diffusion coefficient that is time and additive concentration dependent, but is in the range of 10^{-8} cm^2/s initially. This has been shown to decrease with time leaving a water rich surface region.

Figure 7.6, obtained by Xizhong Li, shows a typical light scattering profile in a valinomycin membrane after 40 hrs of exposure to water on both sides. In general, the distribution is uniform in the central region with weak light scattering observed. A large change is observed at the edges, however, and this has been attributed to a water rich surface region. This water distribution requires ≈ 24 hrs to develop and it is stabilized within 40 hrs. When the water is removed from one interface (Figure 7.6), however, the water rich region at the surface disappears very rapidly, in ≈ 15 min. Also, the decrease in light scattering in the bulk of the membrane appears as a moving front, rather than as a Fickian diffusion process distributed across the entire bulk region.

We can now, therefore, evaluate the observed water desorption behavior with respect to the results from Li *et al.* The initial rapid loss of water that was seen to occur in the first half hour can be attributed to desorption from this water rich surface region. This is then followed by a diffusion of water from the rest of the membrane phase. In contrast to the optical experiments, however, another stage of water movement with a diffusion coefficient ≈ 10^{-8} cm^2/s was not resolved. Water desorption measurements by gravimetry determine only the total loss of water mass from the membrane sample. Any phase transformation (droplet formation or otherwise) in the membrane phase should not have any effect unless this somehow impeded the overall movement of water out of the membrane.

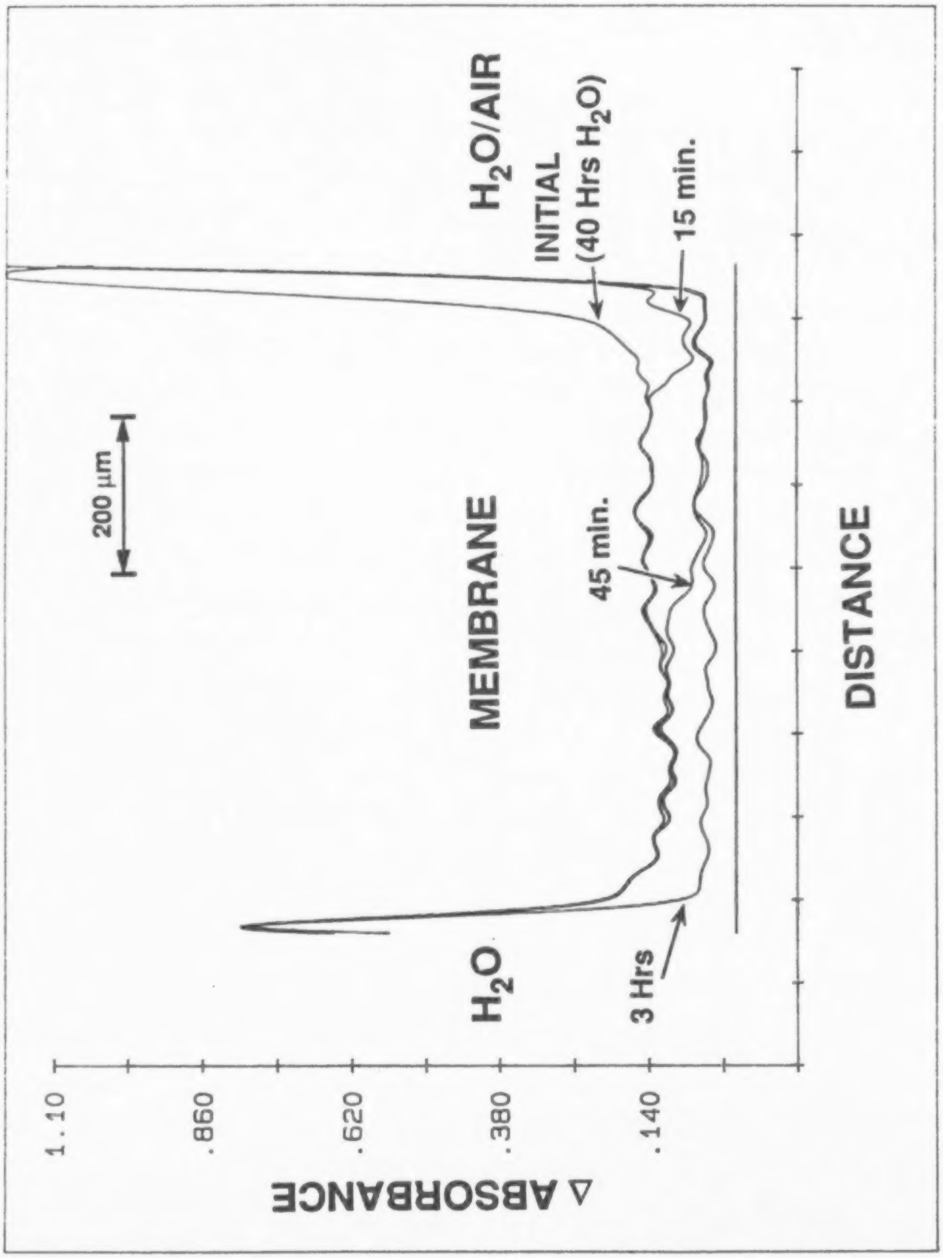

Figure 7.6 Light scattering profile in a 66% DOA/PVC membrane containing valinomycin after 40 hrs equilibration with water on both sides. A decrease in absorbance with time is then initiated when water is removed from the right side. (Taken from reference [20].)

7.3.4.2 Modified Interpretation of Desorption Behavior

The measured desorption behavior is re-interpretted in this section, based on the results of the optical experiments conducted by Li *et al*. The essence of this modified interpretation is to consider that water in the membrane exists in two separate physical regions. Thus, the overall water desorption can be treated as desorption from these two regions: (1) water is initially desorbed from a water rich surface region in the membrane, and (2) this is then followed by desorption of the remaining dissolved water from the bulk regions of the membrane.

7.3.4.2.1 Initial Desorption from a Surface Rich Region

The width of the water rich surface region depends on both the concentration and the nature of additives incorporated into the membrane phase [7,20]. The thickness of this region has been shown to decrease with decreasing hydrophilicity of the additive. For example, the region is about 90 μm thick for 0.05 % $CoCl_2$ additive and about 20 μm thick for a standard K^+-sensitive membrane containing valinomycin and $KBPh_4$. In comparison to the macroscopic dimensions of the "giant" membrane samples studied, the width of this region can be justifiably considered as insignificant. The water desorption from the surface rich region may, therefore, be modelled as non-steady state diffusion from a plane sheet so thin that all the diffusing substance enters or leaves through the parallel faces with negligible amounts through the edges.

The diffusion in such a plane sheet of material is a well-studied system [17,18]. We can define the thickness of this sheet as 2B and consider one-dimensional diffusion in the material along the x-axis (normal to the surface) and bounded by the two parallel faces at $x = B$ and $x = -B$. If initially the sheet is at a uniform concentration of C_o, and the surfaces are kept at constant and equal concentrations C_1, then the initial condition is :

$$C = C_o, \qquad -B < x < +B, \qquad t = 0$$

and the boundary condition is:

$$C = C_1, \qquad x = \pm B, \qquad t > 0.$$

It can be shown that the total amount of diffusing substance remaining in the sheet, M_t, after time t can be expressed as [17]:

$$\frac{M_t}{M_\infty} = \frac{8}{\pi^2} \sum_{n=0}^{\infty} \frac{1}{(2n+1)^2} \exp\left[- \frac{(2n+1)^2 \pi^2}{4B^2} Dt \right] \tag{7.6}$$

where M_∞ is the total amount of diffusing substance initially in the sheet. In the case of short times, equation (7.6) is reduced to [18]:

$$\frac{M_t}{M_\infty} = 1 - \frac{2}{B} \left(\frac{Dt}{\pi} \right)^{1/2} \tag{7.7}$$

Thus, D can be determined by plotting M_t *versus* $t^{1/2}$.

For our particular system, however, there is actually only desorption at one surface since water is evaporating from the surface rich region into the atmosphere. The other surface may be considered to be totally impermeable. In order to evaluate the solution to this problem, the concept of reflection at a boundary may be invoked [17]. In the original problem, half of the diffusing substance was moving in the direction of positive x and the other half in the direction of negative x. With an impermeable boundary at $x = 0$, however, all the diffusion must now occur in the direction of positive x. We can consider the original diffusion going in the direction of negative x to be now reflected in the plane $x = 0$ and superposed on the diffusion already going in the direction of positive x. Thus, the overall rate of loss of diffusing substance from the plane sheet will be the same for both cases and equations (7.6) and (7.7) will still be valid. Under otherwise identical conditions, however, the concentration of diffusing substance at any point in the actual diffusion region, $0 < x < B$, will be twice as high compared to the corresponding position (relative to $x = 0$) for the case with diffusion going in both directions, $-B < x < +B$.

From Figure 7.4, the plot of M_t/M_∞ *versus* $t^{1/2}$ used for the first interpretation of water desorption, there appears to be a discontinuity in the behavior in the vicinity of around 60 min. This point in time can be taken as the approximate time for which desorption of water from the surface region of the membrane is completed. The mass of water, M_t, which remains in the surface region of the membrane after time t can, therefore, be calculated by using an expression analogous to equation (7.5):

$$M_t = w(t) - w(3600) \tag{7.8}$$

where $w(t)$ = weight of soaked membrane after time t

$w(3600)$ = weight of soaked membrane after 3600 sec (*i.e.* when the surface region is dry)

In equation (7.8), t is clearly restricted to the time interval $0 \leq t \leq 3600$ sec. The total amount of water, M_∞, initially present in the surface region can be evaluated from this equation when t = 0 sec.

The desorption of water from the surface region can be determined by plotting the ratio M_t/M_∞ *versus* $t^{1/2}$, according to the short time relationship given by equation (7.7). Such a plot is shown in Figure 7.7 and there is indeed a substantial linear region observed. From a linear regression analysis, the slope of this plot can be used to calculate a diffusion coefficient for water desorption from the surface region ($D_{surface}$). A value of B = 20 μm was chosen for the thickness of the water rich surface region. The results of these calculations are summarized in Table 7.4 for both membrane samples. It should be pointed out that the errors in estimating B will produce corresponding errors in the values calculated for $D_{surface}$. The light scattering changes are not abrupt between the surface and bulk regions, and the exact behavior depends on membrane composition.

The substantial linear region observed in Figure 7.7, in fact, is perhaps a bit surprising. By definition, the slope of M_t/M_∞ *versus* $t^{1/2}$ should be zero when $M_t/M_\infty = 0$. We should, therefore, expect the slope in the plot to begin to decrease noticeably at longer times when $M_t/M_\infty < 0.5$. The simplest explanation for this paradox is that the time required to

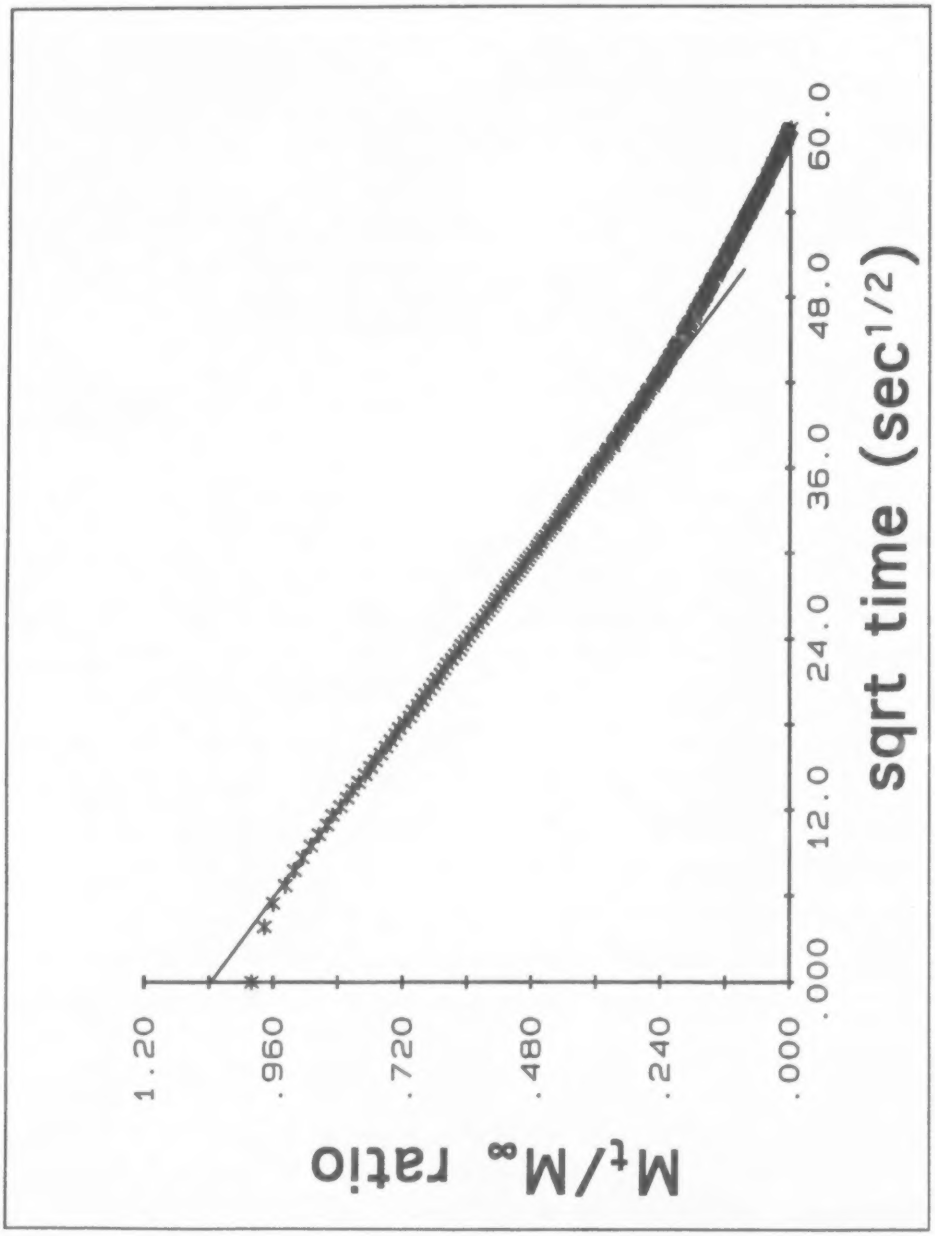

Figure 7.7 Plot of M_t/M_∞ *versus* square root of time for water desorption from surface region of membrane sample #2. The solid line results from linear regression of the early data.

Table 7.4 Summary of calculated results for water desorption from surface region of membrane.

	membrane sample #1	**membrane sample #2**
M_∞	0.0593 g	0.0842 g
volume$^{(a)}$	0.091 cm^3	0.103 cm^3
$[H_2O]$	36.2 M	45.5 M
$D_{surface}$	3.09×10^{-10} cm^2/s	2.94×10^{-10} cm^2/s
desorption time	3600 sec	3600 sec

(a) Assuming a thickness of 20 μm for the surface region.

completely dry the surface region has been grossly underestimated, *i.e.* the M_t/M_∞ ratio is actually far from zero at t = 3600 sec. This is rather unlikely, however, based on the light scattering profile in Figure 7.6 which clearly shows the disappearance of the surface rich water region after about 45 min. Instead, it is most likely that the surface rich region is essentially dried out by around 30 to 45 min, and it is water desorption from the bulk membrane region that is contributing to an apparently greater rate of desorption. This will also lead to errors in the calculation of $D_{surface}$. Alternatively, the substantial linear region observed might actually be real thereby suggesting that the rate of water desorption from the surface region is increasing as the water leaves. It has been reported that the M_t/M_∞ *versus* $t^{1/2}$ relationship for desorption does tend to hold up to substantially lower values of M_t/M_∞ for a diffusion coefficient which increases with decreased concentration [21]. For example, the diffusion coefficient of water in polyisoprene rubber containing 0.1% NaCl has been found to be inversely proportional to the square of the water concentration [13]. Clearly, the nature of the present desorption experiment does not allow any definitive conclusions to be reached regarding the desorption behavior of the surface rich water region in the later stages.

7.3.4.2.2 Subsequent Desorption from a Solid Cylinder

After the initial desorption of water from the surface rich region, the desorption of the remaining water in the membrane bulk can be modelled as subsequent desorption from a solid cylinder using equations (7.2) and (7.4). Based on the discussions from the preceding section, we can estimate that this desorption from the bulk interior begins to occur after ≈ 30 min. At this point in time, the majority of the surface water has presumably already all desorbed. Unlike the preceding model for desorption from the surface region, the accuracy in this estimate is not expected to be critical given the very long overall desorption times involved. The mass of water, M_t, which remains in the membrane bulk after any time t can be calculated using the same expression given by equation (7.5):

$$M_t = w(t) - w(\infty) \tag{7.9}$$

where t = overall experiment time - 1800 sec

since time zero for the bulk desorption process begins one half hour (*i.e.* 1800 sec) after the overall desorption experiment has been initiated. The total amount of water, M_∞, initially present in the membrane bulk can be calculated from equation (7.9) when $t = 0$ sec.

A plot of the ratio M_t/M_∞ *versus* $t^{1/2}$ for membrane bulk water desorption is given in Figure 7.8. The diffusion coefficient (D_{bulk}) can be calculated from the slope of the linear region at short times according to the short time relationship given by equation (7.4). These results are given in Table 7.5 for both membrane samples. The value for D_{bulk} may then be used to model the overall desorption behavior from the bulk region, using the more general relationship for the desorption at all times given by equation (7.2). This theoretical fit is shown in Figure 7.9. It can be seen that this analysis provides a much better fit compared to the original interpretation which did not assume an initial prior desorption of water from a water rich surface region (*cf.* Figure 7.5).

7.3.5 Proposed Interpretation of Desorption Behavior

The proposed model for the behavior of water in an ISE membrane can now be summarized. The initial distribution of water within a membrane soaked in water can be regarded as generally uniform in the bulk region with a concentration of ≈ 0.25 M. At the surface (≈ 20 μm), however, there appears to exist a water rich region with a concentration of ≈ 41 M. This region accounts for approximately 43 % of the total mass of water absorbed by the membrane.

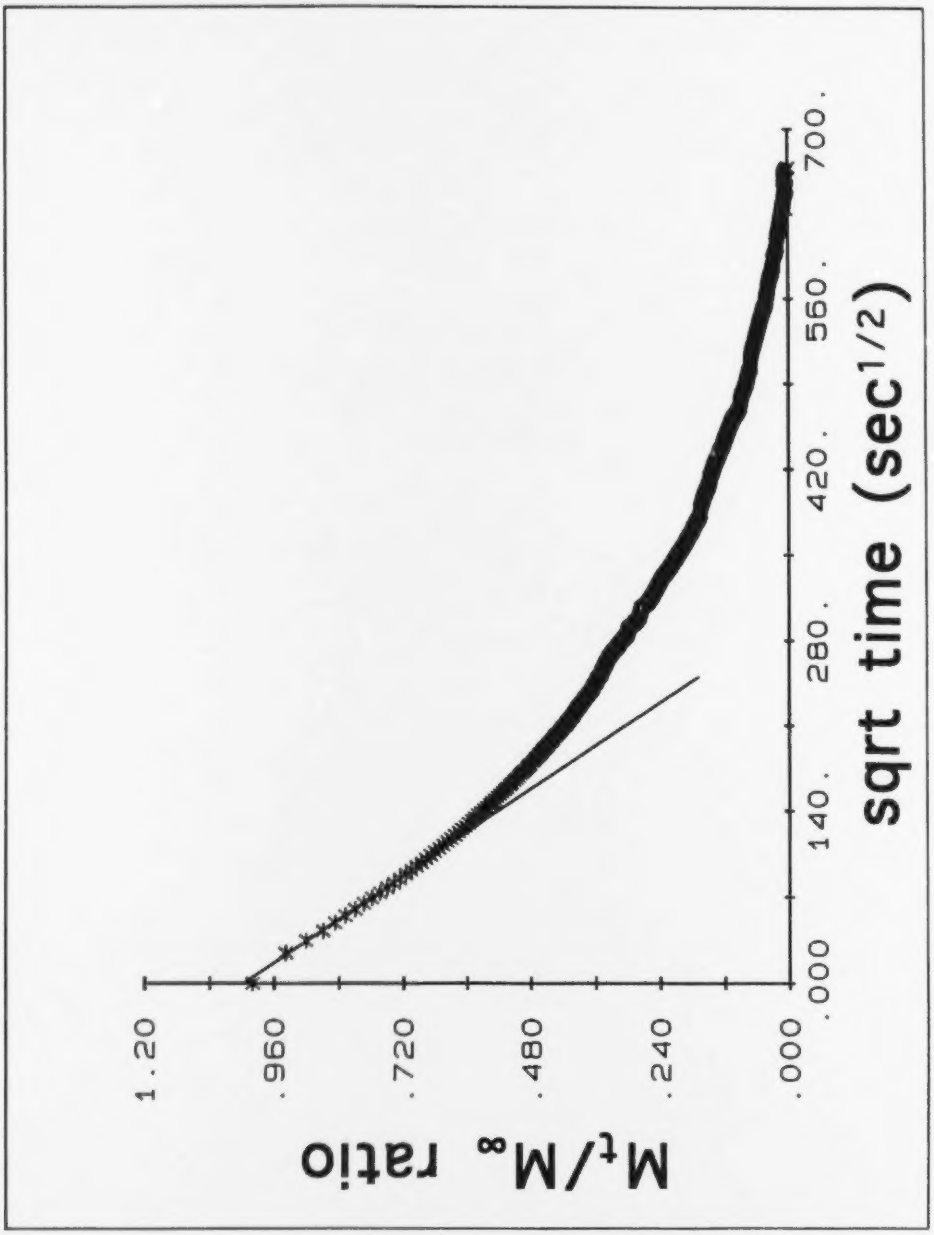

Figure 7.8 Plot of M_t/M_∞ *versus* square root of time for water desorption from bulk region of membrane sample #2. Every tenth data point is plotted. The solid line results from linear regression of the early data.

Table 7.5 Summary of calculated results for water desorption from bulk region of membrane.

	membrane sample #1	**membrane sample #2**
M_∞	0.0946 g	0.1331 g
volume[(a)]	22.67 cm^3	27.91 cm^3
$[H_2O]$	0.23 M	0.26 M
D_{bulk}	3.3 x 10^{-6} cm^2/s	2.7 x 10^{-6} cm^2/s
desorption time	82.8 hrs	124.5 hrs

(a) bulk volume = total volume - surface region volume

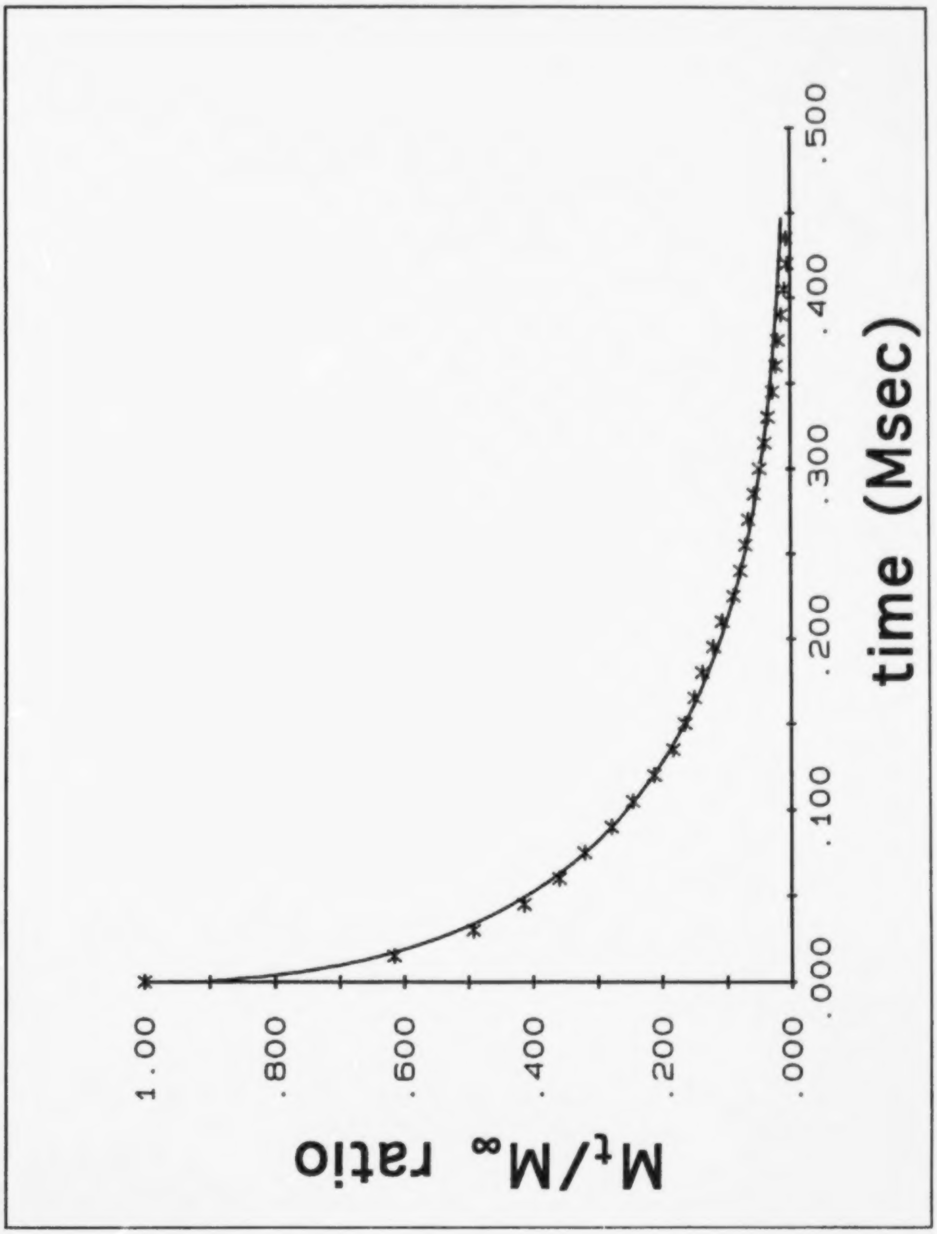

Figure 7.9 Theoretical and experimental data for water desorption from bulk regions of membrane sample #2. Points (*) represent every twentieth experimental data point, and solid line is theoretical fit using $D_{bulk} = 2.7 \times 10^{-6}$ cm^2/s.

The measured properties for the two distinct states of water in the membrane are summarized in Table 7.6. For comparison, the corresponding properties for pure water are also shown. (The control experiment for the evaporation of pure water demonstrates that the rate of water transport in the polymer is rate limiting, not the rate of water evaporation.) It can be seen that the surface region consists mostly of water, but unlike pure water it moves with a diffusion coefficient that is five orders of magnitude slower. In contrast, the bulk membrane has about a 165-fold lower concentration of water, but it moves much faster with a diffusion coefficient of about four orders of magnitude faster than the water in the surface region.

7.4 Conclusions

When the membrane is allowed to dry, there is an initial rapid loss of water in the first half hour. The water appears to be moving out very rapidly with an "apparent" diffusion coefficient of $\approx 1.6 \times 10^{-5}$ cm^2/s. This first stage, however, is believed to be due entirely to desorption of water from the surface rich region and, therefore, does not truly represent water movement out of the entire membrane sample. The actual diffusion coefficient of water from this surface region has been estimated to be 3.0×10^{-10} cm^2/s. The exact value, however, depends on the accuracy of the estimate of the surface region thickness, and the mass of water initially in this region. Following the desorption of water from the surface region, the remaining dissolved water in the bulk region leaves with a diffusion coefficient of around 3.0×10^{-6} cm^2/s.

Table 7.6 Summary of measured properties of water in a 66% DOA/PVC membrane.

	bulk region	surface region	total membrane	pure water
wt% H_2O	0.41 ± 0.04	68 ± 11	0.61 ± 0.09	100
$[H_2O]$ (M)	0.25 ± 0.02	41 ± 6	0.36 ± 0.05	55.5
D (cm^2/s)	3.0×10^{-6} $\pm 0.4 \times 10^{-6}$	3.0×10^{-10} $\pm 0.1 \times 10^{-10}$	(a)	$\approx 2 \times 10^{-5}$ (b)
avg. flux ($ng/s*cm^2$)	6.4 ± 0.8	410 ± 60	9.3 ± 0.8	3255 (c)

(a) Total water in the membrane not well-described by a single diffusion coefficient.

(b) Self-diffusion coefficient for water [22].

(c) Measured from rate of desorption of water from a 50 mL beaker.

7.5 References

1. Morf, W.E. *The Principles of Ion-Selective Electrodes and of Membrane Transport*, Elsevier: New York, 1981.

2. Morf, W.E.; Simon, W. *Helv. Chim. Acta* **1986**, *69*, 1120.

3. Armstrong, R.D.; Horvai, G. *Electrochim. Acta* **1990**, *35*, 1.

4. Marian, S.; Jagur-Grodzinski, J.; Kedem, O.; Vofsi, D. *Biophysical J.* **1970**, *10*, 901.

5. Thoma, A.P.; Viviani-Nauer, A.; Arvanltis, S.; Morf, W.E.; Simon, W. *Anal. Chem.* **1977**, *49*, 1567.

6. Armstrong, R.D.; Handyside, T.M.; Johnson, B.W. *Corrosion Sci.* **1990**, *30*, 569.

7. Harrison, D.J.; Li, X. *IEEE Int. Conf. on Solid-State Sensors and Actuators, Tech. Digest*, p.777, San Francisco, June 1991.

8. Li., X; Petrovic, S; Harrison, D.J. *Sensors and Actuators* **1990**, *B1*, 275.

9. Verpoorte, E.M.J.; Harrison, D.J. "Calibration of Anion Permeation in K^+-Ion Selective Electrode Membranes Using Impedance Methods", in press.

10. Craggs, A.; Moody, G.J.; Thomas, J.D.R. *J. Chem. Ed.* **1974**, *51*, 541.

11. *CRC Handbook of Chemistry and Physics,* 62nd ed.; Weast, R.C., Astle, M.J., Eds.; CRC Press: Boca Raton, 1981.

12. *Encyclopedia of PVC*, 2nd ed., vol.1; Nass, L.I., Heiberger, C.A., Eds.; Marcel Dekker: New York, 1986.

13. Southern, E. *Rubber Offshore Eng., Proc. Conf.*. Stevenson, A., ed. Hilger: Bristol, p.262, 1983.

14. Briggs, G.J.; Edwards, D.C.; Storey, E.B. *Rubber Chem. and Tech.* **1963**, *36*, 64.

15. Thomas, A.G.; Muniandy, K. *Polymer* **1987**, *28*, 408.

16. McCall, D.W. *J. Polym. Sci.* **1957**, *26*, 151.

17. Crank, J. *The Mathematics of Diffusion*, 2nd ed. Clarendon Press: Oxford, 1975.

18. Vergnaud, J.M. *Liquid Transport Processes in Polymeric Materials*, Prentice-Hall: Englewood Cliffs, New Jersey, 1991.

19. *CRC Standard Mathematical Tables,* 25th ed.; Beyer, W.H., Ed.; CRC Press: Boca Raton, 1978.

20. Li, X., Ph.D. Thesis, University of Alberta, Edmonton, in preparation.

21. Park, G.S. in *Diffusion in Polymers*, Chapter 5; Crank, J., Park, G.S., Eds.; Academic Press: London, 1968.

22. Eisenberg, D.; Kauzmann, W. *The Structure and Properties of Water*, Oxford Univ. Press: London, 1969.

Chapter 8

Quantitative Measurements of Membrane Adhesion onto Solid Substrates

8.1 Introduction

Integrated potentiometric sensors such as the ion-sensitive field effect transistor (ISFET) have borrowed from existing ion selective electrode (ISE) technology to produce solid-state devices specific to a variety of ions. In these devices, a conventional ion-sensitive membrane is cast directly on the solid surface with no internal reference electrolyte solution [1-3]. The typical poly(vinyl chloride) (PVC) based liquid-liquid junction membranes used with an ISE, however, are not ideally suited to application with these devices. Problems with membrane performance and lifetime arise.

An inherent problem is the poor adhesion of the membrane to the surface of the integrated sensor. The gradual detachment of the membrane can lead to unpredictable electrochemical potential and limit the lifetime of the device by forming electrolyte shunts around the membrane [3-4]. This problem has been addressed by mechanical attachment of the membrane [4], use of other materials [5-6], and modification of the existing PVC matrix [7-9]. Harrison *et al* have reported improved membrane adhesion via chemical modification of the PVC backbone [8-9]. An OH functionality is introduced at about 0.7 wt% and this site is covalently bound to hydroxyl-bearing surfaces via reaction with a hydrolytically unstable compound such as $SiCl_4$. Commonly, the active region of a chemically sensitive semiconductor device is SiO_2, Si_3N_4, Al_2O_3 or metallic (*i.e.* metal oxide) [1,10], and all of these materials can be silanized by reaction with hydrolytically unstable silane derivatives. These PVC-OH based membranes have shown significantly improved adhesion to glass and Si surfaces with minimal changes in electrochemical properties.

The mechanical adhesion of a membrane to a given substrate is clearly an important parameter. Common methods for characterizing this property, however, can be hard to reproduce and may be subject to several problems. These include the tape, blister, scratch/scrape, ultrasonic bath and peel tests, as briefly described in reference [11]. The simple Scotch Tape® test has been previously used to indicate the adhesive qualities of various hydroxyl-modified membranes [8]. This involves cutting the membrane, still mounted on the original substrate on which they were cast, into small squares, applying adhesive tape to the membrane, peeling off the tape and finally observing the percentage of squares that were removed from the substrate. Unfortunately, this popular method for characterizing adhesion is only semi-quantitative and often imprecise [11]. The adhesion of the tape can vary with membrane material and this may make comparisons between different types of membrane matrices difficult. Furthermore, it cannot be used on wet membranes which is the condition of most interest.

Brown *et al* have recently reported the development of an ingenious peel test that is capable of quickly yielding precise, quantitative results for both wet and dry membranes [11-12]. In this method, a programmable diamond saw is first used to cut a scribe lane along the center of the substrate (*e.g.* a silicon wafer). The membrane is then cast in a glass ring placed on the frontside centered over the backside scribe lane. After curing, mounting brackets are attached to the backside on either side of the scribe lane. The wafer is then cleaved along the scribe lane and folded forward so that the membrane halves are touching. Membrane adhesion is determined finally by mounting one half to the travelling crosshead of a tensilometer and the other half to a stationary grip. The membrane is then peeled away from the substrate with a constant pulling rate and peel angle. A load cell monitors the pulling force at the membrane/substrate interface as the membrane is peeled. The maximum force value recorded is considered the best representation of the adhesion of the membrane material.

In the present study, the adhesive characteristics of PVC-OH to silicon are re-evaluated using the peel test described by Brown *et al.* As well, the adhesive strengths of new membrane matrices plasticized with polyesters are assessed.

8.2 Experimental

Polymers. Three different polymers were used. Normal PVC was used as received (Polysciences, chromatographic grade). Hydroxyl-substituted PVC derivatives were prepared by Alem Teclemariam through $LiAlH_4$ reduction of 1.8 wt% carboxylated PVC (Aldrich) and 90/10 wt% vinyl chloride/vinyl acetate copolymer (Scientific Polymer Products) as previously described [8]. These are referred to as PVC-OH and PVC-OH(Ac), respectively.

Plasticizers. Three different plasticizers were used. The first was conventional bis-(2-ethylhexyl) adipate (DOA) (Fluka, Selectophore grade). The other two were proprietary polyester plasticizers from *The C.P. Hall Company* with the trade names PlastHall™ P-650 (adipate-based, 1200 molecular weight) and Paraplex® G-25 (sebacate-based, 8000 molecular weight).

Sample preparation. Substrates were 3 cm squares cut from either native (1 0 0) Si wafers or from a wafer onto which 443 Å SiO_2 and 1382 Å Si_3N_4 had been deposited. These were cleaned by immersion into the following series of solvents: 1% HF (Mallinckrodt), H_2O (nanopure, Barnstead), CH_3OH (distilled, Mallinckrodt), $ClCH=CCl_2$ (Fisher), CH_3OH , and H_2O, and then dried at ≈ 70 °C. Membranes were cast directly onto the substrate according to published procedures [13]. First, 150 mg of plasticizer were dissolved in 3 mL of tetrahydrofuran (THF) (BDH, freshly distilled from K). Next, 75 mg of the polymer material was added. After stirring for one hour to effect complete dissolution, these casting solutions were poured into glass rings (21 mm inner diameter) centered on the frontside of the cleaned substrate. In order to maintain a uniform THF atmosphere during casting, pads of filter paper were placed over the rings and weighted down with glass Petri dish covers. $SiCl_4$ reagent (Aldrich, 99.999%), when used, was added dropwise (five drops, ≈ 0.015 mL per drop) from a freshly prepared 5 % solution in THF directly onto the substrate before the casting solution. After curing for 48 hrs at room temperature, the wafers were cleaved in half along one of the crystal planes by carefully "notching" one of the edges of the wafer with a diamond scribe. "L-shaped" brackets, made from 1 mm thick strips of sheet metal (10 mm x 5 mm), were then attached with epoxy to the backside of the wafer. A schematic diagram of the test sample is shown in Figure 8.1.

Adhesion testing. A custom-built tensile test machine (Department of Mechanical Engineering, University of Alberta) was used for the adhesion measurements. The test sample was carefully folded forward so the membrane halves were touching. One of the mounting brackets was then attached to a stationary lower grip while the other bracket was attached to an upper grip connected to a high resolution load cell mounted on a Delrin nut. The upper assembly is able to translate up or down by action of a threaded shaft linked to a variable speed DC electric motor through a reduction gearbox. A peeling rate of 0.20 mm/sec was used for all measurements. The pulling forces, measured by the load cell, were calibrated with standard weights (Ainsworth, Denver Instrument Co.). A schematic diagram of the test configuration is shown in Figure 8.2.

8.3 Results

Typical peel-force curves for different samples are shown in Figure 8.3. Results of adhesive testing for various membranes are summarized in Table 8.1. Since the samples were all of the same size, the

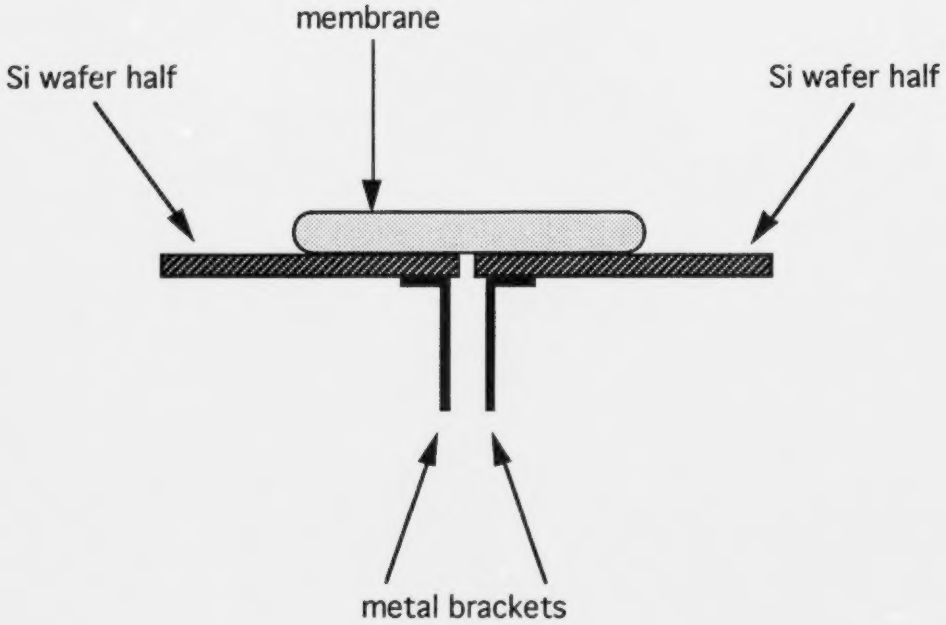
membrane
Si wafer half
Si wafer half
metal brackets

Figure 8.1 Schematic diagram of membrane sample for adhesive testing.

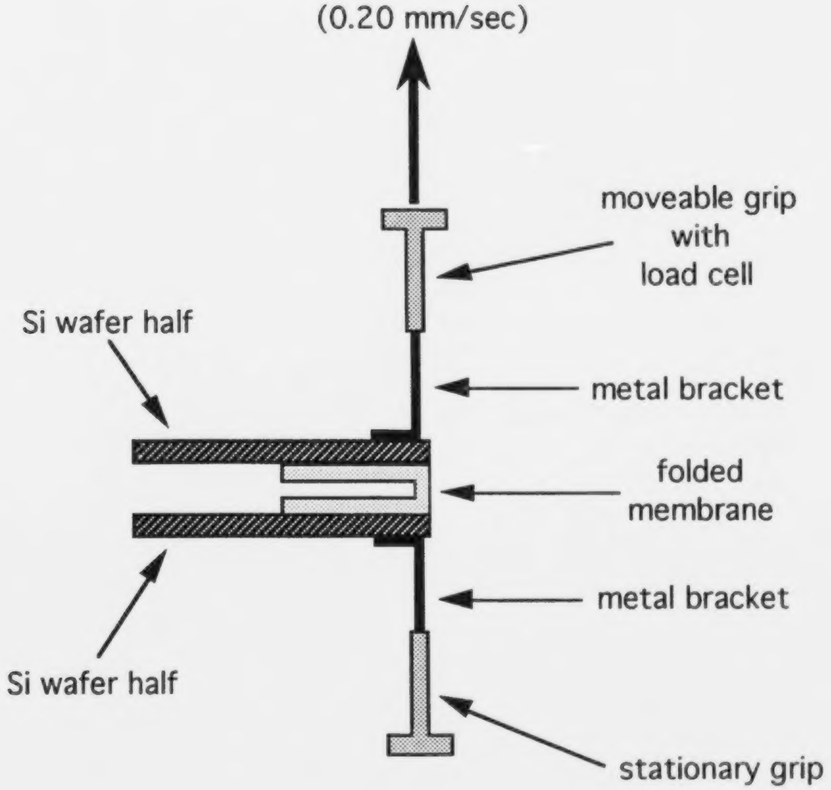
(0.20 mm/sec)
moveable grip with load cell
Si wafer half
metal bracket
folded membrane
metal bracket
Si wafer half
stationary grip

Figure 8.2 Schematic diagram of configuration for adhesive testing.

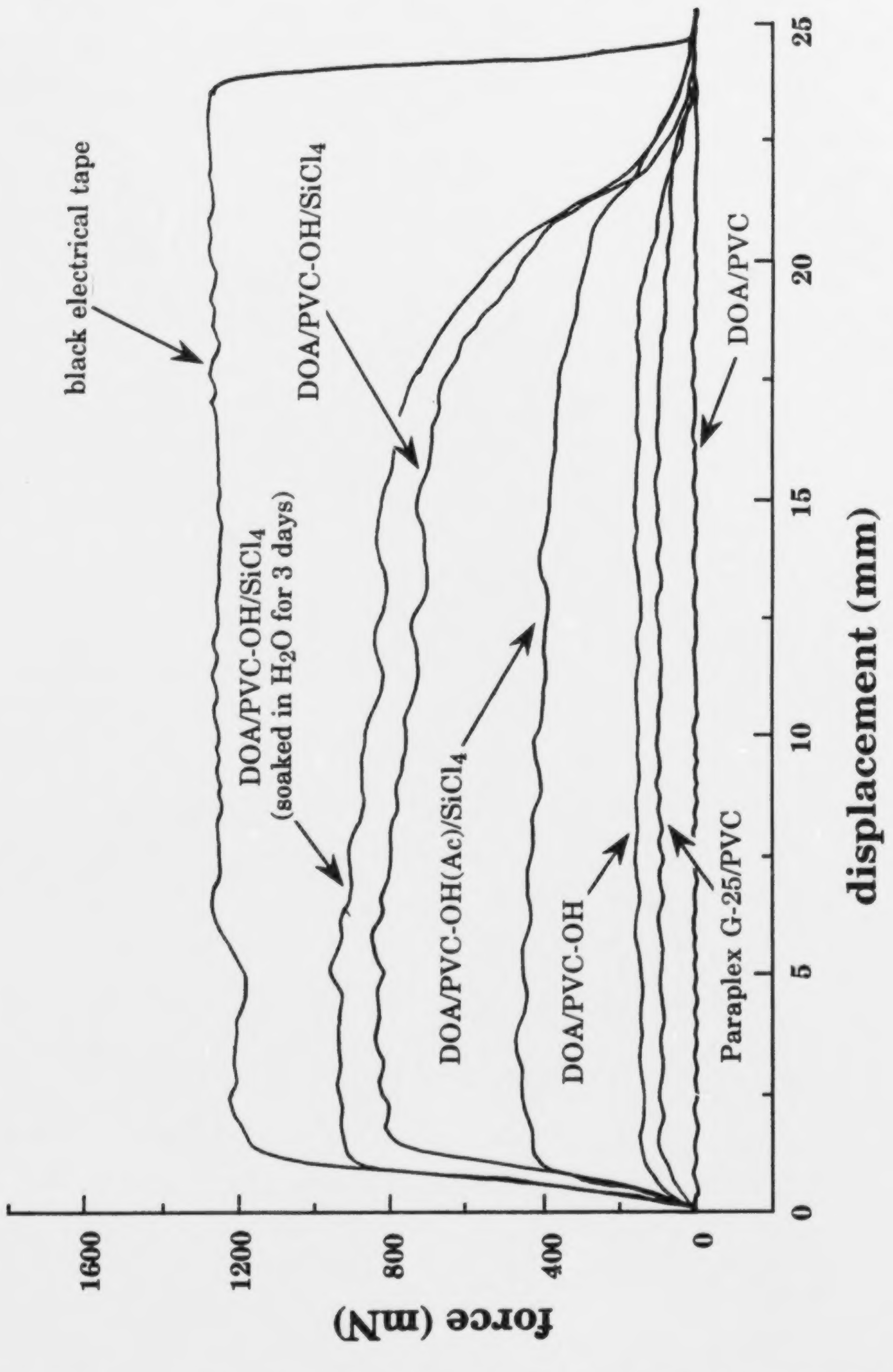

Figure 8.3 Typical peel-force curves for different samples on SiO_2 substrates.

Table 8.1 Results of adhesive testing for various samples.

sample	**surface substrate**	**max. force (mN)**
DOA/PVC	SiO_2	< 5
PlastHall P650/PVC	SiO_2	20
Paraplex G-25/PVC	SiO_2	83
DOA/PVC-OH	SiO_2	137
DOA/PVC-OH/$SiCl_4$	SiO_2	804
DOA/PVC-OH(Ac)/$SiCl_4$	SiO_2	461
DOA/PVC-OH/$SiCl_4$ (soaked in H_2O for 3 days)	SiO_2	942
DOA/PVC-OH/$SiCl_4$	Si_3N_4	1079
black electrical tape	SiO_2	1334

results are comparative. Identical membranes cast on the same day yielded results that agreed to within ≈ 2.5 % while those cast on separate days yielded results that were within ≈ 10.5 %. Relative standard deviations (RSD) of 16 % have been previously reported for measurements averaged over a larger number of samples [11].

8.4 Discussion

The data in Table 8.1 demonstrates that the conventional PVC membrane plasticized with DOA exhibits negligible adhesion to the Si surface (< 0.5 mN). Polyesters plasticizers are much less water soluble than lower molecular plasticizers, such as DOA, and are potentially useful for reducing leaching from the ISE membrane. As a result, better electrochemical performance might be expected. Slightly improved adhesion of these membranes is indicated, but the effect is not too substantial (20 - 83 mN).

The DOA/PVC-OH membrane demonstrated significantly better adhesion (137 mN), and this was drastically increased when $SiCl_4$ was incorporated during membrane preparation. These results provide concrete evidence for the importance of the OH group, which can be covalently linked by $SiCl_4$ to a surface bearing OH functionalities. These results are in perfect agreement with the ordering of bond strength determined by the Scotch Tape® test reported previously for these same materials [8]. It was observed that the adhesion of the DOA/PVC-OH membrane, however, was clearly superior to the DOA/PVC-OH(Ac) membrane (804 *versus* 461 mN). Assuming 100 % conversion of the parent polymer, PVC-OH and PVC-OH(Ac) contain ≈ 0.7 wt% and 2.0 wt% OH functionality, respectively. Referenced to the total membrane weight this corresponds to ≈ 0.2 wt% and 0.7 wt%, respectively. These observations suggest that the higher concentration of OH functionalities may in fact be detrimental to adhesive strength. From the data in Table 8.1, it can be seen that soaking the DOA/PVC-OH/$SiCl_4$ membrane in room temperature water for 3 days does not significantly alter the adhesive characteristics. (The observed apparent increase of ≈ 14 mN is within the accepted 16 % RSD). This is an important observation since chemically-sensitive solid state devices are to be primarily used in aqueous media.

Our results in this study conflict with data recently presented by Brown *et al* [11-12]. In that study, negligible adhesion (< 30 mN) was observed on Si_3N_4 surfaces for hydroxylated PVC membranes prepared with 20 wt% PVC, 20 wt% 80/5/15 vinyl chloride/vinyl acetate/vinyl alcohol copolymer (PVC/Ac/Al), 59 wt% DOA, and 1 wt% neutral carrier. This particular copolymer contains ≈ 5.8 wt% OH functionality. Referenced to the membrane weight this corresponds to ≈ 1.2 wt%. As discussed above, we have observed a decrease in adhesive strength from 804 mN to 461 mN when the concentration of OH functionality in the membrane matrix is increased from 0.2 to 0.7 wt%. By extrapolation of these results, an increase in OH functionality from 0.2 wt% to 1.2 wt% can be expected to produce a poorly adhering membrane with a maximum adhesive strength on the order of only ≈ 200 mN. Granted that this is a very simplistic interpretation, however, this suggests that the polymer OH concentration may indeed play a very significant role in optimizing adhesive characteristics. Nevertheless, the observation by Brown *et al* of a complete lack of any enhanced adhesion for membranes prepared with extensively hydroxylated PVC, compared to those prepared with normal PVC, is a bit surprising. There are a number of experimental factors, however, which may account for the observed differences in adhesive behavior between hydroxylated PVC membranes prepared in different laboratories.

$SiCl_4$ is a very moisture sensitive reagent and the actual amounts incorporated during casting are very susceptible to trace amounts of water. Accurate stock $SiCl_4$/THF solutions must be prepared fresh just prior to each casting using fastidiously dried solvent and glassware. No indication of controlling water contamination was indicated in the studies of Brown *et al* [11-12]. Furthermore, they report excellent Nernstian behavior from their ISE membranes incorporating 10 wt% of $SiCl_4$, referenced to the membrane weight. We [8] and Moody *et al* [7] have clearly shown, however, adverse effects on electrochemical slope when more than 4 wt% of $SiCl_4$ is employed. This suggests that significant hydrolysis of the silanizing reagent may have occurred in their membrane preparations.

The silanizing reagent is believed to promote a single-bridge link between the polymer and an OH functionality at the surface [7]. Better adhesion should, therefore, result when this reagent is added directly to the substrate and, in our experience, this is the case. In the procedure adopted by Brown *et al*, however, the $SiCl_4$ was mixed with the casting solution prior to application. Additionally, the fast 30 min cure employed in ambient atmosphere is not expected to result in uniform films or particularly good castings. (The standard procedure involves slow casting in a THF atmosphere).

Brown *et al*, however, have reported excellent adhesion for moisture-curable silicone rubber membranes prepared without plasticizer. Unfortunately, due to its high resistance, this material also demonstrates somewhat inferior electrochemical properties [11-12]. Maximum adhesive forces of ≈ 2250 mN were reported for these membranes, but this was decreased by ≈ 8 % after a 24 hr soak in water. Similarly, excellent adhesion of ≈ 3150 mN was reported for Tecoflex polyurethane/(PVC/Ac/Al) membranes, but this was decreased ≈ 45 % after a 24 hr soak in water. Before these new materials can be considered for applications in solid state devices, a more complete evaluation of water exposure on the effect of adhesive strength clearly must be carried out. In contrast, it can be seen from Table 8.1 that the adhesive properties of DOA/PVC-OH/$SiCl_4$ membranes do not change significantly after a 72 hr soak in water.

8.5 Conclusions

The adhesive properties of PVC-OH based membranes are quite susceptible to preparation techniques. Much more work must be done to further clarify the particular nature of the chemistry of the adhesive process. Improved mechanical attachment of membranes is required both for practical commercial implementation of existing solid state chemically sensitive devices and for emerging new sensor technologies, such as fiber optic opt(r)ode sensors [14]. The modified peel test for ISE membranes, recently reported in the literature, provides a very useful tool for evaluating this membrane characteristic.

8.6 References

1. Janata, J.; Huber, R.J. *Ion Selective Electrodes in Analytical Chemistry*; Plenum Press: New York, 1980; Vol. 2, Chapter 3.

2. McKinley, B.A.; Houtchens, B.A.; Janata, J. *Ion-Selective Electrode Rev.* **1984**, *6*, 173.

3. Janata, J. In *Solid State Chemical Sensors*; Janata, J., Huber, R.J., Eds.; Academic Press: London, 1985.

4. Blackburn, G.; Janata, J. *J. Electrochem. Soc.* **1982**, *129*, 2580.

5. Wen, C.C.; Lauks, I; Zemel, J.N. *Thin Solid Films* **1980**, *70*, 333.

6. Fujihara, M.; Fukui, M.; Osa, T. *J. Electroanal. Chem.* **1980**, *106*, 413.

7. Moody, G.J.; Thomas, J.D.R.; Slater, J.M. *Analyst* **1988**, *113*, 1703.

8. Satchwill, T.; Harrison, D.J. *J.Electroanal. Chem.* **1986**, *202*, 75.

9. Harrison, D.J.; Cunningham, L.L.; Li, X.; Teclemariam, A.; Permann, D. *J. Electrochem. Soc.* **1988**, *135*, 2473.

10. Zemel, J.N.; Keramati, B.; Spivak, C.W. *Sens. Actuators* **1981**, *1*, 427.

11. Goldberg, H.D.; Cha, G.S.; Brown, R.B. In *Technical Digest of IEEE Solid-State Sensor and Actuator Workshop*, Hilton Head Island, SC, pp. 169-172, June 1990.

12. Cha, G.S.; Liu, D.; Meyerhoff, M.E.; Cantor, H.C.; Midgley, A.R.; Goldberg, H.D.; Brown, R.B. *Anal. Chem.* **1991**, *63*, 1666.

13. Craggs, A.; Moody, G.J.; Thomas, J.D.R. *J. Chem. Ed.* **1974**, *51*, 541.

14. Seiler, K., personal communication.

Chapter 9

Conclusions

As stated in Chapter 1, one of the primary objectives in studies of ion-selective electrode (ISE) membranes is to obtain a better understanding of the ion-selective response mechanisms. Towards this end, the studies presented in this thesis have provided additional insight into the electrical and physical properties of ISE membranes. The purpose of this concluding chapter is to summarize some of the main contributions gained from this work. Also presented are suggested directions for future studies in this field, including extensions of the present work.

9.1 Summary of Contributions

A fast Fourier transform based electrochemical impedance spectroscopy (FFT-EIS) system has been developed for use in our laboratory. The capability of efficiently acquiring low frequency *AC* impedance data has been demonstrated. Using this system, the EIS method was confirmed to be a very sensitive technique for probing low levels of interfering species in the membrane. The study of benzoic acid additive showed that this neutral species has a pronounced effect not only on the bulk membrane behavior, but also on the charge transfer characteristics. This effect is not entirely unexpected since benzoic acid is dissociable, hence, its presence should affect electrical properties in the membrane. The non-monotonic dependence of electrical properties on this additive, however, was somewhat surprising, and this was interpreted on the basis of direct chemical interaction with fixed anionic sites in the membrane. Analogous studies with the non-dissociable methyl benzoate additive clearly demonstrated that direct changes in the ion concentration are only one aspect by which membrane additives can affect electrical properties. Changes in the physical characteristics of the membrane matrix can also be quite significant, and it was observed that the charge transfer resistance was a much more sensitive parameter for these effects than the bulk membrane resistance. This may prove to be very useful in the future for studying membrane permeation by neutral lipophilic species from sample solutions such as biological media.

In the study of the Ca^{+2}-sensitive ion exchanger membrane system, a plausible theory to account for inductive characteristics in the impedance of this system was developed. There is sufficient experimental data to support the existence of an adsorbed intermediate species in the transport of Ca^{+2} across the membrane/solution interface. These results justify an extension of the "closed-circuit shuttle carrier" mechanism to include adsorption of intermediate carrier-complexed species. The possibility of adsorption processes has not been previously considered within this mechanism.

The use of analytical methods other than electrochemically based methods proved to be quite useful for studying the ISE membrane system. Important information regarding physical properties was provided. Physical membrane characteristics, particularly the complex effects of water, are known to play a major role in determining electrical properties.

^{13}C NMR spin-lattice (T_1) relaxation time measurements were used to probe microscopic interactions in the membrane matrix by directly observing the effects on plasticizer and polymer mobilities. These studies showed that, within the limits of resolution of the method, the DOA/PVC matrix can be considered to be a homogeneous mixture over a wide range of plasticization. Additionally, the particular 66 wt% plasticizer composition typically used for most ISE membrane preparations did not demonstrate any unique properties in terms of mobility *versus* plasticization level. In this regard, the use of a 66 wt% DOA/PVC matrix is not significant. The membrane matrix composition should, therefore, be optimized with respect to other criteria such as structural integrity.

The studies of water in the membrane have shown that lipophilic salts, such as potassium tetraphenylborate, do not have passive effects on physical properties of the membrane. These salts are normally deliberately incorporated within an ISE membrane to enhance Donnan exclusion. Their presence, however, also affects both the concentration and distribution of water in the membrane. At low levels of salt, water in the membrane was shown to exist as small water clusters *ca.* 0.016 μm in diameter. At higher levels of salt, phase separation into larger water droplets was shown to occur. These different forms of water also were shown to perturb the membrane microviscosity as reflected by ^{13}C T_1 relaxation times. Small water clusters increased membrane microviscosity; larger water droplets decreased membrane microviscosity.

Studies of water desorption by gravimetry further demonstrated that the behavior of water in the ISE membrane is quite complex. These studies provided strong, physical evidence for the existence of a surface rich water region in the membrane. This was shown to correlate very well with conclusions obtained by a very different, optically based method using a spatial imaging photometer [1].

Another physical characteristic that was examined was the physical adhesion of ISE membranes to solid surfaces. Although this problem is not very enlightening from the perspective of understanding response mechanisms and electrical behavior, this is a very important practical consideration with respect to the development of new technologies based on these membranes. Quantitative data obtained from a modified peel-test employing a tensilometer unequivocally demonstrated that reaction of a hydroxylated PVC polymer with a hydrolytically unstable compound such as $SiCl_4$ results in enhanced membrane adhesion. This is a significant confirmation of previous studies since a recent literature publication suggests no adhesive enhancement [2].

9.2 Directions for Future Research

A logical extension of the studies involving membrane additives is to systematically evaluate the possible effects by which neutral species can affect electrical behavior. This would involve the examination of various series of additives which exhibit progressive changes in properties such as viscosity, hydrophilicity, lipophilicity and dielectric strength. Such a base of knowledge would allow *a priori* predictions of the effects of interfering species which can permeate the membrane. Also, studies should be extended into real membrane matrices which incorporate ion-sensing components and lipophilic salt. Such studies have already been carried out with respect to bulk membrane resistances [3]. It has been shown that membrane charge transfer resistances provide additional useful information that can be used to interpret impedance data. For real ISE membrane systems, however, this data may not be accessible, since these resistances are significantly reduced in real membrane systems.

The study of inductive *AC* impedance behavior in membranes should be extended to examine other membrane systems. As indicated, preliminary studies have suggested that the tris(2-ethylhexyl) phosphate and PVC matrix incorporating the nonactin ionophore also demonstrates inductive characteristics. The use of direct analytical methods to observe and measure the proposed surface adsorbed intermediate species might also be feasible (*e.g.* attenuated total reflectance infrared spectroscopy). The implications of these absorbed intermediates also has not been considered to any great extent with respect to membrane transport theories. For this, more detailed studies are required, for example, the analysis of interfacial ion-transfer kinetics with transient currents [4].

Additional information on molecular dynamics can be obtained from the temperature dependence of NMR relaxation times [5,6]. Hence, $^{13}C\ T_1$ experiments can be carried out at different temperatures to provide a more detailed look at the interaction of membrane components. For example, Maklakov *et al* [7] have used broadband ^1H relaxation studies at temperatures below 298 K to demonstrate two plasticizer states for a system of PVC plasticized with dibutyl phthalate at similar levels used for ISE membranes. Measurement of ^{1}H T_1 relaxation can also complement the information gained from the ^{13}C T_1 studies. Since very poorly resolved solution state ^{1}H spectra were observed for most of the plasticized samples, such studies would most likely entail the use of more sophisticated solid state NMR techniques involving magic angle spinning [8]. Relaxation studies of the ^{1}H nuclei from the absorbed water, however, should be feasible with simple solution phase techniques since adequate resolution of the water resonances was observed. Other than ^{13}C and ^{1}H nuclei, relaxation methods involving other nuclei have not been extensively used to study polymer systems. An investigation of molecular motion in Nafion membranes, however, has been reported using ^{19}F NMR relaxation [9]. The use of ^{39}K or ^{23}Na relaxation, however, might prove to be very useful as a direct probe of the dynamics of ionophore complexation reactions involving valinomycin provided their concentrations were high enough for detection.

The use of ^{1}H and ^{2}D NMR spectroscopy was shown to be quite useful in the study of the nature of water in the membrane. In an analogous fashion, ^{39}K or ^{23}Na NMR might also prove useful in studying the nature of K^+ and Na^+ transport in ionophore-containing systems. For example, the use of ^{35}Cl NMR has been reported in the study of chloride transport through model biological membranes [10].

All of the studies of water in the membrane have been directed towards understanding its physical behavior in the membrane matrix. Studies are also warranted which involve the effects of water on determining the electrical behavior. By correlating the results of the physical and electrical effects of water, the complex role of water in the membrane may be clarified.

The adhesion of membranes to solid substrates is very important for developing new technologies involving conventional ISE membranes. A more extensive study on more membrane materials is required to supplement the preliminary results presented. Also, the fundamental chemistry of the adhesion process needs to better understood, especially the role of polymer hydroxyl group concentrations.

Armed with a better understanding of ISE membrane properties and behavior, a more systematic approach towards optimizing existing ISE membrane systems is possible. This theoretical basis will also facilitate the transfer of existing ISE membrane technology to new configurations and technologies.

9.3 References

1. Harrison, D.J.; Li, X. *IEEE Int. Conf. on Solid-State Sensors and Actuators, Tech. Digest*, p.777, San Francisco, June 1991.

2. Cha, G.S.; Liu, D.; Meyerhoff, M.E.; Cantor, H.C.; Midgley, A.R.; Goldberg, H.D.; Brown, R.B. *Anal. Chem.* **1991**, *63*, 1666.

3. Verpoorte, E.M.J.; Harrison, D.J. "Calibration of Anion Permeation in K^+-Ion Selective Electrode Membranes Using Impedance Methods", in press.

4. Sandifer, J.R.; Iglehart, M. L.; Buck, R.P. *Anal. Chem.* **1989**, *61*, 1624.

5. Quinn, F.X.; Kampff, E.; Smyth, G.; McBrierty, V.J. *Macromolecules* **1988**, *21*, 3191.

6. Albert, B.; Jérôme, R.; Teyssié, P.; Smyth, G.; Boyle, N.G.; McBrierty, V.J. *Macromolecules* **1985**, *18*, 388.

7. Maklakov, A.I.; Maklakov, A.A.; Temnikov, A.N.; Teplov, B.F. *Polymer Sci. USSR* **1979**, *20*, 1492.

8. Fukushima, E.; Roeder, S.B.W. *Experimental Pulse NMR: A Nuts and Bolts Approach*, Addison-Wesley: London, 1981.

9. Boyle, N.G.; McBrierty, V.J.; Eisenberg, A. *Macromolecules* **1983**, *16*, 80.

10. Riddell, F.G.; Arumugam, S.; Patel, A. *J. Chem. Soc. Chem. Commun.* **1990**, 74.

Appendix A: Chapter 2 Computer Programs

```
\ ASYST FILE:          NEWWDATA.ASY

\ This program generates a waveform by a Fourier synthesis of various
\ sine waves using random phase angles.  The user is prompted for
\ the number of sine wave components along with the amplitude per
\ component.  Frequencies are entered as the number of integral wave
\ cycles per waveform period.

\              Created by:    Andy Chan
\                             January 23, 1988

\ ------------------------------------------------------------------


REAL  SCALAR COMPONENTS               \ Number of Fourier components
      SCALAR AMP                      \ Amplitude identical for components
      DIM[ 50 ] ARRAY PHI             \ Phase angle per component
      DIM[ 50 ] ARRAY WAVE.CYCLES     \ Number of wave cycles per component
      DIM[ 2048 ] ARRAY TIME          \ Arbitrary time scale for waveform
INTEGER DIM[ 2048 ] ARRAY WDATA       \ Array containing waveform data

15 STRING FILENAME                    \ Used for disk file access


:  WAVEFORM.PARAMETERS.INPUT
      NORMAL.DISPLAY
      CR ." Input number of Fourier components - " #INPUT 1 +   COMPONENTS :=
      CR ." Input amplitude per component - " #INPUT   AMP :=
      COMPONENTS 1 DO
            CR CR ." Component #" I .
            CR ." Number of integral wave cycles - " #INPUT  WAVE.CYCLES [ I ] :=
      LOOP
;

: RANDOM.PHASE.ANGLES    \ Generates array of random numbers between 0 and 2 PI
      COMPONENTS 1 DO
            RAND.UNIF 2. * PI *  PHI [ I ] :=
      LOOP
;
```

Program A.1: ASYST file NEWWDATA.ASY

```
: SINES.SUMMATION       \ Performs Fourier synthesis of the waveform
       RAD
       STACK.CLEAR
       CR CR CR ." I AM CALCULATING THE WAVEFORM . . . . . "

       TIME  []RAMP         \ Generation of an arbitrary time scale
       TIME  1.  - TIME :=  \ for the waveform

       0
       COMPONENTS 1 DO
              2. PI *  WAVE.CYCLES [ I ] * TIME * 2048 / PHI [ I ] + SIN  AMP *
              +
       LOOP
       FIX   WDATA :=
;

: SCALE.WDATA           \ Scales WDATA waveform to limits of +/- 8000 counts
       WDATA []MIN ABS  WDATA []MAX ABS  >
          IF      8000. WDATA []MIN ABS / WDATA * WDATA :=
          ELSE    8000. WDATA []MAX ABS / WDATA * WDATA :=
       THEN
;

: WDATA.SAVE            \ Saves waveform data to disk
       FILE.TEMPLATE
              2 COMMENTS
              REAL  DIM[  50  ] SUBFILE
              REAL  DIM[  2048  ] SUBFILE
       END

       NORMAL.DISPLAY
       CR CR ." Filename:  "  "INPUT " .WAV" "CAT FILENAME ":=
       FILENAME DEFER> FILE.CREATE
       FILENAME DEFER> FILE.OPEN
              " Subfile 1:   WAVE.CYCLES" 1 >COMMENT
              1 SUBFILE WAVE.CYCLES ARRAY>FILE
              " Subfile 2:   WDATA" 2 >COMMENT
              2 SUBFILE WDATA ARRAY>FILE
       FILE.CLOSE
;

: NEW.WDATA             \ Final colon definition
       WAVEFORM.PARAMETERS.INPUT
       HORIZONTAL AXIS.FIT.OFF
       BEGIN
              RANDOM.PHASE.ANGLES
              SINES.SUMMATION
```

Program A.1: ASYST file NEWWDATA.ASY (continued)

```
        TIME []RAMP  TIME WDATA XY.AUTO.PLOT
        CR CR ." Do you like    this waveform?  "
        "INPUT 1 "LEFT    " Y" "=
    UNTIL
    SCALE.WDATA
    WDATA.SAVE
    AXIS.FIT.ON
    CR CR ." WDATA limits:  "  WDATA []MIN/MAX . .
;
```

Program A.1: ASYST file NEWWDATA.ASY (continued)

```
\ ASYST FILE:          RS232.PAR

\ This program sets parameters for the PAR-273 as an ASYST RS-232 device.
\ The file contains words for communication across the interface and for
\ sending and receiving waveform data.

\               Created by:    Jed Harrison and Andy Chan
\                              January 25, 1988

\  --------------------------------------------------------------------


DIM[ 1 , 40 ] STRING.ARRAY COMM              \ Communication buffer variable
15 STRING BD.STRING                          \ BD specification string
INTEGER  DIM[ 2048 ] ARRAY DATA.L1           \ High byte data array
         DIM[ 2048 ] ARRAY DATA.L2           \ Low byte data array
         DIM[ 4096 ] ARRAY DATA.UNPACK       \ Unpacked binary format data


760    RS232.DEVICE PAR.273                  \
PAR.273                                      \
9600 SET.BAUD                                \
0 SET.PARITY                                 \ PAR-273 device configuration
8 SET.DATA.BITS                              \ for the COM2 communications
2 SET.STOP.BITS                              \ port at hexadecimal 2F8
4 SET.INT.LINE                               \
13 RS232.EOS.CHAR                            \
RS232.EOS.ON                                 \
RS232.POL.MODE                               \
DSR.ON                                       \


:  CHECK.ERROR
       42 <> IF  CR ." ERROR MAY HAVE OCCURRED IN RS232 COMMUNICATION " CR
       THEN
;

: SEND                \ Send COMM string without error check
       COMM ":=
       COMM "RS232.BUFFER
       BUFFER>RS232
       13 RS232.OUT
;

: SEND.COM            \ Send COMM string to PAR-273
       SEND
       RS232.IN
```

Program A.2: ASYST file RS232.PAR

```
        CHECK.ERROR
;

: GET.RESPONSE    \ Get a response from PAR-273 and deposit into COMM
        SEND
        RS232>BUFFER
        RS232.IN
        CHECK.ERROR
        CR COMM "TYPE
;

: CLEAR.RS232     \ Clears multiple points from RS-232 communications port
        -1 4 FIX.FORMAT
        BEGIN
                RS232.IN DUP .
                42 =
        UNTIL
;

: FIX.RS232                 \ Fixes RS-232 communication after single error
        " STIR 0
        SEND
        RS232.IN .
;


\ The following word retrieves waveform data from the PAR-273 as specified
\ by the parameters contained in BD.STRING.  The result is stored in the
\ array DATA.L2

: GET.DATA
        BEGIN
                STACK.CLEAR
                BD.STRING SEND
                2049 1 DO
                        RS232.IN  DATA.L1 [ I ] :=        \ input high byte
                        RS232.IN  DATA.L2 [ I ] :=        \ input low byte
                LOOP
                RS232.IN  42  =    ?DUP
                IF
                ELSE BELL CR ." ERROR IN RS232 COMMUNICATION " CLEAR.RS232
                THEN
        UNTIL
        DATA.L1 DATA.UNPACK SUB[ 2 , 2048 , 2 ] :=        \ combines high and low
        DATA.L2 DATA.UNPACK SUB[ 1 , 2048 , 2 ] :=        \ bytes and data stored
        DATA.UNPACK PACK DATA.L2 :=                       \ in DATA.L2
;
```

Program A.2: ASYST file RS232.PAR (continued)

```
\ The following word sends the waveform WDATA to the PAR-273.  It assumes
\ the source curve is curve 0.

: SEND.CURVE
        " NC ; BL 0,2048
        SEND
        WDATA UNPACK DUP
        SUB[ 1 , 2048 , 2 ] DATA.L2 :=     \ low byte
        SUB[ 2 , 2048 , 2 ] DATA.L1 :=     \ high byte
        2049 1 DO
                DATA.L1  [ I ] RS232.OUT     \ sends high byte
                DATA.L2  [ I ] RS232.OUT     \ sends low byte
        LOOP
        RS232.IN
        CHECK.ERROR
;
```

Program A.2: ASYST file RS232.PAR (continued)

```
\ ASYST FILE:           COMM.PAR

\ This program contains words that sets up the PAR-273 to do experiments.
\ It must be loaded after the RS232.PAR file.

\               Created by:     Andy Chan
\                               January 28, 1988

\ ------------------------------------------------------------------


\ Variable declarations for PAR-273 parameters

REAL     SCALAR   TMB.VALUE
         SCALAR   S/P.VALUE
INTEGER  SCALAR   I/E.VALUE
         SCALAR   FILTER.VALUE
         SCALAR   EGAIN.VALUE
         SCALAR   IGAIN.VALUE
         SCALAR   SAM.VALUE
         SCALAR   SWPS.VALUE
         SCALAR   PAM.VALUE
         SCALAR   BIAS.VALUE
         SCALAR   MR.VALUE
REAL     SCALAR   DELAY.VALUE


\ Settings for default parameters

500    TMB.VALUE    :=
1      S/P.VALUE    :=
- 7    I/E.VALUE    :=
0      FILTER.VALUE :=
50     EGAIN.VALUE  :=
10     IGAIN.VALUE  :=
1      SAM.VALUE    :=
16     SWPS.VALUE   :=
1      PAM.VALUE    :=
0      BIAS.VALUE   :=
0      DELAY.VALUE  :=
1      MR.VALUE     :=

REAL   DIM[ 2048 ] ARRAY IDATA        \ Current waveform
       DIM[ 2048 ] ARRAY EDATA        \ Potential waveform

: SCALE.IDATA
```

Program A.3: ASYST file COMM.PAR

```
        1000. / IGAIN.VALUE / 10. I/E.VALUE **  *
;

: SCALE.EDATA
        EGAIN.VALUE 9 > IF  10000. /  ELSE    1000. /  THEN
;

: SHOW.VALUES                \ Display list of PAR-273 parameters
        NORMAL.DISPLAY
        -1  4 FIX.FORMAT
        CR CR ." Note: These may NOT be the actual PAR-273 settings!"
        CR ." TMB.VALUE = " TMB.VALUE .
        CR ." S/P.VALUE = " S/P.VALUE .
        CR ." SAM.VALUE = " SAM.VALUE .
        CR ." SWPS.VALUE = " SWPS.VALUE .
        CR ." PAM.VALUE = " PAM.VALUE .
        CR ." FILTER.VALUE = " FILTER.VALUE .
        CR ." EGAIN.VALUE = " EGAIN.VALUE .
        CR ." I/E.VALUE = " I/E.VALUE .
        CR ." IGAIN.VALUE = " IGAIN.VALUE .
        CR ." BIAS.VALUE = " BIAS.VALUE .
        CR ." DELAY.VALUE (msec) = " DELAY.VALUE .
        CR ." MR.VALUE = " MR.VALUE .
;

:  EXPT.TIME                 \ Calculates expt time for parameter value settings
        -1  4 FIX.FORMAT
        TMB.VALUE 1.0E-6 * S/P.VALUE * 2048 * SWPS.VALUE * 60. / .  ." min
;

:  PAR.INIT                  \ Initialize PAR-273 for impedance experiments
        " MSK 0 ; DCL ; DD 44"
        SEND.COM
        " FP 0 ; LP 2047"
        SEND.COM
        " SCV 0 ; DCV 2 "
        SEND.COM
        " MM 2 ; SIE 3"
        SEND.COM
;

:  SEND.PARVALUES            \ Send PAR-273 parameter value settings
        " PAM " PAM.VALUE "." "CAT
        SEND.COM
        " INTRP 1
        SEND.COM
        " TMB " TMB.VALUE "." "CAT " ;S/P " "CAT S/P.VALUE "." "CAT
```

Program A.3: ASYST file COMM.PAR (continued)

```
        SEND.COM
        " FLT " FILTER.VALUE "." "CAT " ;I/E " "CAT I/E.VALUE "." "CAT
        SEND.COM
        " EGAIN " EGAIN.VALUE "." "CAT " ;IGAIN " "CAT IGAIN.VALUE "." "CAT
        SEND.COM
        " SAM " SAM.VALUE "." "CAT " ;SWPS " "CAT SWPS.VALUE "." "CAT
        SEND.COM
        " BIAS " BIAS.VALUE "." "CAT " ;MR " "CAT MR.VALUE "." "CAT
        SEND.COM
        " CELL 1"
        SEND.COM

        DELAY.VALUE    MSEC.DELAY
;

:  GET.IE                \ Retrieves and scales current and potential data
        " BD 2048,2048"  BD.STRING ":=
        GET.DATA
        DATA.L2 SCALE.IDATA SWPS.VALUE / IDATA :=
        CR ." IDATA RETRIEVED    "
        -1 4 SCI.FORMAT IDATA []MIN/MAX . .

        " BD 4096,2048"  BD.STRING ":=
        GET.DATA
        DATA.L2 SCALE.EDATA SWPS.VALUE / EDATA :=
        CR ." EDATA RETRIEVED    "
        -1 4 FIX.FORMAT EDATA []MIN/MAX . .
;

:  RUN                    \ Initiate impedance experiment
        SEND.PARVALUES
        CR ." EXPERIMENT IN PROGRESS . . . .
                " PCV 2;NC;TC;WCD;CELL 0"
                SEND
        CR ." USE *** END.RUN WORD *** WHEN CELL TURNS OFF"
        CR
;

:  END.RUN             \ Complete impedance experiment
        RS232.IN
        CHECK.ERROR
        GET.IE
;

:  AUTO.RUN            \ Initiate and complete impedance experiment
        EXPT.TIME
        SEND.PARVALUES
```

Program A.3: ASYST file COMM.PAR (continued)

```
          CR ." Experiment in progress . . . . . "
                    " PCV 2;NC;TC;WCD
                    SEND.COM
               ." Experiment finished
                    " CELL 0"
                    SEND.COM
          BELL
          GET.IE
;
```

Program A.3: ASYST file COMM.PAR (continued)

```
\ ASYST FILE :          IMPCALC.ASY

\ This program performs impedance calculations from the experimental
\ voltage and current waveform outputs of the potentiostat.

\               Created by:    Andy Chan
\                              February 3, 1988

\  -----------------------------------------------------------------


REAL   DIM[ 50 ] ARRAY Z.REAL               \ Real component of impedance
       DIM[ 50 ] ARRAY Z.IMAG               \ Imaginary component of impedance
       DIM[ 50 ] ARRAY Z.MAG                \ Magnitude of impedance vector
       DIM[ 2048 ] ARRAY DATA               \ Temporary data array
       DIM[ 50 ] ARRAY FREQ                 \ Applied frequency array
       DIM[ 50 ] ARRAY W                    \ Applied angular frequency array
       SCALAR MINIMUM                       \ Minimum threshhold for PICKOUT.DATA
       SCALAR AXIS.MAX                      \ Axis maximum for NYQUIST.PLOT
INTEGER   SCALAR IND                        \ FFT-domain index for one frequency
          DIM[ 200 ] ARRAY POINTER          \ Indices for all the frequencies
COMPLEX   DIM[ 2048 ] ARRAY EDATA.FFT1          \ Freq. domain of EDATA waveform
          DIM[ 2048 ] ARRAY IDATA.FFT1          \ Freq. domain of IDATA waveform
          DIM[ 50 ] ARRAY A                     \ Admittance data
          DIM[ 50 ] ARRAY IDATA.FFT             \ Selected freq. domain of current
          DIM[ 50 ] ARRAY EDATA.FFT             \ Selected freq. domain of potential


:  CALC.TIME&FREQ                 \ Calculation of time and frequency data
       TIME  []RAMP
       S/P.VALUE TMB.VALUE * 1.E-6 * TIME *   TIME :=
       WAVE.CYCLES TIME [ 2048 ] /   FREQ :=
       2. PI * FREQ *   W :=
;


:  PICKOUT.DATA                   \ Pick out only applied frequency points
       WDATA FFT DUP CONJ * ZREAL  DATA :=
       DATA []MAX 3. / MINIMUM :=
       1 IND :=
       1025 1 DO
              DATA [ I ]  MINIMUM >
              IF     I  POINTER [ IND ] :=
                     IND 1 +   IND :=
              THEN
       LOOP
       IND 1 DO
```

Program A.4: ASYST file IMPCALC.ASY

```
                EDATA.FFT1  [ POINTER [ I ] ]   EDATA.FFT [ I ]  :=
                IDATA.FFT1  [ POINTER [ I ] ]   IDATA.FFT [ I ]  :=
        LOOP
;

: DATA.CALC
\ Calcuation of admittance data . . .
        IDATA.FFT EDATA.FFT CONJ *
        EDATA.FFT DUP CONJ *
        / A :=

\ Calculation of real component of impedance . . .
        A ZREAL DUP * A ZIMAG DUP * +
        A ZREAL SWAP / Z.REAL :=

\ Calculation of imaginary component of impedance . . .
        A ZREAL DUP * A ZIMAG DUP * +
        A ZIMAG SWAP / Z.IMAG :=

\ Calculation of magnitude of impedance vector . . .
        Z.REAL DUP * Z.IMAG DUP *  + SQRT  Z.MAG :=
;

:  NYQUIST.PLOT              \ Equal axes screen plot of impedance data
        HORIZONTAL AXIS.FIT.OFF VERTICAL AXIS.FIT.OFF
        GRAPHICS.DISPLAY  VUPORT.CLEAR
        Z.REAL []MAX   Z.IMAG []MAX   >
        IF       Z.REAL    []MAX AXIS.MAX :=
        ELSE     Z.IMAG    []MAX AXIS.MAX :=
        THEN
        0 AXIS.MAX                    HORIZONTAL WORLD.SET
        0 AXIS.MAX 0.93056 *    VERTICAL    WORLD.SET
        XY.AXIS.PLOT
        " *" SYMBOL
        Z.REAL Z.IMAG XY.DATA.PLOT
;

:  BODE.PLOT                         \ Log-log plot of Z.MAG vs w
        W LOG  Z.MAG LOG
        XY.AUTO.PLOT
;

:  IMP.CALC             \ Final colon definition
        CR ." Impedance calc . . . "
        EDATA FFT EDATA.FFT1 :=
        -1 IDATA * FFT IDATA.FFT1 :=
        CALC.TIME&FREQ
```

Program A.4: ASYST file IMPCALC.ASY (continued)

```
        PICKOUT DATA
        DATA.CALC
        Z.IMAG -1. *  Z.IMAG :=
        ." DONE"
;
```

Program A.4: ASYST file IMPCALC.ASY (continued)

```
\ ASYST FILE:          CORRIMP.ASY

\ This program provides words for use in the deconvolution of the instrument
\ response function from the impedance results.

\              Created by:     Andy Chan
\                              April 14, 1988

\  ------------------------------------------------------------------


COMPLEX  DIM[ 50 ] ARRAY A.CORR          \ true or corrected admittance
         DIM[ 50 ] ARRAY G(W)            \ instrument response function


:  RESPONSE.R                 \ Calibration with a known resistance
      CR CR CR ." Enter value of calibration resistor:   "
      #INPUT
      1. SWAP /                         \ calculates known admittance
      A CONJ * A / A CONJ /    G(W) :=
      CR ." G(w) function = " G(W) .
;

:  RESPONSE.C                 \ Calibration with a known capacitance
      CR CR CR ." Enter value of calibration capacitor:   "
      #INPUT
      2 * PI * FREQ * Z=0+IY         \ calculates known admittance
      A CONJ * A / A CONJ /    G(W) :=
      CR ." G(w) function = " G(W) .
;

:  CORR.IMP                   \ Corrects observed impedance data
      IDATA.FFT EDATA.FFT CONJ *                  \
      EDATA.FFT DUP CONJ *                        \ calculates observed admittance
      / A :=                                      \
      G(W)  A *     A.CORR :=              \ calculates corrected admittance
      A.CORR ZREAL DUP * A.CORR ZIMAG DUP * +                  \
      A.CORR ZREAL SWAP / Z.REAL :=                            \
      A.CORR ZREAL DUP * A.CORR ZIMAG DUP * +                  \ re-calculates the
      A.CORR ZIMAG SWAP / Z.IMAG :=                            \ corrected quantities
      Z.REAL DUP * Z.IMAG DUP * + SQRT Z.MAG :=                \
      Z.IMAG -1. *   Z.IMAG :=                                 \
;
```

Program A.5: ASYST file CORRIMP.ASY

```
\ ASYST FILE:          HPPLOT.ASY

\ This program contains words for plotting data on the HP7475A plotter.
\ Plotting of data is performed by the following words:

\            1 ) HPPLOT  (to begin plotting)
\            2 ) HPPLOT.DATA  (repeat for all x and y arrays on the stack)
\            3 ) HPPLOT.END  (to finish plotting)


\            Created by:     Andy Chan
\                            August 19, 1988

\  -------------------------------------------------------------


INTEGER  SCALAR #LEGEND.LINES

:  HPPLOT.INIT              \ Initialize plotter
      HP7475 DEVICE.INIT PLOTTER.DEFAULTS
      NORMAL.COORDS ABSOLUTE
      .63 .74        VUPORT.SIZE          \ for 11" x 8.5" paper size
      .15 .15        AXIS.ORIG
      .15 .15        AXIS.POINT
      .768 .790      AXIS.SIZE            \ for 200mm x 150mm axes
      0  0           DATA.ORIG
      1  1           DATA.SIZE
      HORIZONTAL  0 1 LABEL.POINTS
      VERTICAL    0 1 LABEL.POINTS
      4 AXIS.COLOR  4 LABEL.COLOR  4 COLOR
;

:  HPPLOT.AXES              \ Draw plot axes
      CR CR
      CR ." X-AXIS LIMITS:  "  #INPUT #INPUT
      HORIZONTAL AXIS.FIT.OFF WORLD.SET
      CR ." Y-AXIS LIMITS:  "  #INPUT #INPUT
      VERTICAL   AXIS.FIT.OFF WORLD.SET
      .008 .02 CHAR.SIZE
      VUPORT.CLEAR XY.AXIS.PLOT
;

:  HPPLOT.LABELS            \ Draw title and axes labels
      NORMAL.COORDS CR CR

      CR ." TITLE:   "  "INPUT
      .015 .04 CHAR.SIZE   .20 .97  POSITION LABEL
```

Program A.6: ASYST file HPPLOT.ASY

```
      CR ." X-AXIS:   "   "INPUT
      .015 .04 CHAR.SIZE   .55 .05  POSITION CENTERED.LABEL

      CR ." Y-AXIS:  "   "INPUT
      90 LABEL.DIR          .045 .5  POSITION CENTERED.LABEL
      0  LABEL.DIR
;

: HPPLOT.DATA               \ Word for plotting x and y data arrays
      WORLD.COORDS
      .005 .015 CHAR.SIZE
      CR ." COLOR:  " #INPUT COLOR
      ."    PLOTTING SYMBOL:  "  "INPUT SYMBOL
      XY.DATA.PLOT
;

:  HPPLOT.LEGEND            \ Plot legend for the graph
      NORMAL.COORDS

      CR ." LEGEND (#char):    "      #INPUT
      CR ."         (#lines):  "     #INPUT  DUP  #LEGEND.LINES :=
      KEY.SIZE
      .006 .017 CHAR.SIZE
      .85 .85  KEY.ORIG  CR

      #LEGEND.LINES 0 DO
            ." COLOR:  "        #INPUT  COLOR
            ."    SYMBOL:  "   "INPUT  SYMBOL
            ."    TITLE:  "    "INPUT
            I  KEY.LINE  CR
      LOOP
      KEY.OUTLINE KEY.DONE 0 COLOR
;

:  HPPLOT                   \ Word to begin a plot
      NORMAL.DISPLAY
      HPPLOT.INIT
      HPPLOT.AXES
      HPPLOT.LABELS
;

:  HPPLOT.END               \ Word to finish a plot
      HPPLOT.LEGEND
      IBM.GRAPHICS GRAPHICS.DISPLAY DEVICE.INIT  AXIS.DEFAULTS
      NORMAL.DISPLAY
;
```

Program A.6: ASYST file HPPLOT.ASY (continued)

```
\ ASYST FILE:          HPLASER.ASY

\ This file contains words required in order for the HP-LaserJet III printer
\ to emulate an HP7475A plotter.

\ Printer settings:    I/O=SERIAL,  SERIAL=RS-232
\                      BAUD RATE=9600, PAGEPROTECT=LTR

\              Created by:   Andy Chan
\                            August 13, 1991

\ -----------------------------------------------------------------


1016   RS232.DEVICE HP.LASERJET              \
HP.LASERJET                                  \
9600 SET.BAUD                                \
0 SET.PARITY                                 \ HP-LaserJet III device
8 SET.DATA.BITS                              \ configuration for the COM1
1 SET.STOP.BITS                              \ communications port at
4 SET.INT.LINE                               \ hexadecimal 3F8
13 RS232.EOS.CHAR                            \
RS232.EOS.ON                                 \
RS232.POL.MODE                               \
DSR.ON                                       \


: HPLASER.INIT
      HP.LASERJET                        \ Set LaserJet as current RS-232 device

      27 ASCII" " %0A" "CAT  SEND            \ Enter PCL mode
      27 ASCII" " &l1H" "CAT  SEND           \ Paper tray auto feed
      27 ASCII" " &l2A" "CAT  SEND           \ Letter paper size
      27 ASCII" " &l1O" "CAT  SEND           \ Landscape orientation
      27 ASCII" " %0B" "CAT  SEND            \ Enter HP-GL/2 mode
;

: HPLASER.END
      27 ASCII" " %0A" "CAT  SEND            \ Enter PCL mode
      27 ASCII" " &l0H" "CAT  SEND           \ Eject page

      PAR.273                            \ Reset PAR-273 as current RS-232 device
;
```

Program A.7: ASYST file HPLASER.ASY

```
\ ASYST FILE:          START.PAR

\ This program initiates the PAR-273 for impedance experiments,
\ loads a WDATA waveform from disk and then transfers this waveform
\ to the PAR-273.

\             Created by:    Andy Chan

\ ---------------------------------------------------------------


: NEW.SEED
      CR ." Input a random SEED number:  " #INPUT SEED :=
;

: START.PAR
      PAR.273                      \ Define RS-232C settings
      9600 SET.BAUD
      0 SET.PARITY
      8 SET.DATA.BITS
      2 SET.STOP.BITS
      4 SET.INT.LINE
      13 RS232.EOS.CHAR
      RS232.EOS.ON
      RS232.POL.MODE
      DSR.ON
      ?RS232.DEVICE

      NEW.SEED
      51  COMPONENTS :=
      800 AMP :=

      CR CR ." Waveform filename:  " "INPUT " .WAV" "CAT FILENAME ":=
      FILENAME DEFER> FILE.OPEN
            1 SUBFILE WAVE.CYCLES FILE>ARRAY
            2 SUBFILE WDATA FILE>ARRAY
      FILE.CLOSE

      CLEAR.RS232          \ Clear RS-232C communication channel
      PAR.INIT             \ Initialize PAR-273 potentiostat
      SEND.CURVE           \ Transfer WDATA excitation waveform
;
```

Program A.8: ASYST file START.PAR

```
\ ASYST FILE:          AUTOEXPT.ASY

\ This program provides words for automatic calibration and execution of
\ impedance experiments on the PAR-273.

\               Created by:     Andy Chan
\                               March 25, 1989

\ ---------------------------------------------------------------------


REAL    DIM[ 2048 ] ARRAY EDATA.OLD
        DIM[ 50 ] ARRAY ZR1              \
        DIM[ 50 ] ARRAY ZI1              \
        DIM[ 50 ] ARRAY ZR2              \
        DIM[ 50 ] ARRAY ZI2              \  real and imaginary impedance
        DIM[ 50 ] ARRAY ZR3              \  results for experiments 1-4
        DIM[ 50 ] ARRAY ZI3              \
        DIM[ 50 ] ARRAY ZR4              \
        DIM[ 50 ] ARRAY ZI4              \
        SCALAR R.CAL                 \ resistance of calibration resistor
COMPLEX  DIM[ 50 ] ARRAY G1(W)           \
         DIM[ 50 ] ARRAY G2(W)           \ correction functions for
         DIM[ 50 ] ARRAY G3(W)           \ experiments 1-4
         DIM[ 50 ] ARRAY G4(W)           \


: PAR.CALIBRATE
        NORMAL.DISPLAY
        -1 4 SCI.FORMAT

        CR ." Enter value of calibration resistor (ohms):  " #INPUT R.CAL :=

        CR  ." Calibration of PAR-273 with "  R.CAL .
            ." ohm resistor in progress . . . " CR

        500 TMB.VALUE :=   1 S/P.VALUE :=    16 SWPS.VALUE :=
         AUTO.RUN
        IMP.CALC
        1. R.CAL / A CONJ * A / A CONJ /  G1(W) :=
        ."  >>> G1(W) OBTAINED" CR
        EDATA EDATA.OLD :=

        150 TMB.VALUE :=   1 S/P.VALUE :=    16 SWPS.VALUE :=
        AUTO.RUN
        EDATA.OLD EDATA := IMP.CALC
        1. R.CAL / A CONJ * A / A CONJ /  G2(W) :=
```

Program A.9: ASYST file AUTOEXPT.ASY

```
        ." >>> G2(W) OBTAINED" CR

        500 TMB.VALUE :=   5 S/P.VALUE :=    16 SWPS.VALUE :=
        AUTO.RUN
        IMP.CALC
        1. R.CAL / A CONJ * A / A CONJ /  G3(W) :=
        ." >>> G3(W) OBTAINED" CR

        500 TMB.VALUE :=   50 S/P.VALUE :=    10 SWPS.VALUE :=
        AUTO.RUN
        IMP.CALC
        1. R.CAL / A CONJ * A / A CONJ /  G4(W) :=
        ." >>> G4(W) OBTAINED" CR

        CR ." Calibration completed." BELL BELL BELL
;

: EXPT1
        CR CR ." EXPERIMENT 1:  "
        500 TMB.VALUE :=   1 S/P.VALUE :=    16 SWPS.VALUE :=
        AUTO.RUN
        IMP.CALC
        G1(W)  G(W) :=
        CORR.IMP
        Z.REAL ZR1 :=
        Z.IMAG ZI1 :=
;

: EXPT2
        CR CR ." EXPERIMENT 2:  "
        150 TMB.VALUE :=   1 S/P.VALUE :=    16 SWPS.VALUE :=
        AUTO.RUN
        EDATA.OLD EDATA := IMP.CALC
        G2(W)  G(W) :=
        CORR.IMP
        Z.REAL ZR2 :=
        Z.IMAG ZI2 :=
;

: EXPT3
        CR CR ." EXPERIMENT 3:  "
        500 TMB.VALUE :=   5 S/P.VALUE :=    16 SWPS.VALUE :=
        AUTO.RUN
        IMP.CALC
        G3(W)  G(W) :=
        CORR.IMP
        Z.REAL ZR3 :=
```

Program A.9: ASYST file AUTOEXPT.ASY (continued)

```
        Z.IMAG ZI3 :=
;

: EXPT4
        CR CR ." EXPERIMENT 4:  "
        500 TMB.VALUE :=    50 S/P.VALUE :=     10 SWPS.VALUE :=
        AUTO.RUN
        IMP.CALC
        G4(W)  G(W) :=
        CORR.IMP
        Z.REAL ZR4 :=
        Z.IMAG ZI4 :=
;

: AUTO.EXPT
        NORMAL.DISPLAY    -1 4 FIX.FORMAT
        EXPT1
        EDATA EDATA.OLD :=
        EXPT2
        EXPT3
        EXPT4
        CR CR ." Impedance experiments completed." BELL BELL BELL
;
```

Program A.9: ASYST file AUTOEXPT.ASY (continued)

```
\ ASYST FILE:          CALSAVE.ASY

\ This program stores in computer memory the calibration data for various
\ PAR-273 settings and allows them to be recalled for use at a later
\ time.

\             Created by:    Andy Chan
\                            February 22, 1991

\ ---------------------------------------------------------------


COMPLEX  DIM[ 50 , 4 ] ARRAY CALA
         DIM[ 50 , 4 ] ARRAY CALB
         DIM[ 50 , 4 ] ARRAY CALC
         DIM[ 50 , 4 ] ARRAY CALD
         DIM[ 50 , 4 ] ARRAY CALE

: STORE.CALA
        G1(W) CALA XSECT[ ! , 1 ] :=
        G2(W) CALA XSECT[ ! , 2 ] :=
        G3(W) CALA XSECT[ ! , 3 ] :=
        G4(W) CALA XSECT[ ! , 4 ] :=
;

: STORE.CALB
        G1(W) CALB XSECT[ ! , 1 ] :=
        G2(W) CALB XSECT[ ! , 2 ] :=
        G3(W) CALB XSECT[ ! , 3 ] :=
        G4(W) CALB XSECT[ ! , 4 ] :=
;

: STORE.CALC
        G1(W) CALC XSECT[ ! , 1 ] :=
        G2(W) CALC XSECT[ ! , 2 ] :=
        G3(W) CALC XSECT[ ! , 3 ] :=
        G4(W) CALC XSECT[ ! , 4 ] :=
;

: STORE.CALD
        G1(W) CALD XSECT[ ! , 1 ] :=
        G2(W) CALD XSECT[ ! , 2 ] :=
        G3(W) CALD XSECT[ ! , 3 ] :=
        G4(W) CALD XSECT[ ! , 4 ] :=
;

: STORE.CALE
```

Program A.10: ASYST file CALSAVE.ASY

```
        G1(W) CALE XSECT[ ! , 1 ] :=
        G2(W) CALE XSECT[ ! , 2 ] :=
        G3(W) CALE XSECT[ ! , 3 ] :=
        G4(W) CALE XSECT[ ! , 4 ] :=
;

: RECALL.CALA
        CALA XSECT[ ! , 1 ] G1(W) :=
        CALA XSECT[ ! , 2 ] G2(W) :=
        CALA XSECT[ ! , 3 ] G3(W) :=
        CALA XSECT[ ! , 4 ] G4(W) :=
;

: RECALL.CALB
        CALB XSECT[ ! , 1 ] G1(W) :=
        CALB XSECT[ ! , 2 ] G2(W) :=
        CALB XSECT[ ! , 3 ] G3(W) :=
        CALB XSECT[ ! , 4 ] G4(W) :=
;

: RECALL.CALC
        CALC XSECT[ ! , 1 ] G1(W) :=
        CALC XSECT[ ! , 2 ] G2(W) :=
        CALC XSECT[ ! , 3 ] G3(W) :=
        CALC XSECT[ ! , 4 ] G4(W) :=
;

: RECALL.CALD
        CALD XSECT[ ! , 1 ] G1(W) :=
        CALD XSECT[ ! , 2 ] G2(W) :=
        CALD XSECT[ ! , 3 ] G3(W) :=
        CALD XSECT[ ! , 4 ] G4(W) :=
;

: RECALL.CALE
        CALE XSECT[ ! , 1 ] G1(W) :=
        CALE XSECT[ ! , 2 ] G2(W) :=
        CALE XSECT[ ! , 3 ] G3(W) :=
        CALE XSECT[ ! , 4 ] G4(W) :=
;
```

Program A.10: ASYST file CALSAVE.ASY (continued)

```
\ ASYST FILE:           SAVE.ASY

\ This program saves impedance results for experiments 1-4 onto
\ floppy diskette.

\               Created by:     Andy Chan

\  ----------------------------------------------------------------


:  NEW.TEMPLATE
        FILE.TEMPLATE
        4 COMMENTS
        REAL DIM[ 50 ] SUBFILE
        9 TIMES
        END
;

: DATA.SAVE
        NEW.TEMPLATE
        CR CR ." FILENAME ?   "  " A:" "INPUT "CAT " .DAT" "CAT  FILENAME ":=
        FILENAME DEFER> FILE.CREATE
        FILENAME DEFER> FILE.OPEN

        CR ." COMMENT #1: "   "INPUT  1 >COMMENT
        CR ." COMMENT #2: "   "INPUT  2 >COMMENT
        CR ." COMMENT #3: "   "INPUT  3 >COMMENT
        CR ." COMMENT #4: "   "INPUT  4 >COMMENT

        1  SUBFILE  ZR1   ARRAY>FILE
        2  SUBFILE  ZI1   ARRAY>FILE
        3  SUBFILE  ZR2   ARRAY>FILE
        4  SUBFILE  ZI2   ARRAY>FILE
        5  SUBFILE  ZR3   ARRAY>FILE
        6  SUBFILE  ZI3   ARRAY>FILE
        7  SUBFILE  ZR4   ARRAY>FILE
        8  SUBFILE  ZI4   ARRAY>FILE
        9  SUBFILE  WAVE.CYCLES ARRAY>FILE

        FILE.CLOSE
;
```

Program A.11: ASYST file SAVE.ASY

```
\ ASYST FILE:          READ.ASY

\ This programs reads impedance results from experiments 1-4 from
\ floppy diskette.

\               Created by:     Andy Chan

\  -------------------------------------------------------------


: DATA.READ
      CR CR ." FILENAME ?   "   " A:" "INPUT "CAT " .DAT" "CAT FILENAME ":=
      FILENAME DEFER> ?FILE

      1  SUBFILE  ZR1   FILE>ARRAY
      2  SUBFILE  ZI1   FILE>ARRAY
      3  SUBFILE  ZR2   FILE>ARRAY
      4  SUBFILE  ZI2   FILE>ARRAY
      5  SUBFILE  ZR3   FILE>ARRAY
      6  SUBFILE  ZI3   FILE>ARRAY
      7  SUBFILE  ZR4   FILE>ARRAY
      8  SUBFILE  ZI4   FILE>ARRAY
      9  SUBFILE  WAVE.CYCLES FILE>ARRAY

      FILE.CLOSE
;
```

Program A.12: ASYST file READ.ASY

```
\ ASYST FILE:           PLOT.ASY

\ This file plots the impedance results for experiments 1-4 on the screen,
\ the HP-7475A plotter or the HP-LaserJet III.

\               Created by:     Andy Chan

\ ---------------------------------------------------------------


1 STRING CELL#       \ reference number for impedance cell

: MOHMS      \ divides top two entries by 1E6
      SWAP 1.E6 / SWAP 1.E6 /
;

: PLOT.SETUP
      HPPLOT.INIT
      CR CR
      CR ." CELL#:  "                "INPUT  CELL# ":=
      CR ." X-AXIS LIMITS:   "       #INPUT  #INPUT
      HORIZONTAL AXIS.FIT.OFF WORLD.SET
      CR ." Y-AXIS LIMITS:   "       #INPUT  #INPUT
      VERTICAL AXIS.FIT.OFF WORLD.SET

      NORMAL.COORDS CR CR
      .015 .04 CHAR.SIZE
      CR ." TITLE:   "  "INPUT      .20 .97 POSITION LABEL
      " Z.REAL (Mohms)"          .55 .05 POSITION CENTERED.LABEL
      " Z.IMAG (Mohms)"          90 LABEL.DIR  .045 .5 POSITION CENTERED.LABEL
      0 LABEL.DIR

      .005 .015 CHAR.SIZE
      FILENAME                    .86 .80 POSITION LABEL

      .008 .02 CHAR.SIZE
      VUPORT.CLEAR XY.AXIS.PLOT
;

: PLOT
      PLOT.SETUP

      WORLD.COORDS
      .005 .015 CHAR.SIZE
      2 COLOR  " *" SYMBOL  ZR1 ZI1 MOHMS XY.DATA.PLOT
      3 COLOR  " -" SYMBOL  ZR2 ZI2 MOHMS XY.DATA.PLOT
      6 COLOR  " o" SYMBOL  ZR3 ZI3 MOHMS XY.DATA.PLOT
```

Program A.13: ASYST file PLOT.ASY

```
        1 COLOR  " +" SYMBOL  ZR4 ZI4 MOHMS XY.DATA.PLOT

        NORMAL.COORDS
        12 4 KEY.SIZE
        .006 .017 CHAR.SIZE
        .85 .85 KEY.ORIG
        2 COLOR  " *" SYMBOL  " Z1 CELL#" CELL# "CAT  0 KEY.LINE
        3 COLOR  " -" SYMBOL  " Z2 CELL#" CELL# "CAT  1 KEY.LINE
        6 COLOR  " o" SYMBOL  " Z3 CELL#" CELL# "CAT  2 KEY.LINE
        1 COLOR  " +" SYMBOL  " Z4 CELL#" CELL# "CAT  3 KEY.LINE
        KEY.OUTLINE  KEY.DONE  0 COLOR

        IBM.GRAPHICS
        GRAPHICS.DISPLAY DEVICE.INIT AXIS.DEFAULTS
        NORMAL.DISPLAY
;

: HPLASER.PLOT
        HPLASER.INIT
        PLOT
        HPLASER.END
;

: SCREEN.PLOT
        ZR4 Z.REAL :=
        ZI4 Z.IMAG :=
        NYQUIST.PLOT
        ZR3 ZI3 XY.DATA.PLOT
        ZR2 ZI2 XY.DATA.PLOT
        ZR1 ZI1 XY.DATA.PLOT
;
```

Program A.13: ASYST file PLOT.ASY (continued)

```
\ ASYST FILE:          FASTCMDS.ASY

\ This file contains useful abbreviated colon definitions and function
\ key definitions.

\                  Created by:     Andy Chan

\   ---------------------------------------------------------------------


: AP
        XY.AUTO.PLOT
;

:  DP
        XY.DATA.PLOT
;

: ND
        NORMAL.DISPLAY
;

: GD
        GRAPHICS.DISPLAY
;

\ The following four words are useful for quickly changing plotting symbols.

: STAR
        " *" SYMBOL
;

: SLASH
        " \" SYMBOL
;

:  PLUS
        " +" SYMBOL
;

: OOO
        " o" SYMBOL
;

: SC
        STACK.CLEAR
;
```

Program A.14: ASYST file FASTCMDS.ASY

```
: FP.NOTATION
        -1 4 FIX.FORMAT
;

: SCI.NOTATION
        -1 4 SCI.FORMAT
;

: CC
        CREATE.COPY
;

: AR
        ARRAY.READOUT
;

: CLS
        SCREEN.CLEAR
;

: S.D.
        STACK.DISPLAY
;

: SCALES?
        CR ." X " LABEL.SCALE.X .
        CR ." Y " LABEL.SCALE.Y .
;

: MIN/MAX
        []MIN/MAX . .
        CR
;

: HWS
        HORIZONTAL AXIS.FIT.OFF WORLD.SET
;

: VWS
        VERTICAL AXIS.FIT.OFF WORLD.SET
;

: NEW.AXIS
        VUPORT.CLEAR  XY.AXIS.PLOT
;
```

Program A.14: ASYST file FASTCMDS.ASY (continued)

```
: GRIDS.ON
        VERTICAL      GRID.ON
        HORIZONTAL    GRID.ON
;

: GRIDS.OFF
        VERTICAL      GRID.OFF
        HORIZONTAL    GRID.OFF
;

: CALC.F1
        500 TMB.VALUE :=
        1 S/P.VALUE :=
        CALC.TIME&FREQ
;

: CALC.F2
        150 TMB.VALUE :=
        1 S/P.VALUE :=
        CALC.TIME&FREQ
;

: CALC.F3
        500 TMB.VALUE :=
        5 S/P.VALUE :=
        CALC.TIME&FREQ
;

: CALC.F4
        500 TMB.VALUE :=
        50 S/P.VALUE :=
        CALC.TIME&FREQ
;

: NP
        Z.IMAG :=
        Z.REAL :=
        NYQUIST.PLOT
;

F7  FUNCTION.KEY.DOES  SCI.NOTATION
F8  FUNCTION.KEY.DOES  FP.NOTATION
F9  FUNCTION.KEY.DOES  MIN/MAX
```

Program A.14: ASYST file FASTCMDS.ASY (continued)

```
\ ASYST FILE:          RCMODEL.ASY

\ This file contains words to model the impedance of single and double
\ parallel RC electronic circuits.  The results are stored in Z1 to Z4
\ and can, therefore, be plotted, etc. just like actual experimental
\ data sets.

\                      Created by:    Andy Chan
\                                     July 19, 1988

\ ------------------------------------------------------------


REAL  SCALAR RS               \ solution R
      SCALAR RB               \ bulk R
      SCALAR CG               \ geometric C
      SCALAR RCT              \ charge transfer R
      SCALAR CDL              \ double layer C


: CALC.SINGLE.MODEL
      RS

      1. RB /
      W CG * Z=0+IY
      +
      1. SWAP /

      +

      ZRE&IM
      -1. * Z.IMAG :=
      Z.REAL :=
;

: CALC.DOUBLE.MODEL
      RS

      1. RB /
      W CG * Z=0+IY
      +
      1. SWAP /

      1. RCT /
      W CDL * Z=0+IY
      +
      1. SWAP /
```

Program A.15: ASYST file RCMODEL.ASY

```
        + +

        ZRE&IM
        -1. * Z.IMAG :=
        Z.REAL :=
;

: SINGLE.RC.MODEL
        CALC.F1 CALC.SINGLE.MODEL
        Z.REAL ZR1 :=
        Z.IMAG ZI1 :=

        CALC.F2 CALC.SINGLE.MODEL
        Z.REAL ZR2 :=
        Z.IMAG ZI2 :=

        CALC.F3 CALC.SINGLE.MODEL
        Z.REAL ZR3 :=
        Z.IMAG ZI3 :=

        CALC.F4 CALC.SINGLE.MODEL
        Z.REAL ZR4 :=
        Z.IMAG ZI4 :=
;

: DOUBLE.RC.MODEL
        CALC.F1 CALC.DOUBLE.MODEL
        Z.REAL ZR1 :=
        Z.IMAG ZI1 :=

        CALC.F2 CALC.DOUBLE.MODEL
        Z.REAL ZR2 :=
        Z.IMAG ZI2 :=

        CALC.F3 CALC.DOUBLE.MODEL
        Z.REAL ZR3 :=
        Z.IMAG ZI3 :=

        CALC.F4 CALC.DOUBLE.MODEL
        Z.REAL ZR4 :=
        Z.IMAG ZI4 :=
;
```

Program A.15: ASYST file RCMODEL.ASY (continued)

Appendix B: Chapter 7 Computer Programs

```
\ ASYST FILE:                BALANCE.ASY

\ This program sets parameters for Mettler AE200 balance as an ASYST RS-232
\ device via the COM1 port.  Weights can be read at preselected fixed time
\ intervals defined by WAIT.VALUE (in msec) into the WEIGHT data array.
\ The balance should be configured for even parity, send continuous and
\ 2400 baud rate.
\ The following cable is required: IBM pins 1, 3, 6, 7, 20 to
\ AE200 balance 1, 3, 20, 7, (5,6), respectively

\            Created by:          Andy Chan
\                                 May 22, 1990

\ ----------------------------------------------------------------


DIM[ 1 , 50 ] STRING.ARRAY BAL
REAL DIM[ 5000 ] ARRAY WEIGHT
SCALAR WAIT.VALUE

1016 RS232.DEVICE AE.BALANCE
AE.BALANCE
2400 SET.BAUD
2 SET.PARITY
7 SET.DATA.BITS
1 SET.STOP.BITS
13 RS232.EOS.CHAR
RS232.EOS.ON
RS232.POL.MODE
DSR.ON

15000 WAIT.VALUE :=        \ 15000 msec default period

: MEASURE.WEIGHTS
      BAL "RS232.BUFFER
      WAIT.VALUE SYNC.PERIOD
      0 WEIGHT :=

      5001 1 DO
            SYNCHRONIZE
            BEGIN
                  "RS232.RESET
                  RS232>BUFFER
```

Program B.1: ASYST file BALANCE.ASY

```
                        BAL "[ 1 ] 2 1 "SUB  " S"   "=   \ Error check for S in id block
                        ?DUP
                        IF
                        ELSE BELL CR ." ERROR IN RS232.COMMUNICATION"
                        THEN
                UNTIL
                CR I .
                BAL "TYPE
                BAL "[ 1 ]
                32 "NUMBER
                WEIGHT [ I ] :=
        LOOP
;
```

Program B.1: ASYST file BALANCE.ASY (continued)

```
10   ' BASIC FILE:              BALANCE.BAS
20   '
30   ' This program reads data at fixed time intervals from a Mettler AE200
40   ' balance equipped with an Option 011 Data Output Interface.
50   ' The balance is connected to the IBM-XT COM1 port via a direct
60   ' RS-232 ribbon cable and should be configured for even parity,
70   ' send continuous and 2400 baud rate.
80   ' The weight data is stored in the array WT and saved onto disk
90   ' in ASCII data format.
100  '
110  '        Created by:           Andy Chan
120  '                              December 10, 1990
130  ' --------------------------------------------------------
140  '
1000 INPUT "Enter the number of weight points to collect"; PTS
1010 DIM  WT(PTS)
1020 OPEN "COM1:2400,E,7,1" AS #1
1030 FOR X= 1 TO PTS
1040     GOSUB 2000 : '    Store one weight every 15 sec into WT(X)
1050     PRINT  X,WT(X)
1060 NEXT X
1070 CLOSE #1
1080 BEEP :BEEP :BEEP
1090 GOSUB 3000 : '        Store WT array as an ASCII file
1100 STOP
2000 '
2010 '         *** DATA ACQUISITION AND TIMED STORAGE ***
2020 '
2030 BAL$=INPUT$(16,#1)  :      ' Read in balance data train.
2040 SEC=VAL(RIGHT$(TIME$,2))
2050 IF SEC=0  GOTO 2100 :      ' These conditional statements are used
2060 IF SEC=15 GOTO 2100 :      ' to collect data at any desired time
2070 IF SEC=30 GOTO 2100 :      ' interval.  Simply change numbers to
2080 IF SEC=45 GOTO 2100 :      ' appropriate multiples.
2090 GOTO 2030
2100 WT(X)=VAL(MID$(BAL$,4,9))  :      ' This extracts weight from data train.
2110 FOR I=1 TO 1000 : NEXT I :        ' Short 1 sec delay.
2120 RETURN
3000 '
3010 '        *** ASCII SAVE OF WT(PTS) DATA ***
3020 '
3030 INPUT "Enter filename for weight data";N$
3040 OPEN "A:"+N$+".ASC" FOR OUTPUT AS #2
3050 FOR X=1 TO PTS
3060     WRITE #2, WT(X)
3070 NEXT X
3080 CLOSE #2
```

Program B.2: BASIC file BALANCE.BAS

```
\ ASYST FILE:                    READBAS.ASY

\  This word reads a BASIC ASCII format data file into an ASYST array
\  called WEIGHT.  The dimensions of this array should match the
\  number of data entries in the data file.
\  Note that data must have been stored in BASIC via the WRITE #1
\  command to be properly read in ASYST via BASIC.READ command.

\              Created by:              Andy Chan
\                                       December 14, 1990

\  --------------------------------------------------------------------


15 STRING FILENAME
REAL DIM[ 5000 ] ARRAY WEIGHT

:  READ.BASIC.DATA
        CR ." Input filename:   "   " A:" "INPUT "CAT " .ASC" "CAT FILENAME ":=
        FILENAME DEFER> BASIC.OPEN

        5001 1 DO
                BASIC.READ
                DROP             \ Remove "1" counter from stack.
                WEIGHT [ I ] :=
        LOOP

        BASIC.CLOSE
;
```

Program B.3: ASYST file READBAS.ASY

```
\ ASYST FILE:          DIFFUS.ASY

\ This file allows the diffusion in a plane sheet and also the diffusion
\ of a solid cylinder of finite length in which diffusion is radial and
\ longitudinal to be modelled.
\ Reference:   J.M. Vergnaud, Liquid Transport Processes in Polymeric
\              Materials, 1991, Chapters 1 and 2.

\                      Created by:   Andy Chan
\                                    November 17, 1991

\   ----------------------------------------------------------------


REAL DIM[ 7 ] ARRAY ALPHA          \ Roots of Bessel function of the first kind
                                   \ of order zero
SCALAR D                           \ Diffusion coefficient
SCALAR R                           \ Radius of cylinder
SCALAR L                           \ Half length of cylinder
SCALAR B                           \ Half thickness of plane sheet

REAL DIM[ 1000 ] ARRAY T           \ Time in seconds
REAL DIM[ 1000 ] ARRAY MT/MI       \ Ratio of amount of substance remaining
                                   \ to amount initially


2.4048       ALPHA [ 1 ] :=
5.5201       ALPHA [ 2 ] :=
8.6537       ALPHA [ 3 ] :=
11.7915      ALPHA [ 4 ] :=
14.9309      ALPHA [ 5 ] :=
18.0711      ALPHA [ 6 ] :=
21.2116      ALPHA [ 7 ] :=


:  CALC.MT/MI.CYLINDER
       1001 1 DO
            32. PI DUP * /

            \ calculate first summation
            0
            8 1 DO
                 1. ALPHA [ I ] DUP * /
                 -1. ALPHA [ I ] DUP * * D * T [ J ] * R DUP * /
                 EXP
                 *
                 DUP 1E-10 < IF LEAVE THEN
```

Program B.4: ASYST file DIFFUS.ASY

```
            +
        LOOP

        \ calculate second summation
        0
        500 0 DO
            1. 2. I * 1. + DUP * /
            -1. 2. I * 1. + DUP * * PI DUP * * D * T [ J ] * 4. / L DUP * /
            EXP
            *
            DUP 1E-10 < IF LEAVE THEN
            +
        LOOP

        * * MT/MI [ I ] :=
    LOOP
;

: CALC.MT/MI.SHEET
    1001 1 DO
        8. PI DUP * /

        \ calculate summation
        0
        500 0 DO
            1. 2. I * 1. + DUP * /
            -1. 2. I * 1. + DUP * * PI DUP * * D * T [ J ] * 4. / B DUP * /
            EXP
            *
            DUP 1E-10 < IF LEAVE THEN
            +
        LOOP

        * MT/MI [ I ] :=
    LOOP
;
```

Program B.4: ASYST file DIFFUS.ASY (continued)

Appendix C: Blank Membrane Data

membrane matrix	bathing solution	bulk characteristics		charge-transfer characteristics	
		ρ_b (MΩ cm)	ε_r	ρ_{ct} (MΩ cm^2)	C_{dl} (nF)
DOA/PVC	10 mM KCl	1430	8.2	49.4	8.8
NPOE/PVC	10 mM KCl	540	21.6	not resolved	
DOS/PVC-OH	10 mM KCl	1025	7.0	1.1	20
DOPP/PVC	1 mM $CaCl_2$	310	11.9	not resolved	

DOA = dioctyl adipate
NPOE = 2-nitrophenyl octyl ether
DOS = dioctyl sebacate
DOPP = dioctyl phenylphosphonate
PVC = poly(vinyl chloride)
PVC-OH = hydroxyl-substituted PVC
ρ_b = bulk resistivity
ε_r = dielectric constant
ρ_{ct} = charge transfer resistivity
C_{dl} = double-layer capacitance